Akinetic Tuneable Optical Sources with Applications

Radu-Florin Stancu

School of Physical Sciences
University of Kent

Thesis submitted for the Doctor of Philosophy degree

July 2015

Abstract

Optical Coherence Tomography (OCT) is a modern, non-invasive imaging technique in biomedical research and medical diagnostics. It was initially developed for clinical applications in ophthalmology, providing high-resolution, cross-sectional images of the retina, retinal nerve fibre layer and the optic nerve head. Today, OCT is used for *in vivo* imaging of almost every type of tissue and it also branched out in fields outside medicine, like industrial or pharmaceutical applications.

OCT is a continuously improving imaging technique, benefiting from the development of advanced optical components and broadband optical sources. The objective of the work presented in the thesis was the development of both short and, respectively, long cavity akinetic optical devices, employing several types of dispersive optical fibre components in the cavity, like chirped fibre Bragg gratings, single mode or dispersion compensating fibre, and actively radio-frequency tuned semiconductor optical amplifiers, used as gain media. The use of external modulators, like Fabry-Perot assemblies, rotating mirrors and other mechanical devices is therefore completely eliminated, while versatility is added in the control of the coherence length, output bandwidth, repetition rate and power.

The short cavity source was developed in the 1060 nm region, the output power and bandwidth showing a slow decay with the increase of repetition rate up to 250 kHz. Without any booster, the power achieved was 2 mW at 100 kHz.

A novel dual-mode-locking mechanism was developed in order to tune an akinetic swept source based on dispersive cavities at a repetition rate close to, but different from the inverse of the cavity roundtrip. Several optical source configurations emitting in the 1060 nm or 1550 nm wavelength region were developed, characterised and tested in OCT applications. For the 1550 nm swept source employing a Faraday Rotating Mirror in a dispersive cavity, sweeping rates in the range of MHz were achieved, from 782 kHz to up to 5 times this value, with proportional decrease in the tuning bandwidth. Linewidths smaller than 60 pm and output powers exceeding 10 mW were measured. OCT topographic imaging was demonstrated.

The thesis ends with a proposed broadband investigation of microresonators written in silica glass employing akinetic optical sources at 1550 nm.

The work presented in this thesis resulted in several peer reviewed papers, one patent application and several conference presentations, listed after the final conclusions.

The work presented in this thesis was performed within the Applied Optics Group at the University of Kent, School Physical Sciences, Canterbury, CT2 7NH, United Kingdom, supported by the European Research Council (ERC) grant number **249889**.

Acknowledgements

I would like to thank my main supervisor, Prof. Adrian Podoleanu, for his constant support, guidance and patience throughout the last four years. Thank you for sharing your vast knowledge, professionalism and innovative ideas in the fields of Optical Coherence Tomography and wavelength swept fibre lasers. Special thanks to Prof. George Dobre, my second supervisor, and Emer. Prof. David A. Jackson, for all the good advice and scientific ideas exchanged during my work. I would also like to express my gratitude and thanks to all my professors from Romania that taught me in my undergraduate and master studies and helped me shaping in the professional I am today.

Many thanks to my former postgraduate colleagues in the group, Chris Costa, Mantas Zurauskas, Hannah Irons and Andrew Payne. Together we have founded in 2012 the OSA Student Chapter at the University of Kent, which represents a great achievement and initiative which hopefully will endure for many years in the future. Also many thanks to Manuel Marques, Jong Hu and Michael Maria for continuing the projects started within the chapter. I also want to thank all of them, including here our newest colleagues, Catherin Chin and Florin Toadere, for their friendship, the lovely dinners and cinema evenings, the trips organised through the United Kingdom, France, Belgium or Romania.

I would like to express my appreciation and warm thanks to dr. Ramona Cernat for being the voice of reason whenever I had stressful times and failures in my experiments. I would also like to thank her for all the help and support she provided me during my experiments. Many thanks to dr. Adrian Bradu for the good advice and for training me in using several important pieces of equipment and software in the lab, without which I would have been completely lost in my work, and to dr. Jingyu Wang for helping me out in always finding the components I needed urgently in my experiments.

I would like to express my gratitude and love to my parents, Gheorghe and Cristina, and my sister, Mihaela, for their love, support and good advice that guided me in my life so far and for always being encouraging towards even my craziest endeavours. Special thanks and lots of love to my family in the UK, Daniel and Jane Dobre, and their three wonderful children, Elena, Issy and Jack, for helping me integrating quickly in the British society, for the kind words, for their constant support, advice and encouragement. To all my close friends in the UK and Romania: I love you guys, thank you for your camaraderie, for being there for me whenever I needed it and for the awesome time we spend together.

Table of contents

List of abbreviations/ acronyms

OCT – Optical Coherence Tomography

FDML – Fourier Domain Mode-Locking

RF – Radio Frequency

SMF – Single Mode Fibre

FRM – Faraday Rotating Mirror

NIR – Near Infra-Red

CM – Confocal Microscopy

MRI – Magnetic Resonance Imaging

LCI – Low Coherence Interferometry

AOG – Applied Optics Group

SLO – Scanning Laser Ophthalmoscopy

OCT/SLO – Optical Coherence Tomography/ Scanning Laser Ophthalmoscopy

MSI – Master Slave Interferometry

FP – Fabry-Perot

AKSS – Akinetic Swept Source

SS – Swept Source

SS-OCT – Swept Source Optical Coherence Tomography

MEMS – Micro Electrical Mechanical Scanning

DCF – Dispersion Compensating Fibre

cFBG – chirped Fibre Bragg Grating

SLD – SuperLuminiscent Diode

TD-OCT – Time Domain Optical Coherence Tomography

SD-OCT – Spectral Domain Optical Coherence Tomography

SB-OCT – Spectrometer Based Optical Coherence Tomography

FT – Fourier Transformation

PSF – Point Spread Function

FWHM – Full Width Half Maximum

OPD – Optical Path Difference

Sp-OCT – Optical Coherence Tomography

CMOS – Complementary Metal–Oxide–Semiconductor

SN – Shot Noise

RIN – Relative Intensity Noise

SOA – Semiconductor Optical Amplifier

PCF – Photonics Crystal Fibre

FSR – Free Spectral Range

RFA – Radio Frequency Amplifier

VCO – Voltage Controlled Oscillator

STG – Saw-Tooth Generator

VCSEL – Vertical-Cavity Surface-Emitting Laser

FBG – Fibre Bragg Grating

ISO – (Fibre Optic) Isolators

FFT – Fast Fourier Transformation

ASE – Amplified Spontaneous Emission

TFPF – Tuneable Fabry Perot Filter

PM – Polarisation Maintaining

RFSG – Radio Frequency Signal Generator

PMF – Polarisation Maintaining Fibre

PMD – Polarisation Mode Dispersion

PC – Polarisation Controller

PhD – PhotoDetector

DML – Dual Mode-Locking

MS – Master-Slave

TS – Translation Stage

OSA – Optical Spectrum Analyser

InGaAs – Indium Gallium Arsenium

BS – Beam Splitter

GS – Galvo-Scanner

WGM – Whispering Gallery Modes

Q – Quality

WDM – Wavelength Division Multiplexing

FC/APC – Fiber-optic Connector/ Angle Physical Contact

List of figures

1

Introduction

1.1. Synopsis

The work presented in the thesis is organised within the following chapters:

Chapter 2 reveals a brief history of OCT that shows the evolution from a basic interferometric imaging system to the modern OCT technologies and applications used today in various fields, like biomedicine, biology, art, material testing and so on. This chapter also includes a short description and theory of the two main types of OCT, time domain and spectral domain and concludes with the main types of optical broadband sources integrated in OCT systems.

Chapter 3 illustrates the types of fibre based optical swept source devices used in imaging and discusses some of the performance indicators that have established high resolution, state of the art OCT imaging technologies. A summary of optical sources that have been successfully integrated in commercial OCT imaging apparatuses, like FDML or the dispersion tuning based swept lasers is also covered in this chapter.

Chapter 4 presents the theoretical considerations that stand behind the akinetic swept sources based on dispersive cavities and use only one mode-locking mechanism. A brief illustration of the proposed mode-locking RF configurations and the optical swept source cavities that can support those configurations is included.

Chapter 5 covers experimentally the design considerations and measurements of the optical parameters of a 1060 nm central wavelength akinetic swept source based on short dispersive cavities that comprise chirped fibre Bragg grating. A proposed 1310 nm cavity design is also proposed.

Chapter 6 focuses on the theory of the recently patented dual-mode-locking mechanism created to tune an akinetic swept source based on dispersive cavities at a repetition rate close to but different from the inverse of the cavity roundtrip.

Chapter 7 exemplifies the types of swept sources and RF mechanisms described in chapter 6 for the cavities that comprise SMF, for the 1060 nm and 850 nm wavelengths. It also illustrates how a particular upgrade in the optical design by integrating a Faraday rotating mirror (FRM) can determine an improvement in several output measured parameters. The chapter ends with the presentation of a basic OCT application that integrates the dual mode-locked 1060 nm swept source, depicting the type of topographic images of a pressure sensitive adhesive that are acquired.

Chapter 8 describes the experiments and measurements done on akinetic swept sources based on dispersion compensating fibre at 1550 nm. Again, the role of the FRM integration in the cavity is illustrated, while considering both the single and the dual mode-locking RF mechanisms. As in the previous chapter, the utility of the swept laser at 1550 nm is illustrated in an OCT application. Also, a proposed application that involves the broadband characterisation of whispering gallery mode microresonators is included.

Chapter 9 summarizes the achievements of the work presented and proposes ideas for future work.

The references used in this work are listed at the end of each chapter.

The thesis ends with a series of annexes that enumerate the scientific papers, patent and conference dissemination that resulted as a consequence of the work presented here.

1.2. Overview

Optical properties in tissues

The field of lasers developed for biomedical applications, either therapeutic or used in diagnosing, is a rapidly growing field. The *in vivo* light-tissue interaction in the diagnostic approach results in the study of the physiology or pathology of the tissue, with no damage being induced at cellular level. The three main optical properties that characterise this type of interaction are the absorption, scattering and refractive index.

The refractive index n of an optical medium is a number calculated by dividing the speed of light in vacuum to the light propagation speed in the medium: c_0/v. Refraction is an optical phenomenon that occurs when light is incident at the boundary between two media of different indices of refraction and it is defined by Snell's law, $v_1 \cdot sin(\theta_1) = v_2 \cdot sin(\theta_2)$, where θ_1 is the angle of incidence, θ_2 is the angle of refraction, and v_1 and v_2 represent the speeds of light in the media. Biological tissue is a multi-structured media, each constituent being characterised by a different index of refraction.

Another important parameter that characterises tissues is absorption. The transmitted light intensity $I(x)$ across a homogeneous and non-scattering medium of thickness x, which is illuminated by a collimated beam of light is given by the following equation:

$$I(x) = I_0 e^{-\mu_{abs} x}, \qquad (1.2-1)$$

where I_0 represents the intensity of the incident light and μ_{abs} is the absorption coefficient characteristic for a given wavelength λ. In tissues, the compounds that absorb light in a certain spectral region of interest are known as chromophores. The therapeutic window, depicted in Fig. 1.2.1 [1], represents the chromophores absorption window in the near-infrared range (NIR). The major absorbents in the soft tissues are water (H_2O), oxyhaemoglobin (Hb) and deoxyhaemoglobin (HbO_2), while the minor ones are other chromophores like melanin and lipids (fat).

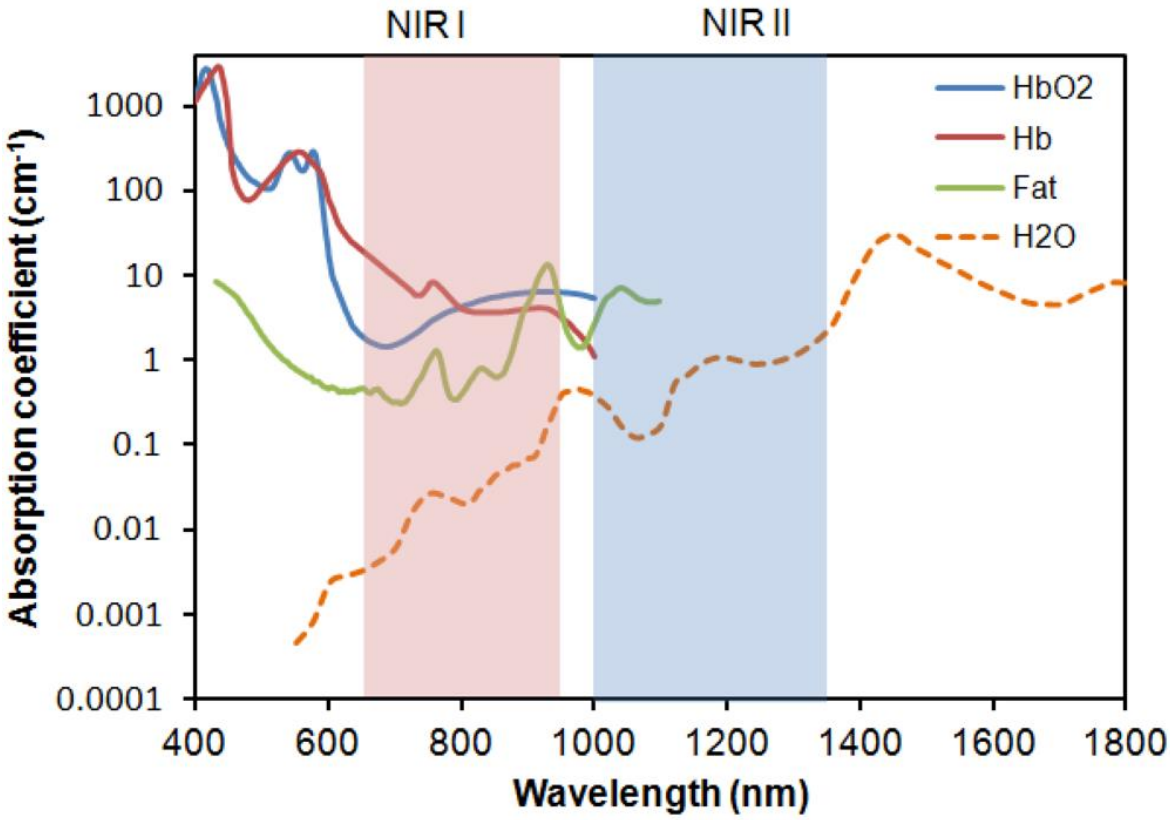

Fig. 1.2.1. The therapeutic window – reprinted from [1]

Scattering is defined very similarly as the absorption:

$$I(x) = I_0 e^{-\mu_{scatt} x}, \qquad (1.2-2)$$

where μ_{scatt} is the scattering coefficient of the medium, corresponding to a certain wavelength λ of the incident light. It is a physical process through which light transmitted in a tissue changes its direction when interacting with particles of variable size or when there is a change in the refractive index determined by various tissue components, like membranes.

Optical Coherence Tomography – a brief history

Helmholtz invented the first ophthalmoscope in 1851, which was later commercialised in 1920 by Zeiss, naming the technique applied with this back of the eye imaging device fundus photography. This technology was quite straight forward; a carbon-arc lamp illuminated the back of the eye using a partially reflective mirror. The light reflected from the retina was

magnified to form an image, first of this kind being achieved in 1886, showing the optic disk and the larger blood vessels.

In 1957 the confocal microscopy (CM) was invented by Marvin Minsky [2]. While with the fundus photography ophthalmoscope the whole retina was illumined in the same time on the whole surface, the confocal microscope uses point by point illumination and a pinhole in an optically conjugate plane in front of the detector to eliminate the reflected signal that is not in focus [3]. This method creates a 2D image with about 300 μm depth resolution, but on the on the other hand it is not fast. The confocal scanning laser microscopy became the standard technique used worldwide by the end of the 1980s.

Another technique uses ultrasound imaging and it is mainly used for ocular distance quantitative measurements [4] or glaucoma diagnosing [5]. The depth resolution is rather limited, of about 150 μm and the method itself is quite invasive, the probe emitting the sound waves needs to be placed in direct contact with the cornea (or indirect, by putting a liquid state substance between the eye and the probe), which creates discomfort for the patient. The sound waves are also quite severely attenuated by the various layers in the eye.

Other methods considered are the magnetic resonance imaging (better known as MRI) [6] and the computed tomography [7], but despite their efficiency as diagnosing tools for other parts of the body, they do not offer enough resolution in order to achieve an image of the retinal layers.

Optical Coherence Tomography (OCT), a non-invasive technique based on low coherence interferometry (LCI), offered the solution to correct the insufficiencies of the techniques described above. Late 1980's papers [8, 9] revealed the first *in vivo* human eye distance measurement, offering a significant increase in resolution and sensitivity.

The axial resolution of an OCT system is influenced directly by the coherence properties of the optical source used. In comparison with CM, OCT enables micrometre resolution imaging in all directions separating the axial and transversal resolution. The first papers illustrated 2D and 3D OCT imaging of the retinal layers with resolution values approaching histology [10-12]. Another important feature greatly appreciated by doctors is the non-invasiveness of this method in clinical investigations.

The first commercial OCT device was manufactured by Carl Zeiss Meditec in 1996 [13], and since then the research and market developing biomedical OCT solutions increased significantly. OCT benefits continuously from the development of fibre optics market and advanced optical fibre based components and broadband optical sources [14]. Faster and broader band fibre lasers are developed on this growing market, which ultimately will lead

to improved and sophisticated OCT technologies. The OCT imaging market is currently dominated by 19 companies, reaching $800 million in 2012 [15]. The growing interest in research activities in the pharmaceutical and biotechnology sectors, and the continuous development in optical imaging techniques for therapeutic and diagnostic purposes will determine a further market growth up to $1,669.2 million in 2019 [16].

OCT applications – a general view

As mentioned before, OCT was initially developed as an alternative to the confocal microscopy and other techniques used to image the eye. The clinical studies of OCT in ophthalmology are crucial in detecting macular degeneration [17, 18], offering a method of axonal integrity assessment in multiple sclerosis and represent an efficient tool in investigating the progression of glaucoma (a disease responsible of severe optical nerve damage that in time leads to blindness).

OCT was also introduced in other biomedical fields, with extensive clinical studies and *in vivo* applications, like cardiovascular [19] (to detect the coronary arteries that are susceptible to lipid plaque depositions), gastrointestinal [20], pulmonary [21] or cancer research [22]. Scanning probes of small dimensions (millimetre and submillimetre) placed at the tip of a fibre are inserted through a catheter into blood vessels, capillaries or air tracts without hurting or creating any unpleasant effects on the patients [23]. Recently, OCT was also introduced in dentistry [24], in order to identify and examine possible damages, like micro-fissures, cavities or to check root canals. Brain imaging was also performed with OCT on animal subjects (mice) [25].

Due to the improved depth resolution and imaging speed, OCT became very attractive in industrial applications, like non-destructive testing, silicon wafer and semiconductor composites thickness [26], topographic surface and roughness characterisation, volume loss measurements. As in the biomedical applications using fibre based OCT systems, small probes can be used in environments exhibiting extreme conditions like radioactivity and hot or cryogenic temperatures. OCT also represents a viable solution as quality control tool in the pharmaceutical industry, being capable to validate the production flow of medicine by fast evaluation of the coatings applied on pills [27].

In the Applied Optics Groups (AOG) at the University of Kent, several OCT applications were pioneered: the *en-face* imaging of the human retina, simultaneous OCT/SLO imaging system [28], the Shack-Hartmann coherence gated wavefront sensing

[29] and the master-slave interferometry (MSI) [30]. By continuously improving and combining optical configurations and signal processing methods, the AOG is aiming to combine spectral domain with time domain imaging in order to achieve long axial range and simultaneous imaging at several depths.

Therefore, between 2008 and 2011, more work was dedicated by AOG (in collaboration with Multiwave, Portugal) on optical swept source research, especially the ones using Fabry-Perot (FP) filters as tuning mechanisms [31, 32]. Recently, a new line of research was designated on akinetic swept sources (AKSS) based on dispersive intra-cavity elements [32, 33]. A novel dual mode-locking mechanism was also developed [34] and it will represent one of the main novel features of the work described in the following chapters.

1.3. Motivation

The method considered the most promising today for OCT is based on sweeping the frequency of a narrow band laser, usually termed as a swept source. Swept source optical coherence tomography (SS-OCT) represents a modern, non-invasive technique of tissue biomedical imaging that uses fast swept narrow linewidth lasers, where sweeping takes place within a sufficiently wide tuning bandwidth [36]. OCT experiments are either performed *in vivo*, especially retinal imaging, which requires a SS with a large axial range, or *in vitro*, for thin, microscopic tissue samples. The latter applications do not necessarily need fast sweeping or narrow linewidth, but in turn could benefit from the use of more cost effective lasers, with enhanced versatility in terms of allowing control of the output optical parameters, such as linewidth, pulse repetition rate or power.

Several principles of sweeping the laser emission have been developed. The current trend in SS-OCT is to increase its axial range, by achieving coherence lengths longer than 1 cm. However, such optical sources are expensive and they do not serve all ranges of OCT applications. Our group has pioneered multiple path SS-OCT configurations using active loops equipped with frequency shifters that can deliver reflectivity profiles in several axial ranges simultaneously [37]. Such a configuration, when driven by a SS with a coherence length shorter than 0.5 mm, can achieve axial imaging in tens of simultaneous channels, regaining in this way an overall axial range larger than 5 mm [37], achievable otherwise with a conventional configuration driven by a long coherence SS. In this way, multiple and simultaneous interrogation is achieved in several axial optical path differences.

The most common principle employed is that of a spectral filter in a closed loop, where the tuneable laser apparatus uses a FP filter, as disclosed in [21], a polygon filter [38], or a micro electrical mechanical scanning (MEMS) filter, as shown in [39]. Commercial vendors exist, such as Axsun and Santec, companies using MEMS filters. Such filters limit the tuning to several hundreds of kHz. In [40] a large tuning frequency has been reported using FP filters and principles of Fourier domain mode-locking (FDML) that allowed sweeping rates exceeding several MHz. Linewidths achieved are usually narrower than 0.1 nm. However, the reliability of FP and the complexity of buffering limit the applicability of such principles. The filters mentioned above are based on mechanical movement of parts which limits their reliability. Therefore, there is an interest in akinetic laser sources that achieve tuning with no mechanical movement of parts. Simultaneously, in modern

applications of OCT there is an increasing demand in 3D imaging at high speed, with increased axial range.

Examination of microscopic thin samples represents an inefficient use of a state of the art long coherence optical swept source. Also, there are applications where the *en-face* image [2], to be software generated, demands integration over many pixels along depth. Using a SS with a selectable coherence length would allow quicker calculation of an *en-face* image as less axial pixels are involved. Another application is that of coherence gated wavefront sensing [29, 41], where elimination of stray reflections in the system is always more important than providing depth resolved aberrations. In this case, a small tuning bandwidth is acceptable, as no depth resolved data are needed. Also, a small linewidth is not necessary to cover a large axial range, as inference of an *en-face* image of coherence gated Shack Hartmann spots at a shallow depth is all what is needed.

In order to target an axial range limited to sub mm, linewidth narrower than 0.5 nm to several nm are needed. State of the art sources on the market that use resonant micro-electro-mechanical system (MEMS) filters exhibit a fixed tuning rate and a fixed axial range (so a fixed coherence length), close to 1 cm. Other solutions that are employing rotating polygon mirrors in the spectral filter determine a fixed scanning rate, together with the penalty of high cost.

The interest in AKSSs has been raised by the demonstration of fast, wide tuning bandwidth and large coherence length tuneable lasers based on VCSEL devices [42]. An AKSS concept using mode-locking in an anomalous dispersive cavity employing dispersion compensating fibre (DCF) was recently introduced [43, 44]. In order to achieve wide and fast tuning with a narrow spectral linewidth, it was shown that the dispersion characteristic of DCF and the modulation frequency should be as large as possible, while the cavity length should be as small as possible. However, this method has limited tuning capabilities, due to the significant decrease in output power when driving it at high frequency repetition rates. A solution to this issue problem is presented, which includes a positive dispersion region, a negative dispersion region and two modulators in a ring resonator, assembly which brings the amount of wavelength dispersion to approximately zero [45]. This solution relies though on externally driven modulation units, such as acousto-optic or electro-optic modulators.

In [46] a wavelength swept fibre laser apparatus using a partially reflective chirped fibre Bragg (cFBG) grating as dispersive medium is presented. Although the tuning wavelength range obtained is broad, the OCT imaging speed achieved was only up to 250 kHz, which is below the values demanded by modern swept source OCT applications.

Therefore, there is an interest in developing broadband akinetic swept lasers that can address the disadvantages of the concepts briefly presented above by providing much larger tuning speeds, possibly at multiples of cavity resonance and with an adjustable coherence length for the type of application where the source is used. It would also be desirable if the RF mode-locking mechanism is easy to integrate and the AKSS prototype is as compact and cost effective as possible.

References

[1] Chai-Hoon Quek, Kam W. Leong, "Near-Infrared Fluorescent Nanoprobes for *in Vivo* Optical Imaging", Nanomaterials, 2(2), 92-112 (2012)

[2] M. Minsky "Memoir on Inventing the Confocal Scanning Microscope", Scanning, vol.10 pp. 128-138 (1988)

[3] R. H. Webb, G. W. Hughes, F. C. Delori, "Confocal scanning laser ophthalmoscope", Applied Optics, 26(8), 1492-1499 (1987)

[4] T. Olsen, "The accuracy of ultrasonic determination of axial length in pseudophakic eyes", Acta Ophthalmologica, 67(2), 141-144 (2009)

[5] C. J. Pavlin, F. S. Foster, "Ultrasound biomicroscopy in glaucoma", Acta Ophthalmologica – Suppl.1992; 204:7–9 (1992)

[6] L. Fanea, A. J. Fagan, "Review: Magnetic resonance imaging techniques in ophthalmology", Molecular Vision 2012; 18, 2538-2560 (2012)

[7] D.V. Beard, E. D. Pisano, K. M. Denelsbeck, and R. E. Johnston, "Eye Movement During Computed Tomography Interpretation: Eyetracker Results and Image Display-Time Implications", Journal of Digital lmaging, 7(4), 189-192 (1994)

[8] A. F. Fercher, E. Roth, "Ophthalmic laser interferometry", Proc. SPIE 658, 48-51 (1986)

[9] A. F. Fercher, K. Mengedoht, W. Werner, "Eye-length measurement by interferometry with partially coherent light", Optics Letters, 13(3), 186-188 (1988)

[10] D. Huang, E. A. Swanson, C. P. Lin, J. S. Schuman, W. G. Stinson, W. Chang, M. R. Hee, T. Flotte, K. Gregory, C.A. Puliafito et al., "Optical Coherence Tomography", Science, 254(5035), 1178-1181 (1991)

[11] A. F. Fercher, C. K. Hitzenberger, W. Drexler, G. Kamp, H. Sattmann, "In vivo optical coherence tomography", American Journal of Ophthalmology, 116(1), 113-114 (1993)

[12] E. A. Swanson, J. A. Izatt, M. R. Hee, D. Huang, C. P. Lin, J. S. Schuman, C. A. Puliafito, J. G. Fujimoto, "In vivo retinal imaging by optical coherence tomography", Optics Letters, 18(21), 1864-1866 (1993)

[13] U. Rimayanti, Y. Kiuchi, R. Maulidia, "Review Article: The Development and Applications of Optical Coherence Tomography", Austin Journal of Clinical Ophthalmology 2014;1(7): 1032 (2014)

[14] A. G. Podoleanu, “Fiber optics, From sensing to non invasive high resolution medical imaging”, Journal of Lightwave Technology, 28(4), 624-640 (2010)

[15] G. Smolka, “Optical Coherence Tomography: Technology, Markets and Applications 2008-2012”, Technical report, PennWell Corporation

[16] MarketsandMarkets,“Optical Imaging Market by Technique (Optical Coherence Tomography, Hyperspectral Imaging, Photoacoustic Tomography), Product (Imaging System, Imaging software) & by Application (Ophthalmology, Neurology, Oncology, Cardiology) - Global Forecasts to 2019”, MD 2818 (2014)

[17] C. A. Puliafito, M. R. Hee, C. P. Lin, et al. “Imaging of macular diseases with optical coherence tomography”, Ophthalmology 102:217–229 (1995)

[18] F. Coscas, G. Coscas, E. Souied, S. Tick, G. Soubrane. “Optical coherence tomography identification of occult choroidal neovascularization in age-related macular degeneration”, American Journal of Ophthalmology 144:592–599 (2007)

[19] O. C. Raffel, T. Akasaka, I.-K. Jang, “Cardiac optical coherence tomography”, Heart, 94(9), 1200-1210 (2008)

[20] T. S. Kirtane, M. S. Wagh, “Endoscopic Optical Coherence Tomography (OCT): Advances in Gastrointestinal Imaging”, Gastroenterology Research and Practice Volume 2014, Article ID 376367 (2014)

[21] Z. Dai, Y. Fukumoto, S. Tatebe, K. Sugimura, Y. Miura, K. Nochioka, T. Aoki, S. Miyamichi-Yamamoto, N. Yaoita, K. Satoh, H. Shimokawa, “OCT Imaging for the Management of Pulmonary Hypertension”, JACC Cardiovascular Imaging, 7(8), 843-845 (2014)

[22] M. Mogensen, L. Thrane L, T. M. Jørgensen, P. E. Andersen, G. B. Jemec, “OCT imaging of skin cancer and other dermatological diseases”, J. Biophotonics, 2(6-7):442-51 (2009)

[23] N. R. Munce, G. A. Wright, A. Mariampillai, B. A. Standish, M. K. Leung, L. Tan, K. Lee, B. K. Courtney, A. A. Teitelbaum, B. H. Strauss, I. A. Vitkin, V. X. Yang, “Doppler optical coherence tomogprahy for interventional cardiovascular guidance: in vivo feasibility and forward-viewing probe flow phantom demonstration”, Journal of Biomedical Optics, 15(1), 011103 (2010)

[24] B.T. Amaechi, A. Podoleanu, S.M. Higham et al, “Correlation of quantitative light-induced fluorescence and optical coherence tomography applied for detection and quantification of early dental caries,” Journal of Biomedical Optics 8 (4), 642-647 (2003)

[25] S. J. Madsen, “Optical Methods and Instrumentation in Brain Imaging and Therapy”, Springer, pp. 163, ISBN 978-1-4614-4978-2 (2013)

[26] W. J. Walecki et al., “Determining thickness of slabs of materials”, US Patent 7,116,429 (2006)

[27] D. Markl, G. Hannesschlager, S. Sacher, M. Leitner, J. G. Khinast, “Optical coherence tomograpy as a novel tool for in-line monitoring of pharmaceutical film-coating process”, Eur. J. Pharm. Sci., 13:55:58-67 (2014)

[28] A. G. Podoleanu, D. A. Jackson, “Combined optical coherence tomograph and scanning laser ophthalmoscope”, Electronics Letters, 34(11), 1088-1090 (1998)

[29] J. Wang, A. Podoleanu, “Demonstration of real-time depth-resolved Shack–Hartmann measurements”, Optics Letters, 37(23), 4862-4864 (2012)

[30] A. G. Podoleanu, A. Bradu, “Master-Slave interferometry for parallel spectral domain interferometry sensing and versatile 3D optical coherence tomography”, Optics Express, 21(16), 19324-19338 (2013)

[31] I. Trifanov, P. Caldas, L. Neagu, R. Romero, M. O. Berendt, J.R. Salcedo, A. G. Podoleanu, A. B. Lobo Ribeiro, “Combined Nedymium-Ytterbium Doped ASE Fiber Optic Source for Optical Coherence Tomography Applications”, IEEE Photonics Technology Letters, 23(1), 21-23 (2011)

[32] I. Trifanov, A. Bradu, L. Neagu, P. Guerreiro, A. B. L. Ribeiro, A. G. Podoleanu, “Experimental method to find the optimum excitation waveform to quench mechanical resonances of Fabry–Pérot tunable filters used in swept sources,” IEEE Photonics Technology Letters, 23(12), 825–827 (2011)

[33] R. F. Stancu, D. A. Jackson, “Versatile Swept Source with Adjustable Coherence Length”, IEEE Photonics Technology Letters 26 (16), 1629-1632 (2014)

[34] R. F. Stancu, D. A. Jackson, A. G. Podoleanu, “Akinetic swept source with adjustable coherence length for SS-OCT”, Proc. SPIE 9312, SPIE BiOS 931238-931238-5 (2015)

[35] R. F. Stancu, A. G. Podoleanu, “Dual-mode-locking mechanism for an akinetic dispersive ring cavity swept source”, Optics Letters 40(7), 1322-1325 (2015)

[36] A. G. Podoleanu, “Optical coherence tomography”, J. Microscopy 247(3), 209-219, (2012)

[37] A. Bradu, L. Neagu, A. Podoleanu.,” Extra long imaging range swept source optical coherence tomography using re-circulation loops”, Optics Express, 18(24), 25470 (2010)

[38] S. H. Yun, G. Boudoux, G. J. Tearney, B. E. Bouma, “High-speed wavelength-swept semiconductor laser with a polygon-scanner-based wavelength filter”, Optics Letters 28(20), 1981-1983 (2003)

[39] J. Masson, R. St-Gelais, A. Poulin, and Y.-A. Peter, “Tunable Fiber Laser Using a MEMS-Based In Plane Fabry-Pérot Filter”, IEEE J. Quantum Electron. 49, 9, (2010)

[40] R. Huber, M. Wojtkowski, J.G. Fujimoto, “Fourier Domain Mode-locking (FDML): A new laser operating regime and applications for optical coherence tomography”, Optics Express 14(8), 3225-3237 (2006)

[41] S. Tuohy, A. Gh. Podoleanu, “Depth-resolved wavefront aberrations using a coherence-gated Shack-Hartmann wavefront sensor”, Optics Express 18, 3458-3476 (2010)

[42] T.-H. Tsai; O. O. Ahsen; H.-C Lee; K. Liang; M. G. Giacomelli; B. Potsaid; Y. K. Tao; V. Jayaraman; M. F. Kraus; J. Hornegger; M. Figueiredo; Q. Huang; H. Mashimo; A. E. Cable; J. G. Fujimoto, “Ultrahigh speed endoscopic swept source optical coherence tomography using a VCSEL light source and micromotor catheter”, Proc. SPIE 8927, Endoscopic Microscopy IX; and Optical Techniques in Pulmonary Medicine, 89270T (2014)

[43] S. Yamashita, M. Asano, “Wide and fast wavelength-tunable mode-locked fiber laser based on dispersion tuning”, Optics Express 14(20), 9399-9306 (2006)

[44] Y. Nakazaki, S. Yamashita, “Fast and wide tuning range wavelength-swept fiber laser based on dispersion tuning and its application to dynamic FBG sensing”, Optics Express 17(10), 8310-8318 (2009)

[45] K. Furusawa et al., “Laser apparatus, driving method of the same and optical tomographic imaging apparatus”, US Patent 8605768 B2, Dec. 10 (2013)

[46] Y. Takubo, S. Yamashita, “High-speed dispersion-tuned wavelength-swept fiber laser using a reflective SOA and a chirped FBG”, Optics Express, 21(4), 5130-5139 (2013)

2

Optical Coherence Tomography

OCT is a modern, non-invasive, high resolution optical imaging technique based on Michelson interferometry, in which interference occurs between the signal reflected by an investigated object and the reference signal [1]. A 2D real time cross section image of the object is produced. The axial resolution is determined by the optical source used in the system, therefore in ophthalmology applications, the human retina can be imaged with an axial resolution 100 times better than with a CM system [2]. A high depth resolution is achieved even when using small diameter beams to image eyes, additionally subject to chromatic aberration. Unlike the CM, the depth resolution does not depend anymore on the aperture of a microscope objective [1]. In [3], for example, by using a 150 nm bandwidth SLD around 890 nm central wavelength, a depth resolution of approximately 3 μm was achieved, the OCT system being able to acquire an image with a lateral size of 7.5 mm, vertical size 0.725 mm, where the following layers of the retina are identifiable: the inner limiting membrane, nerve fibre layer, ganglion cell layer, inner plexiform layer, inner nuclear layer, outer plexiform layer, outer nuclear layer, external limiting membrane, the junction between the inner and outer photoreceptors, the pigment epithelium, the choriocapillaris and the choroid.

There are two types of OCT techniques, time domain (TD-OCT) and spectral domain (SD-OCT). TD-OCT is historically the first that appeared and it relies on depth scanning done with mechanical means, while SD-OCT represents a more modern approach which eliminates this need. There are also two types of SD-OCT developed, the spectrometer based OCT (SB-OCT) and the one that uses a swept source or a broadband tuneable laser (SS-OCT). The similarity in the TD-OCT and SB-OCT comes in the fact that the depth resolution

depends on the optical source bandwidth, while in SS-OCT the same parameter depends on the tuning bandwidth.

In order to achieve an efficient and competitive *in vivo* OCT tissue imaging, the following demands need to be fulfilled: visualisation of cellular and subcellular morphology, 3D imaging, high contrast, biochemical compatibility, molecular sensitivity and acceptable tissue absorption limits, localised tissue information and sufficient tissue penetration with as reduced attenuation as possible.

The design of an OCT system is based on free space Michelson interferometry, but also includes several additional features like delay lines, dispersion compensating elements, signal chirping and other optical assemblies in order to improve the quality of the image being acquired [1, 2, 4-11].

The low coherent electromagnetic wave electric field is a complex parameter expressed as follows:

$$E_i = s(k,\omega)e^{i(kz-\omega t)}, \qquad (2-1)$$

where $s(k,\omega)$ is the amplitude of the electrical field as function of the wavenumber $k = 2\pi/\lambda$ (also named spatial frequency) and the angular frequency $\omega = 2\pi\nu$ (also considered temporal frequency).

The sample imaged is considered to have a depth dependent reflectivity profile along the z-axis determined by N discrete delta functions:

$$r_S(z_S) = \sum_1^N r_{Sp}\delta\left(z_S - z_{Sp}\right), \qquad (2-2)$$

where r_S represents the electric field reflectivity, and z_S is the path length from the beam splitter separating the incident beam into a reference beam, respectively an object beam. The electric field returned by backscattering from the sample is given by the following expression:

$$E_S = \frac{s(k)}{\sqrt{2}}\left[r_S(z_S) \otimes e^{2ikz_S}\right] = \frac{s(k)}{\sqrt{2}}\sum_{p=1}^N r_{Sn}\left(z_{Sp}e^{2ikz_{Sp}}\right) \qquad (2-3)$$

where "⊗" means convolution. The electrical field returning from the reference arm is expressed as:

$$E_R = \frac{s(k)}{\sqrt{2}} r_R(z_R) e^{2ikz_R}, \qquad (2-4)$$

where r_R represents the electrical field reflectivity and z_R represents the distance from the beam splitter.

The photodetected current due to interference of the two fields can be written as:

$$I_D = \langle E \cdot E^* \rangle = \langle |E^2| \rangle \qquad (2-5)$$

Considering that the photodetector has a responsivity ρ, (2-5) becomes:

$$I_D(k, \omega) = \frac{\rho}{2} \langle (E_R + E_S)(E_R + E_S)^* \rangle \qquad (2-6)$$

By introducing (2 – 3), (2 – 4) in (2 – 6), considering $z = 1$ and introducing the power reflectivities $R_R = |r_R|^2$, $R_{Sn} = |r_{Sn}|^2$ and the low coherence source power spectral density $S(k) = \langle |s(k, \omega)|^2 \rangle$, the spectral interferogram $I(D_k)$ is obtained as:

$$I(D_K) = \frac{\rho}{4} [S(k)(R_R + R_{S1} + R_{S2} + \cdots)] + \\ + \frac{\rho}{2} \left[S(k) \sum_{p=1}^{N} \sqrt{R_S R_{Sp}} \left(e^{2ik(z_R - z_{Sp})} + e^{-2ik(z_R - z_{Sp})} \right) \right] + \\ + \frac{\rho}{2} \left[S(k) \sum_{p=1}^{N} \sqrt{R_{Sp} R_{S_m}} \left(e^{2ik(z_{Sp} - z_{Sm})} + e^{-2ik(z_{Sp} - z_{Sm})} \right) \right] \qquad (2-7)$$

The first term in equation (2 – 7) represents the DC component, which although contain some sample information, cannot be used to provide depth resolved information.
. The second term, called cross correlation, represents the desired OCT signal containing the information regarding the sample reflectivity profile. The third term is known as autocorrelation term and represents interference due to signals originating at different depth inside the sample. Usually, the term to the total photodetected current is reduced by increasing the power in the reference arm.

On top of the autocorrelation term, several other stray reflections within the interferometer can add up to the photodetected signal. The totality of such reflections constitute a coherent noise, that can be easily subtracted by first acquiring the interference signal where the object was removed and replaced with a mirror.

To decode the photodetected low coherent optical signal a Gaussian shaped optical spectrum is considered due to that fact that when applying Fourier transformation (FT), a single peak is obtained.

The inverse Fourier transform of the source power spectrum (also known as correlation function) is denoted $\gamma(z)$ and it is defined by the spectral bandwidth Δk:

$$\gamma(z) = e^{-z^2 \Delta k^2} \tag{2 – 8}$$

The correlation function is a very important parameter in OCT, because its shape and width define point spread function (PSF) that determines the axial resolution in the system. The axial PSF is defined as the FWHM value of the coherence length of the optical source.

Assuming a Gaussian spectrum shape, the coherence length l_c is defined either as a function of wavenumber k or wavelength λ as:

$$l_c = \frac{2\sqrt{ln2}}{\Delta k} = \frac{2ln2}{\pi} \frac{\lambda_0^2}{\Delta \lambda}, \tag{2 – 9}$$

where $\lambda_0 = 2\pi/k_0$ and $\Delta k = 0.83 \cdot \Delta\lambda/\lambda_0^2$, λ_0 represents the central wavelength, and $\Delta\lambda$ represents the FWHM bandwidth. From the last expression it is concluded that the broader the bandwidth of the optical source, the better the axial resolution. In practice, several other factors limit the quality of the OCT imaging system like the non-Gaussian spectral output of the source, the spectral response of the optical components, the chromatic dispersion or the non-linear optical properties of the sample being imaged.

In continuation, a brief theoretical presentation will be performed on TD-OCT and SD-OCT, also revealing the main advantages and disadvantages of both methods.

2.1. Time-domain OCT

A typical TD-OCT system, as depicted in Fig. 2.1.1, uses an assembly comprising a broadband optical source, a Michelson interferometer and a photodetector integrated in a processing unit, responsible with registering and analysing the interference signal [1].

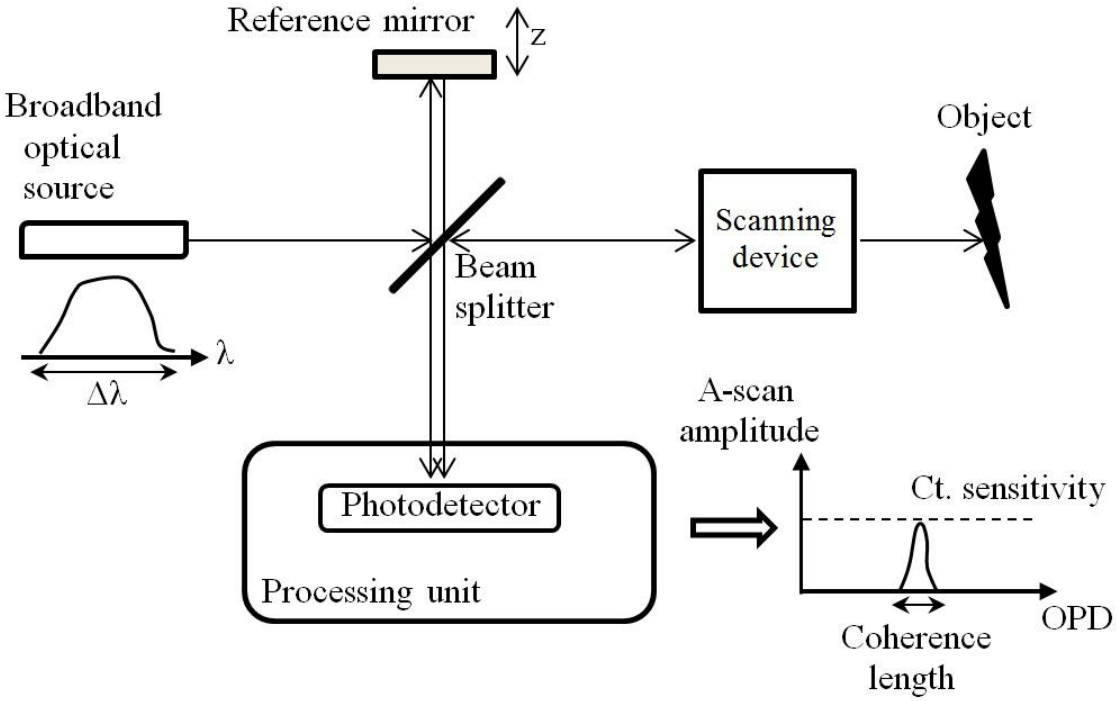

Fig. 2.1.1. Typical TD-OCT system [1]

The beam from the reference mirror has large field amplitude, while electric field from the sample beam is week. Therefore, the reference arm signal contributes to an amplification effect on the object signal, increasing the magnitude of the oscillating term that is detected by the detector. The interferometer produces heterodyne gain for weak optical signals. The photodetector senses the variations in the interference result as long as the optical path difference (OPD), which represents the difference between the reference arm optical path length and the object arm optical path length, is smaller than the coherence length l_c of the broadband source.

By integrating equation (2 – 7) over all wavenumbers k and eliminating the autocorrelation terms, the wavenumber dependent detector current is obtained as:

$$I(D_{z_R}) = \frac{\rho}{4} S_0[(R_R + R_{S1} + R_{S2} + \cdots)] + \frac{\rho}{2} S_0\{\gamma(z) \otimes \sum_{n=1}^{N} \sqrt{R_R R_{Sn}} \cos[2k_0(z_R - z_{Sn})]\} \quad (2.1-1)$$

where $S_0 = \int_0^\infty S(k)dk$ represents the spectrally integrated power emitted by the optical source. The second term of equation (2.1 – 1) encodes the sample reflectivity profile. This is convolved with the source correlation function and modulated by a cosinusoidal carrier with a frequency proportional with k_0, the central wavenumber of the source, and the path length difference between the reference and sample arms. The DC offset is proportional with the summed up power reflectivities due to both arms.

The samples imaged in OCT are generally multi-layered. Each layer reflects part of the incoming wavetrain, delayed accordingly. By moving the reference mirror along the z-axis, each layer that satisfies the condition $OPD < l_c$ is selected, a maximum of interference being achieved in the position where OPD = 0. The system outputs a reflectivity profile in depth named A-scan. A mechanical scanning device is added to the object arm in the low coherence Michelson interferometer in order to laterally scan the beam over the sample [13]. This allows the collection of adjacent A-scans for successive pixels along a transversal coordinate (z-axis), which ultimately leads to a cross-section image called B-scan. The imaging method described so far is also called longitudinal TD-OCT. Fig. 2.1.2 illustrates a descriptive representation of the A-scans and B-scans.

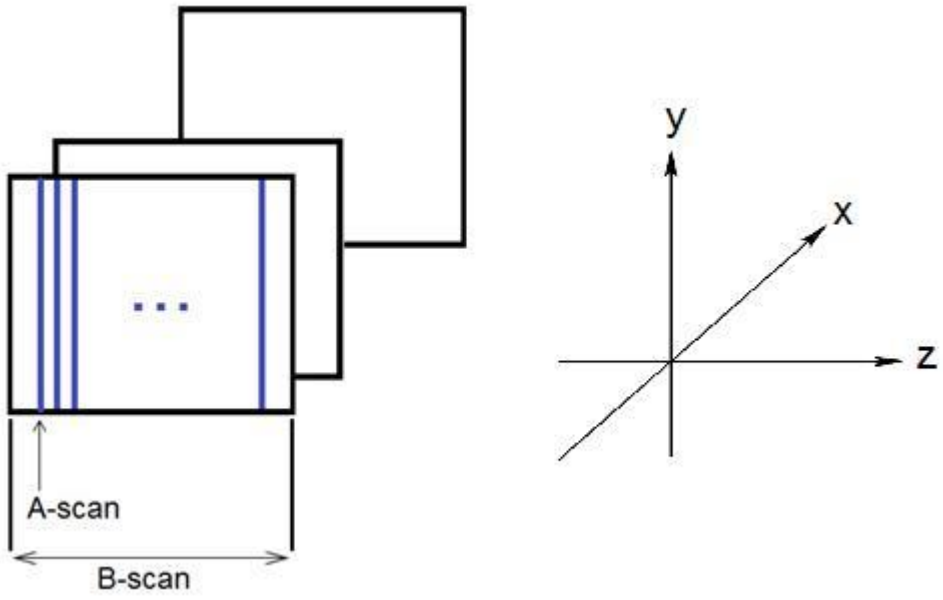

Fig. 2.1.2. Explicit representation of an A-scan, a B-scan and, respectively, a C-scan

Another variation of TD-OCT is the *en face* OCT [3, 14], where 1D reflectivity profiles called T-scans are collected by the spot flown transversally (on the x-axis), while the z-coordinate of the reference mirror is kept fixed. The C-scan is basically constructed from T-scans repeated at successive pixels in depth. This is achieved by slow axial scanning and fast lateral scanning. The *en face* OCT system also permits the real time acquisition of C-scans, by repeating the T-scans for adjacent values of the orthogonal lateral coordinate [14]. Fig. 2.1.3 depicts an explicit representation of T-scans and a C-scan constructed from consecutive T-scans acquired from a multi-layered sample.

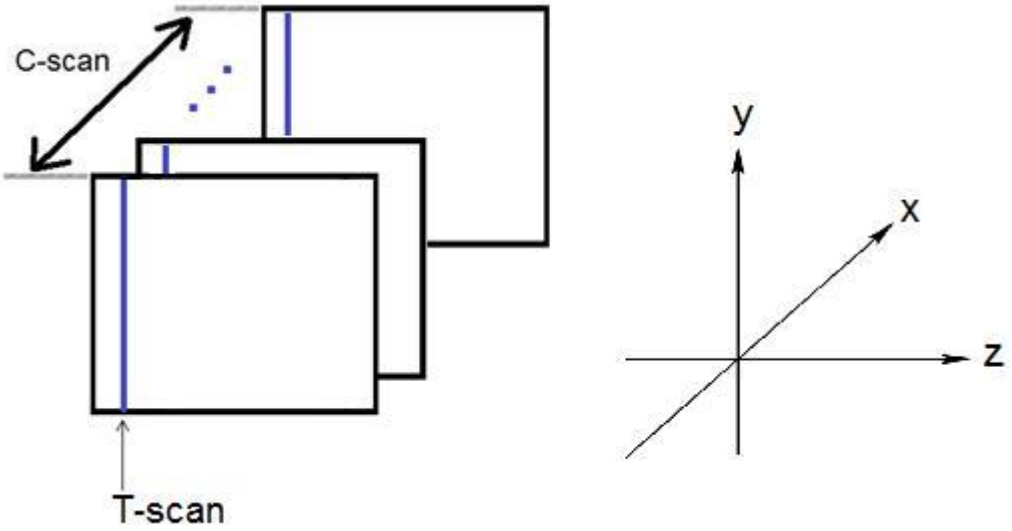

Fig. 2.1.3. Explicit representation of a T-scan and a C-scan

2.2. Spectral domain OCT

The SD-OCT (also known as Fourier Domain OCT, FD-OCT) includes two types of systems which are governed by the same theoretical equations, while the same rules of signal processing techniques are applied, but differ in terms of light sources and acquisition devices. In the SD-OCT setup, illustrated in Fig. 2.2.1, a broadband optical source (an SLD) inputs light into the interferometer, while the detection of the interference signal is performed via a spectrometer. Each spectral component is captured simultaneously at the detector array.

In the SS-OCT, each narrow band spectral line of the source is acquired sequentially in a single point detector, while the wavenumber is swept synchronously with the detector.

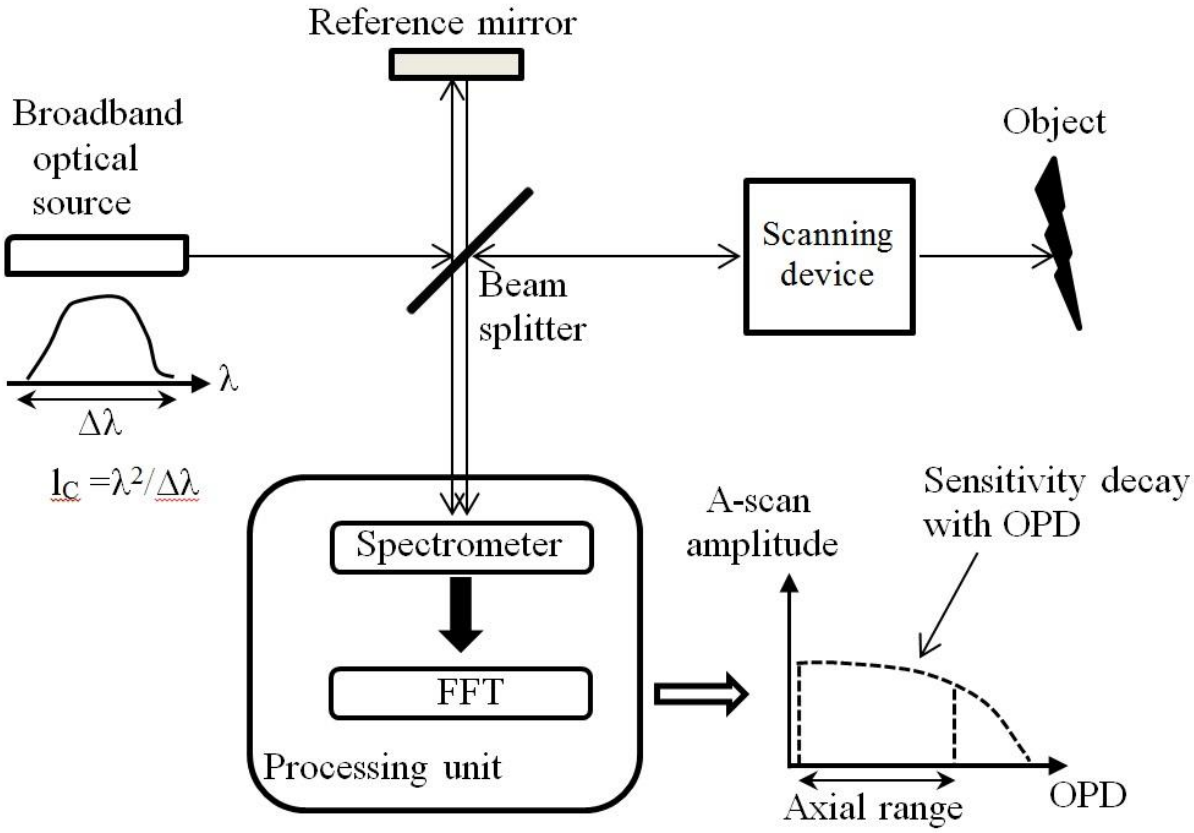

Fig. 2.2.1. General illustration of a SB-OCT system [1]

The linear photodetecting array devices uses in spectrometer based OCT are either a charged coupled device (CCD) or a complementary metal oxide semiconductor (CMOS) linear camera.

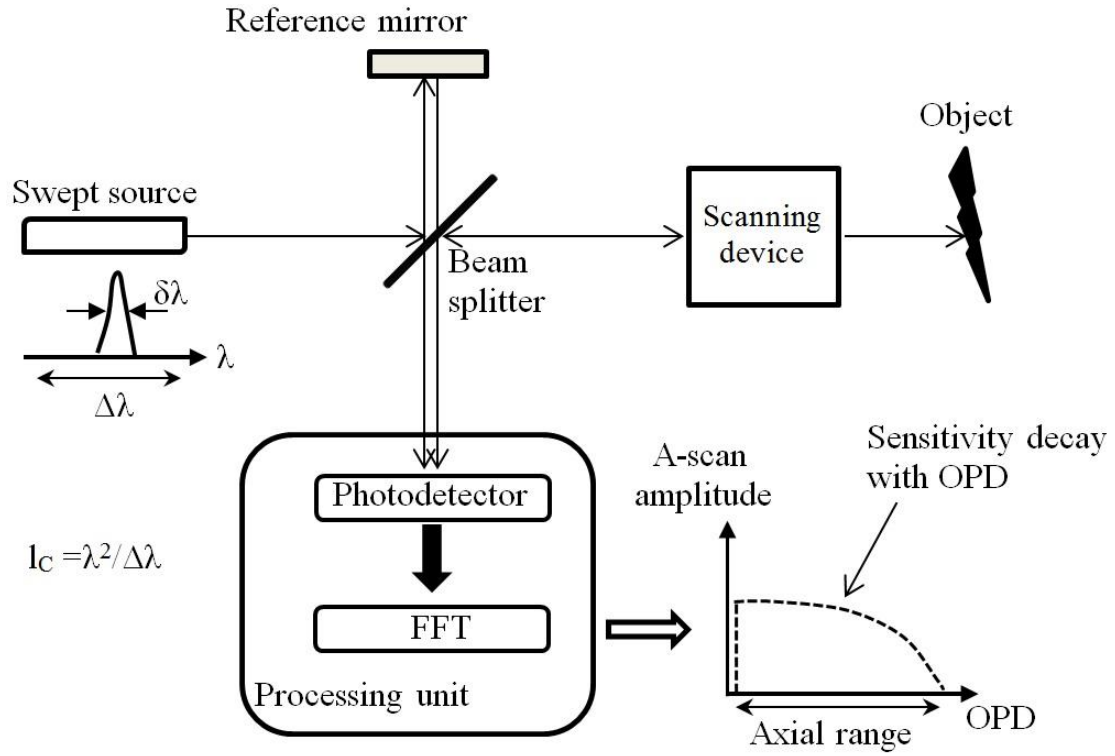

Fig. 2.2.2. General illustration of a SS-OCT system [1]

The detector current, $I(D_k)$, is processed using Fourier analysis. The reflectivity profile of the imaged object is calculated from the inverse Fourier transform of $I(D_k)$ defined in equation (2 – 7), while for simplicity, the auto-correlation terms are removed:

$$i_D(z) = \frac{\rho}{8}[\gamma(z)(R_R + R_{S1} + R_{S2} + \ldots)] + \frac{\rho}{4}\left[\gamma(z) \otimes \sum_{p=1}^{N} \sqrt{R_R R_{Sp}} \left(\delta\left(z \pm 2\left(z_R - z_{Sp}\right)\right)\right)\right] \quad (2.2 - 1)$$

The cross-correlation term convolved with the coherence length of the source give the sample reflectivity profile. After the convolution is performed, the previous equation becomes:

$$i_D(z) = \frac{\rho}{8}[\gamma(z)(R_R + R_{S1} + R_{S2} + \ldots)] + \frac{\rho}{4}\sum_{p=1}^{N} \sqrt{R_R R_{Sp}} \left[\gamma\left(2\left(z_R - z_{Sp}\right)\right) \pm \gamma\left(-2\left(z_R - - z_{Sp}\right)\right)\right] \quad (2.2 - 2)$$

As previously explained, the OPD represents the difference between the reference arm optical path length and the object arm optical path length. A dual balanced

photodetector measures the intensity difference between both interferometer outputs cancels out the contributions not arising from interference between the sample beam and the reference beam. The photodetector senses the variations in the interference signal as long as the OPD is smaller than the coherence length l_c of the broadband source. The interference signal registered by the photodetector is after that relayed to a specialised acquisition board, synchronised with both the repetition rate of the swept source and the speed of the scanning device and connected to a computer which uses software to decode the signal and illustrate a representation of the acquired image taken from a section in the sample.

One disadvantage of the SD-OCT is the fact that the symmetry of the inverse Fourier transformation in respect to the OPD signal introduces a complex conjugate artefact, which consists in the appearance of a mirror image on the opposite side of the OPD axis. This artefact is not present in TD-OCT. It can be avoided though, by restricting the sample on the negative or positive side of the OPD. The last equation shows that the zero position of the reflectivity profile appears in the reference reflector position and the OPD is doubled.

The Sp-OCT technique is inspired from the white light interferometry with applications in ranging and sensing [16] and it is based on the interferometer optical output spectrum demodulation. The modulated output, comprising peaks and troughs, is called channelled spectrum and it is proportional with the OPD [17]. The larger the OPD, the larger the number of peaks in the channelled spectrum. The suitable CMOS camera used in Sp-OCT is required to have a sufficiently small pixel size in order to be able to sample the channelled spectrum up to its maximum density. The camera converts the received optical signal in electrical signals, each layer of the object having a correspondent modulation periodicity dependent on depth. The fast Fourier transform (FFT) applied on the signal registered by the camera is translating the channelled spectrum periodicity in peaks of different frequency, represented versus OPD. SD-OCT offers improved sensitivity and it became attractive due to the expanding market of fast digital cameras [18]. Generally, cameras used in Sp-OCT are faster than the 16 kHz achieved with TD-OCT and far superior to the *en face* OCT using mechanical galvo-scanners [19]. The record of speed in OCT retinal imaging was achieved with a multitap camera that ensured 312.5 kHz line rates [20]. Recently, using 4 fast linear cameras and two optical switches, over 1 MHz line rate was reported [21].

The axial resolution improvement achieved with ultra-broadband sources was one of the main technological advances in TD-OCT [22]. From the beginning of the second decade of OCT until today, more research was dedicated to increase the imaging speed, especially

accomplished by SS-OCT [23-25]. While in Sp-OCT the acquisition speed is determined by the readout time of a fast camera integrated in a spectrometer, in SS-OCT the wavelength tuning speed of swept sources represents the main feature. The maximum spectral resolution is limited by the instantaneous linewidths of the source. The exponential A-scan amplitude with depth, as shown in Fig. 2.2.2 is quantifiable by defining the sensitivity fall at 6 dB:

$$z_{6dB} = \frac{ln2}{\pi}\frac{\lambda_0^2}{\delta\lambda} \qquad (2.2-3)$$

SD-OCT presents several advantages in comparison with TD-OCT: better acquisition rate, SD-OCT returning reflectivity values for all points along the axial range at once, while TD-OCT delivers the reflectivity profile in depth at the point where OPD is 0 only. A SD-OCT system also has a better signal-to-noise ratio [26]. On the other hand, in SD-OCT, the focus control cannot be synchronised with the axial scanning, while TD-OCT is more suitable in this case, where adaptive optics can be introduced in order to visualise human tissue [27]. On the other hand, SD-OCT is better for the case of imaging moving organs, like the human eye. In imaging the human eye, a sufficiently long depth of focus is secured comparable with the retina or cornea thickness. In cases where the depth of focus is surpassed by the thickness of the imaged tissues layer, imaging using SD-OCT needs to be repeated at several focus position. An image can be therefore reconstructed by stitching together several cross-section images, each in focus, according to the Gabor based method [28].

In TD-OCT, the sensitivity remains constant regardless of the *OPD* value (as illustrated in Fig. 2.1.1).

The limiting factor is given by the spatial extension of the interfering wavetrains, *CL*, considered as equivalent coherence length and defined by the following equation [1]:

$$CL = \frac{\lambda^2}{\delta\lambda} \qquad (2.3-4)$$

In Sp and SS-OCT there is a decay of sensitivity, because both techniques need resolution in separating channelled spectrum peaks, which corresponds to a need of large number of grating lines and also a large number of pixel cameras and, respectively a narrow linewidth $\delta\lambda$.

In order to ensure interference between the incoming reference wave with the object waves backscattered from the surface and, respectively, the deepest layer, *CL* must be greater than $2\Delta z$, where $2\Delta z$ represent the OPD axial extension of the object. Thus, the sensitivity decay with *OPD* depends on how much the interfering reference and object wavetrains overlap. In Sp-OCT, the number of pixels needed by the camera to register the interference signal is $M > 4\Delta z\Delta\lambda/\lambda^2$. Similarly, in SS-OCT, $M = 2\Delta\lambda/\delta\lambda$, the factor of "2" coming from the fact that at least two steps in the wavelength change per cycle in the channelled spectrum are required for accurate sampling of the channelled spectrum [1].

Another problem that can appear is SD-OCT is the effect induced by mirror terms, which arise from the ambiguity of the sign of the OPD, which generate the same frequency in the channelled spectrum when the Fourier transform is applied to the signal at the interferometer output. A solution to this matter, applicable to Sp-OCT is based on Talbot bands [29], where no required phase shifts, no calculations or cancellation algorithms are necessary, making the OCT system impervious to movements of the sample or instabilities in the imaging environment.

To summarise, the key parameters of an OCT system are the following: axial resolution, sensitivity, roll-off performance, dynamic range and imaging speed. Due to the nature of the work presented in this thesis, only the SS-OCT parameters will be briefly reminded.

In SS-OCT, the axial resolution is given by the wavelength swept range of the swept source. Sensitivity defines the minimum reflectivity in the sample arm still detected. Limiting factors for the sensitivity are the shot-noise (SN) or the high values of relative intensity noise (RIN) in the swept source. The roll-off performance represents the decrease in OCT signal with the ranging depth, which is caused by the instantaneous coherence length of the swept source. The dynamic range is the ratio between the strongest and weakest reflection measured simultaneously in one A-scan. Depending on the type of imaging being performed (1D, 2D or, respectively, 3D), the imaging speed in SS-OCT is defined by the number of A-scans per second, number of B-scans per second or number of voxels per second.

Apart from these parameters, the optical power that reaches the object also plays an important part. While scanning, safety standards differ in respect to the central wavelength of the source used in any OCT system. For example, a maximum of 0.7 mW at the cornea for imaging the retina at 830 nm, 2 mW at 1060 nm [30], 15 mW in the anterior chamber at 1300 [31], and much more when imaging skin layers [32]. Assuming the optical power losses

exhibited in the system, the input power from the source must be at least 2-10 times larger, depending on the interferometer configuration.

A comparison between the TD-OCT, SB-OCT and SS-OCT is summarised and illustrated in the following table [1]:

Parameter	TD-OCT	SB-OCT	SS-OCT
Depth resolution determined by	Optical source bandwidth	Optical source bandwidth	Tuning bandwidth
Axial scan range	Unlimited	Limited by the spectrometer resolution	Limited by the optical source linewidth
Sensitivity versus OPD	Constant	Maximum in OPD=0	Maximum in OPD=0
Line rate determined by	Transversal/ axial scanner	Reading the linear camera	Tuning the swept source
Maximum achievable line rate	16 – 100 Hz	300 kHz	5 MHz
Time to create an en face image	Given by the time to produce a C-scan frame, 31 ms	Given by the time to acquire a volume made from 500 B-scan frames of 500 line scans, ~0.83 s	Given by the time to acquire a volume made from 500 B-scan frames of 500 line scans, ~50 ms
Time to acquire a volume of 500 × 500 × 500 pixels at the maximum achievable line rate	2.5 – 15.5 s	0.83 s	50 ms

References

[1] A. Podoleanu, “Optical Coherence Tomography”, Journal of Microscopy, 247 (3) 209-219 (2012)

[2] W. Drexler W. & Fujimoto, J. G. (2008a), “State-of-the-art retinal optical coherence tomography. Progress in retinal and eye research”, **27**, 45–88 (2008)

[3] R. G. Cucu, A. Gh. Podoleanu, J. A. Rogers, J. Pedro, R. B. Rosen, “Combined confocal scanning ophthalmoscopy/*en face* T-scan based ultrahigh resolution OCT of the human retina *in vivo*.” Optics Letters **31**(11), 1684–1687 (2006)

[4] B. Bouma, J. Tearney, “Handbook of Optical Coherence Tomography”, Taylor&Francis, USA (2001)

[5] A. F. Fercher, W. Drexler, C. K. Hitzenberger, T. Lasser, “Optical Coherence Tomography – principles and applications”, Reports on progress in Physics, 66(2), 239-303 (2003)

[6] A. Gh. Podoleanu, “Optical Coherence Tomography”, Br. J. of Radiology, 78(935), 976-988 (2005)

[7] M. E. Brezinski, “Optical Coherence Tomograpy: Principles and Applications”, Academic Press 1st Edition (2006)

[8] J. J. Schuman, C. Puliafito, and J. G. Fujimoto, Everyday OCT: A Handbook for Clinicians and Technicians, SLACK Incorporated, USA (2007)

[9] M. Wojtkowski, “High-speed optical coherence tomography: basics and applications”, Applied Optics 49(16):D30-D61 (2010)

[10] A. F. Fercher, “Optical coherence tomography – development, principles, applications”, Zeitschrift fr. Medizinische Physik 20(4), 251-276 (2010)

[11] W. Drexler, M. Liu, A. Kumar, T. Kamali, A. Unterhuber, R. A. Leitgeb, “Optical coherence tomography today: speed, contrast, and multimodality”, Journal of Biomedical Optics 19(7), 071412 (2014)

[12] J. G. Fujimoto et al., “Optical biopsy and imaging using optical coherence tomography,” Nat. Med. 1(9), 970–972 (1995)

[13] D. Huang, E. A. Swanson, C. P. Lin, J. S. Schuman, W. G. Stinson, W. Chang, M. R. Hee, T. Flotte, K. Gregory, C.A. Puliafito et al., “Optical Coherence Tomography”, Science, 254(5035), 1178-1181 (1991)

[14] A. Gh. Podoleanu Podoleanu, R. B. Rosen, R.B. “Combinations of techniques in imaging the retina with high resolution. *Prog. Retin. Eye Res.* **27**(4), 464–499 (2008)

[15] R. Reif, R. K. Wang, “Label-free imaging of blood vessel morphology with capillary resolution using optical microangiography”, Quantitative imaging in medicine and surgery **3**(2) (2012)

[16] L. M. Smith, C. C. Dobson, “Absolute displacement measurements using modulation of the spectrum of white light in a Michelson interferometer.”, Applied Optics **28**(15), 3339–3342 (1981)

[17] S. Taplin, A. Gh. Podoleanu, D. J. Webb, D. A. Jackson, D.A., “Displacement sensor using channelled spectrum dispersed on a linear CCD array.”, Electronics Letters 29(10), 896–897 (1993)

[18] M. Wojtkowski, V. J. Srinivasan, T. H. Ko, J. G. Fujimoto, A. Kowalczyk, J. S. Duker, “Ultrahigh-resolution, highspeed, Fourier domain optical coherence tomography and methods for dispersion compensation.”, Optics Express 12(11), 2404-2422 (2004)

[19] C. K. Hitzenberger, P. Trost, P. Lo, Q. Zhou, “Three-dimensional imaging of the human retina by high-speed optical coherence tomography.”, Optics Express 11, 2753–2761 (2003)

[20] B. Potsaid, I. Gorczynska, V. J. Srinivasan, Y. Chen, J. Jiang, A. Cable, J. G. Fujimoto, “Ultrahigh speed Spectral /Fourier domain OCT ophthalmic imaging at 70,000 to 312,500 axial scans per second”, Optics Express **16**(19), 15149–15169 (2008)

[21] O. P. Kocaoglu, T. L. Turner, Z. Liu, D. T. Miller, “Adaptive optics optical coherence tomography at 1 MHz”, Biomedical Optics Express 5, 4186(2014)

[22] W. Drexler et al., “In vivo ultrahigh-resolution optical coherence tomography”, Optics Letters 24(17), 1221–1223 (1999)

[23] B. Golubovic et al., “Optical frequency-domain reflectometry using rapid wavelength tuning of a Cr4+:forsterite laser”, Optics Letters 22(22), 1704–1706 (1997)

[24] S. Yun et al., “High-speed optical frequency-domain imaging”, Optics Express 11(22), 2953–2963 (2003)

[25] R. Huber, M. Wojtkowski, J. G. Fujimoto, "Fourier domain mode-locking (FDML): a new laser operating regime and applications for optical coherence tomography", Optics Express 14(8), 3225–3237 (2006)

[26] T. Mitsui, "Dynamic range of optical reflectometry with spectral interferometer", Jpn. J. Appl. Phys. 38, 6133–6137 (1999)

[27] C. Costa, A. Bradu, J. Rogers, P. Phelan, A. Podoleanu, "Swept source optical coherence tomography Gabor fusion splicing technique for microscopy of thick samples using a deformable mirror", Journal of Biomedical Optics 20(1), 016012 (2015)

[28] J. P. Rolland, P. Meemon, S. Murali, K. P. Thompson, K-S Lee, "Gabor-based fusion technique for Optical Coherence Microscopy", Opt. Express. 18, 3632–3642 (2010)

[29] A. Bradu, A. Gh. Podoleanu, "Attenuation of mirror image and enhancement of the signal-to-noise ratio in a Talbot bands optical coherence tomography system", J. Biomed. Opt. 16(7), 076010-1–10. (2011)

[30] S. Hariri, A. A. Moayed, A. Dracopoulos, C. Hyun, S. Boyd, S, K. Bizheva, K. "Limiting factors to the OCT axial resolution for *in-vivo* imaging of human and rodent retina in the 1060 nm wavelength range. Opt. Express **17**, 24304–24316 (2009)

[31] D. Huang, Y. Li, M. Tang, "*Optical Coherence Tomography Technology and Applications"* – "Biological and Medical Physics", Biomedical Engineering, XXVIII (edited by W. Drexler, J. Fujimoto), 961–981, Springer, Berlin/Heidelberg (2008)

[32] G. J. Tearney, M. E. Brezinski, B. E. Bouma, B.E., S. A. Boppart, C. Pitris, J. F. Southern, J. G. Fujimoto, "*In Vivo* endoscopic biopsy with optical coherence tomography", Science 276(5321), 2037–2039 (1997)

3

Optical swept sources based on fibre optics and diode laser technologies

3.1. General criteria and types of optical sources used in OCT

The main parameters that characterise an optical source used in OCT applications are wavelength, bandwidth, output power and stability. In optical swept lasers, another important parameter to take into account is the repetition rate (also known as the sweep rate).

The linewidth of a laser is the width (typically measured as the full width at half-maximum, FWHM) of its optical spectrum. More precisely, it is the width of the power spectral density of the emitted electric field in terms of frequency, wavenumber or wavelength. The bandwidth of either a superluminiscent diode or a swept source represents the width of the optical spectrum of the output of the light source. For OCT imaging, wide bandwidth (of at least 30 nm) and narrow linewidth (100 pm or less) are necessary in order to achieve respectively good axial range and sufficient signal from large values of depth. When imaging tissue *in vivo*, an axial range of 2 mm is necessary with a resolution of at least 10 microns. This sets a number of pixels along the depth coordinate of at least 100. Typical number of pixels in depth is 500 – 2000, to acquire detailed B-scans.

Swept sources are used in OCT (SS-OCT) for in vivo retinal imaging, because they enable the acquisition of large 3D-volumes in a very short time, thereby minimizing the impact of motion artefacts caused by movements of the eye. By rapid modulation of the pump current (operating the source at hundreds of kHz repetition rates), the light source spectrum is optimised and ultimately leads to improvement in the depth resolution achievable in OCT imaging.

In regards to the optical output power, the swept sources do not need to emit a beam of more than a few mW, in order to ensure that no thermally induced tissue damage occurs during in vivo imaging.

The stability of the output beam is related to the noise. In a single-frequency laser, there are two types of noise occurring: amplitude noise and phase noise. The latter causes a finite laser linewidth and it limits the temporal coherence. In a laser operating on multiple resonator modes, there is a beating noise which generates fluctuations of the power distribution over the resonator modes. The power in one of these modes may fluctuate much more than the total power. A mode-locked laser exhibits noise in the temporal position of the pulses but also noise in the centre frequency and pulse duration. Therefore, in order to achieve a stable laser output, it is crucial to reduce or even eliminate the various sources of noise.

In order to be able to integrate them in portable equipment used for clinical *in vivo* imaging, a laser developer must also take in consideration size, ease of use, maintenance and compatibility with the environment where it is going to be used. Also, the costs of manufacturing and retail must be reduced as much as possible in order to make it attractive commercially.

Returning to the scientific aspect of an optical source used in OCT, the axial resolution ΔL in imaging is given by the following equation:

$$\Delta L = \frac{2ln2}{\pi}\left(\frac{{\lambda_0}^2}{\Delta\lambda}\right) = 0.44\left(\frac{{\lambda_0}^2}{\Delta\lambda}\right), \qquad (3.1-1)$$

where λ_0 represents the central wavelength, $\Delta\lambda$ is the full with half maximum (FWHM) spectral width (bandwidth), while a Gaussian spectral distribution is considered. This equation shows that there is a proportional relationship between the resolution and bandwidth. A simple calculation shows that in order to achieve a 10 μm resolution at λ_0 = 850 nm, a bandwidth $\Delta\lambda$ = 31.45 nm is necessary. On the other hand, if we repeat this calculation for λ_0 = 1550 nm, the bandwidth required increases significantly, to 94.6 nm.

The power *P* of the optical source to achieve OCT imaging is given by the following expression [1]:

$$P = \sqrt{\pi/4ln2}\,\Delta\nu_{FWHM}P(\nu_0) \qquad (3.1-2)$$

where $\Delta\nu_{FHWM}$ represents the optical frequency bandwidth measured at FWHM (assuming a Gaussian spectral density of the output), and $P(\nu_0)$ represents the power spectral density at the central optical frequency. The above equation could also be rewritten in respective to the wavelength λ, by replacing $\Delta\nu$ with $\Delta\lambda$ (optical bandwidth) and ν_0 with λ_0 (central emission wavelength).

Superluminescent diodes

The first A-scans of the human eye and retina were performed using a superluminescent diode (SLD), emitting at 850 nm central wavelength, providing penetration in both the vitreous region of the eye and the retina [2, 3]. The retinal layers are rather delicate and their transparency is superior in comparison with other types of tissue, where the scattering induces significant attenuation. Also, in terms of safety, the exposure level must be kept as low as possible. If OCT is applied to other types of tissues (for example skin, bone, muscle), other wavelengths are more suitable. It is known that the larger the wavelength, less is the scattering, therefore in tissue the penetration depth increases with the wavelength used. However, water absorption picks up for wavelengths larger than 1 micron.

There are several companies producing SLDs, such as Superlum [4, 5], Covega, InPhenix and Thorlabs covering the near IR range (800 nm - 1550 nm).The main advantage of the semiconductor sources stand in stability, compact design and ease of operation. They generally provide a smooth Gaussian spectrum output and the ones that equip many ophthalmic sytems can reach 20 mW power levels. On the other hand, the 3 dB bandwidth $\Delta\lambda$ is quite limited and they are not suitable for applications that require very fast speed imaging. There also issues regarding polarisation and noise performance that need addressing.

Semiconductor optical amplifiers

In 1997, AFC Inc. developed an advanced type of semiconductor based source called a multiple quantum well semiconductor optical amplifier (SOA), which achieved bandwidths up to 80 nm and output powers as high as 30 mW. The semiconductor chip of the source come is a butterfly 14 pin package, containing several quantum wells with chirped periods, the varied size of the wells determining the broad spectrum. It has two fibres, one used as

input and one as output. In order to increase the gain and achieve an improved output power, the chip was placed in a loop and was spectrally filtered in order to avoid the gain narrowing occurring after a second roundtrip of the light in the cavity. Despite the significant value in power and bandwidth, the output is not polarised, therefore the SOA is inefficient in polarisation sensitive OCT experiments.

Nevertheless, the source manufactured by AFC Inc. was successfully used in clinical studies of the gastro-intestinal tract [6].

Solid state lasers

This type of lasers rely on a crystalline gain medium (YAG, YVO_4, Al_2O_3 etc.), generally cylindrical or disk shaped, doped with ions of rare earth elements (Nd^{3+}, Yb^{3+}, Tm^{3+}). The combination between various crystals and dopants is chosen in order to satisfy different excitation possibilities and to achieve the emission in a certain wavelength range. The phonon-broadened solid state laser sources provide large spectral bandwidths [7]. Solid state lasers with broadband emission are used in OCT imaging in a regime that resembles the superluminiscent diodes [8] or in mode-locking [9, 10].

The solid state lasers represent a viable solution for *in vitro* OCT imaging, because they provide high power and broad spectrum, low coherence that can determine high speed and resolution OCT. On the other hand, such devices are expensive and bulky. Due to reduced efficiency in optical pumping of the active medium (generally less than 10%), they are usually accompanied by an external water cooling system; thus, using them outside the confinements of a lab could prove difficult.

Rare-earth doped fibre lasers

This type of lasers is extremely appreciated in a wide range of applications. The active medium of these sources is constituted by fibres doped with rare-earth ions like Nd^{3+}, Yb^{3+}, Tm^{3+} pumped by laser and array of diode sources. Also called superfluorescent fibre sources, they generally emit in the 1000-2000 nm IR region, are compact, have a very high conversion efficiency (50% and above), capable of output power from a few mW up to MW level, they have an estimated lifetime of 100000-200000 hours and usually exhibit a polarised output. Depending on the type of application they are used in, the rare-earth doped laser can emit

either a narrow band or a broadband spectrum. The versatility of such optical sources makes them ideal for integration in OCT systems.

The main disadvantage of these sources is the limited optical bandwidth, which is less than 100 nm. A way around this issue would be combining sources with various central wavelengths in one apparatus capable to emit a broad output. This comes though with a high cost penalty.

Several configurations of such sources were developed, based on combinations of rare-earth doped fibres [11, 12], SOA and doped fibre [13] and SLD based [14, 15].

Supercontinuum source

The supercontinuum sources are based on photonic crystal fibres (PCFs) pumped by femtosecond laser pulses [16]. The principle of operation is represented by the nonlinear propagation of femtosecond laser pulses in the vicinity of zero dispersion of the fibre, while several nonlinear phenomena are superposed: self-phase modulation, multiple-wave mixing, and stimulated Raman scattering. These phenomena are responsible for the super continuum generation and optical bandwidth broadening, while the PCF is modelled in order to determine the values of dispersion and the linear propagation effects.

The development of supercontinuum sources came from the need of replacing the bulky Titanium Sapphire (Ti:Sapphire) lasers. Yb^{3+} doped fast fibre lasers can also be converted to supercontinuum sources by launching laser light into a holey fibre. Such devices were already integrated in retinal thickness measurements [17].

Main manufacturers on the market producing supercontinuum sources are NKT [18-20] and Fianium [21]. Handling of such sources is rather complicated and any mechanical shocks must be avoided in order to prevent misaligning of optical components. They are also very expensive, and integration in an OCT system for commercial purposes can prove cost ineffective.

3.2. Swept sources based on mechanical tuning mechanisms

State-of-the-art swept sources enabled the progress in OCT imaging acquisition speed. The SS-OCT method introduced tuning rates which are hundreds of times faster than any other OCT application.

The optical swept sources based on mechanical tuning mechanism is also called wavelength swept lasers, as depicted in Fig. 3.2.1, comprising a gain medium (typically a SOA) and a tuning filter, noted as λ(t). The laser parameters are dependent on several conditions: limited tuning rate due to the maximum frequency sweep of the filter, also influenced by the quality of the gain medium and the filter FSR,

The linewidth during sweeping operation is better than that exhibited by the light passing through the filter when is in static position; the output power determined by the gain through multiple roundtrips in the cavity.

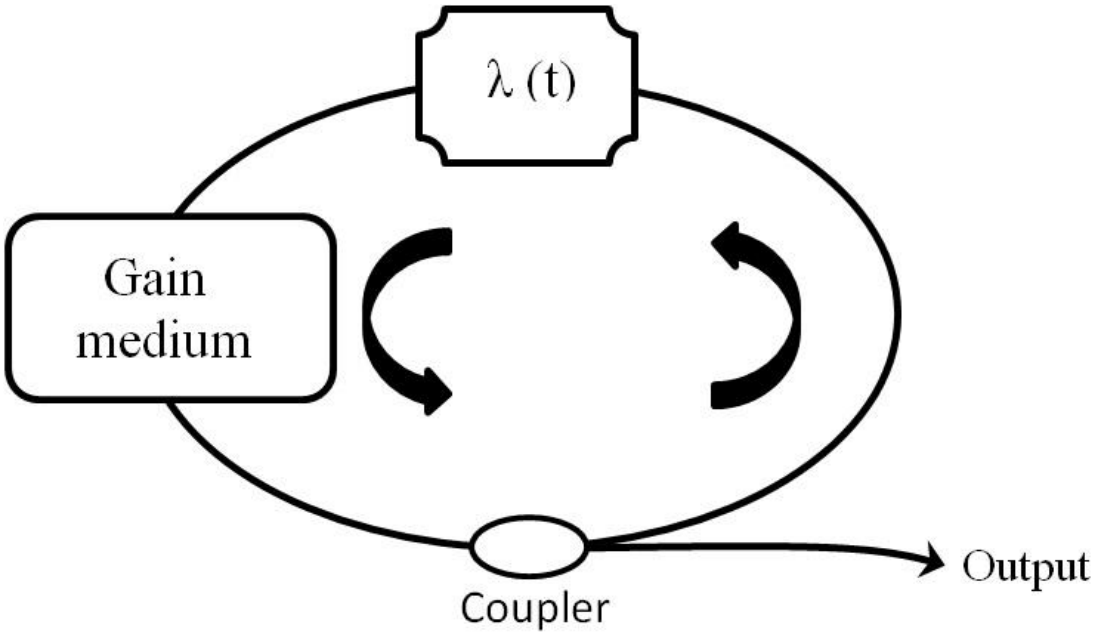

Fig. 3.2.1. General configuration of a wavelength swept laser using a tuning filter

Polygon mirror swept source

Such an optical swept source [22] is generally based on a reflective filter comprising a diffraction grating, an afocal telescope and a polygonal scanner (polygon mirror). The telescope is constructed from an infinite-conjugate configuration of lenses, with the grating

placed at the focal plane of the first lens, while the polygon is situated at the back focal plane of the second lens. The telescope converts diverging angular dispersion from the grating into converging angular dispersion after the second lens, controls the light beam size and convergence on the polygon. The polygon reflects only the narrowly resolved band spectral component normal to the front mirror facet of it. After that, the reflected beam is re-dispersed by the grating.

A similar concept utilizes a diffraction grating coupled with a mechanically resonant galvo-scanner [23].

Such sources are inefficient from several points of view. First of all it is difficult to compensate for the dead time due to polygon edges. Secondly, the polygon mirror is susceptible to electrical shocks and requires a high current specialised driver and it is subject to misalignments provoked by mechanical shocks.

Fabry-Perot filter

Rotating mirrors are generally bulky and sensitive, and difficult to integrate them into portable OCT equipment. The fibre coupled Fabry-Perot (FP) filter based swept sources represent a more viable solution. Several publications disclosed the implementing of such devices in SS-OCT systems [24, 25]. There is a major challenge though in addressing intra-cavity effects which influence and beat with the useful optical signal, thus increasing the noise level in the output. A method of addressing this issue was proposed in [24], which improves the noise reduction and output parameters. Although having a good ratio between cost and utility, The FP filters are RF controlled and they are also rather sensitive to electrical shocks.

Axsun Technologies is one of the main producers on the market developing swept sources based on FP filters, achieving minimum 100 kHz sweep rates and narrow linewidths.

Despite the good stability and competitive results obtained so far in imaging applications, there is a high demand of higher repetition rates in OCT.

3.3. Fourier Domain Mode-Locked (FDML) swept sources

In the wavelength swept lasers presented so far, an important limitation comes from the build-up lasing gain (photon life time) in the cavity. In 2006, a new swept source concept was introduced in order to overcome this limitation and achieve fast repetition rates [26, 27]. Depicted in Fig. 3.3.1, the FDML laser is based on a narrow band optical filter swept in time at rates equal to the round-trip time of the laser cavity, determined by the several kilometres of delay single mode fibre (SMF) used in a ring cavity. Each frequency component is forced to circulate in the cavity in such a way that is transmitted through the filter at every roundtrip.

If initially high repetition rates achieved were about 370 kHz [28], recently the FDML laser broke the MHz barrier [29].

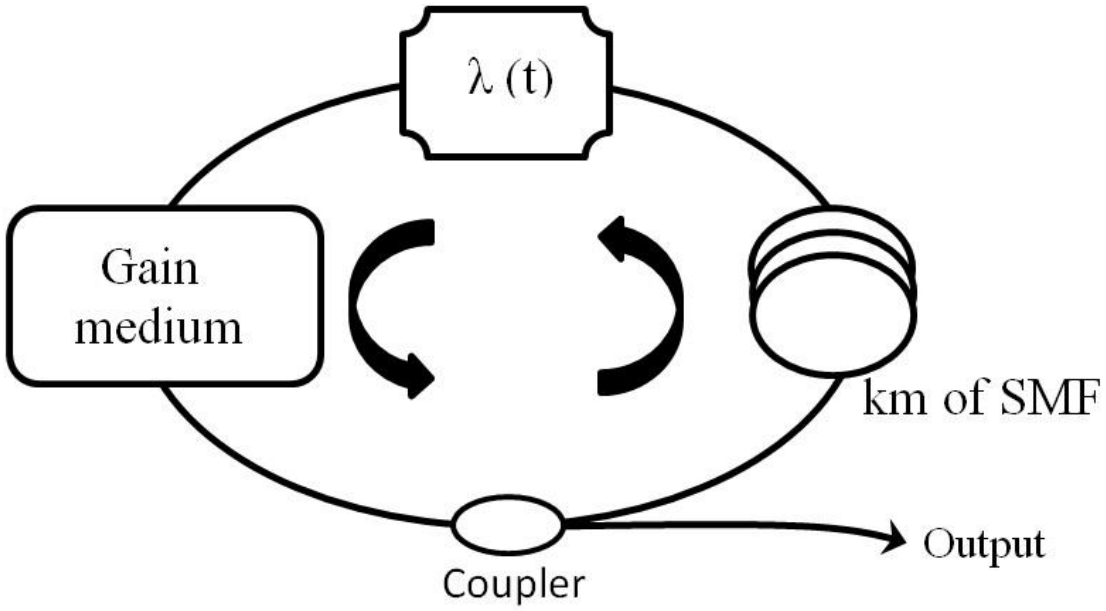

Fig. 3.3.1. General configuration of a wavelength swept laser

Apart from the very fast repetition rates achieved, the FDML laser is a concept that exhibits improved stability, coherence length and output power [30], and was recently transposed into a commercial product.

3.4. Swept sources using dispersion tuning

Dispersive tuning, illustrated in Fig. 3.4.1, replaces the mechanical tuning mechanisms described in the previous chapter with a dispersive compensating fibre (DCF) [31, 32]. A 1550 nm central wavelength SOA represents the gain medium. More recent concepts are meant to reduce the cavity length by replacing DCF with partially reflective chirped fibre Bragg gratings (cFBGs). The use of cFBGs enables the application of dispersion tuning at other wavelengths, like 1050 nm [33]. While in the previous concepts, tuning was achieved by setting an RF control signal on the FP filter, galvoscanner or rotating mirror, this akinetic mechanism involves radio frequency tuning control applied directly to the SOA gain medium, while the amount of dispersion in the circular cavity ensure the laser pulse tuning.

Hundreds of kHz repetition rates were achieved in [33] by shortening the cavity length, but there is a strong decay in power with the sweep rate increase, while quality of OCT imaging is still inferior to the one achieved with Axsun or FDML sources.

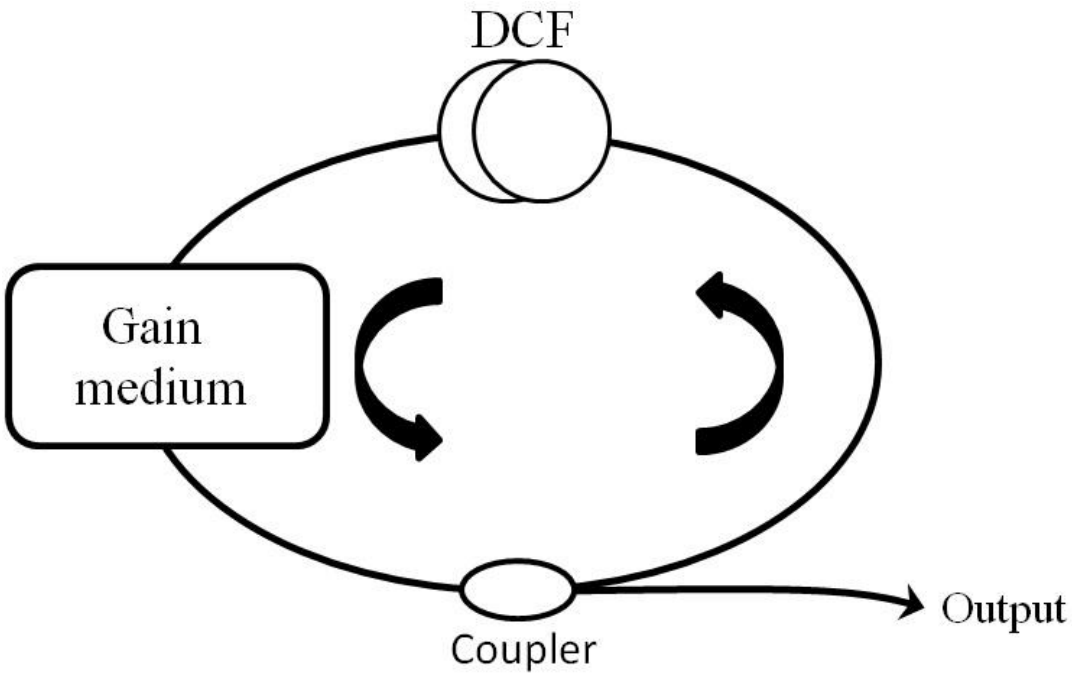

Fig. 3.4.1. General configuration of a wavelength swept laser using DCF

References

[1] R. Leitgeb, C. K. Hitzenberger, A. F. Fercher, “Performance of fourier domain vs. time domain optical coherence tomography”, Optics Express 11(8), 889-894 (2003)

[2] A. F. Fercher, C. K. Hitzenberger, W. Drexler, G. Kamp, and H. Sattmann, " In Vivo Optical Coherence Tomography," Am. J. Ophthalmol, 116 (1), pp. 113-114 (1993)

[3] Swanson, E. A.; Izatt, J. A.; Hee, M. R.; Huang, D.; Lin, C. P.; Schuman, J. S.; Puliafito, C. A.; Fujimoto, J. G.. “In vivo retinal imaging by optical coherence tomography", Optics Letters 18(21): 1864–6 (1993)

[4] http://www.superlumdiodes.com

[5] E. V. Andreeva, P. I. Lapin, V. V. Prokhorov, V. R. Shidlovski, M. V. Shramenko, S. D. Yakubovich, “Novel superluminiscent diodes and SLD-based light sources for optical coherence tomography”, Proc. of SPIE, 662703-662703-10, Munich (2007)

[6] B. E. Bouma, G. J. Tearney, “Power-efficient nonreciprocal interferometer and linear-scanning fiber-optic catheter for optical coherence tomography”, Optics Letters 24(8), 531–533 (1999)

[7] W. Koechner, “Solid-State Laser Engineering”, Springer Ser Opt Sci, Vol 1. New York: Springer-Verlag (1998)

[8] X. Clivaz, F. Marquis-Weible, R. P. Salthe, P. P. Novak, H. H. Gilgen, “High-resolution reflectometry in biological tissues”, Optics Letters 17:4–6 (1992)

[9] B. E. Bouma, G. J. Tearney, S. A. Boppart, M. R. Hee, M. E. Brezinski, J. G. Fujimoto, “High resolution optical coherence tomographic imaging using a modelocked Ti : Al2O3”, Optics Letters 20:1486–1488 (1995)

[10] W. Drexler, U. Morgner, F. X. Kartner, C. Pitris, S. A. Boppart, X. D. Li, E. P. Ippen, J. G. Fujimjoto, “In vivo ultrahigh-resolution optical coherence tomography.”, Optics Lettert 24:1221–1223 (1999)

[11] R. Paschotta, J. Nilsson, A. C. Tropper, D. C. Hanna, “Efficient superfluorescent light sources with broad bandwidth”, Selected Topics in Quantum Electronics, IEEE, 3(4), 1097-1099 (1997)

[12] H. Chen, G. W. Schinn, “Hybrid broadband superfluorescent fiber source consisting of both thulium-doped fiber and erbium-doped fiber”, Optics Communications, 229 (1-6), 141-146 (2004)

[13] K. Haroud, E. Rochar, R Dandliker, “A broad-band superflourescent fiber laser using single-mode dopes silica fiber combinations”, IEEE Journal of Quantum Electronics, 36(2), 151-154 (2000)

[14] D. Beitel, L. Carrion, L. R. Chen, R. Maciejko, “Development of broadband sources based on semiconductor optical amplifiers and erbium-doped fiber amplifiers for optical coherence tomography”, Selected Topics in Quantum Electronics, IEEE, 14(1), 243-250 (2008)

[15] E. V. Andreeva, P. I. Lapin, V. V Prokhorov, V. R. Shidlovski, M. V. Shramenko, S. D. Yakubovich, “Novel Superliminiscent Diodes and SLD-based Light Sources for Optical Coherence Tomography” – “Optical Coherence Tomography and Coherence Techniques III”, Proceeding of SPIE-OSA Biomedical Optics, 6627 (2007)

[16] H. Wang, C. P. Fleming, A. M. Rollins, “Ultrahigh-resolution optical coherence tomography at 1.15 μm using photonic crystal fiber with no zero-dispersion wavelengths”, Optics Express 15(6), 3085-3092 (2007)

[17] Y. Ikuno, I. Maruko, Y. Yasuno et al., “Reproducibility of retinal and choroidal thickness measurements in enhanced depth imaging and high-penetration Optical Coherence Tomography”, Investigative Ophthalmology & Visual Science (2011)

[18] P. Cimalla, J. Walther, M. Mehner, M. Cuevas, E. Koch, “Simultaneous dual-band optical coherence tomography in the spectral domain for high resolution in vivo imaging”, Optics Express 17(22), 19486-19500 (2009)

[19] Z. Zhi, L. An, J. Qin, R. K. Wang, “Ultra-high-resolution and ultra-high-sensitive optical micro-angiography based on supercontinuum light source”, SPIE proceedings Vol. 7889 (2011)

[20] M. Jiang, T. Liu, X. Liu, S. Jiao, “Simultaneous optical coherence tomography and lipofuscin autofluorescence imaging of the retina with a single broadband light source at 480nm”, Biomedical Optics Express, 5(12), 4242-4248 (2014)

[21] F. E. Robles, C. Wilson, G. Grant, A. Wax, “Molecular imaging true-colour spectroscopic optical coherence tomography”, Nature Photonics 5, 744–747 (2011)

[22] S. H. Yun, G. Boudoux, G. J. Tearney, B. E. Bouma, “High-speed wavelength-swept semiconductor laser with a polygon-scanner-based wavelength filter”, Optics Letters 28(20), 1981-1983 (2003)

[23] S. H. Yun, C. Boudoux, M. C. Pierce, J. F. de Boer, G. J. Tearney, B. E. Bouma, “Extended-Cavity Semiconductor Wavelength-Swept Laser for Biomedical Imaging”, IEEE Photonics Tech. Letters 16(1), 293-295 (2004)

[24] F. D. Nielsen, L. Thrane, K. Hsu, A. Bjarklev, P. E. Andersen, “Semiconductor optical amplifier based swept wavelength source at 1060 nm using a scanning Fabry–Perot filter and an YDFA-based booster amplifier”, Optics Communications 271, 197–202 (2006)

[25] I. Trifanov, A. Bradu, L. Neagu, P. Guerreiro, A. B. L. Ribeiro, and A. G. Podoleanu, “Experimental method to find the optimum excitation waveform to quench mechanical resonances of Fabry–Pérot tunable filters used in swept sources”, IEEE Photon. Technol. Lett., vol. 23, no. 12, pp. 825–827, 2011

[26] R. H. Huber, M. Wojtkovski, J.G. Fujimoto, “Fourier Domain Mode-locking (FDML): A new laser operating regime and applications for optical coherence tomography”, Optics Express 14(8), 3225-3237 (2006)

[27] C. Jirauschek, B. Biedermann, R. Huber, “A theoretical description of Fourier domain mode locked lasers”, Optics Express 17(26), 24013-24019 (2009)

[28] R. Huber, D. C. Adler, J. G. Fujimoto, “Buffered Fourier domain mode-locking: unidirectional swept laser sources for optical coherence tomography imaging at 370,000 lines/s”, Optics Letters 31(20), 2975-2977 (2006)

[29] W. Wieser, T. Klein, D. C. Adler, F. Trépanier, C. M. Eigenwillig, S. Karpf, J. M. Schmitt, R. Huber, “Extended coherence length megahertz FDML and its application for anterior segment imaging”, Biomedical Optics Express 3(10), 2647-2657 (2012)

[30] B. R. Biedermann, W. Wieser, C. M. Eigenwilling, T. Klein, R. Huber, “Dispersion, coherence and noise of Fourier domain mode locked lasers”, Optics Express 17(12), 9947-9961 (2009)

[31] S. Yamashita, Y. Nakazaki, R. Konishi, O. Kusakari, “Wide and fast wavelength-swept fiber laser based on dispersion tuning for dynamic sensing“, Journal of Sensors, Vol. 2009, 572835 (2009)

[32] Y. Nakazaki, S. Yamashita, “Fast and wide tuning range wavelength-swept fiber laser based on dispersion tuning and its application to dyamic FBG sensing”, Optics Express 17(10), 8310-8318 (2009)

[33] Y. Takubo, S. Yamashita, “High-speed dispersion-tuned wavelength-swept fiber laser using a reflective SOA and a chirped FBG”, Optics Express, vol.21, no.4, pp.5130-5139 (2013)

4

Single mode-locking mechanisms for akinetic swept sources based on dispersive cavities

4.1. Theoretical considerations

The wavelength swept lasers represent a modern solution for telecom, sensing and also proved to be versatile in SS-OCT applications. In applications like telecom and sensing, narrow linewidth lasers, less than 10 pm, and tuned within a bandwidth of hundreds of GHz, at repetition rates lower than 1 KHz are utilised. For OCT imaging, wide tuning range and narrow spectral linewidth are necessary in order to achieve respectively good axial range and sufficient signal from large values of depth. When imaging tissue, an axial range of 2 mm is necessary with a resolution of at least 10 microns. This sets a number of pixels along the depth coordinate of at least 100. Typical number of pixels in depth is 500 – 2000, to acquire detailed B-scans. In the previous chapter, several optical sources and mechanical tuning mechanisms were briefly presented. In continuation, a theoretical description of a rather recent development in akinetic swept sources based on dispersive tuning elements is presented, where mode-locking is achieved by direct AC tuning of the SOA driving current via a bias tee.

The theory of mode-locking was formulated shortly after the invention of the laser [1, 2]. This technique is applied by establishing a fixed-phase relationship between the longitudinal modes of the resonant cavity (between the laser output spectral lines). Mode-locking is used as a method to obtain to obtain ultrashort pulses from lasers.

If the laser emission is mono-modal, the pulses are released by the cavity one by one, at a certain repetition rate. If several modes are superposed in the cavity, the output is

constituted by a train of pulses (multi-mode emission), produced by the laser source at a certain repetition rate. The larger the number of frequency components, the shorter the duration of the generated pulses.

There are two types of laser mode-locking, passive or active. The passive mode-locking is performed by introducing a saturable absorber in the cavity [3, 4]. By using such elements inside the cavity, the laser continuous wave emission is temporarily stopped until the energy accumulated in the absorber surpasses a threshold level and a pulse is released. The pulse shape and duration are determined by the geometry and the non-linear effects in the saturable absorber.

The active mode-locking is produced by using external devices such as acousto-optic or electro-optic modulators, Mach–Zehnder integrated-optic modulators, or a semiconductor electro-absorption modulator [5]. Synchronising the modulation with roundtrips in the laser cavity leads to ultrashort pulses generation.

Yamashita et al. [6-9] proposed an akinetic swept source concept using active mode-locking in an anomalous dispersive cavity (negative dispersion), and achieved sweeping rates of hundreds of kHz. The mode-locking mechanism is achieved by applying RF tuning to the SOA gain module at frequencies that represent integer numbers of the resonator mode frequency (equal to the inverse of the round trip time). A dispersive element is introduced in the optical cavity. This makes the roundtrip dependent on wavelength. A typical dispersive element can be implemented by using a long length of dispersion compensating fibre (DCF). The generation of broadband spectra is possible due to dispersion compensating, which ensures that the mode frequencies are approximately equidistant. This was also shown in the past in fibre wavelength swept lasers which are not akinetic [10].

In order to achieve wide and fast tuning with a narrow spectral linewidth, they concluded that the dispersion characteristic of the DCF and the modulation frequency should be as large as possible, while the cavity length should be as small as possible.

In a ring fibre laser configuration, the resonance condition is formulated as:

$$\beta(\omega_K)L = 2K\pi \,, \qquad (4.1-1)$$

where $\beta(\omega_k)$ represents the propagation constant at an angular frequency ω, K is the integer value of the mode number and L is the cavity length. The first equation can be re-written as:

$$\big(\beta(\omega_{k+1}) - \beta(\omega_k)\big)L = 2\pi \qquad (4.1-2)$$

The resonance frequency f_R, also known as free spectral range (*FSR*), represents the spacing between adjacent modes in the cavity and it is defined as:

$$FSR = f_R = \frac{c_0}{nL} = \frac{\omega_{K+1} - \omega_K}{2\pi}, \qquad (4.1-3)$$

where c_0 represents the speed of light in vacuum and n denotes the cavity's index of refraction. Each value of mode-locking frequency f_m represents a multiple N of the resonance frequency, $N \cdot f_R$. Without chromatic dispersion in the cavity, the value of f_R is constant, independent on the angular optical frequency, ω.

The larger L, the smaller the spacing between the adjacent modes, therefore (4.1 – 2) becomes:

$$(\omega_{K+1} - \omega_K)\frac{d\beta}{d\omega}L = 2\pi, \qquad (4.1-4)$$

expression which eventually determines a general relation for FSR:

$$FSR = \left[\frac{d\beta}{d\omega}L\right]^{-1} \qquad (4.1-5)$$

By introducing a highly chromatic dispersive element like a length of DCF in the cavity, the *FSR* becomes dependent on ω. After expanding $\beta(\omega)$ around ω_0 with Taylor series and eliminating the considerably smaller high order chromatic dispersion terms (β_3 and above), the equation for the *FSR* variation is achieved:

$$\Delta FSR(\omega) = -F_0 \frac{\beta_2}{\beta_1}\Delta\omega \qquad (4.1-6)$$

The chromatic dispersion in the cavity can be expressed as a function of wavelength λ. When signal of frequency f_m modulates the gain in a dispersive cavity, mode-locking is induced at the inverse of the roundtrip of light in the cavity. Therefore, the laser operates at a wavelength that meets the harmonic mode-locking condition. The wavelength tuning range $\Delta\lambda$ is expressed as:

$$\Delta\lambda = -\frac{n_0}{cDf_{m0}}\Delta f_m, \qquad (4.1-7)$$

where f_{m0} is the central mode-locking frequency, n_0 is the refractive index evaluated at the central frequency ω_0 , D is the dispersion parameter of the DCF, and Δf_m represents the change in the modulation frequency. When Δf_m reaches the *FSR*, maximum tuning range is achieved, given by:

$$\Delta\lambda_{max} = \frac{1}{|D|Lf_{m0}} \qquad (4.1-8)$$

The output pulses emitted by the dispersion tuned swept source are chirped and wide due to the dispersion in the cavity. Assuming the emission is Gaussian, the spectral half width $\delta\omega$ is given by the following expression:

$$\delta\omega = \left(\pi\frac{f_{m0}}{\lambda}\right)^{1/2}\left(\frac{8\pi cM}{|D|L}\right)^{1/4} \qquad (4.1-9)$$

where M represents the modulation depth.

A direction not contemplated in [8] was the control of the coherence length value. We explore here the dependence of the linewidth on the combination of lengths of dispersion compensation fiber (DCF), and of single mode fiber (SMF), in correlation with the mode-locking frequency applied on the SOA. Having involved two types of fibre in the cavity, equation (4.1 – 8) is rewritten as follows:

$$\Delta\lambda_{max} = \frac{1}{|D_{DCF}L_{DCF}+D_{SMF}L_{SMF}|f_{m0}} = \frac{1}{|D_{total}|f_{m0}}, \qquad (4.1-10)$$

where the modulus value represents the total dispersion in the laser cavity D, L_{DCF} and L_{SMF} represent the lengths of DCF and of SMF, respectively, while $L_{DCF}+L_{SMF}$ is equal to L, the total cavity length.

The maximum achievable sweeping rate f_s for a single short cavity roundtrip, is defined as [11]:

$$f_{s,max} = \frac{\delta\lambda c_0}{\Delta\lambda Ln}, \qquad (4.1-11)$$

where $\delta\lambda$ represents the linewidth. In order to achieve sufficient gain for lasing, the sweep rate f_s must be smaller than the maximum value $f_{s,max}$.

Fig 4.1.1 illustrates the optical spectrum of a single mode-locking mechanism applied to the cavity gain, with a repetition rate f_s, where v_{-1}, v_{-2}, v_0, v_1, v_2 represent the corresponding optical frequencies due to excitation signal of frequencies $f_{m0}- 2f_s, f_{m0}- f_s, f_{m0}, f_{m0} + f_s, f_{m0} + 2f_s$, respectively. The span Δf_m around the central mode-locking value f_m in the RF input determines an optical span of Δv_m in the optical spectrum.

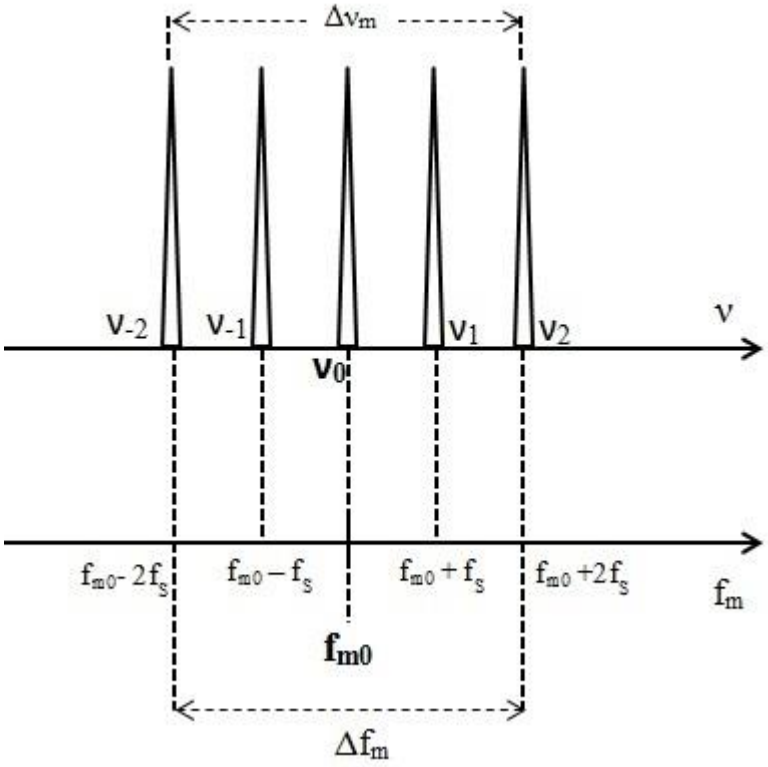

Fig. 4.1.1. AKSS single mode-locking spectrum

4.2. Proposed RF configurations

Several RF configurations were considered. The simplest employs a commercial RF pulse generator, capable to emit a wide range of RF signals: sinusoidal, saw-tooth, triangular etc. In the present work, an Agilent pulse generator, model 81160A was employed, which offers a limited frequency range (10Hz-500 MHz), up to 5 V_{pp} amplitudes. The mode-locking can be either controlled statically, by manually inputting the central frequency and the amplitude, or dynamically, be setting a central frequency value f_m and a span around this value, Δf_m. If for the desired application, the RF tuning signal is not strong enough, a radio frequency amplifier (RFA) is used to further boost the RF signal injected in the SOA through the bias tee.

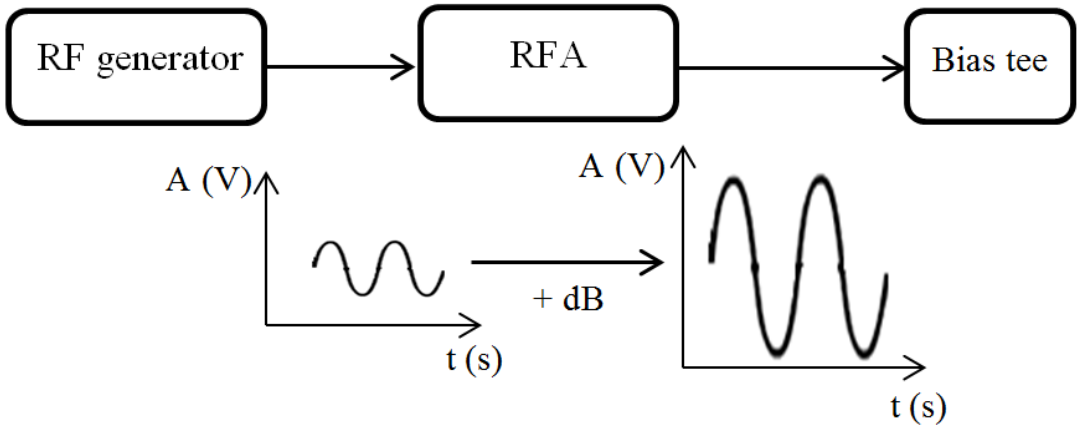

Fig. 4.2.1. Basic mode-locking RF mechanism

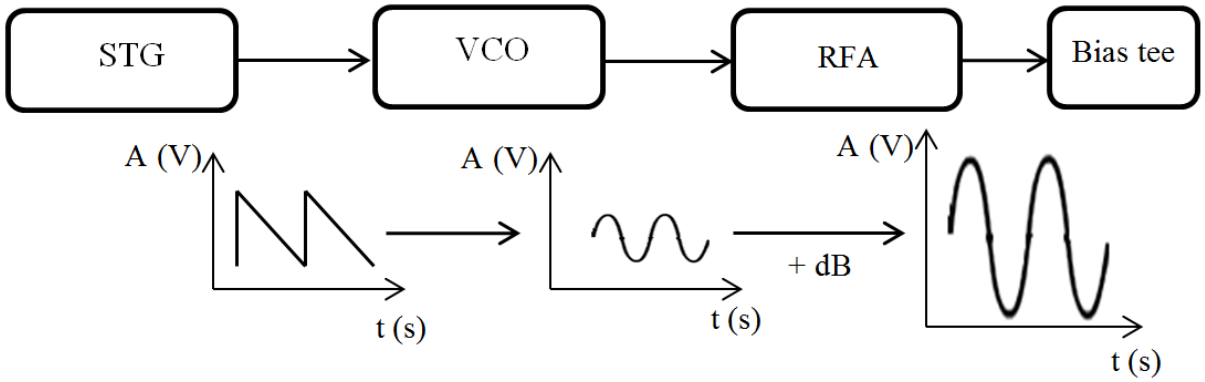

Fig. 4.2.2. Mode-locking RF mechanism employing a VCO

In Fig. 4.2.2 an alternative to the signal generator is offered by employing a voltage controlled oscillator (VCO). The same RF generator described above can be used this time as a saw tooth generator (STG) in order to tune the VCO frequency. The central locking frequency f_{m0} generated can be controlled by the offset value set on the STG. A VCO offers limited range, but on the other hand it is compact, low cost and easy to integrate into a more advanced electronic laser control board. Also, some models can generate frequencies in the GHz region in dynamic regime. Possible VCOs can be purchased from companies like Mini-Circuits, offering a wide range in terms of bandwidth and power, for example ZX95-368S+, that operates at 360- 420 MHz, delivers 2.5 dBm and can be tuned in a bandwidth of over 60 MHz, representing more than 10% from the central oscillating frequency. Generally, the VCO emits 0.2 – 1 V amplitude sinusoidal signals, therefore a radio frequency amplifier (RFA) is needed to boost the signal driving the SOA via the bias tee in order to tune the gain in the laser cavity.

References

[1] W. E. Lamb Jr., “Theory of an optical laser”, Phys. Rev. 134 (6A), A1429 (1964)

[2] L. E. Hargrove, R. L. Fork, M. A. Pollack, “Locking of He–Ne laser modes induced by synchronous intracavity modulation”, Appl. Phys. Lett. 5, 4 (1964)

[3] U. Keller et al., “Semiconductor saturable absorber mirrors (SESAMs) for femtosecond to nanosecond pulse generation in solid-state lasers”, IEEE Journal Selected Topics Quantum Electronics 2, 435 (1996)

[4] A. Schmidt et al., “Passive mode-locking of Yb:KLuW using a single-walled carbon nanotube saturable absorber”, Optics Letters 33 (7), 729 (2008)

[5] R. Paschotta, Field Guide to Laser Pulse Generation, SPIE Press, Bellingham, WA (2007)

[6] Shinji Yamashita, Masahiro Asano, “Wide and fast wavelength-tunable mode-locked fiber laser based on dispersion tuning”, Optics Express 14(20), 9299-9306 (2006)

[7] S. Yamashita, Y. Nakazaki, R. Konishi, O. Kusakari, “Wide and fast wavelength-swept fiber laser based on dispersion tuning for dynamic sensing“, Journal of Sensors, Vol. 2009, 572835 (2009)

[8] Y. Nakazaki, S. Yamashita, “Fast and wide tuning range wavelength-swept fiber laser based on dispersion tuning and its application to dyamic FBG sensing”, Optics Express 17(10), 8310-8318 (2009)

[9] Y. Takubo, S. Yamashita, “High-speed dispersion-tuned wavelength-swept fiber laser using a reflective SOA and a chirped FBG”, Optics Express, vol.21, no.4, pp.5130-5139 (2013)

[10] L. Shenping, K. T. Chan, “Electrical wavelength tunable and multiwavelength actively mode-locked fiber ring laser”, Applied Physics Letters 72(16), 1954-1956 (1998)

[11] H. D. Lee, M. Y. Jeong, C.-S. Kim, J. G. Shin, B. H. Lee, T. J. Eom, “Linearly Wavenumber-Swept Active Mode-locking Short-Cavity Fiber Laser for In-Vivo OCT Imaging”, IEEE Journal of Selected Topics in Quantum Electronics, 20(5), 1101008 (2014)

5

Akinetic swept source based on a short dispersive cavity comprising a chirped fibre Bragg gratings

Introduction

The interest on the AKSS has been raised by the demonstration of fast, wide tuning bandwidth and large coherence length tuneable lasers based on VCSEL devices [1]. An AKSS concept using mode-locking in an anomalous dispersive DCF was recently introduced [2, 3]. In order to achieve wide and fast tuning with a narrow spectral linewidth, it was shown that the dispersion characteristic of DCF and the modulation frequency should be as large as possible, while the cavity length should be as small as possible. Also, it was demonstrated that by combining two lengths of fibre, one with anomalous dispersion (DCF) and the other with normal dispersion, such as single mode fibre (SMF), the coherence length can be adjusted slightly by controlling the dispersion in the cavity and the mode-locking frequency of the signal applied to the SOA that tunes the gain medium [4].

One of the current trends in AKSS developments is to achieve high performance in terms of optical output parameters and axial range by using a short cavity, with compact dispersive elements that can replace tenths or even hundreds of meters of DCF and SMF.

A fibre Bragg grating (FBG) is defined as a periodic or aperiodic perturbation of the effective refractive index in the core of an optical fibre. The perturbation is periodic over a certain length of a few millimetres or centimetres, and the period is of the order of hundreds of nanometres, or much longer for long-period fibre gratings. The refractive index perturbation leads to the reflection of light propagating along the fibre in a narrow range of wavelengths for which the Bragg condition (the equation determining the value of the wavelength λ in vacuum) is satisfied:

$$\lambda = 2n_e\Lambda, \qquad (5.1-1)$$

where n_e represents the effective index of refraction of the fibre glass and Λ is the FBG period.

The FBGs with the narrowest bandwidth values possible are useful in the construction of single-frequency fibre lasers or optical filters. Large bandwidths are achieved using aperiodic designs. FBGs with aperiodic index modulation exhibit reflectivity curves without side lobes, multiple tailored reflection bands, or special chromatic dispersion profiles. For dispersion compensation, the chirped fibre Bragg gratings (CFBG) are used [5], where the Bragg wavelength varies with position. Large group delay dispersion is achievable in a short length of fibre, sufficient for compensating the dispersion of a long span of a transmission fibre. Another application where the CFBG is useful is the pulse compression within a chirped-pulse amplifier system [6]. CFBGs also represent a viable solution in sensing [7]. Recent proposed solutions employ the use of partially reflective CFBGs as dispersive element in a linear cavity [8].

In this chapter, a short ring cavity AKSS based on a highly reflective broadband CFBG used as dispersive element, is described.

5.1. 1060 nm akinetic swept source based on a reflective cFBG

In this chapter, a short ring cavity AKSS based on a highly reflective (R>98%) broadband CFBG used as dispersive element, is described. The mode-locking was achieved totally electronically, by injecting RF modulated current directly into the SOA. A tuning bandwidth larger than 30 nm and sweeping rate over 100 kHz were achieved.

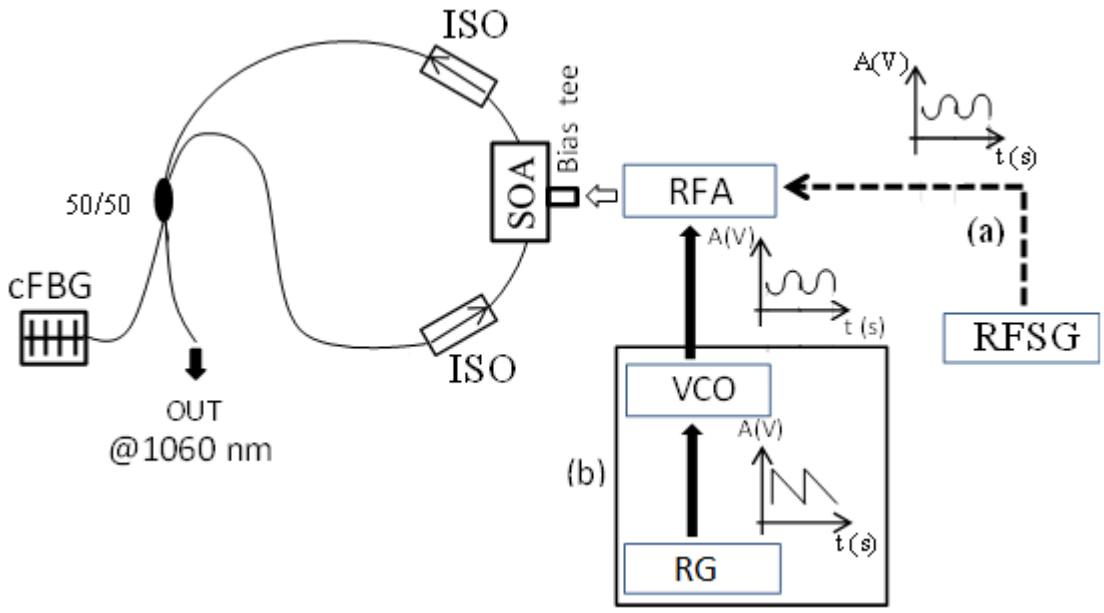

Fig. 5.1.1. AKSS set-up, showing the two mode-locking RF circuits for: (a) static regime operation; (b) dynamic regime operation

The experimental setup, as depicted in Fig. 5.1.1, uses a single mode fibre (SMF, Corning, Hi1060, dispersion parameter -38 ps/nm·km) ring cavity in which a SOA (QPhotonics-1050), operating at a central wavelength of 1060 nm, with a bandwidth larger than 100 nm, is used as a medium. This is driven by a Thorlabs LDC200 power supply, while temperature stability is ensured by a Thorlabs TED200. The SOA is isolated by two polarization insensitive fibre optic isolators (ISO), which ensure unidirectional lasing. The cavity is closed via a 50:50 coupler and a CFBG (QPS Photronics, 36 nm bandwidth, central wavelength at 1060 nm, dispersion parameter -11 ps/nm, reflectivity R>98%). The other output of the coupler delivers 50% of the power from the cavity. The total cavity length was minimized to 4.73 m. We have initially employed a circulator to close the loop via the cFBG, but this was soon ruled out due to large polarization mode dispersion (PMD) [9]. In fact, the extra losses introduced by the coupler allow utilization of larger current through the SOA

for similar ASE contribution, current which determines a wider SOA bandwidth. To drive the laser into mode-locking, sinusoidal RF signal is applied to the SOA from one generator of a dual signal generator HP8648C (RFSG, 9 kHz-3.2 GHz that can deliver up to 2.5 V_{pp} maximum output). This is employed for static tuning operation, by manually changing the input signal frequency. For dynamic regime, signal from a voltage controlled oscillator (VCO) is applied to the SOA, where the VCO is driven by a ramp signal generated, RG (in fact the other half of the same Agilent RFSG, model 81160A).

The offset of the ramp signal determines the central mode-locking frequency generated by the VCO, while its amplitude sets the frequency tuning range Δf of the VCO. The repetition frequency of the RFSG ramp determines the tuning rate, f_s.

Two VCOs were tested, to generate mode-locking at $10f_R$ and $20f_R$, respectively: ZX95-368S+ (368 MHz central frequency, 60 MHz 3 dB modulation bandwidth, 0.5-10 V voltage range, 2.5 dBm output power) and ZX95-928CA+ (928 MHz central frequency, 90 MHz 3 dB modulation bandwidth, 0.5-10 V voltage range, 4.6 dBm output power). Ramps were applied to the VCO from a ramp generator (RG). The signal from either the RFSG or from the VCO is further amplified by a radio frequency amplifier (RFA), before being delivered to the SOA via a bias tee. As amplifier RFA, two Mini-Circuits RF amplifiers, ZFL-2500VH+, 0-2.5 GHz, 26 dBm and a ZHL-42W, 0-4.2 GHz, 28 dBm, placed in series are used. The laser output characteristics of the AKSS configuration are measured with an Agilent 86145B optical spectrum analyser (OSA). The dynamic sweeping was evaluated by probing the channelled spectrum of a Mach-Zehnder interferometer driven by the AKSS.

The photodetected signal output was measured using a balanced photo-detector (Newport 1617), and displayed with a LeCroy Wave Runner 104 MXi-A 1GHz oscilloscope. It was noted that when ramps drive the optical frequency from high to low this leads to larger tuning bandwidth and better signal to noise ratio than when using ramps driving the optical frequency from low to high.

When operating the AKSS in static regime, the mode-locking frequency f_m of the driving signal is adjusted to tune the laser within a bandwidth $\Delta\lambda$=30 nm, measured by the OSA. The difference of the RF values corresponding to the tuning bandwidth edges denotes a static frequency band Δf around each central f_m, multiple of f_R. The larger the f_m, the larger the span Δf, according to the graph in Fig. 5.1.2 (blue). The linewidth was also measured in static regime, a value of 60 pm being obtained at 1 GHz mode-locking. The practical linewidth is expected to be better, due to the limited resolution of the OSA, of 60 pm.

Pulses at the mode-locking frequency f_m = 43.27 MHz are measured using the fast photodetector. Applying equations (4.1–7) and (4.1–10) leads to a theoretical output bandwidth larger than that achievable and measured by the OSA, as represented in Fig 5.1.3. In practice, the tuning bandwidth is limited by the CFBG bandwidth (32 nm with the reflectivity R>98% around the central 1060 nm emission wavelength, according to the manufacturer). As the sweeping rate increases, the OSA measured output power (in dBm) and bandwidth (in nm) both decrease. The power exhibits a slow decay, the slope being calculated as $36 \cdot 10^{-6}$ dB/Hz. At a 100 mA current driving the SOA, the power measured at the output was approximately 2 mW at 100 kHz sweep rate. Above this level, amplified spontaneous emission (ASE) is noticeable. The ripples observed in the optical output measured by the OSA occur due to the modulation characteristics of SOA [10].

For mode-locking at $10 \cdot f_R$ = 432.7 MHz, Fig. 5.1.4 illustrates the tuning bandwidth versus the RF tuning bandwidth Δf when operating the AKSS dynamically, at 1 kHz sweep rate, using the RSFG. A slight decrease in the output power is also registered, about 10% when tripling the tuning bandwidth. For a 30 nm tuning bandwidth, assuming a Gaussian shape of the spectrum, the axial resolution achievable is $0.44 \cdot \lambda_0^2/\Delta\lambda$ = 0.016 mm.

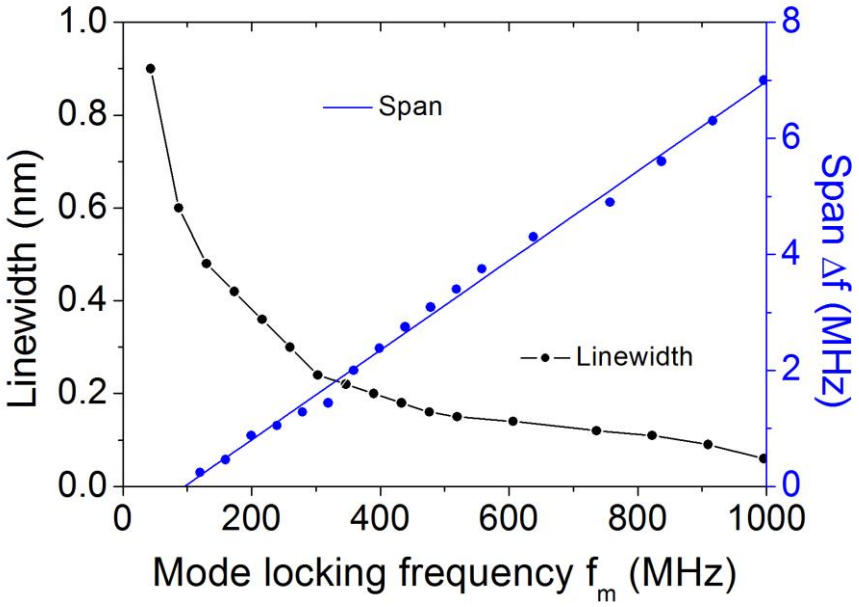

Fig. 5.1.2. Static regime measurements: linewidth and frequency band measured in the 0-1 GHz mode-locking frequency interval

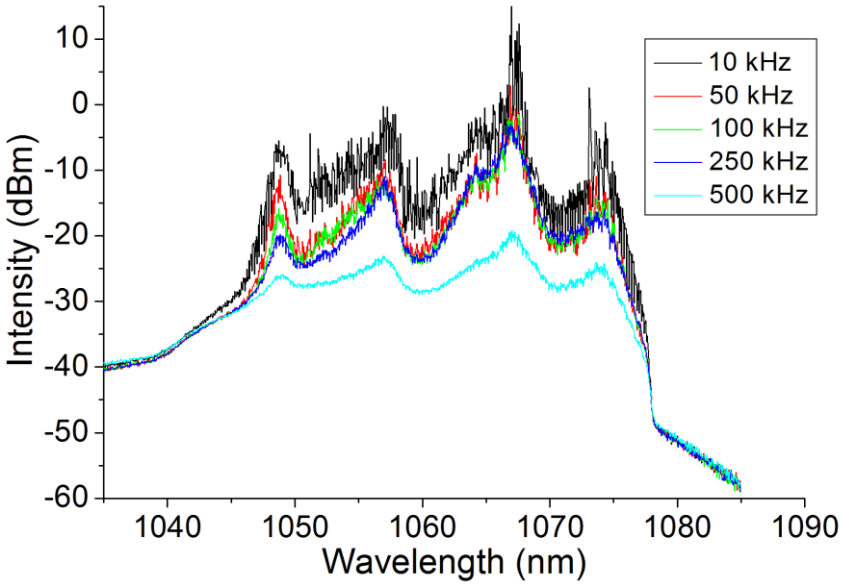

Fig. 5.1.3. AKSS optical output spectrum for different sweeping rates applied by the RG

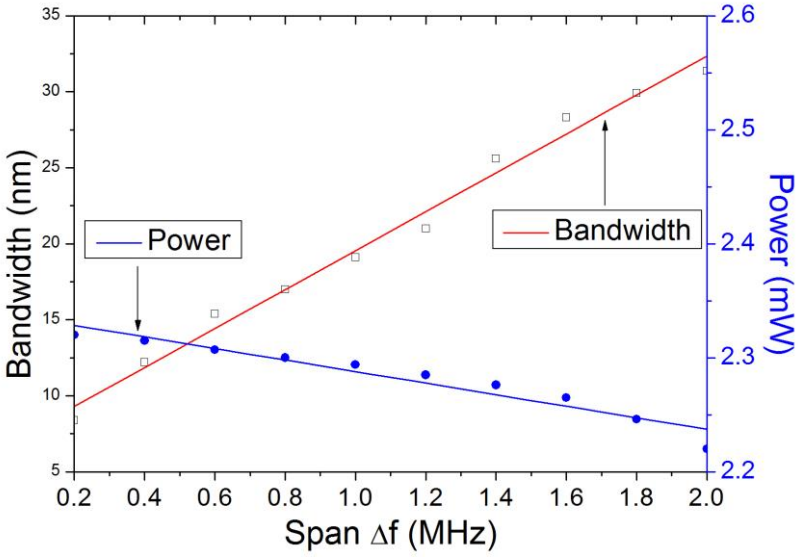

Fig. 5.1.4. Optical power and bandwidth measured dynamically for a 0-2 MHz frequency range around $10f_R$ = 432.7 MHz

The flexibility of the dispersion tuned short ring laser cavity based on CFBG is given by the possibility of dynamically tuning output optical parameters at high sweeping rates, making it a possible solution for OCT applications. Thus, we evaluated the AKSS mode locked at $10f_R$ (corresponding to 432.7 MHz), swept at 1 kHz, 10 kHz, 25 kHz, 50 kHz and 100 kHz rate, by scanning through the channelled spectrum of a Mach-Zehnder interferometer, depicted in Fig. 5.1.5.

The configuration uses two broadband directional 50/50 couplers. The object arm comprising a collimator assembly C, from which the light travels to an achromatic lens L (25 mm focal length) that focuses light on a mirror (used to act as object, in order to acquire A-scans). The distance between the collimator C and the lens L is the same as that between the lens L and the mirror M, equal to the L focal length. The reference arm comprises two identical collimator assemblies C (similar to that in the object arm), fixed on a translation stage allowing 3D manual adjustment. The light returning from the two arms is received by a balanced photodetector (PhD), New Focus model 1817, DC-80 MHz, 900-1700 nm bandwidth, which is connected to a digital oscilloscope, LeCroy 104Mxi-A, 10 Gyga Samples/s, capable of acquiring A-scans and calculating the FFT of the photodetected light.

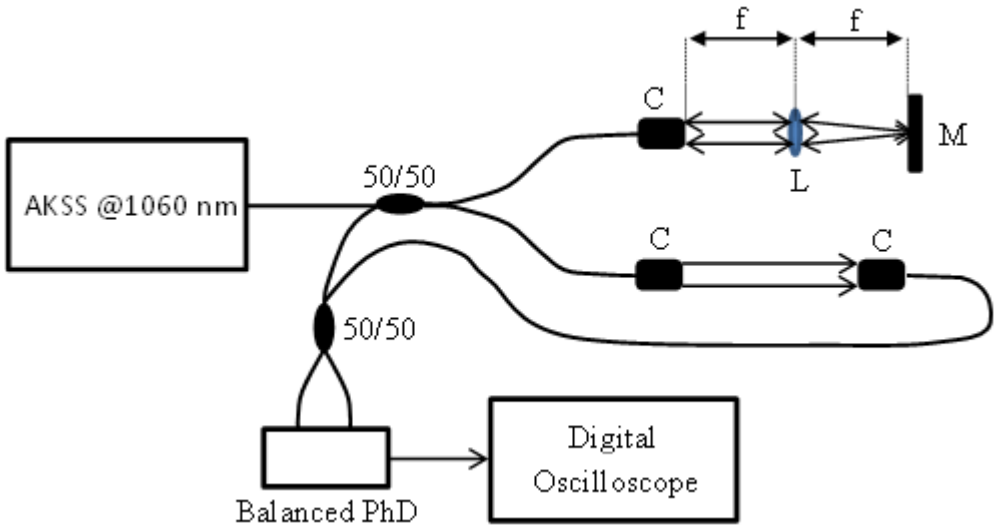

Fig. 5.1.5. Mach-Zehnder interferometer used to test the AKSS emitting in the 1060 nm range, where, C – collimator, L – lens (f – focal length = 25 mm), M – mirror, PhD – photodetector

Fig. 5.1.6 depicts the photo-detected signal at the interferometer output for at 1 kHz sweep rate, 1 mm OPD, when applying a 1.2 V_{pp} amplitude triangular signal from the RG. The larger the voltage, the larger the RF frequency and smaller the optical frequency. When the RG signal drives the optical frequency from low to high amplitude, the resulting fringes have 17% larger amplitude than the ones measured when driving the SOA frequency from high to low.

A Fast Fourier Transformation (FFT) of the photo-detected signal delivers an A-scan [11]. The amplitude decay of A-scan peaks with the increase in the OPD in the interferometer

is depicted in Fig. 5.1.7. Also, the faster the sweeping rate, the steeper the decay. The OPD values where the decay registered 12 dB, is 0.64 mm, 0.39 mm, 0.30 mm, 0.24 mm and 0.13 mm at 1 kHz, 10 kHz, 25 kHz, 50 kHz and, respectively, 100 kHz.

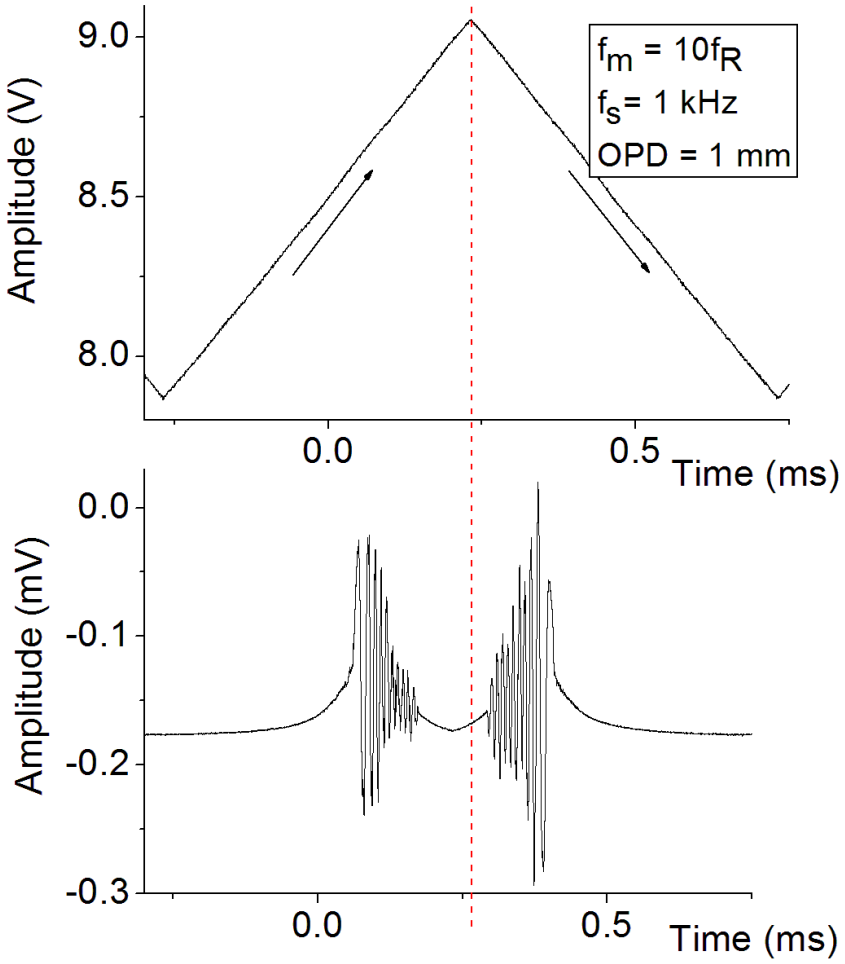

Fig. 5.1.6 Triangular VCO driving signal (top); Photodetected signal at the interferometer output (bottom)

The A-scans show a decrease in the axial range, as sweeping rate increases, this being attributed to the fact that the AKSS coherence decreases with the increase in the sweeping speed [12]. At $10f_R$ we have measured a value of 0.182 nm for the instantaneous linewidth λ_l. The coherence length l_c of the setup comprising the interferometer and the AKSS, which represents twice the depth at which the signal intensity drops by half, is calculated according to the expression (2 – 9), where λ_0 represents the central optical wavelength, 1060 nm.

At $10f_R$ mode-locking, l_c is 2.71 mm. At $20f_R$, as the mode-locking frequency increased, the linewidth narrows to 0.104 nm, as predicted by the measurements done in the static regime (Fig. 5.1.2, black graph). With this value, the coherence length increases up to

4.75 mm. This means improved axial scanning range. This in confirmed by the A-scan decay measurements performed at $20f_R$, depicted in Fig. 5.1.7 (b), for 1 kHz, 10 kHz 25 kHz, 50 kHz and, respectively, 100 kHz. On the other hand, if we take into consideration equation (4), as the linewidth becomes narrower, and assuming the bandwidth and cavity length remain constant, the maximum sweeping rate that can be achieved decreases as well.

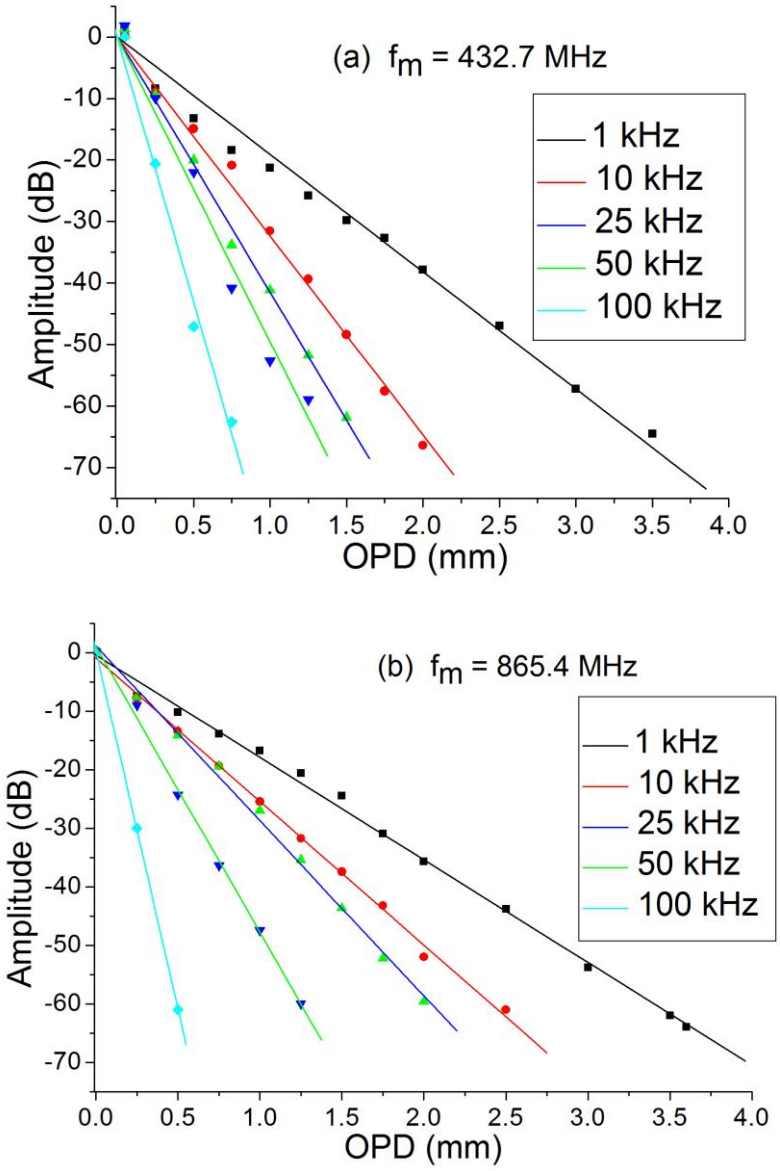

Fig. 5.1.7. Decay of modulation intensity with increasing OPD, for several sweeping rates delivered by the RG between 1-100 kHz, (a) $10f_R$ mode-locking frequency; (b) $20f_R$ mode-locking frequency

In our case, by applying equation (4.1 – 11) we obtain a maximum theoretical sweeping rate $f_{s,max}$ of 264.54 kHz at $10f_R$ and 150.59 kHz at $20f_R$. The sweep rate f_s must be smaller than the maximum value $f_{s,max}$ in order to achieve sufficient gain for lasing. Thus, in

order to achieve better axial range at hundreds of kHz repetition rate, when mode-locking at high frequencies, from (4.1 – 11) a shorter cavity length L would be required for further improvement.

The sensitivity S of the interferometer used for reflectivity measurement, is calculated as $20 \cdot log(A_{OPD}/A_{noise})$, where A_{OPD} is amplitude of the FFT peak for an OPD close to 0, while A_{noise} represents the amplitude of the noise floor measured outside the peak [13]. The S values measured while operating the AKSS mode locked at $10f_R$ and $20f_R$ and a sweep rate of 1 kHz, were 85.3 dB and 83.6 dB, respectively.

Summary

A short ring cavity AKSS at 1060 nm was demonstrated, with controllable mode-locking and optical output parameters, coherence length and repetition rate. The main parameters of the 1060 nm AKSS are illustrated in the following table:

Parameter	**Value**
Central wavelength	1060 nm
Mode-locking frequency	50 – 1000 MHz (adjustable)
Maximum Output Power	2.55 mW
Linewidth	0.104 nm
Bandwidth	32 nm
Maximum repetition rate	500 kHz

It was shown that using a CFBG as dispersive element significantly shortens the cavity length in comparison with DCF based AKSS concepts [2-4], while maintaining good optical output parameters. Power and bandwidth show a slow decay with the increase of repetition rate up to 250 kHz. The sweeping rate achieved can be uplifted to 500 kHz, but at this level, there is not sufficient gain for lasing and the decay in power is more significant. Without any booster, the power achieved was 2 mW at 100 kHz. These parameters could be improved by further reducing the cavity length, and by using a larger bandwidth CFBG. We believe that there is also a reserve in the RF injection. By further strengthening the RF driving signal, while lowering the bias, the ASE may be further reduced.

References

[1] T.-H. Tsai; O. O. Ahsen; H.-C Lee; K. Liang; M. G. Giacomelli; B. Potsaid; Y. K. Tao; V. Jayaraman; M. F. Kraus; J. Hornegger; M. Figueiredo; Q. Huang; H. Mashimo; A. E. Cable; J. G. Fujimoto, "Ultrahigh speed endoscopic swept source optical coherence tomography using a VCSEL light source and micromotor catheter", Proc. SPIE 8927, Endoscopic Microscopy IX; and Optical Techniques in Pulmonary Medicine, 89270T (2014)

[2] S. Yamashita, Y. Nakazaki, R. Konishi, O. Kusakari, "Wide and fast wavelength-swept fiber laser based on dispersion tuning for dynamic sensing", Journal of Sensors, Vol. 2009, 572835 (2009)

[3] Y. Nakazaki, S. Yamashita, "Fast and wide tuning range wavelength-swept fiber laser based on dispersion tuning and its application to dyamic FBG sensing", Optics Express 17(10), 8310-8318 (2009)

[4] R.-F. Stancu, D. A. Jackson, A. Gh. Podoleanu, "Versatile Swept Source With Adjustable Coherence Length", IEEE Phot. Tech. Lett., Vol. 26, Issue 16, pp. 1629-1632 (2014)

[5] N. M. Litchinitser et al., "Fiber-based tunable dispersion compensation", J. Opt. Fiber Commun. Rep. 4, 41 (2007)

[6] F. Röser et al., "Millijoule pulse energy high repetition rate femtosecond fiber chirped-pulse amplification system", Optics Letters 32 (24), 3495 (2007)

[7] A. D. Kersey et al., "Fiber grating sensors", J. Lightwave Technol. 15 (8), 1442 (1997)

[8] Y. Takubo, S. Yamashita "High-speed dispersion-tuned wavelength-swept fiber laser using a reflective SOA and a chirped FBG", Optics Express, vol. 21, no. 4, pp. 5130-5139 (2013)

[9] N. Gisin et al., "Polarization mode dispersion of short and long single-mode fibers", J. Lightwave Technol. 9 (7), 821 (1991)

[10] H. D. Lee, M. Y. Jeong, C.-S. Kim, J. G. Shin, B. H. Lee, T. J. Eom, "Linearly Wavenumber-Swept Active Mode-locking Short-Cavity Fiber Laser for In-Vivo OCT Imaging", IEEE Journal of Selected Topics in Quantum Electronics, vol. 20, no. 5, 1101008 (2014)

[11] A. Gh. Podoleanu, "Optical coherence tomography", J. Microscopy, 247 (3) 209-219, 2012

[12] Akira Takada, Makoto Fujino, and Shigenori Nagano, “Dispersion dependence of linewidth in actively mode-locked ring lasers”, Optics Express 20, 4753-4762 (2012)

[13] A. Gh. Podoleanu, A. Bradu, “Master-Slave interferometry for parallel spectral domain interferometry sensing and versatile 3D optical coherence tomography”, Optics Express, Vol. 21, No. 16, 19324-19338 (2013)

6

Dual mode-locking mechanisms for akinetic swept sources based on dispersive cavities

6.1. Theory on dual mode-locking

As shown in the previous chapters, the total cavity length determines a total dispersion D_{total} measureable in the cavity. Applying the single mode-locking mechanism in a cavity with anomalous dispersion, the optical linewidth $\delta\lambda$ and tuning bandwidth $\Delta\lambda$ are evaluated by operating the AKSS in static regime, where the RF of the signal driving the SOA is changed manually.

After that, the AKSS is switched to a dynamic operating regime. A strong decay of the optical output as the sweeping speed increases was illustrated in Chapter 5, and it can be noticed that by using the first mode-locking mechanism alone it is not possible to achieve high sweeping rates f_s. Even with short lengths of the cavity, of a couple of meters, we could not achieve sweeping rates $f_s > 100$ kHz, meaning that the decay of power with the sweeping rate is not due to the length of fibre used.

In continuation, a novel dual mode-locking (DML) principle [1] will be explained. A first locking condition is imposed by driving the optical gain at a high frequency, to induce mode-locking. A second locking mechanism, inspired from the practice of FDML applied to TFPF lasers [2], employs sweeping at a rate close to f_R, however in opposition to [2], at essentially detuned values from f_R. To produce FDML, the roundtrip time needs to be increased to amenable values, which requires several hundreds of meters of fibre, i.e. this strategy is opposed to that suggested in [2].

Initially, the cavity length is adjusted to a value which determines f_R and the VCO is driven with a signal of frequency f_m in the range ΔF. When the signal applied from the synthesizer to the VCO is swept at a sweeping rate of $f_S = f_R$, then the VCO spectrum consists in a comb of frequencies $f_{m0}\pm f_R$, $f_{m0}\pm 2f_R$, $f_{m0}\pm 3f_R$ and so on, i.e. of frequency components distanced apart by f_R steps. The resulting RF signal from the RF synthesizer is amplified and injected into the SOA gain medium of the AKSS. This generates a narrow band laser output, having a linewidth $\delta\lambda$ and f_R repetition rate. If $f_S = f_R$, no tuning is noticed, as illustrated in Fig. 6.1.1.

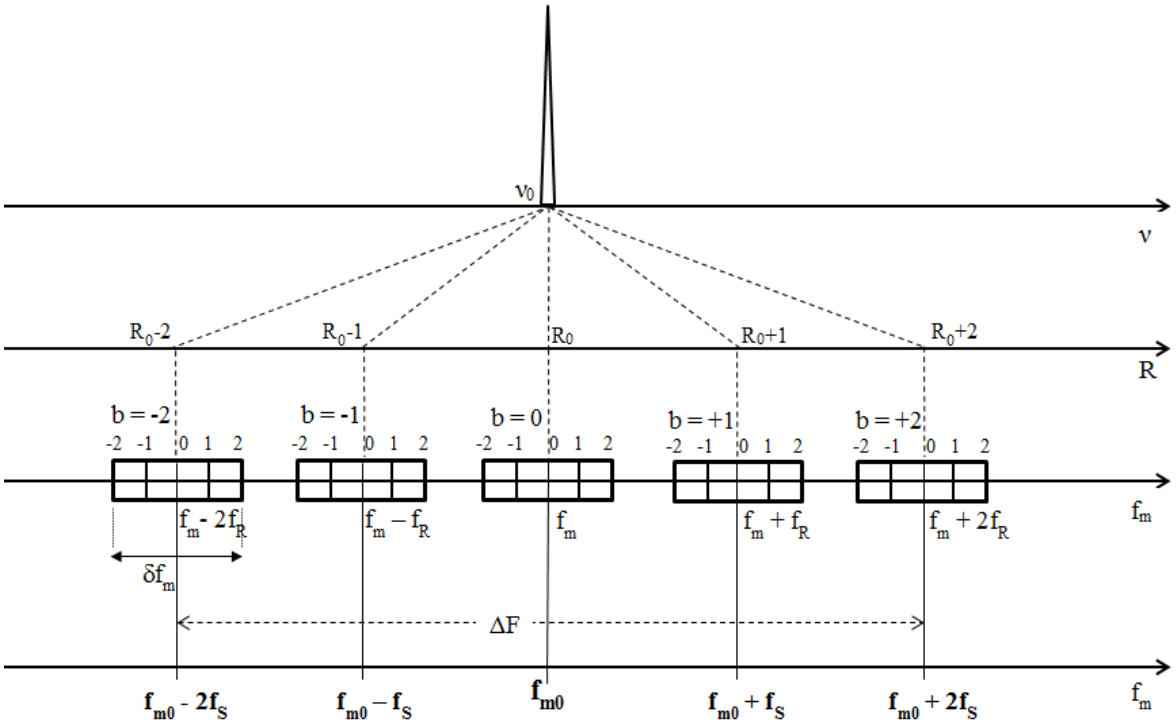

Fig. 6.1.1. DML AKSS output when the VCO is excited by signal pulsating at f_R

To perform tuning, sweeping needs to be performed at a detuned rate, δf_R, from f_R. Therefore, $f_S = f_R\pm\delta f_R$, in which case the VCO is tuned with a comb spectrum consisting in f_m, $f_{m0}+f_R\pm\delta f_R$, $f_{m0}+2f_R\pm 2\delta f_R$, $f_{m0}+3f_R\pm 3\delta f_R$ and so on, as depicted in Fig. 6.1.2. In both this figure and the previous one, b represents the order of the band measured starting from an arbitrary band, corresponding to the central RF value, f_{m0}, while R represents the total frequency value $f_{m0}+b(f_R\pm\delta f_R)$ corresponding to each band order b in the frequency spectrum. ν_0 and $\Delta\nu_m$ represent the optical frequency at 0 detuning, respectively the optical frequency bandwidth in the output when the value of detuning is different from zero. Those quantities can be very well replaced with corresponding wavelength quantities λ_0 and, respectively, $\Delta\lambda$.

The resulting RF signal from the VCO is amplified and injected into the SOA, therefore generating a comb laser output. The output bandwidth $\Delta\lambda$ is given by:

$$\Delta\lambda = \frac{\Delta F}{f_R} C_m \delta f_R \delta\lambda, \qquad (6.1-1)$$

where C_m is a cavity coefficient and ΔF represents the frequency tuning range of the RF synthesiser (VCO). C_m can be calculated from the slope of the graph representing either the increase in optical bandwidth $\Delta\lambda$ with the detuning rate $\delta\lambda$ or, respectively the decay of output power versus detuning rate.

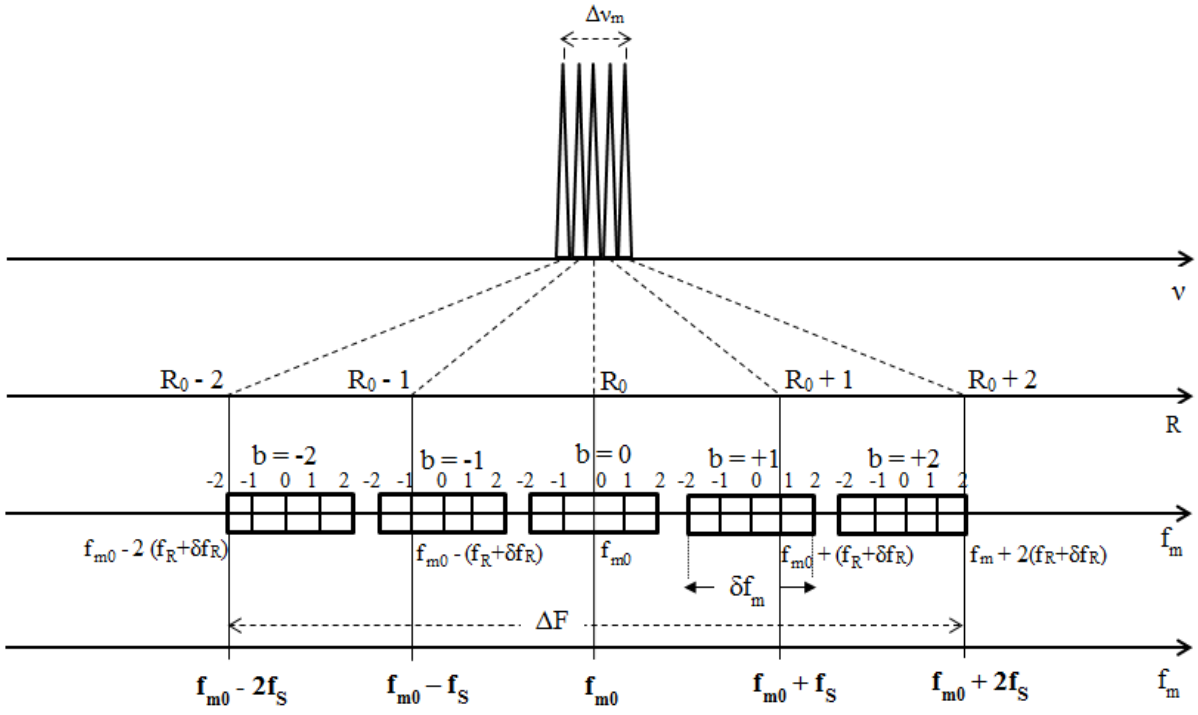

Fig. 6.1.2. DML AKSS output when a detuning step, δf_R from f_R is applied

The spectrum of the RF signal of a carrier f_m when swept in frequency at a rate *fs* consists in a comb of frequencies separated by f_s. The number of resolved frequency points within the spectrum, *S*, is given by the maximum frequency deviation, ΔF, divided by f_S. ΔF depends on the voltage applied to the tuning input of the RF synthesizer. If f_s is low, for example 1 kHz, as ΔF is less than f_R (which is hundreds of times larger), maximum achievable for *S* would be $S = \Delta F/f_S >> 1$. When driving the AKSS at a significantly larger frequency f_R, the only way to maintain a large number of resolved frequency points is to jump the optical frequency of the swept source from one tuning band to the next, in steps of

f_R. In the DML regime, a deviation of frequency as high as $S \cdot f_R = (\Delta F / f_S) \cdot f_R$ would therefore be needed.

6.2. Proposed RF configurations

In order to implement DML, the basic RF configuration depicted in Fig. 4.2.2 can be utilised. The STG is instructed by three parameters: f_R, detuning δf and band order b. Then as a large frequency deviation VCO (for example a Mini-Circuits type ZX-368-S+) in series with a power amplifier (for example a Mini-Circuits, ZFL-2500VH+) are used. This can allow an extremely wide frequency deviation, Δf_m = 60 MHz (in a range from $f_{m,min}$ = 360 MHz for 0 V to $f_{m,max}$ = 420 MHz) for a voltage variation at its input of 10 V. The STG, which delivers a saw-tooth sweeping signal of $5V_{pp}$ amplitude and 2.5V bias, is used to drive the frequency deviation of the large frequency deviation VCO.

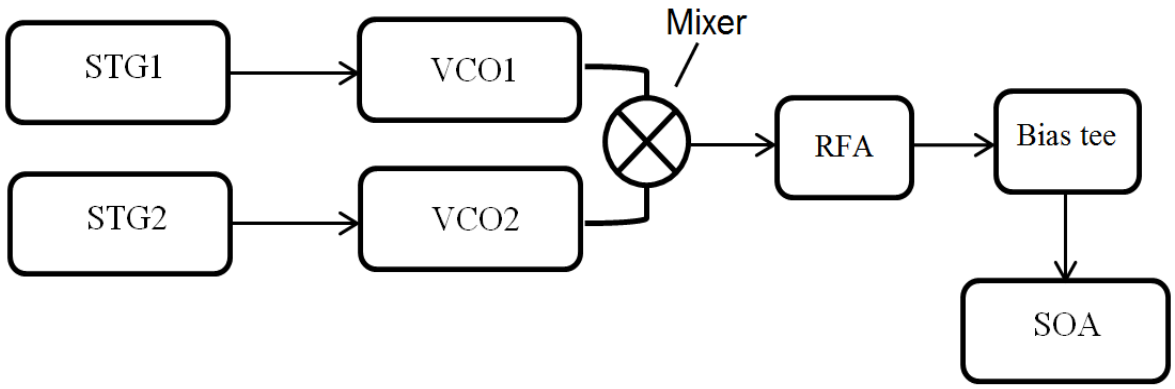

Fig. 6.2.1. RF mode-locking mechanism employing two VCO signals

Fig. 6.2.1 depicts the an alternative to the RF configuration shown in Fig. 4.2.2, an embodiment of a large frequency deviation generator to deliver a wide tuning range RF signal to cover many mode-locking bands, as required by the AKSS DML tuning method. Because the tuning bandwidth of a commercial VCO is limited, two such VCOs are used, denoted as VCO1 and VCO2. They emit at much larger frequency and therefore exhibit a larger tuning bandwidth than a commercially available VCO designed for the central frequency f_m needed. Their output signals are combined with a multiplicative mixer. The two VCO input signals are both sinusoids of specified frequencies f_{m1} and f_{m2}, therefore the output of the mixer will comprise two new sinusoids that have the sum $f_{m1} + f_{m2}$ frequency and the difference frequency absolute value $|f_{m1} - f_{m2}|$.Via a low pass filter, the signal oscillating at the sum of frequencies is attenuated and the signal oscillating at the difference of frequencies is transmitted to the SOA through a custom made bias tee. The two VCOs

need to be swept in antiphase. This is achieved by using an inverter. To adjust the optical frequency, the signals applied to the two VCOs are adjusted in amplitude and bias.

Combination of lower central frequency VCOs can be used to obtain a larger frequency deviation, such as for example, Mini-Circuits type ZH95-1790-S+ and Mini-Circuits, type ZH95-1240-S+ to deliver an RF output of 500 MHz f_m, deviated by Δf_m = 200 kHz.

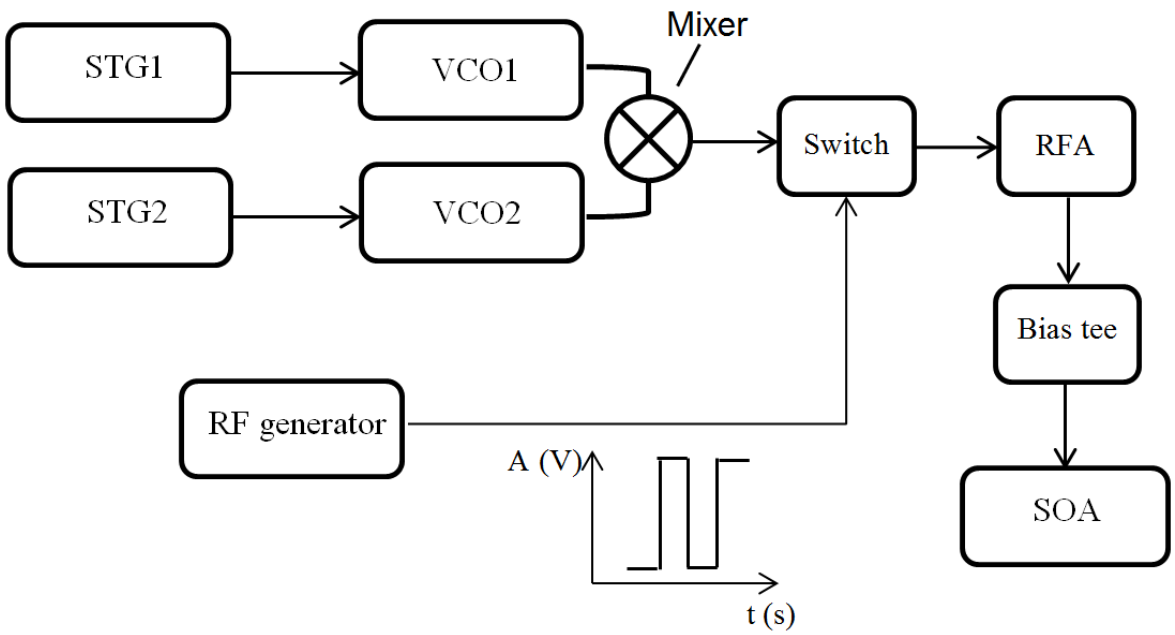

Fig. 6.2.2 RF mode-locking mechanism employing two VCO signals

In Fig. 6.2.2, a quieter VCO generator is disclosed. During the fast transition of the STG1, respectively STG2 signal from maximum to minimum, for any new period, the VCOs 1 and 2 are tuned extremely fast. During this short time, both VCOs emit spurious signals. It is known that the mode-locking requires a quiet, well defined signal. In order to eliminate spurious signals that can disturb the mode-locking, only the smooth useful ramp should be applied to the VCOs. Therefore, a square signal is introduced to delay the ramp emission, as illustrated in Fig. 6.2.3. For further control of the sweeping and enhanced stability, the signal delivered to the output during the turnaround time intervals of the RF signal is clamped using a synchronised switch. The output from the switch is further amplified using a RFA and injected in the SOA through a custom made bias tee.

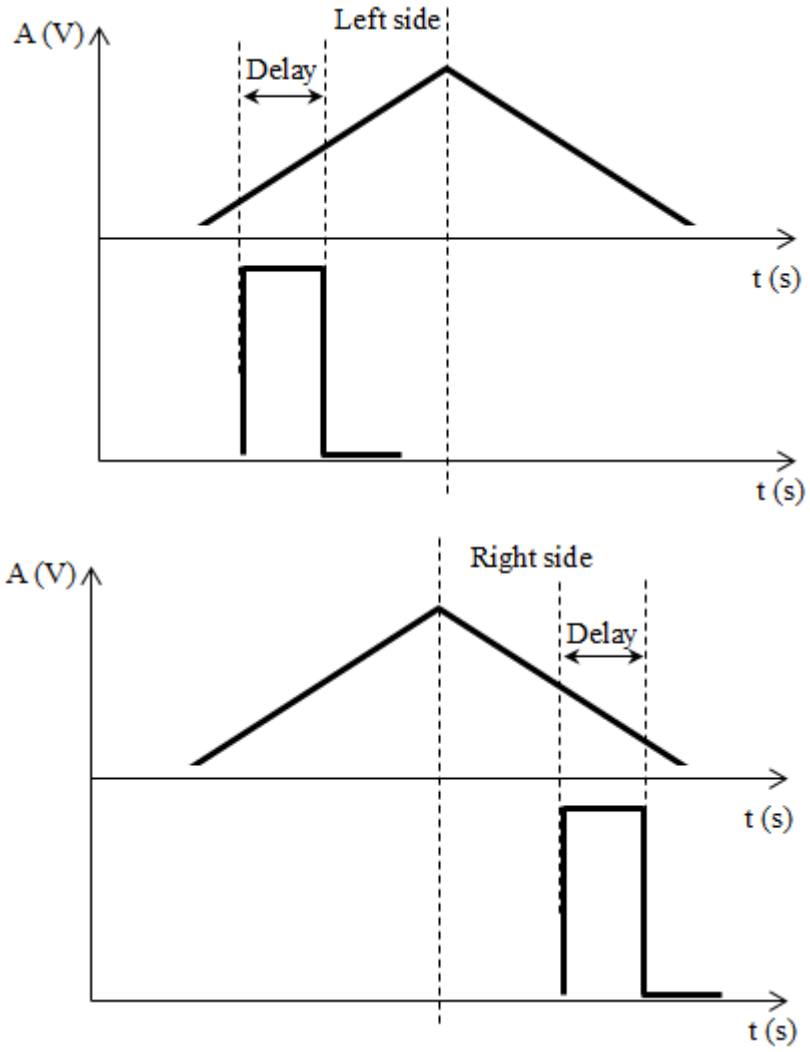

Fig. 6.2.3 Delay introduced in a triangular RF ramp signal, on the left side (above), or right side (bellow)

References

[1] R. F. Stancu, A. G. Podoleanu, “Dual mode-locking mechanism for an akinetic dispersive ring cavity swept source”, Optics Letters 40(7), 1322-1325 (2015)

[2] R. H. Huber, M. Wojtkowski, J.G. Fujimoto, “Fourier Domain Mode-locking (FDML): A new laser operating regime and applications for optical coherence tomography”, Optics Express 14(8), 3225-3237 (2006)

7

Akinetic swept sources based on long dispersive cavities comprising single mode fibre

Introduction

The Fourier domain mode-locking (FDML) method was used in ring fibre laser configurations that employed long dispersion delay fiber in order to achieve the elimination of photon lifetime limitation and improve the laser sweep rate, achieving hundreds . The FDML method is nowadays developed in a commercial wavelength swept laser solution which is capable of achieving MHz level repetition rates (Optores Gmbh).

In this chapter, akinetic AKSSs based on a novel principle, emitting at a 1060 nm central wavelength, is presented. This optical source combines the dispersion tuning principle, that eliminates the need of mechanical tuning elements in the cavity, and the FDML principle, that involves sweeping at periods matching the round trip in the cavity. This requires long cavities to allow amenable repetition rates in the tens to hundreds of kHz and even exceeding 1 MHz. The principle of achieving sweeping at multiples of the resonance frequency f_R is illustrated here. This novel concept is named dual mode-locking mechanism (DML). Furthermore, the integration of Faraday Rotating Mirrors (FRM) in laser cavities is also investigated and comparisons between the swept sources employing and, respectively, not employing FRM in their ring cavities are illustrated. A demonstration of OCT topographic imaging which demonstrates the utility of the 1060 nm AKSS is also included.

This chapter also focuses on the 850 nm single mode-locked swept source. One of the main and most important advantages that SS-OCT has in the 800 nm wavelength region

is the improved imaging resolution. The commercial OCT systems that are generally used for imaging the eye fundus are operating in the 800-900 wavelength region. The great interest for this waveband is justified by the low absorption in the vitreous region of the eye. While interest for longer wavelengths (1060 nm, 1550 nm) is determined by the need for better penetration depth, such as imaging in the choroidal region, the visible to infrared range allowes the development of reduced cost OCT systems, based on the SD-OCT technology. For the moment, there are no competitive swept sources at 800 nm with parameters to trigger development of OCT technology for the human fundus to compete in cost with the spectrometer based OCT. We have therefore constructed and tested an AKSS setup at 850 nm central wavelength, applying the same dispersion tuning principle and RF mode-locking described above at 1060 nm.

7.1. Ring cavity

7.1.1. 1060 nm single mode-locked swept source

The configuration of the 1060 nm AKSS experimented is illustrated in Fig. 7.1.1.1. It comprises a broadband SOA, model QPhotonics QSDA-1050, operating at 1060 nm central wavelength, maximum current 200 mA and a 3 dB bandwidth of 100 nm. The SOA is secured in a Laser Systems mount, model HS501, and it is driven by a Thorlabs LDC 210 power supply. Temperature stability is ensured through thermo-electric cooling provided by a Thorlabs TEC 200 driver (sensor TH 20kΩ). The SOA is delimited by two polarization insensitive broadband isolators I, manufactured by AFW Technologies, which ensure unidirectional lasing. The ring cavity comprises 1000 m length L_{DCF} of Corning Hi1060 SMF, with an anomalous dispersion parameter D = -50 ps/nm, calculated in 1 km fibre, at 1060 nm. The total ring cavity length is about 1005 m. Therefore, the resulting total cavity dispersion is calculated as - 50.25 ps/nm. By using the equation 4.1 – 10, a theoretical mode-locking frequency value of 398 MHz would be necessary in order to achieve a 50 nm bandwidth.

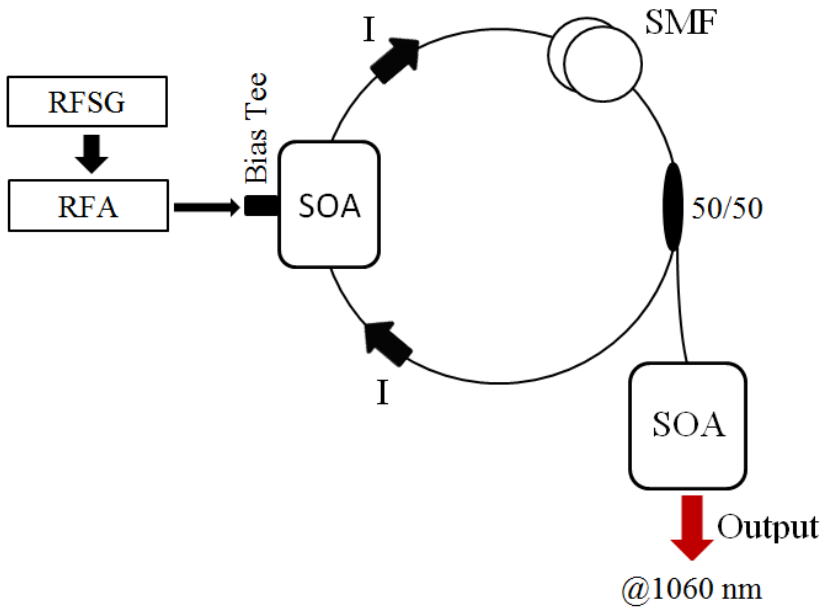

Fig. 7.1.1.1. 1060 nm AKSS setup

Output power is drawn out through a 50/50 coupler and represents half of the light in the cavity further amplified by a similar type of SOA. The laser output characteristics of

the swept source configuration are measured using an Agilent 86145B optical spectrum analyser (OSA), with a resolution of 60 pm. The coherence length of the source is evaluated by driving a Mach-Zehnder interferometer, terminated on a 50/50 coupler ending on a New Focus balanced detector model 1817, DC-80 MHz, 900-1700 nm bandwidth, whose output is displayed with a LeCroy Wave Runner 104 MXi-A 1GHz oscilloscope, with a sampling rate of 10 GS/s (10 Gyga sample points per second).

As illustrated in Fig. 7.1.1.2, the best linewidth of 92 pm was achieved for a mode-locking frequency of 1000 MHz (1 GHz). In fact, it is noticeable that good linewidth is already achieved at 400 MHz, and it improves very slowly towards 1000 MHz mode-locking values. A more rapid change is occurring between 100 MHz and 400 MHz, where a drop of approximately 680 pm is observable. Also statically, the frequency span Δf_m around the mode-locking frequency f_m necessary to achieve a bandwidth $\Delta\lambda$ = 50 nm was measured and it is illustrated in Fig. 7.1.1.3.

Next, the AKSS was operated in dynamic regime. The maximum sweeping frequency of the signal delivered by the Agilent 81160A RF generator is limited to maximum 20 kHz. Either way, we could not achieve any AKSS output above a 10 kHz repetition rate.

Figure 7.1.1.4 depicts the AKSS output measured with the OSA, which exhibits a significant decay in power and bandwidth, from 27.37 nm at 100 Hz to 9.6 nm at 10 kHz. These results suggest that, first of all, an improvement in the ring cavity gain is necessary. Secondly, the implementation of a dual mode-locking RF mechanism is considered.

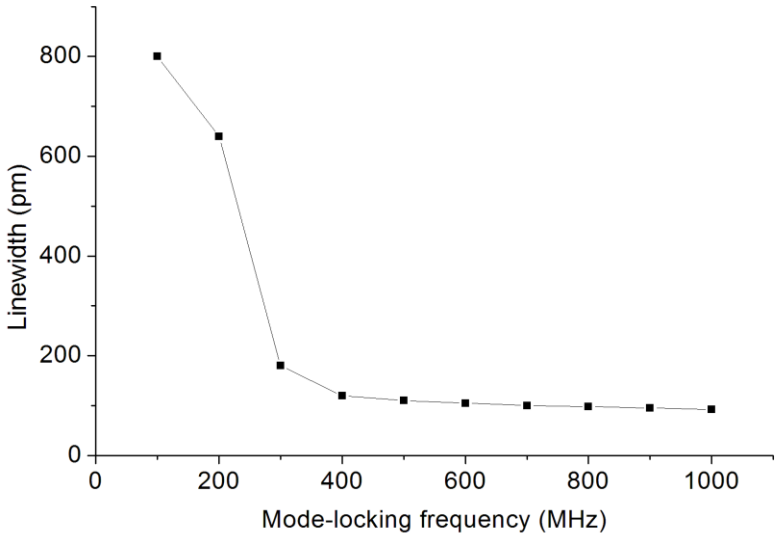

Fig. 7.1.1.2. Linewidth versus mode-locking frequency

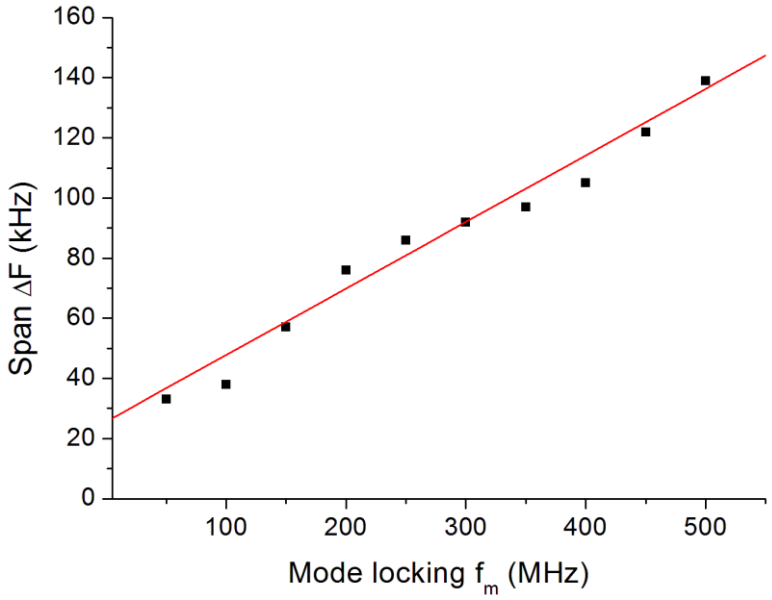

Fig. 7.1.1.3. The frequency span around the mode-locking frequency necessary to achieve a bandwidth $\Delta\lambda$ = 50 nm

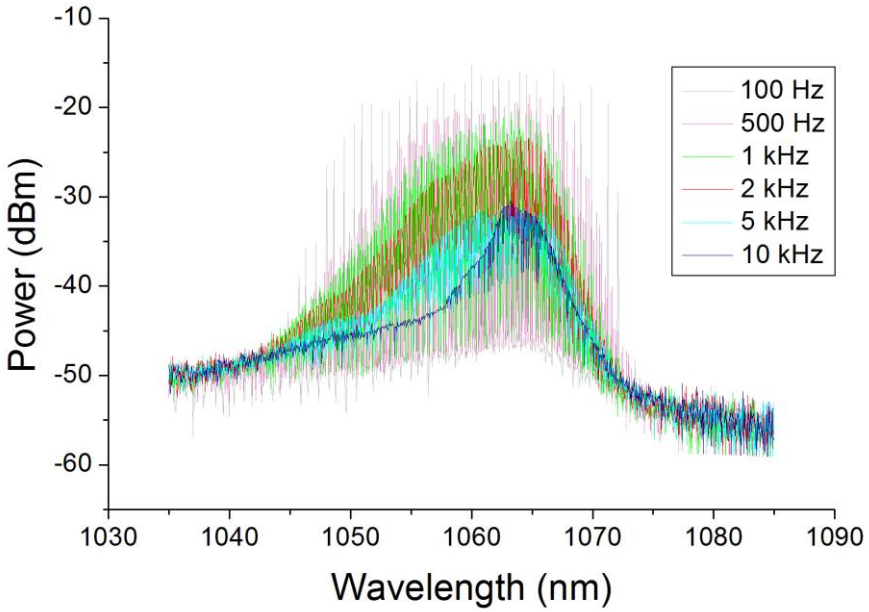

Fig. 7.1.1.4. Dynamic output measured at several repetition rates

The swept source based on the dispersion tuning principle was previously tested in a sensing [1] and in an OCT application [2]. After the measurements targeting linewidth and bandwidth, we have evaluated the AKSS mode-locked at 330 MHz and swept over approximately 25 nm bandwidth at 1 kHz line rate by scanning through the channeled spectrum of a basic Mach-Zehnder interferometer, as illustrated in Fig. 7.1.1.5. The

configuration employs two broadband directional 50/50 couplers. The object arm comprising a collimator assembly C, from which the light travels to an achromatic lens L (25 mm focal length) that focuses light on a mirror (used to act as object, in order to acquire A-scans). The distance between the collimator and the L is the same as the one between the lens L and the mirror M, equal to the L focal length. The reference arm comprises two identical collimator assemblies C (and also same as the one in the object arm), fixed on translation stages capable of with 3D manual adjustment. A balanced photodetector (PhD, New Focus model 1817, DC-80 MHz, 900-1700 nm bandwidth) receives the incoming waves. The measured signal is displayed by a digital oscilloscope, LeCroy 104Mxi-A, 10 Gyga Samples/s/. The oscilloscope is also capable to deliver and display the FFT of the acquired photodetected interference signal, from which the analysis of the A-scan decay versus OPD and the stability of the PSFs are evaluated.

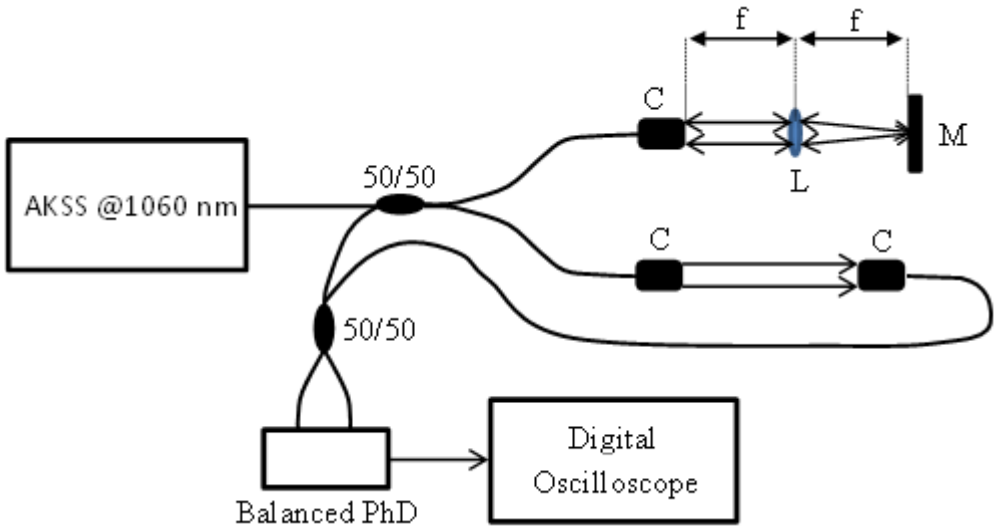

Fig. 7.1.1.5. Mach-Zehnder interferometer used to test the AKSS at 1060 nm range
C: collimator, L: lens (f: focal length = 25 mm), M: mirror, PhD: photodetector

The sensitivity of the interferometer used for reflectivity measurement is calculated as $20 \cdot log(A_{OPD}/A_{noise})$, where A_{OPD} is the amplitude of the FFT peak for an *OPD* close to 0, and A_{noise} represents the amplitude of the noise floor measured outside the peak [3]. A value of 93.3 dB was achieved. Assuming a Gaussian shape of the spectrum with a FWHM = $\Delta\lambda$ = 20 nm tuning bandwidth, the axial resolution achievable is calculated as $0.44 \cdot \lambda^2/\Delta\lambda$ = 0.02 mm.

As the sweeping speed increases, the A-scans showed a decrease in the axial range as measured versus the optical path difference (OPD) in the interferometer, as illustrated in Fig. 7.1.1.6 (above). This can be attributed to the fact that the coherence of the AKSS decreases with the increase of sweeping speed, due to decrease of roundtrips in the cavity, as explained in [4]. Regarding the tuning linearity, depicted in Fig. 7.1.1.6 (bellow), the FWHM width of the point spread function (PSF) obtained has shown insignificant change with the OPD, exhibiting an increase of only 0.12% at *OPD* = 2.5 mm, in comparison with the width measured at *OPD* = 0.1 mm. This fact confirms sufficient tuning linearity in optical frequency, therefore no data resampling is needed when decoding the spectrum modulation in sensing or OCT applications.

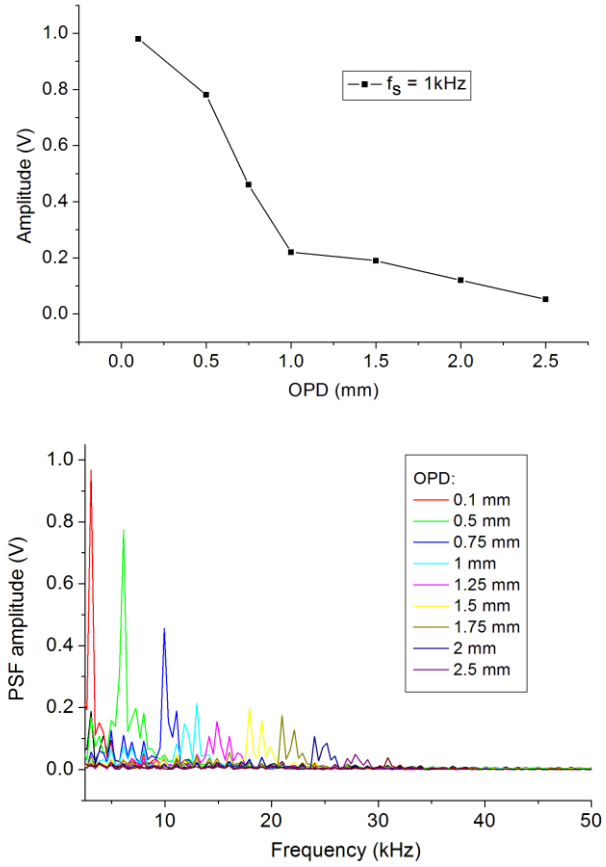

Fig. 7.1.1.6. Graph illustrating the decay of FFT peaks versus OPD (above); the point spread functions (PSF) corresponding for several values of OPD (bellow)

To conclude, a 1060 nm central wavelength AKSS was presented. The linewidth was controlled by varying the mode-locking frequency and improves continuously with the increase in mode-locking reaching GHz level. The sweep rate achieved was relatively low,

not greater than 10 kHz, and the measured tuning bandwidth slightly under 30 nm. Using a booster, the power was increased up to 12 mW. Further studies require optimization of the SMF length to DCF length ratio, cancelation of polarisation effects. Utilisation of a wider bandwidth SOA would be recommended for enhanced axial resolution.

7.1.2. 850 nm single mode-locked swept source

A great interest in OCT was shown for applications performed in the 850 nm wavelength region. One of the main advantages that SS-OCT has in this wavelength region is the improved imaging resolution.

The majority of commercial OCT systems used for imaging the human eye fundus operate at 850 nm. This reflects the interest for this waveband, justified by low absorption in the vitreous. While interest for longer wavelength is determined by the need for better penetration depth, such as imaging in the choroid, that determined studies at 1050 nm, the visible to infrared range allowed assembly of low cost OCT systems, based on the spectrometer based OCT technology. For the moment, there are no swept sources at 800 nm with parameters to trigger development of OCT technology for the human fundus to compete in cost with the spectrometer based OCT. A swept source with sufficient power, of over 10 mW in SMF, with a tuning bandwidth of at least 50 nm and a tuning speed to exceed 50 kHz would be required.

Therefore, swept sources based on external modulators and FP cavities were developed [5]. As explained previously, these solutions are vulnerable to electrical shocks and are limited in sweeping speed. We will therefore investigate an akinetic solution bellow. Unfortunately, there are several disadvantages when configuring an akinetic swept source at this wavelength. All optical components at this wavelength are generally more expensive than their counterparts at 1060 nm, 1310 nm or 1550 nm, while some components, like circulators and optical isolators are bulkier and of even higher cost. The availability of SOAs at this wavelength is also reduced to a handful of companies, such as Superlum, Ireland [6]. Superlum produces broadband emission SOAs or travelling wave amplifiers (TWA) that emit in the 800-900 nm wavelength region, or similar devices in reflection configurations.

We have constructed and tested an AKSS setup at 850 nm central wavelength, applying the same dispersion tuning principle and RF mode-locking described above at 1060 nm.

The results presented here are only part of a preliminary research effort that aims to develop novel AKSSs for OCT eye imaging. As far as we are aware, there was not much progress in this direction so far, although some groups, such as that of Yamashita et al attempted a similar avenue [1]. Therefore, development of such tuning solutions at this wavelength is sufficiently novel research direction, as explained in the motivation chapter.

The configuration of the 850 nm AKSS experimented is illustrated in Fig. 7.1.2.1. This comprises a broadband Superlum SOA travelling wave amplifier (SOA-TWA), model PM-SOA-372, operating at 850 nm central wavelength, maximum current limited to 200 mA and a 3 dB bandwidth of 50 nm. The SOA is secured in a Thorlabs universal diode mount, fitted with a customised type 1 control board that accommodates RF input, and it is driven by a Thorlabs LDC 200 power supply. Temperature stability is established through typical thermo-electric cooling provided by a Thorlabs TEC 200 driver (sensor TH 20 kΩ). The SOA is delimited by two identical isolators I, model IO-F-SLD150-895, made by Thorlabs, which ensure unidirectional lasing.

The ring cavity comprises a length of 400 m length L_{DCF} of Corning SMF, with an anomalous dispersion parameter of -100 ps/nm·km at 850 nm. The total ring cavity length is approximately 410 m, resulting in a total dispersion of approximately -50 ps/nm and a cavity frequency resonance f_R of approximately 500 kHz. By using the equation 4.1 – 10, a theoretical mode-locking frequency value of approximately 400 MHz would be necessary in order to achieve a 50 nm bandwidth.

Output power is drawn out through a 50/50 coupler and represents half of the light in the cavity further amplified by a passive Superlum booster, model SOA-840. The laser output characteristics of the swept source configuration are measured using a Yokogawa AQ 6373, 350-1200 nm bandwidth optical spectrum analyser (OSA), with a resolution of 10 pm.

To drive the laser into mode-locking, sinusoidal RF signal is applied to the SOA from one generator of a dual signal generator Agilent 81160A (RSFG) that can deliver up to 5 V_{pp} maximum output for a value of f_m of maximum 330 MHz. This is employed for static tuning operation, by manually changing the input signal frequency. For dynamic regime, the RSFG is set to work in sweeping mode, by setting a central mode-locking frequency f_m and a span ΔF around this value. The sinusoidal signal is further amplified by a Mini-Circuits ZHL-42 RF amplifier (RFA).

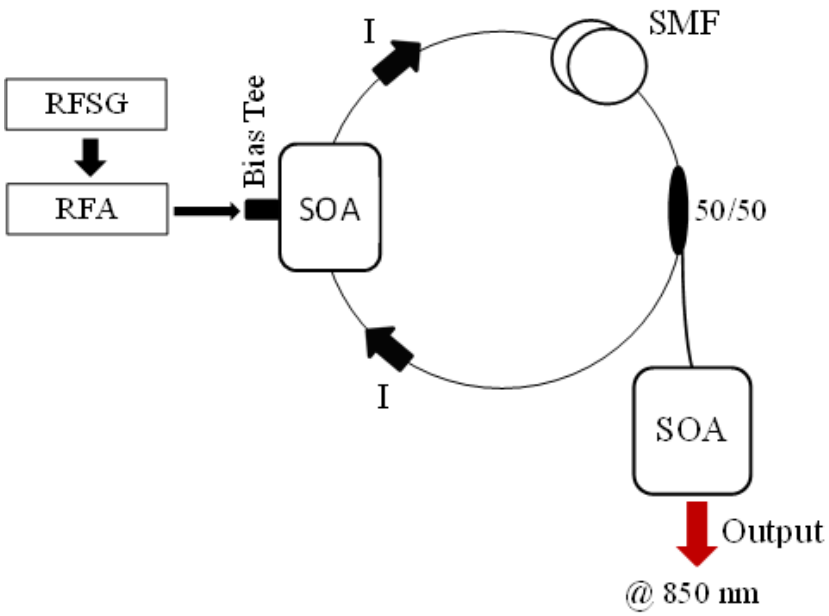

Fig. 7.1.2.1. 850 nm AKSS setup

Both statically and dynamically, a 25 nm bandwidth was achieved for an f_m = 300 MHz. The output power measured at 100 mA injection was 2.98 mW. The booster amplifies the power to a maximum of 13.2 mW. Sweeping was achieved up to 20 kHz (the output at 2 kHz, 5 kHz and, respectively 10 kHz are represented in Fig. 7.1.2.2, Fig. 7.1.2.3 and, respectively, Fig. 7.1.2.4).

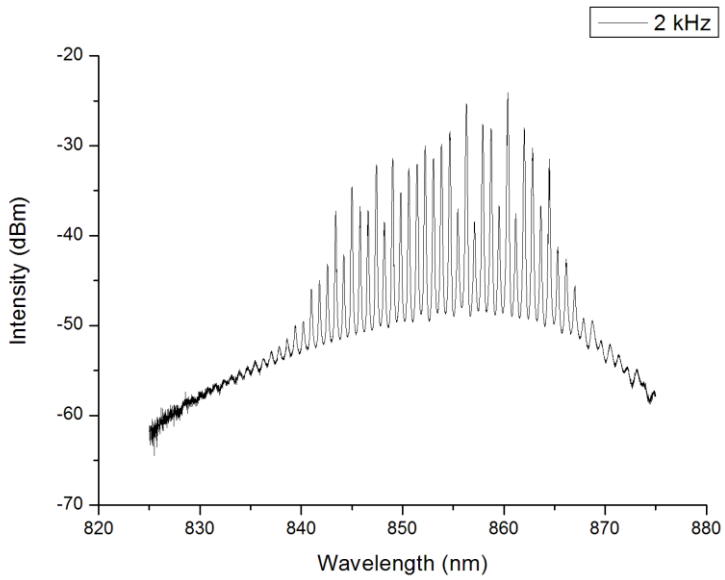

Fig. 7.1.2.2. Dynamic output at 2 kHz repetition rate

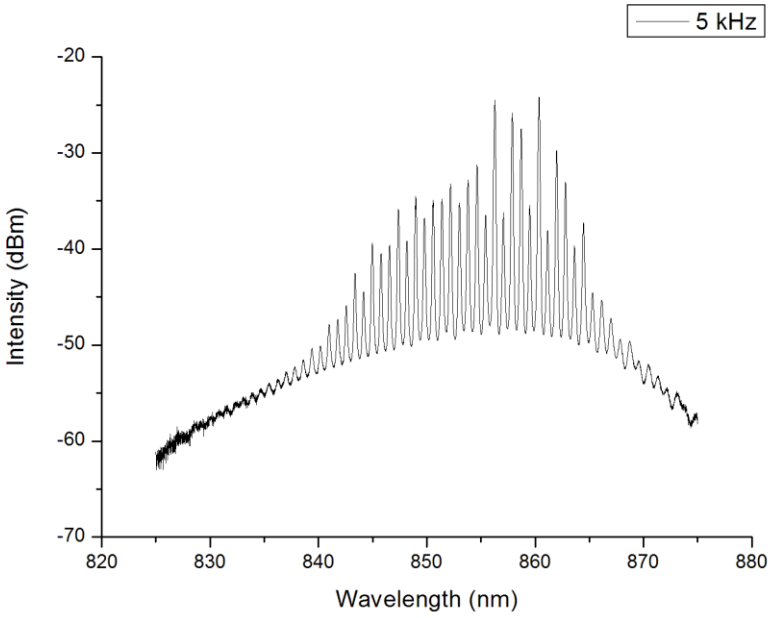

Fig. 7.1.2.3. Dynamic output at 5 kHz repetition rate

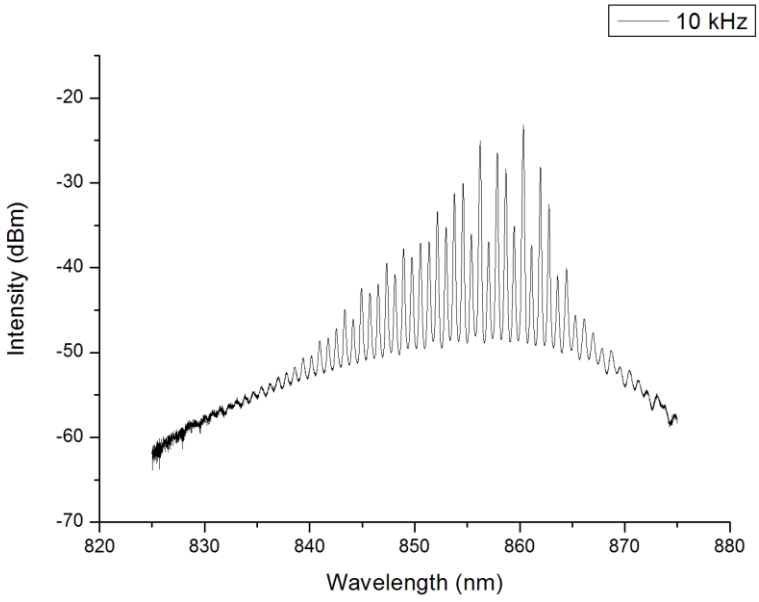

Fig. 7.1.2.4. Dynamic output at 10 kHz repetition rate

As observed in the figures above, the emission spectra measured by the OSA is a comb. This is attributed to the polarisation maintaining fibre (PMF) leads equipping the SOA, where two waves are created, of linear polarisation states, orthogonal to each other, travelling at different speed. These two waves propagate through the cavity at different times, as it was previously demonstrated in [7]. The comb channel spacing due to superposition of the two waves, $\Delta\lambda_{space}$, is given by the following equation:

$$\Delta\lambda_{space} = \frac{\lambda_0^2}{\Delta n_{br} \cdot L}, \qquad (7.1.2 - 1)$$

where λ_0 = 850 nm represents the central wavelength, Δn_{br} is the birefringence, and L represents the total length of PMF used in the cavity. For Δn_{br} = 0.00038 and for a length L = 2 m of PMF in the cavity, a comb spacing of 0.95 nm is calculated. Indeed, this value is verified if we check the number of peaks registered for the output measured by the OSA and displayed in figures 7.1.2.2, 7.1.2.3 and 7.1.2.4; for a 10 nm bandwidth 10-11 combs are observed. The spectra of each output is presented with and OSA resolution measurement of 0.1 nm.

This effect can be reduced or even eliminated by selecting a single polarisation state. However, fibre polarisation controllers act as waveplates only, therefore no such control of linear polarisation in the cavity can be implemented. Solutions exist, such as that employing a $\lambda/2$ polarisation controller to rotate the fast axis angles of the adjacent PMF fibre segments.

To summarize, an akinetic swept source emitting at 850 nm central wavelength was presented. These are preliminary results obtained so far. The limitations given by the current technologies at this wavelength would require extensive work in the near future, by implementing new and improved commercial solutions in the swept source concept presented. Therefore, we explored a different, novel avenue, that of dual mode-locking, presented in the next section.

7.1.3. Dual mode-locked swept source

The Fourier domain mode-locking (FDML) method was used in ring fibre laser configurations that employed long dispersion delay fiber in order to achieve the elimination of photon lifetime limitation and improve the laser sweep rate, achieving 370 kHz repetition rates [8, 9]. The FDML method is nowadays developed in a commercial wavelength swept laser solution which is capable of achieving MHz level repetition rates (Optores Gmbh). Also, the interest on akinetic principles has been brought back to attention recently by the demonstration of fast and wide tuning bandwidth AKSSs based on vertical cavity surface emitting lasers (VCSEL) [10]. We present here an akinetic AKSS based on a different principle, inspired by that of FDML, emitting at a 1060 nm central wavelength. This combines the dispersion tuning principle, that eliminates the need of mechanical tuning elements in the cavity, and the FDML principle, that involves sweeping at periods matching the round trip in the cavity. This requires long cavities to allow amenable repetition rates in the tens to hundreds of kHz and even exceeding 1 MHz. We illustrate here this principle achieving sweeping at multiples of the resonance frequency f_R, and denominate this novel concept as a dual mode-locking mechanism.

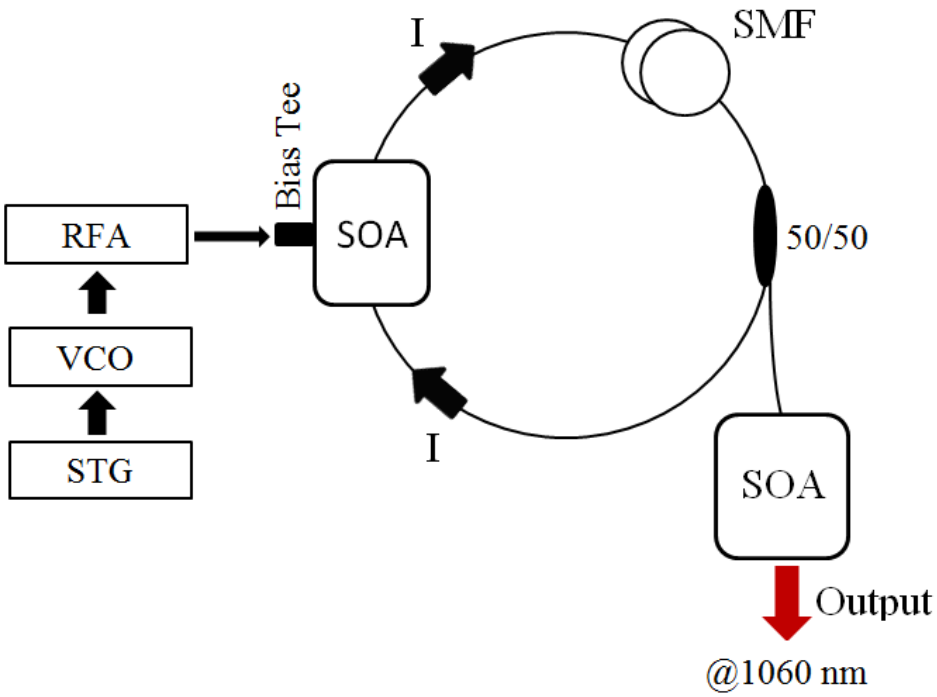

Fig. 7.1.3.1. 1060 nm AKSS setup employing the DML RF mechanism

The optical configuration of the 1060 nm AKSS experimented is illustrated in Fig. 7.1.3.1. A broadband SOA, model QPhotonics QSDA-1050, operating at 1060 nm central wavelength, maximum current 200 mA and a 3 dB bandwidth of 100 nm, is placed in a laser systems mount (dedicated to QPhotonics SOAs), model HS501, and it is driven by a Thorlabs LDC 210 power supply, while temperature stability is ensured through thermo-electric cooling provided by a Thorlabs TEC 200 driver (sensor TH 20kΩ). The SOA is placed between two polarization insensitive broadband isolators I, manufactured by AFW Technologies, which ensure unidirectional lasing within the ring cavity. The ring cavity comprises a total length of 1005 m length LDCF of Corning Hi1060 SMF, with a total anomalous dispersion D = -50.25 ps/nm. 50% of the total power generated in the cavity represents the AKSS optical output, which is further amplified by a Multiwave amplifier. The laser output characteristics of the swept source configuration are measured using an Agilent 86145B optical spectrum analyzer (OSA), with a resolution of 60 pm. The coherence length of the source is evaluated by driving a Mach-Zehnder interferometer. The interference signal in the interferometer is measured with a New Focus balanced detector, model 1817, DC-80 MHz, 900-1700 nm bandwidth, whose output is displayed with a LeCroy Wave Runner 104 MXi-A 1GHz oscilloscope, with a sampling rate of 10 GS/s (Gyga sample points per second).

The AKSS is mode-locked according to the circuit which consists in a low noise voltage controlled oscillator (VCO, Mini Circuits ZX-368S+) and a ZHL-42W Mini Circuits radio frequency amplifier (RFA), that are used to drive the SOA with a 5 V amplitude sinusoidal signal applied to the SOA in series with a 27 ohm resistor. The Agilent 81160A saw-tooth signal generator (STG) provides a saw-tooth signal with adjustable amplitude allowing a versatile control of the tuning bandwidth and of the central frequency of the VCO.

As previously explained in chapters 4 and 6, a first locking condition is imposed by driving the optical gain at a high frequency, to induce mode-locking. A second locking mechanism, inspired from the practice of FDML applied to TFPF lasers [8], employs sweeping at a rate close to f_R, however in opposition to [9], at essentially different values than f_R. To produce FDML, the roundtrip time needs to be increased to amenable values, which requires the use of a considerable cavity length, provided in this case by a long length of Hi1060 SMF, of 1005 m.

The cavity length is adjusted to a value which determines f_R = 201.05 kHz and the VCO is driven with a signal of frequency f_m in the range 360-420 MHz. When the signal applied from the synthesizer to the VCO is swept at a sweeping rate of $f_S = f_R$, then the VCO

spectrum consists in a comb of frequencies $f_m \pm f_R$, $f_m \pm 2f_R$, $f_m \pm 3f_R$ and so on, i.e. in 201 kHz steps. The resulting RF signal from the VCO is amplified and injected into the SOA gain medium of the AKSS. This generates a narrow band laser output, having a linewidth $\delta\lambda$ and f_R repetition rate. If $f_S = f_R$, no tuning is noticed. To perform tuning, sweeping needs to be performed at a detuned rate δf_R from f_R. Therefore, $f_S = f_R \pm \delta f_R$, in which case the VCO is tuned with a comb spectrum consisting in f_m, $f_m + f_R \pm \delta f_R$, $f_m + 2f_R \pm 2\delta f_R$, $f_m + 3f_R \pm 3\delta f_R$ and so on. For the ring cavity length considered, the tuning bandwidth is measured for several values of detuning, δf_R. The larger the detuning, δf_R, less is the output power, while the bandwidth increases, as depicted in Fig. 7.1.3.2.

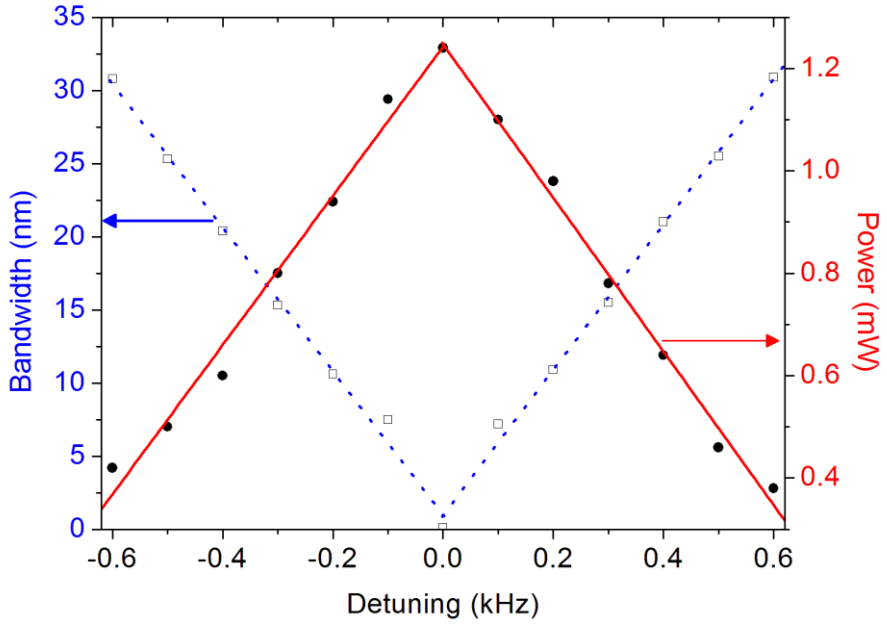

Fig. 7.1.3.2. DML AKSS tuning bandwidth (blue dotted line) and output power versus detuning (red solid line)

Fig. 7.1.3.3 represents a more explicit representation of DML mechanism effects in the AKSS ring cavity. When the frequency of the signal driving the VCO is swept at a rate $f_S = f_R = 201.05$ kHz a narrow laser emission results. For a sweeping rate of $f_S = f_R + 0.2 = 201.25$ kHz, the VCO is tuned from f_m to $f_m + f_R + 0.2$ kHz, to $f_m + 2f_R + 0.4$ kHz, to $f_m + 3f_R + 0.6$ kHz and so on, in the 360-420 MHz range, in 201.25 kHz steps. The emitted spectrum consists in a comb having emission lines with a linewidth of 105 pm and a repetition rate of 201.25 kHz. Similar reasoning can be applied to each value of δf_R, either positive or negative.

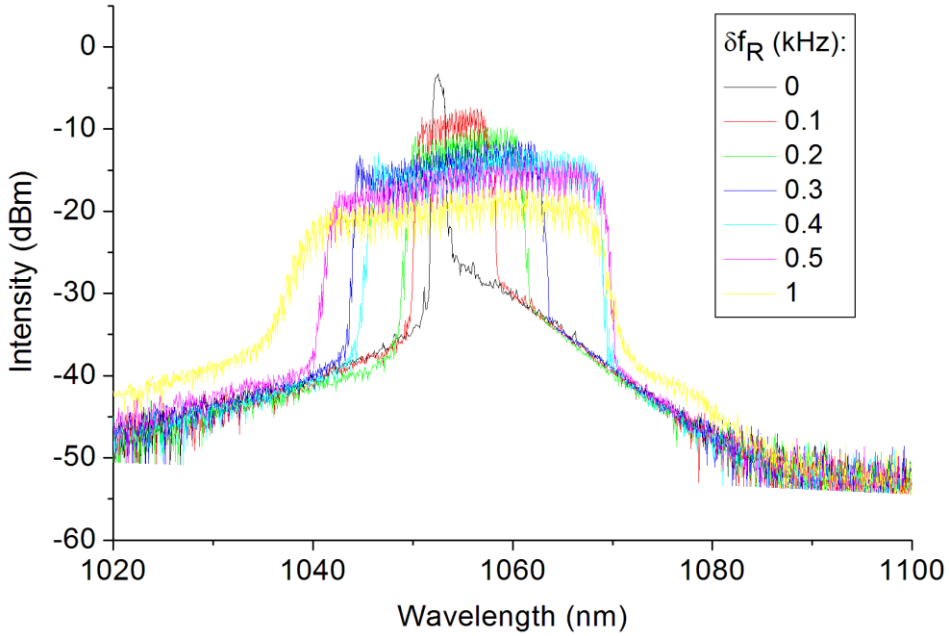

Fig. 7.1.3.3. Dynamic AKSS output measured at several detuning δf_R values from f_R

While it is possible to tune statically the whole tuning bandwidth by ±25 nm by modifying the bias voltage applied to the VCO, it is not possible to achieve the same tuning bandwidth dynamically. This is due to the maximum achievable VCO tuning bandwidth ΔF = 60 MHz for a swing of maximum 10 V_{pp} amplitude of the ramp signal applied to its input while a simple calculation would show that for static tune of 50 nm, the swing should exceed 20V.

Without any optical amplification, the maximum output optical power of the source, measured at no detuning ($f_s = f_R$), is 1.25 mW. Using the SOA booster driven at maximum current, an output power of 10.8 mW is measured.

Next, we evaluated the dynamic linewidth $\delta\lambda$ of the DML AKSS, as the inverse of this parameter determines the axial range in OCT. The AKSS mode-locked at 380 MHz, swept in frequency at 201.25 kHz and using the maximum ΔF = 60 MHz deviation achievable by driving the VCO at 10 V amplitude, is connected to a Mach-Zehnder interferometer, described in more detail in Fig. 7.1.1.5. The Math menu of the LeCroy oscilloscope, type Wave Runner 104 MXi-A, is used to calculate the Fast Fourier Transformation (FFT) of the signal measured delivered by the balance photodetector. For various *OPD* values, we have measured the FFT peaks, as depicted in Fig. 7.1.3.4. The sensitivity *S* is given by $20\cdot\log(A_{OPD}/A_{noise})$, where A_{OPD} represents the corresponding FFT peak amplitude value for the chosen OPD, while A_{noise} is the amplitude of the noise floor

measured outside the FFT peak [3]. A sensitivity value of 89.82 dB is obtained for an *OPD* value close to "0". Assuming a Gaussian shape for the tuning spectrum, and using the *OPD* value measured at 6 dB decay (OPD_{6dB}) from Fig. 7.1.3.4 of 0.57 mm, this leads to a dynamic linewidth $\delta\lambda = \lambda^2/4 \cdot OPD_{6dB}$ = 0.49 nm. In terms of tuning linearity, we have also measured the width of the A-scan peaks obtained by FFT, but no significant change was noticeable with OPD. This suggests sufficient tuning linearity in optical frequency, i.e. no data resampling is needed when decoding the spectrum modulation.

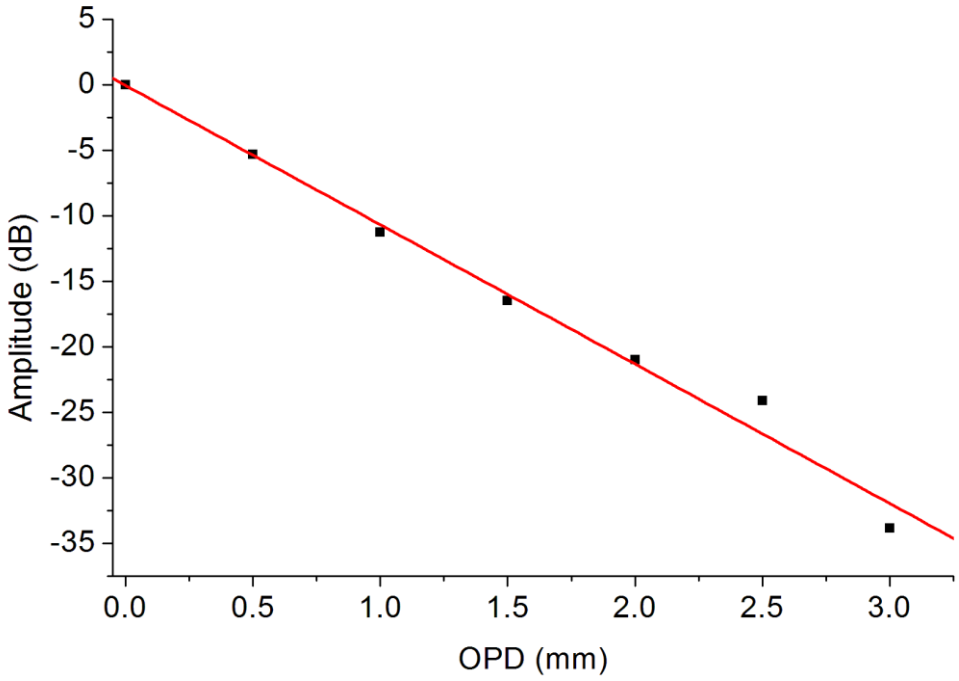

Fig. 7.1.3.4. Decay of the A-scan peak amplitude versus OPD

Using the DML principle, operation at fast sweep rate values of approximately f_R = 200 kHz are demonstrated. Further optimization of the RF tuning and the optical set-up can lead to larger tuning bandwidths and better sensitivity, as it will be shown in the following chapters.

7.2. Ring cavity terminated on a Faraday Rotating Mirror

7.2.1. 1060 nm single mode-locked swept source

In order to improve the parameters obtained above, we have implemented as an upgrade a Faraday Rotating Mirror (FRM), AFW Technologies broadband FRM at 1050 nm, having a bandwidth of 40 nm (±20 nm around the 1060 nm central value). The main advantage of using a FRM in a ring cavity laser is the minimization of polarisation distortions and thus depolarisation loss. By using the FRM, another aim was to achieve an improvement in the results achieved in chapter 7.1 and the stability of the 1060 nm AKSS.

Apart from the optical components used up to this point, the length of the Hi1060 SMF was now halved, to a length now of 500 m, when terminated with the FRM.. The optical assembly, comprising the new length SMF and the FRM, was initially connected to the cavity loop via an optical circulator. The circulator, however, generated significant polarization mode dispersion (PMD) effect in the cavity [11], which could not be compensated for. In principle, such effect can be completely eliminated from the system if components based on polarization maintaining (PM) fibre are used. On the other hand, such a solution is not practical, because the optical components using PM are exhibiting more losses, the polarization directions would have to be aligned at several interfaces and they also come with a great penalty of developing and implementing cost. Therefore, the circulator was replaced with a broadband 50/50 coupler. In fact, the extra losses introduced by the coupler allow utilization of a larger current through the SOA for similar ASE contribution, current which determines a wider SOA bandwidth.

While performing measurements using the 1060 nm AKSS in the configuration described in Chapter 7.1.1, we have noticed that the wave travelling in the cavity is significantly influenced by polarization effects, which reduce output power at some wavelengths. Therefore, a manually adjustable polarisation controller (PC) was employed in the AKSS setup, placed in a point before the light re-enters the SOA after one roundtrip.

To drive the laser into mode-locking, sinusoidal RF signal is applied to the SOA from one generator of a dual signal RFSG (HP8648C, 9 kHz-3.2 GHz frequency range, that can deliver up to 2.55 V_{pp} maximum sinusoidal output). This is employed only for static tuning operation, by manually changing its signal frequency and delivered amplitude.

To achieve mode-locking, two circuits were used.

A first circuit amplified the sinusoidal signal from the RFSG (Agilent 81160A) with a Mini-Circuits ZHL-42W medium power RFA and injected it into the SOA through the bias tee. The second circuit (b) uses a saw-tooth tuned VCO emitting a sinusoidal signal, also amplified by the same type of RFA and injected in the bias tee. The VCO is less versatile though, allowing a maximum range of frequencies of only 60 MHz around a central value of 380 MHz.

The laser output characteristics of the AKSS configuration are measured with an Agilent 86145B optical spectrum analyser (OSA). The dynamic sweeping was evaluated by probing the channelled spectrum of a Mach-Zehnder interferometer that inputs light from the mode-locked AKSS.

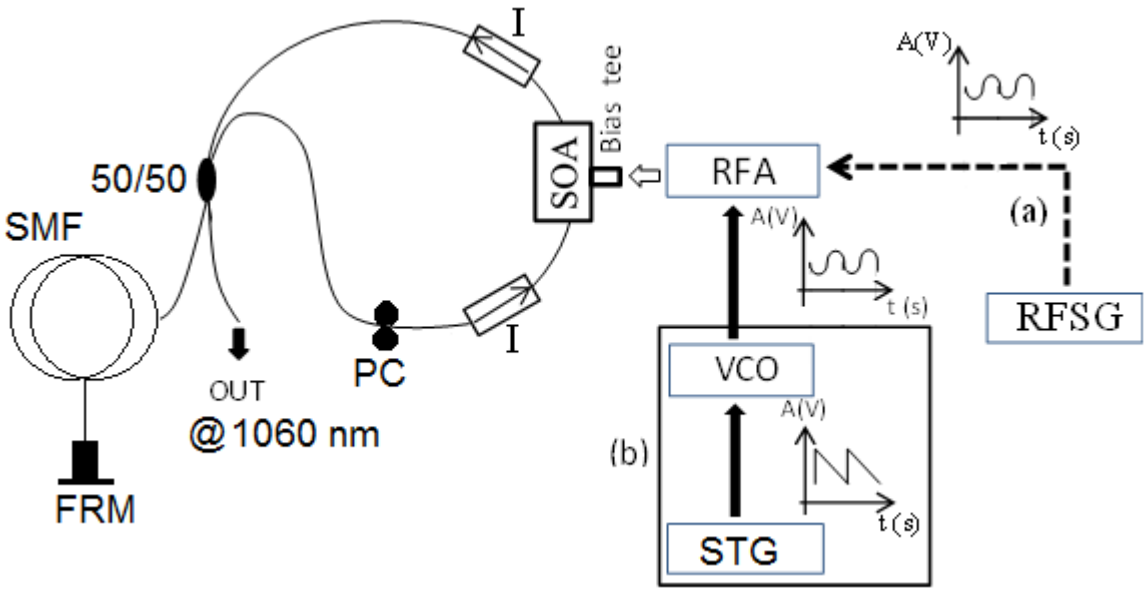

Fig. 7.2.1.1. FRM based 1060 nm AKSS setup, comprising two separate modalities of mode-locking: (a) amplified sinusoidal signal from RFSG; (b) amplified sinusoidal signal from a voltage controlled oscillator (VCO), driven by a saw-tooth generator (STG)

The total ring cavity length is approximately 1005 m, resulting in a total dispersion D of approximately -50.25 ps/nm.

Operating the FRM based AKSS in static regime revealed a slight improvement of several parameters. The linewidth measured at 1 GHz mode-locking before the implementation of the FRM was 92 pm, while now it now 89 pm. This fact is shown in Fig. 7.2.1.2. At 100 MHz mode-locking, linewidths of approximately 800 pm were measured. After that, a substantial improvement is observed between 100 MHz and 400 MHz, 120 pm

linewidth being obtained for the latter mode-locking value. The drop in the linewidth value becomes linear after this point, with a very small slope.

A slight improvement was also seen in the statically measured optical bandwidth, an increase from approximately 50 nm to nearly 60 nm.

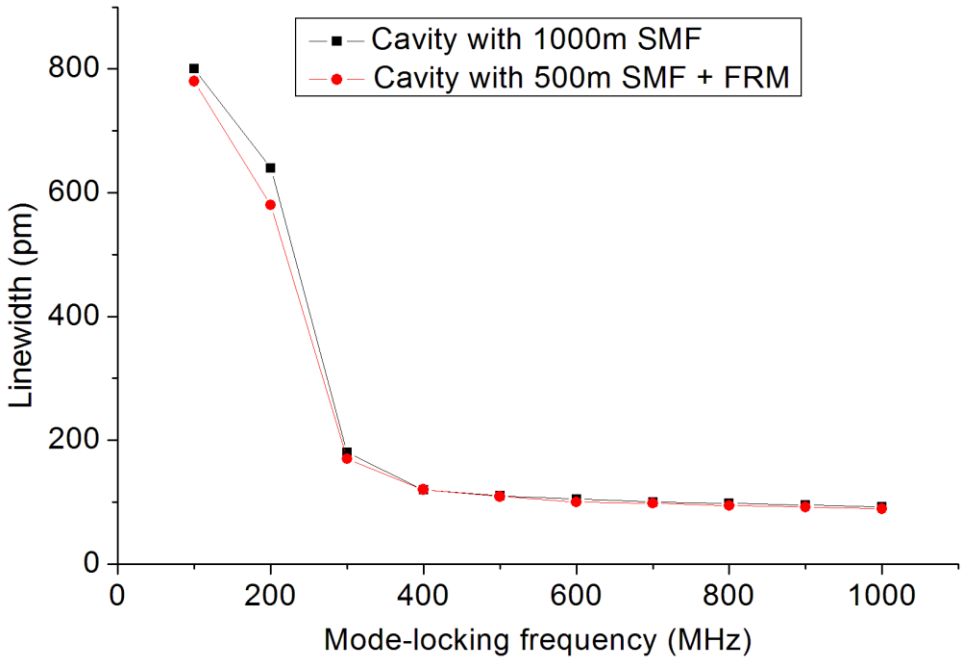

Fig. 7.2.1.2. A comparative graph of linewidth versus mode-locking frequency for two types of circular cavities studied for the AKSS at 1060 nm

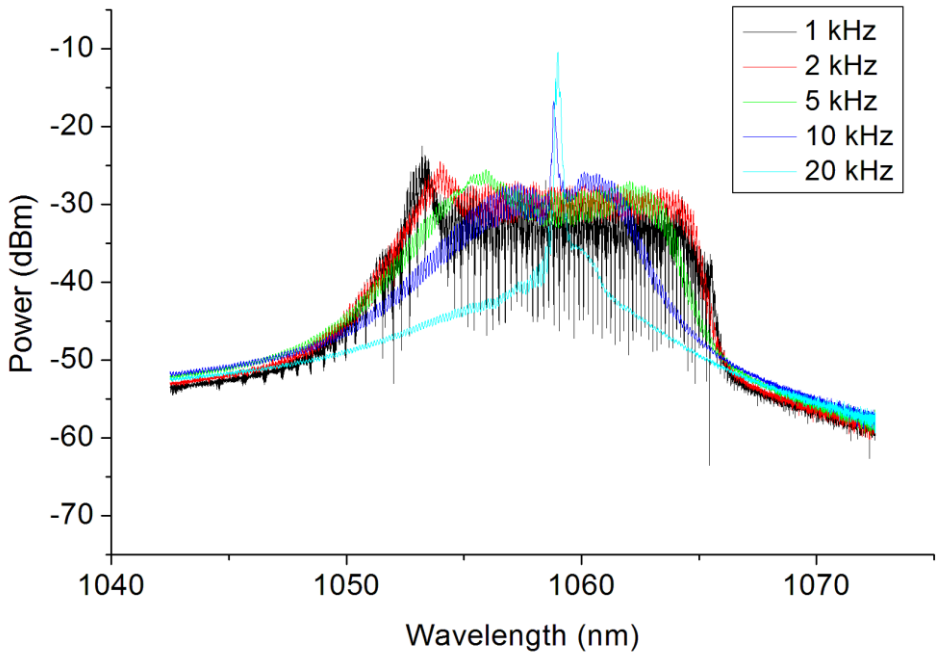

Fig. 7.2.1.3. Dynamic output measured at several sweeping rates for the AKSS with a FRM integrated in the ring cavity

Figure 7.2.1.3 illustrates the dynamic optical output at several values for a sweeping frequency f_s of up to 20 kHz, at a value of f_m = 380 MHz. At 1 and 2 kHz repetition rate, an approximate value of 15 nm bandwidth is achieved. At 5 kHz there is a slight decrease, while at 10 KHz, the bandwidth nearly halves. On the other hand, the output signal intensity (output power) shows insignificant change.

Comparing with the 1060 nm AKSS configuration without the FRM, the maximum repetition rate is doubled. On the other hand, above 10 kHz repetition rate, there is a dominating coherent emission at approximately 1058 nm, which we believe it is due to intra cavity resonances that appear in the SOA chip. A correction was attempted by reducing the current applied to the SOA, but a drop in the gain also meant that the swept source emission was also extinguished. Another solution was to suppress the ASE and the coherent emission by further amplifying the modulation of the SOA gain. This was achieved by adding a Mini-Circuits, model VH1000 in series with the current RFA. This method also proved unsuccessful.

The effect of linear sweeping was investigated, that imprints a different dynamic regime than sinusoidal sweeping. To this goal, the VCO is driven by a ramp signal generated by the RG (in fact the other half of the same Agilent RFSG, model 81160A). The offset of the ramp signal determines the central mode-locking frequency f_m generated by the VCO, while its amplitude sets the frequency tuning range ΔF of the VCO. The repetition frequency of the RFSG ramp determines the tuning rate, f_s. The signal from the VCO is further amplified by the RFA, before being delivered to the SOA. The results regarding the output power and bandwidth are similar; therefore no graphical representations to describe these parameters are included. This proves that a viable mode-locking mechanism is achievable by using a low cost VCO, of small size and easy to integrate in RF configurations.

The power at maximum driving SOA current, 200 mA, is measured as 2.25 W, seen also in Fig. 7.2.1.4. Fig. 7.2.1.5 depicts the output power measured for several values of repetition rate, when driving the SOA at 150 mA and mode-locking at 382 MHz.

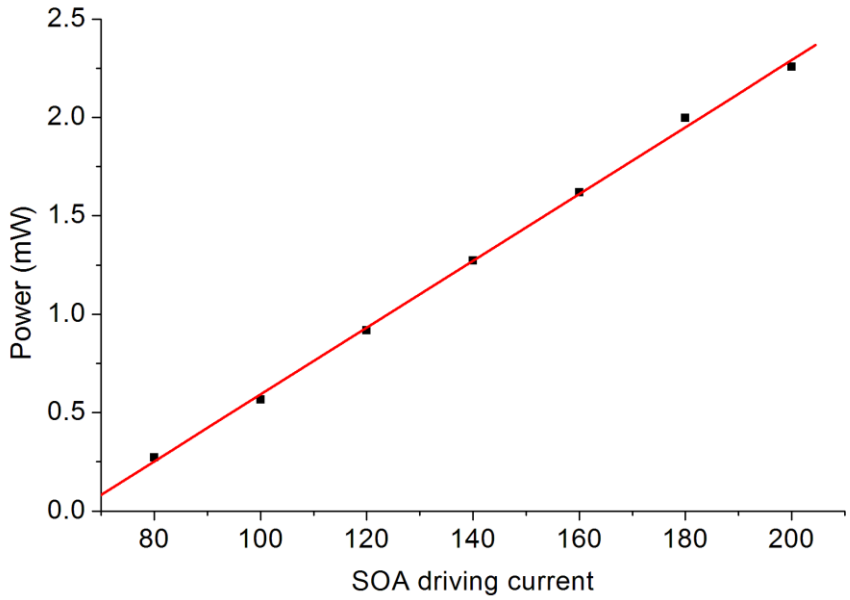

Fig. 7.2.1.4. Power versus SOA driving cavity

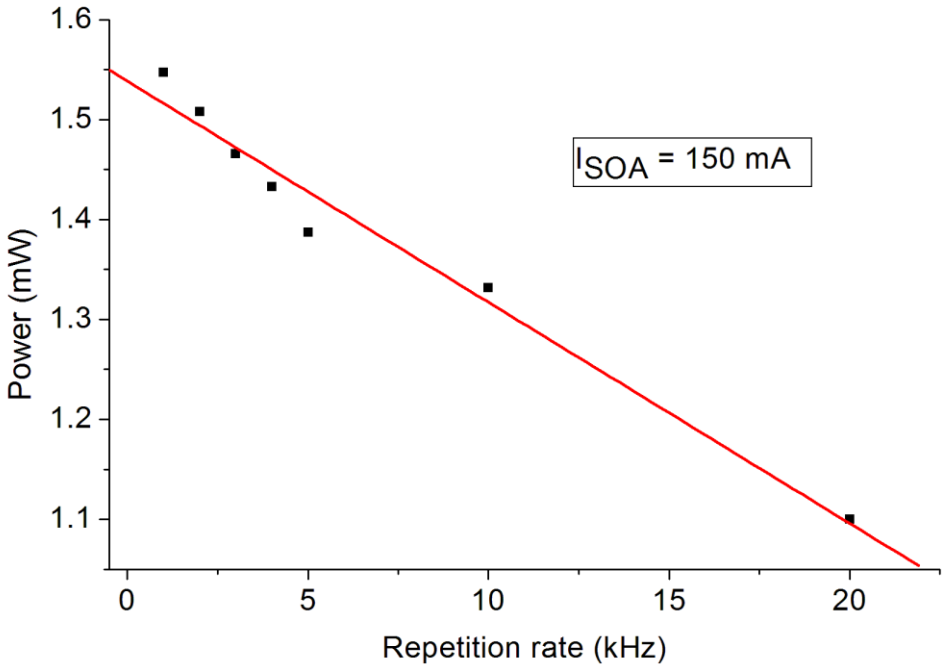

Fig. 7.2.1.5. Power versus sweeping rate at a fixed value of the SOA driving current

In continuation, we evaluated the AKSS mode-locked at 380 MHz and swept at 1 kHz rate by scanning through the channeled spectrum of a basic Mach-Zehnder interferometer, as illustrated in Fig. 7.2.1.6. The configuration uses two broadband directional 50/50 couplers. The object arm comprises a collimator assembly C, from which the light travels to an achromatic lens L (25 mm focal length) that focuses light onto a mirror

(used to act as object, in order to acquire A-scans). The distance between the collimator and the lens L is similar to that between the lens L and the mirror M, equal to the focal length of the lens L. The reference arm comprises two identical collimator assemblies C (similar to that used in the object arm), fixed on micrometre translation stages capable of 3D manual adjustment. The light returning from the two arms is received by a balanced photodetector (PhD), New Focus model 1817, DC-80 MHz, 900-1700 nm bandwidth, which is connected to a digital oscilloscope, LeCroy 104Mxi-A, 10 Gyga Samples/s, capable of acquiring A-scans and displaying the FFT of the photodetected light. The FFT of the photo-detected signal delivers an A-scan [12]. Fig. 7.2.1.5 (left) depicts the point spread functions measured for several values of *OPD*, up to 2.5 mm. The variation in the width of the PSFs was less than 2%. This variation confirms sufficient tuning linearity in optical frequency, therefore no data resampling is needed when decoding the spectrum modulation.

Fig. 7.2.1.7 (right) reveals the decay of the A-scan peak amplitudes versus *OPD*. For *OPD* values up to 3.25 mm, A-scan peaks were obtained with more than 10 dB above noise. A 6 dB decay is measured at an *OPD* = 0.35 mm.

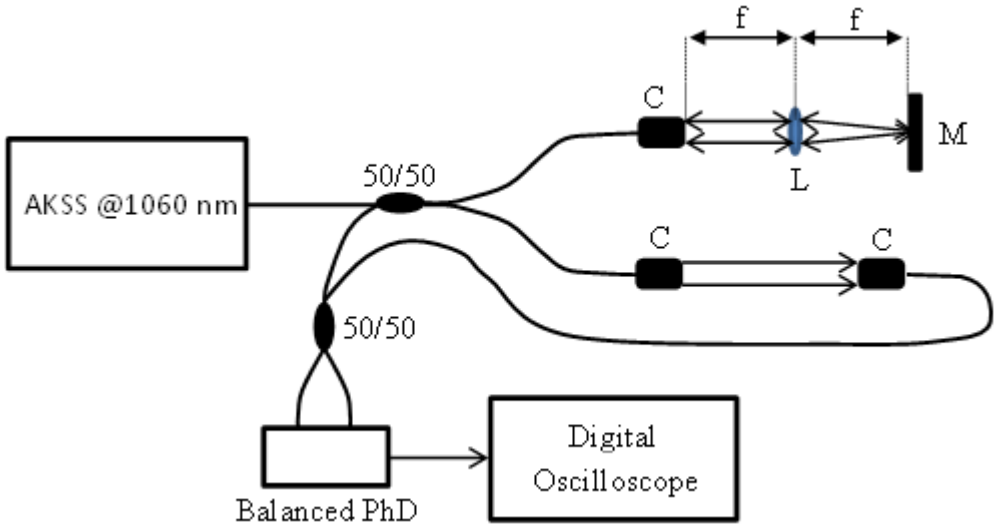

Fig. 7.2.1.6. Mach-Zehnder interferometer used to test the AKSS emitting in the 1060 nm range, where, C: collimator, L: lens (f: focal length = 25 mm), M: mirror, PhD: photodetector.

The sensitivity *S* of the interferometer used for reflectivity measurement, is calculated as $20 \cdot log(A_{OPD}/A_{noise})$, where A_{OPD} is the amplitude of the FFT peak for an *OPD* close to 0, while A_{noise} represents the amplitude of the noise floor measured outside the peak

[3]. The *S* values measured while operating the AKSS mode-locked at 330 MHz and a repetition rate of 1 kHz was calculated as 92.78 dB.

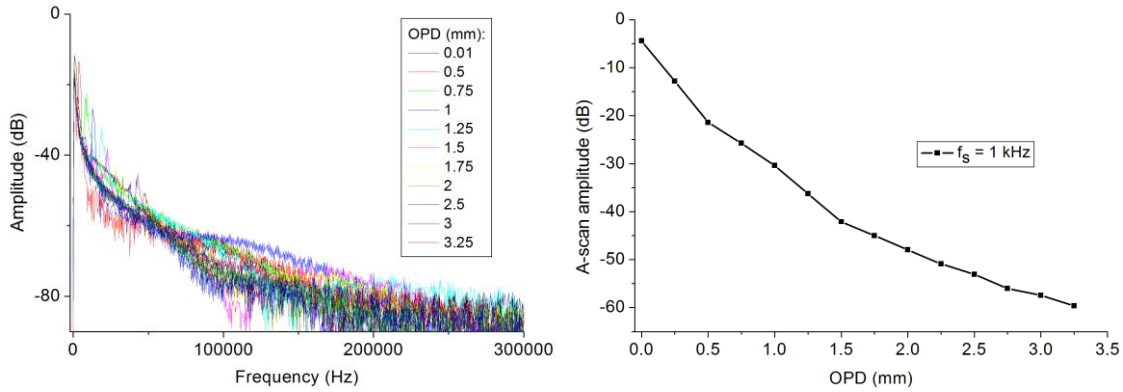

Fig. 7.2.1.7. Graph illustrating the point spread functions (PSF) corresponding to several values of OPD (left); the decay of FFT peaks versus OPD (right)

In conclusion, a 1060 nm AKSS employing a broadband FRM was presented. Comparing with the initial 1060 nm configuration, slight improvements in several parameters such as linewidth, output bandwidth and power are observed. In the following section, 7.2.2, we will show that the dual mode-locking mechanism applied to this type of AKSS can achieve better performance, as proven by tests documented.

7.2.2. 1060 nm dual mode-locked swept source

Next step represented the testing of the AKSS described in Chapter 7.2.1 and illustrated in Fig. 7.2.1.1 in dual mode-locking regime (DML). For the measurements that follow, we have only maintained and used the second circuit (b), employing a STG driving a VCO and a RFA that amplifies the sinusoidal RF signal generated by the VCO. As shown previously, the total cavity length determines a total of -50.25 ps/nm anomalous dispersion value in the system and the best linewidth of 89 pm was measured for mode-locking frequencies f_m close to 1 GHz. Initially, the cavity length is adjusted to a value which determines f_R = 201.05 kHz and the Mini Circuits 368S+ VCO is driven with a signal of frequency f_m in the range 360-420 MHz. When the signal applied from the STG to the VCO is swept at a sweeping rate $f_S = f_R$, then the VCO spectrum consists in a comb of frequencies $f_m \pm f_R$, $f_m \pm 2f_R$, $f_m \pm 3f_R$ and so on, i.e. in 201.05 kHz steps. The resulting RF signal from the VCO is amplified and injected into the SOA gain medium of the AKSS via the bias tee. This generates a narrow band laser output, having a linewidth $\delta\lambda$ and f_R repetition rate. If $f_S = f_R$, no tuning is noticed. To perform tuning, sweeping is performed at a detuned rate from f_R. Therefore, $f_S = f_R \pm \delta f_R$, in which case the VCO is tuned with a comb spectrum consisting in f_m, $f_m + f_R \pm \delta f_R$, $f_m + 2f_R \pm 2\delta f_R$, $f_m + 3f_R \pm 3\delta f_R$ and so on.

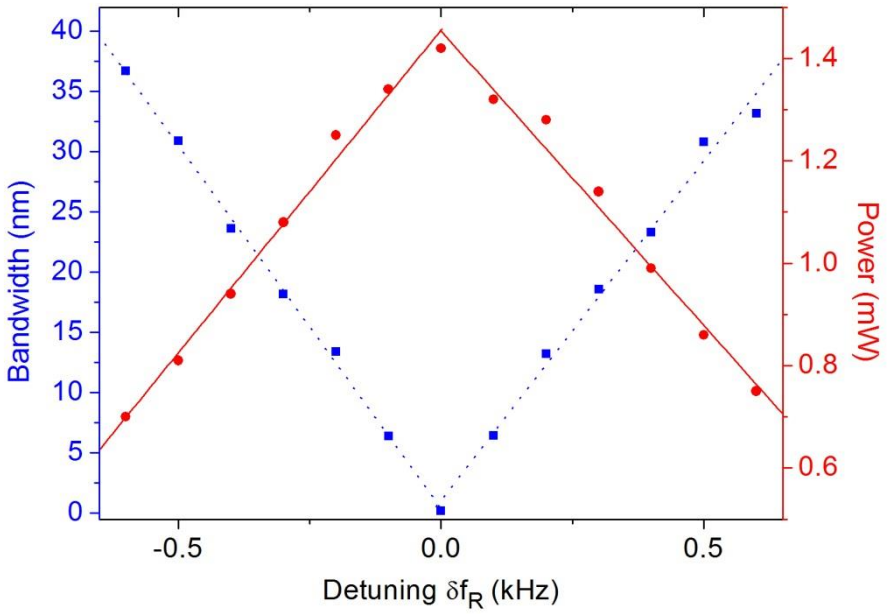

Fig. 7.2.2.1. DML 1060 nm AKSS tuning bandwidth (blue dotted line) and output optical power versus detuning (red solid line)

The cavity coefficient defined in equation (6.1 – 1) is evaluated from the slope $m = \delta\lambda \cdot N \cdot C_m$ calculated from the left graph illustrated in Fig. 7.2.2.1 (blue dotted line) as 1.42 nm/kHz.

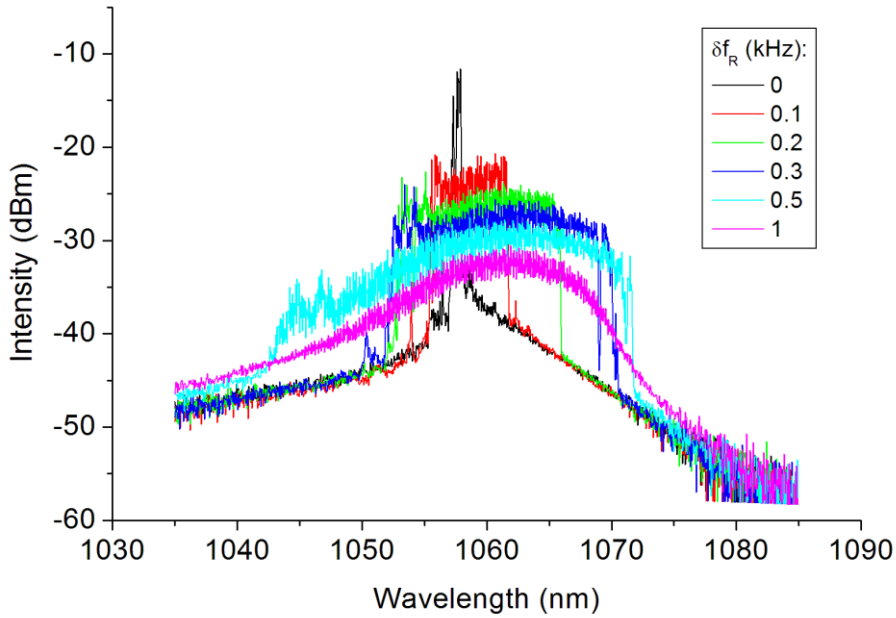

Fig. 7.2.2.2. DML optical spectrum in the dynamic regime for a cavity length determining an f_R = 201.05 kHz, for detuning δf_R = +0.1, +0.2, +0.3, +0.5, +1 kHz respectively

For a mode-locking frequency of 390.4 MHz, at the sweeping rate of 201.35 KHz (10 kHz detuning from f_R), we obtained a tuning bandwidth of 15.82 nm, as shown in Fig. 7.2.2.2. Without any optical amplification, the maximum output power of the AKSS, measured at maximum current (200 mA) injected in the SOA is 3.52 mW. Using the SOA booster (from Multiwave), an output power of 13.12 mW is measured. While it is possible to tune the whole tuning bandwidth by ±30 nm (as illustrated in chapter 7.2.1) by modifying the bias voltage applied to the VCO, it is not possible to achieve the same tuning bandwidth dynamically. This is due to the maximum achievable VCO tuning bandwidth ΔF of 60 MHz for a swing of maximum allowed of 10 V_{pp} amplitude of the ramp signal applied to its input. A simple calculation, 60 nm/15 nm = 4, shows that we would need a VCO with a 4 times larger frequency swing to achieve the available tuning bandwidth of 60 nm.

The dependence of the optical output power and tuning bandwidth on the RF tuning range is depicted in Fig. 7.2.2.3, for several values of detuning, δf_R = 0.1 kHz (a), δf_R = 0.3

kHz (b), and respectively δf_R = 0.3 kHz (c). The variation of tuning bandwidth with amplitude represents an expansion of the number of frequency resolved points in the tuned spectrum. For the same δf_R detuning value, there is a slight decrease in power as the VCO tuning range ΔF increases, while the bandwidth exhibits a significant increase. The graphs depicted in Fig. 7.2.2.3 confirm equation (6.1 – 1), which describes the DML mechanism. For constant f_R, C_m and $\delta\lambda$ values, the tuning bandwidth is proportional to the detuning δf_R. For example, for a 5 Vpp signal driving the VCO, corresponding to ΔF = 30 MHz, a $\Delta\lambda$ value of 3.56 nm is measured for δf_R = 0.1 kHz (a), 7.34 nm for δf_R = 0.2 kHz (b) and respectively, 9.78 nm for δf_R = 0.3 kHz (c).

The DML tuning mechanism for the 1060 nm AKSS is also verified at multiple values of f_R. Equation (6.1 – 1) suggests that the tuning bandwidth, $\Delta\lambda$, is inverse proportional to f_R. For a 10 V signal driving the VCO, a $\Delta\lambda$ =18.4 nm value is measured for a δf_R = 0.3 kHz detuning from f_R. For the same detuning, by modulating the VCO at sweeping rates of $2f_R$ (402.9 kHz), $3f_R$ (604.35 kHz), $4f_R$ (805.8 kHz) and $5f_R$ (1007.25 kHz) we measured $\Delta\lambda$ as 9.75 nm, 6.4 nm, 4.55 nm and, respectively, 3.72 nm, fact that confirms the theoretical hypothesis. The proportional reduction in the tuning bandwidth is accompanied by insignificant power variation though.

The spectrum of the RF signal of a carrier f_m when swept in frequency at a rate fs consists in a comb of frequencies separated by fs. The number of resolved frequency points within the spectrum, S, is given by the maximum frequency deviation, ΔF, divided by f_S. ΔF depends on the voltage applied to the tuning input of the synthesizer (the STG driving the VCO). If fs = 1 kHz, as ΔF is less than f_R = 201.05 kHz, maximum achievable for S would be 201. When driving the AKSS at a much larger frequency f_R, the only way to maintain a large number of resolved frequency points is to jump the optical frequency of the swept source from one tuning band to the next, in steps of f_R. In the DML regime, a deviation of frequency as high as $S{\cdot}f_R = 201{\cdot}201 = 40.4$ MHz would therefore be needed.

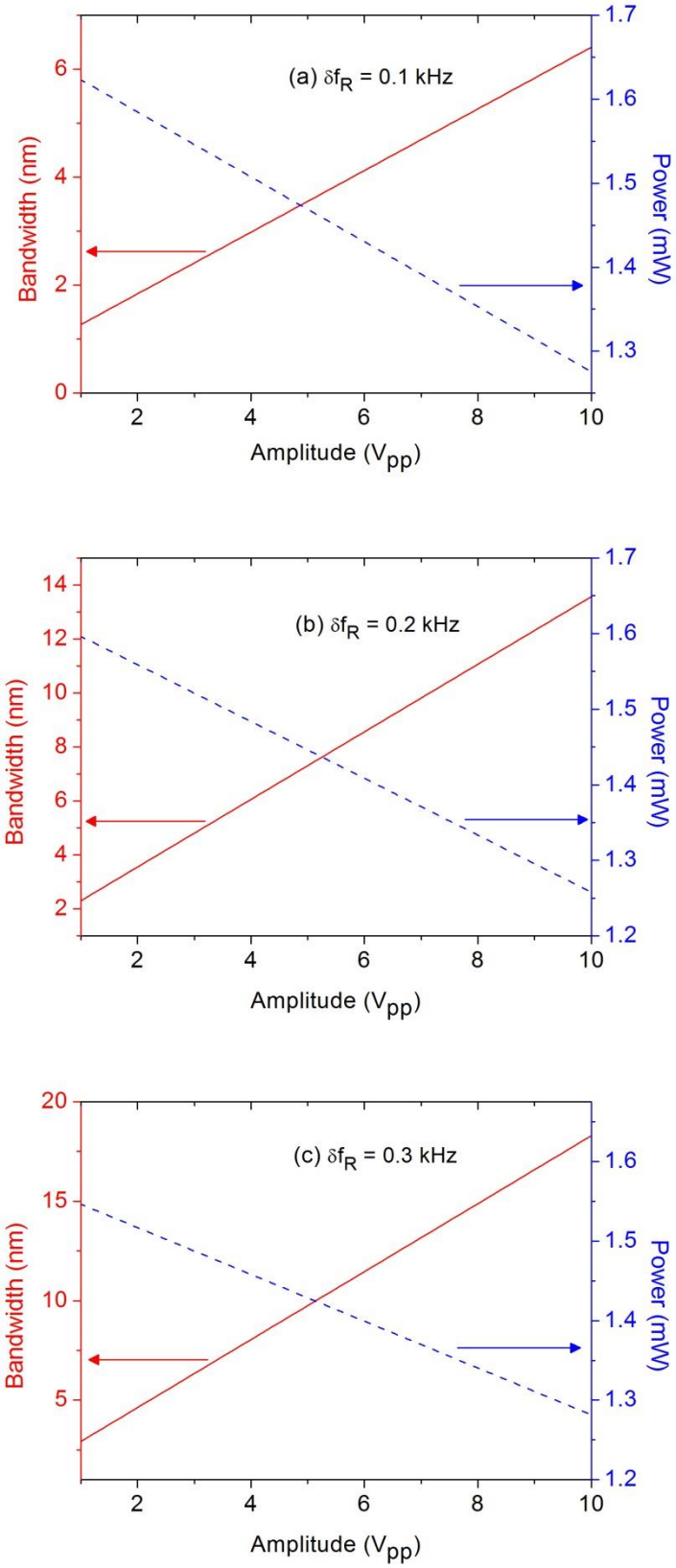

Fig. 7.2.2.3. AKSS optical output power (dashed blue line) and tuning bandwidth (solid red line) versus the amplitude of the ramp applied to the VCO input for a detuning of (a) 0.1 kHz, (b) 0.2 kHz, and (c) 0.3 kHz, respectively

When working with wavelength swept lasers operating at very fast repetition rates, the relative intensity noise (RIN) must be evaluated and reduced as much as possible. According to previous developers of SSs, there are no established methods in measuring this type of noise [12], unlike for SLDs [13] or SOAs [14]. The relative intensity noise (RIN) evaluation in the FDML concept was described in [15]. There are some interesting peculiarities in translating the methods described in this paper into the DML AKSS that deserve a separate and more thorough study. The laser presented here is pulsed at the rate of RF mode-locking, and this presents a problem in measurement, as an average over several mode-locked pulses is required, which equivalently translates in an average over a small window within the tuned spectrum.

In order to evaluate RIN, the laser output was measured with a broadband Newport 1611 Indium Gallium Arsenium (InGaAs) Photoreceiver, 900-1700 nm, 30 kHz to 1 GHz (mentioned in the text already) and displayed in real time with a LeCroy 104Mxi-A oscilloscope (10 Gyga Samples/s). As described in [15], there are two types of measurements, sliding-RIN and ortho-RIN. As commented in [15], increasing the numbers of samples in the sliding-RIN measurement determines an approach in the sliding-RIN values to the ortho-RIN. Therefore, the ortho-RIN measurement should suffice for the AKSS described in this chapter. In the first instance, we have registered 100 neighbouring photo-detected samples and determined the average of the mean power of a selected interval of 50 ns out of 4.97 μs of each sweep. Ortho-RIN was measured by calculating the standard deviation for 100 neighbouring samples (temporal profiles) at the same time interval (50 ns) within each sweep.

For 1 mW output power we measured the ortho-RIN for 3 values of detuning δf_R, of 0.1 kHz, 0.2 kHz and, respectively 0.3 kHz. We obtained for a detuning δf_R of 0.1 kHz a *RIN* = 2.18%, for 0.2 kHz *RIN* = 3.99% and for 0.3 kHz *RIN* = 5.41%. Using a bandwidth of 1 GHz, these values translate into the following *RIN* values: -123.21 dBc/Hz, -117.97 dBc/Hz, and -115.33 dBc/Hz, respectively.

Next, we evaluated the dynamic linewidth $\delta\lambda$ of the AKSS, as the inverse of this parameter determines the axial range in OCT. The AKSS mode-locked at 380 MHz, swept in frequency at 201.25 kHz and using the maximum ΔF = 60 MHz deviation achievable by driving the VCO at 10 V amplitude, is connected to a Mach-Zehnder interferometer, described in more detail in Fig. 7.1.1.5. By applying the Math function of the oscilloscope that calculates the FFT, A-scans produced are directly displayed on the oscilloscope screen in dB scale, as depicted in Fig. 7.2.2.4. The interference measurements for four values of

OPD are shown in Fig. 7.2.2.5. The decay of the amplitude of the A-scan peaks versus *OPD* is illustrated in Fig. 7.2.2.6. The sensitivity *S* is given by $20 \cdot log(A_{OPD}/A_{noise})$, where A_{OPD} represents the corresponding FFT peak amplitude value for the chosen *OPD*, while A_{noise} is the amplitude of the noise floor measured outside the FFT peak [3]. A sensitivity value of 109.68 dB is obtained for an *OPD* value close to "0". The A-scans measured are more than 10 dB above the noise level. Assuming a Gaussian shape for the tuning spectrum, and using the *OPD* value measured at 6 dB decay (OPD_{6dB}) from Fig. 7.2.2.5 of 0.52 mm, this leads to a dynamic linewidth $\delta\lambda = \lambda_0^2/4 \cdot OPD_{6dB}$ = 0.54 nm. In terms of tuning linearity, we have also measured the width of the A-scan peaks obtained, but no significant change was noticeable. This suggests sufficient tuning linearity in optical frequency, i.e. no data resampling is needed when decoding the spectrum modulation.

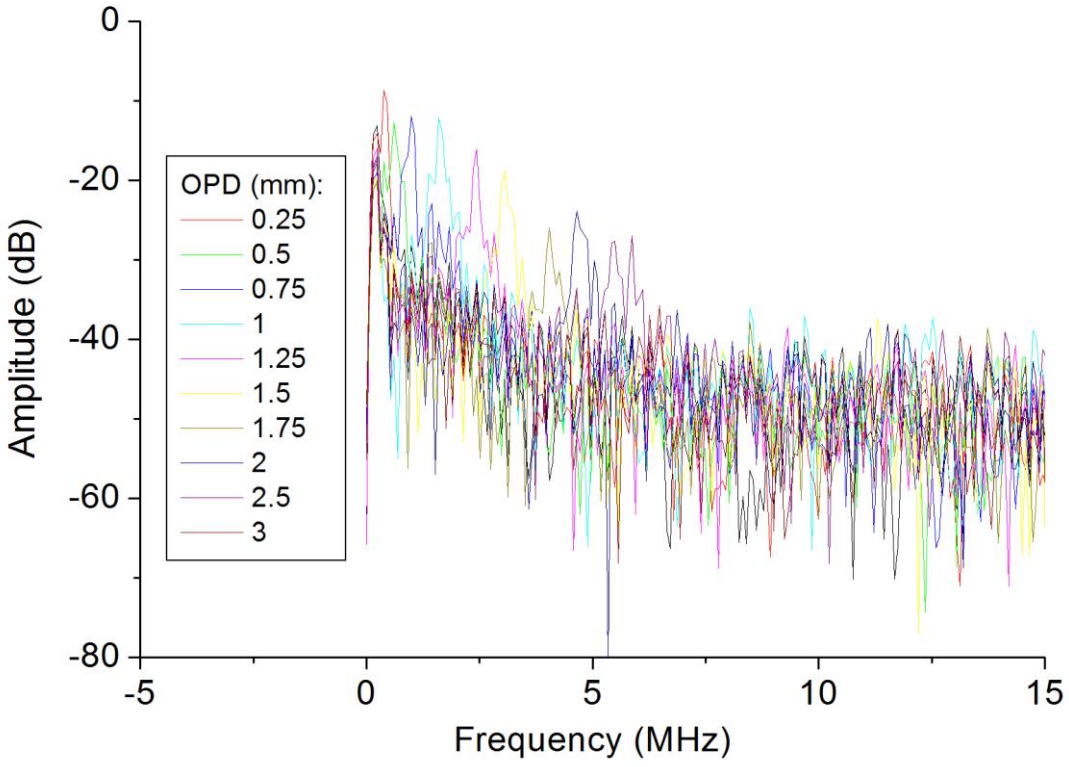

Fig. 7.2.2.4. FFT peaks (PSFs) measured for OPD values up to 3 mm

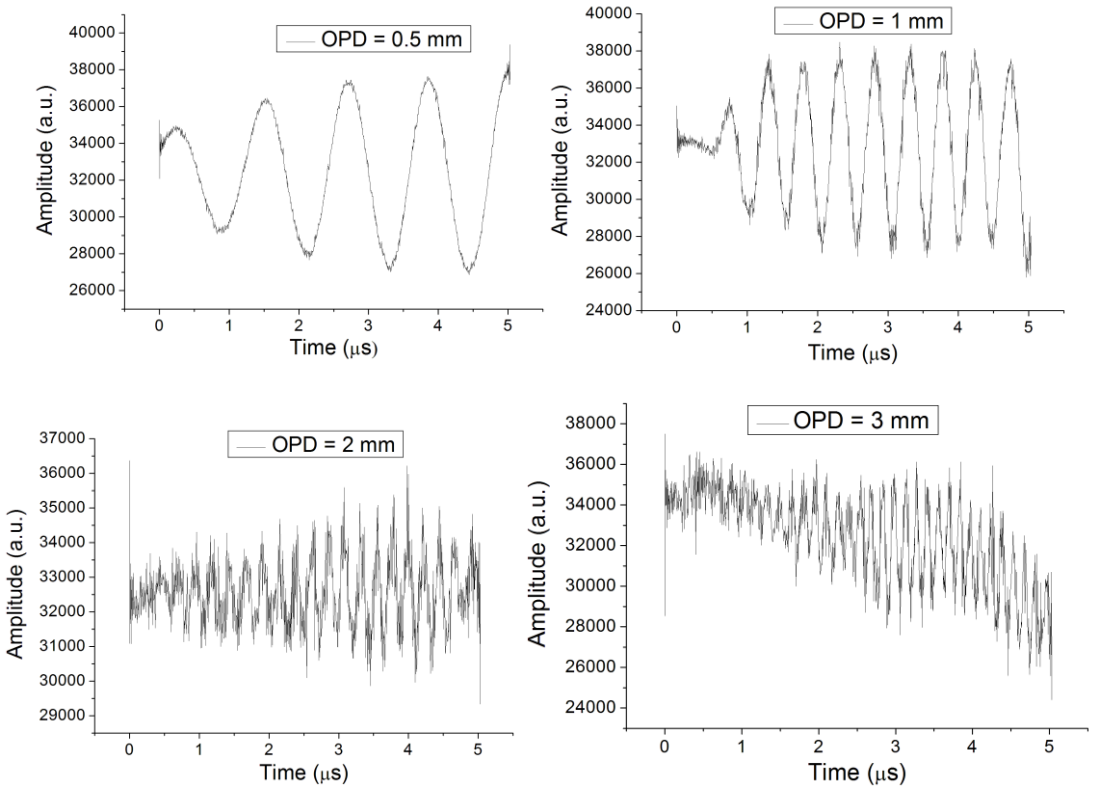

Fig. 7.2.2.5. The channelled spectrum (spectral interference) measured for different OPD values, as shown in the insets

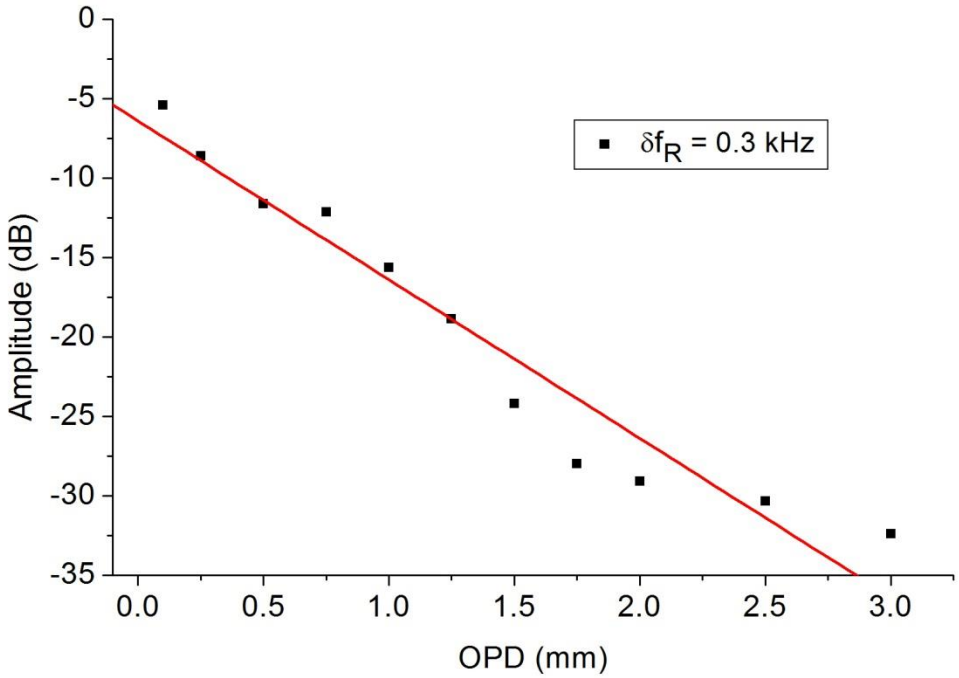

Fig. 7.2.2.6. Decay of the A-scan peak amplitudes versus OPD

A significant improvement was observed also in the OPD range (maximum OPD) achieved for the FRM based AKSS in comparison with the AKSS described in chapter 7.1.3. This is illustrated in the following table:

Table 7.2 – 1. OPD range (mm)

Detuning (kHz)	0.1	0.2	0.3	0.4	0.5
AKSS – no FRM	3	2.5	1.4	1.15	1
AKSS – with FRM	3.4	3.2	3	2	1.5

Summing up, we can conclude that by using the DML principle, operation at sweep rates exceeding 100 kHz becomes possible. More work is required to achieve besides high sweeping rate, sufficient tuning bandwidth and output power values. The 1060 nm AKSS employing a FRM in the cavity halved the necessary fibre in the ring cavity and also showed improvement in output parameters compared with the AKSS without FRM. This proves the importance in handling polarisation in long fibre configurations. Further optimization of the RF tuning can lead to larger tuning bandwidths, improved linewidth and better sensitivity and axial range values. This refers to higher ac current through SOA, not possible to be achieved using the largest RF amplifier at hand, due to the RF circuit driving the SOA having too long leads. These behave like low pass filters. If SOA devices can be paired with waveguides, then larger RF excitation becomes possible with immediate consequence in terms of dynamic linewidth that leads to larger axial range.

7.3. 1060 nm OCT application employing a dual mode-locked 1060 nm AKSS

In order to demonstrate the utility of the 1060 nm dual mode-locked AKSS, in successfully driving OCT systems, several OCT images (B-scans) of pressure sensitive adhesive (blutack) were acquired. Images have been obtained while sweeping at f_R as well as at multiples of f_R.

The 1060 nm OCT system used in acquiring B-scans, and illustrated in Fig. 7.3.1, is the same as that reported in [3], employed to illustrate the novel method of Master Slave (MS) OCT. The MS method is ideal for high speed display of *en-face* SD-OCT, here illustrated based on SS-OCT method. High sweeping rate is essential in capturing substantial volumes of tissue in intervals of time of under 1 second. We used our AKSS, as optical source, at 1060 nm central wavelength, sweeping over 30 nm bandwidth at 3 dB with 200 kHz (and multiples of this value) line rates, connected to a Booster, SOA-L-C-14-FCA (CIP1 from BT), electronically controlled, that ensures a total power of 10 mW. The configuration uses two single mode directional couplers, DC1 and DC2. DC1 has a ratio of 20/80 and DC2 is a balanced splitter, 50/50. 20% from the boosted AKSS power is launched towards the object arm, via lens L1 (focal length 15 mm), which collimates the beam towards a pair of scanners XYSH (2D scanner heads, Cambridge Technology, Bedford, MA, model 6115) followed by an interface optics made from two lenses, L2 and L3, (both of 75 mm focal length). DC2 feeds a balance detection receiver (Thorlabs, Newton, New Jersey, model PDB460C), using two photo-detectors, PhD1 and PhD2 and a differential amplifier DA. The power reaching the imaged object is 2.2 mW, the light incident on the object being focused by using a lens L4 (focal length 22 mm). All lenses used in the system are achromatic in order to reduce any added effects generated by chromatic aberrations.

At the other output of DC1, 80% from the AKSS boosted power is directed towards the reference arm equipped with reference mirrors, M1, respectively M2, placed on a translation stage, TS to adjust the OPD in the interferometer. The TS used is a linear actuator (Newport, Irvine, CA, model UE404CC), having a 1 μm resolution and controlled by a Newport driver MM4005. The collimating lenses L5 and L6 are similar to L1 (focal length 15 mm).

The signal from the balanced detector is sent to one of the two inputs of a dual input digitizer (Alazartech, Quebec, Canada, model ATS9350, 500 MB/s). A trigger signal from the AKSS synchronizes the acquisition (input T).

The software used to acquire and manipulate data was devised in the AOG [3]. This was implemented using Labview 2012, 64 bit, from National Instruments. Two programs were created, progFFT and progCorr. They have a common coding core that acquires and digitizes data via the Alazartech digitizer.

The MS method presents a net advantage in terms of *en-face* imaging as the processing block can provide signals in parallel for each depth for which a memory was created. Further studies are necessary to exploit this advantage in practice together with the use of graphic cards or field-programmable gate arrays and an improved dual mode-locked AKSS.

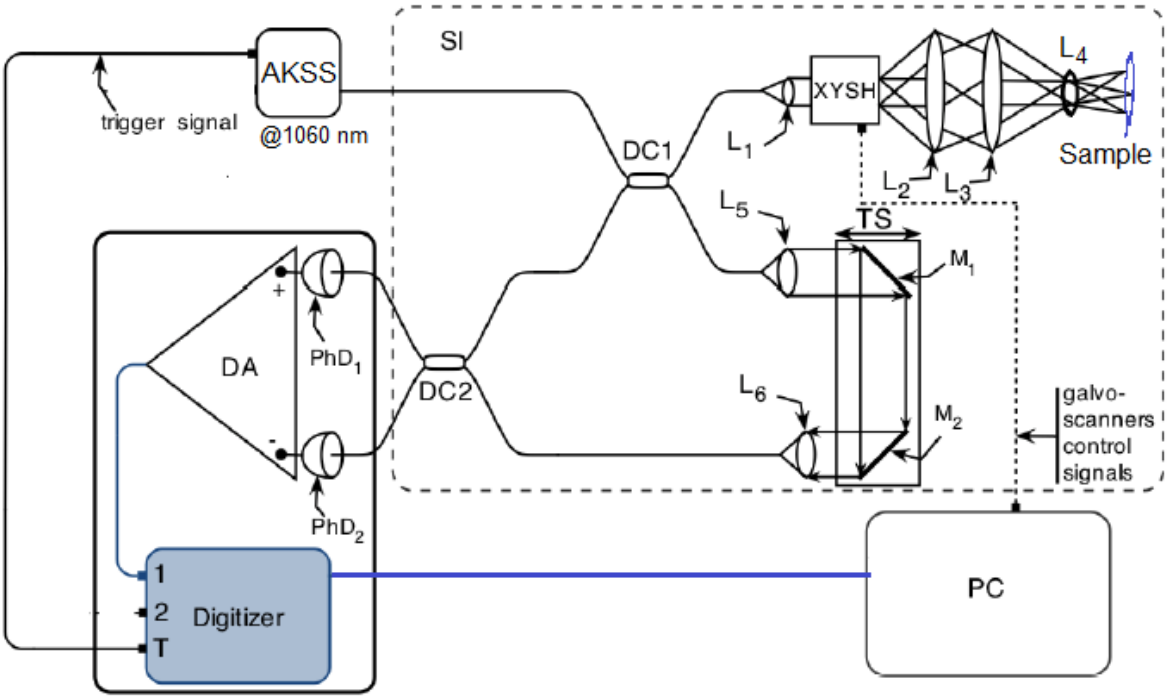

Fig. 7.3.1. 1060 nm OCT system

The pressure sensitive adhesive topographic B-scans acquired are illustrated in Fig. 7.3.2, in which the AKSS bandwidth is swept at approximately 200 kHz line rate, and respectively 7.3.3, where the line rate was doubled, to 400 kHz. The AKSS output power was boosted in order to ensure at least 1 mW of optical power to reach the sample. The images are 2 mm horizontally, while the visible area achieved reaches a depth of around 0.5 mm. The quality of the image represented in Fig. 7.3.3 is visibly inferior to those in Fig.

7.3.2, due to the fact that the AKSS was driven at $2f_R$, which has as effect a reduction in power and also in bandwidth. The reduction in bandwidth leads to an increase in the displayed contour of the interface between the air and the adhesive. No electronic gain or averaging of images was implemented.

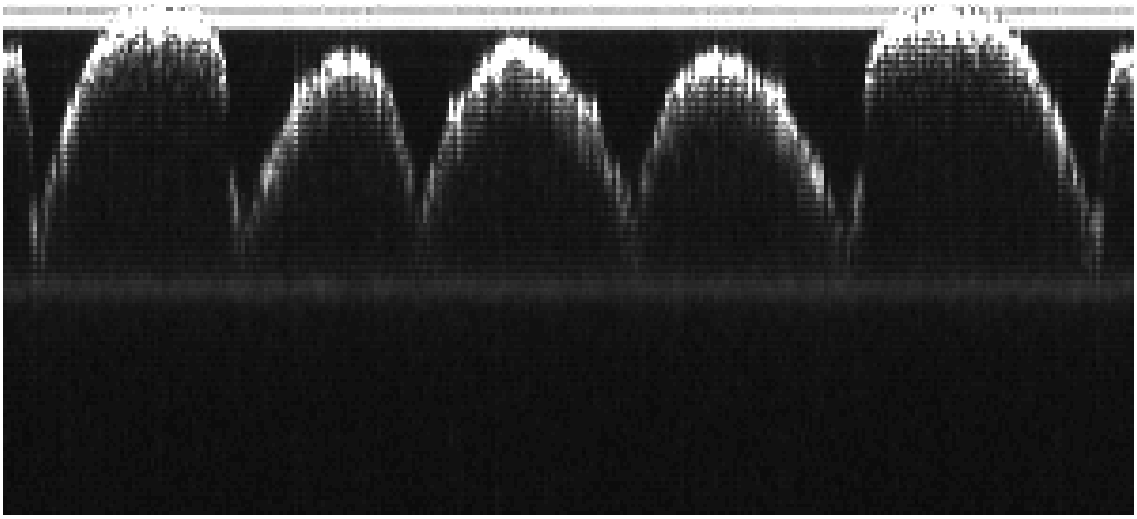

Fig. 7.3.2. OCT image of pressure sensitive adhesive acquired at f_R = 200 kHz

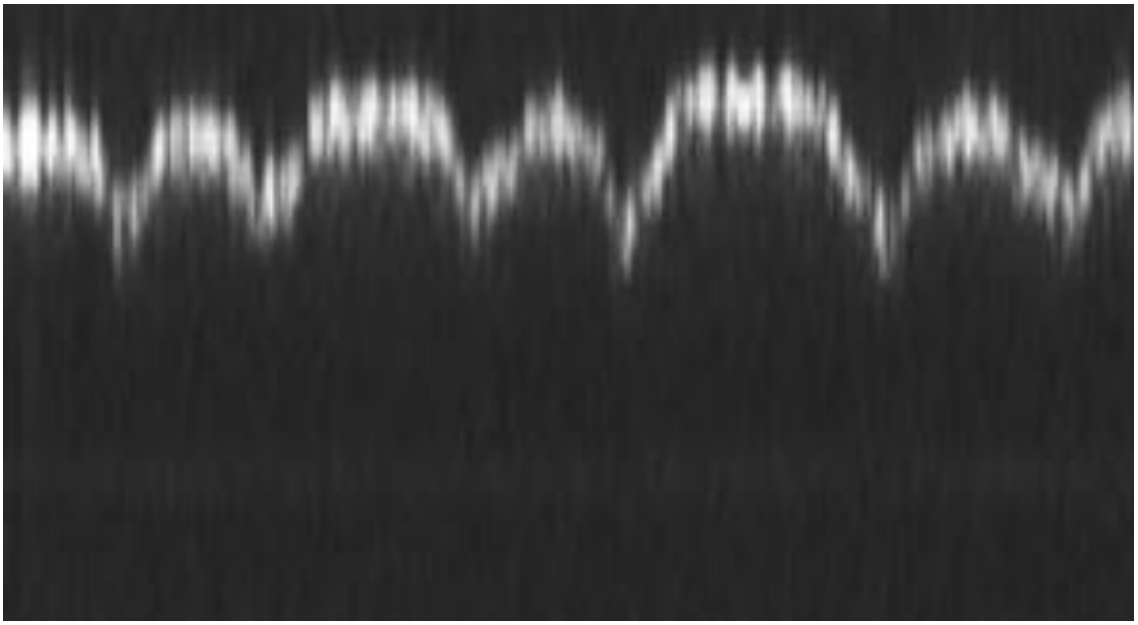

Fig. 7.3.3. OCT image of pressure sensitive adhesive acquired at $2{\cdot}f_R$ = 400 kHz

Images in Fig. 7.3.2 and 7.3.3 represent the topography of the objects imaged, no information is conveyed from inside the material, due to the poor sensitivity, consequence of the low power used. Imaging in depth was attempted in a more transparent material, paper,

scanning over 1 mm length, as illustrated in Fig. 7.3.4, but the penetration of a few microns was insufficient for a good quality image.

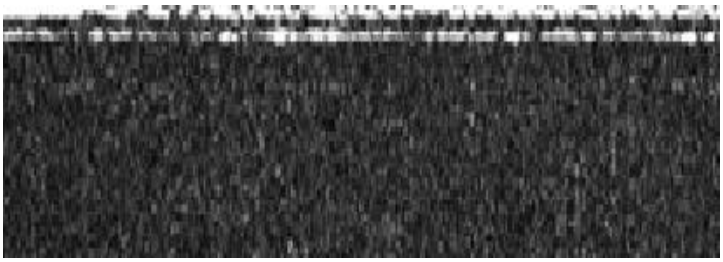

Fig. 7.3.4. Attempt of performing OCT imaging of paper

In conclusion, we have demonstrated that the DML mechanism is a viable modality to achieve high sweeping rate swept source operation, that can be extended beyond MHz by mode-locking at multiple values of f_R. Further improvements in the optical parameters, such as the instantaneous linewidth and the optical power, are necessary in order to achieve better sensitivity at larger depths in the OCT images. Also, it would be necessary to improve the RF excitation conditions, to allow a more efficient use of higher frequencies, such as when operating at multiples of f_R. These improvements shall allow MHz sweep rates without the AKSS exhibiting significant decays in optical tuning bandwidth or output power.

Summary

To conclude, a 1060 nm central wavelength AKSS was presented. The linewidth was controlled by varying the mode-locking frequency and improves continuously with the increase in mode-locking reaching GHz level. The repetition rate achieved was relatively low, not greater than 10 kHz, and the measured tuning bandwidth slightly under 30 nm. Using a booster, the power was increased up to 12 mW. Further studies require optimization of the SMF length to DCF length ratio, cancelation of polarisation effects. Utilisation of a wider bandwidth SOA would be recommended for enhanced axial resolution.

After that, a 1060 nm AKSS employing a broadband FRM was presented. Comparing with the initial 1060 nm configuration, slight improvements in several parameters such as linewidth, output bandwidth and power are observed.

When applying the DML principle, operation at sweep rates exceeding 100 kHz was achieved. The 1060 nm AKSS employing a FRM in the cavity resulted in halving the necessary fibre in the ring cavity and also showed improvement in output parameters compared with the AKSS without FRM. We have demonstrated that the DML mechanism is a viable modality to achieve high sweeping rate swept source operation.

The main parameters of the 1060 nm DML AKSS are illustrated in the following table:

Parameter	**Value**
Central wavelength	1060 nm
Mode-locking	100 – 1000 MHz
Maximum Output Power	10.8 mW
Linewidth	92 pm
Bandwidth	50 nm (@1 KHz), 32 nm (@200 kHz)
Repetition rate	201.65 kHz or multiples of this value
Relative intensity noise	2.18%

The main parameters of the 1060 nm DML AKSS employing FRM are illustrated in the following table:

Parameter	**Value**

Central wavelength	1060 nm
Mode-locking	100 – 1000 MHz
Maximum Output Power	13.12 mW
Linewidth	89 pm
Bandwidth	60 nm (@1 kHz), 38 nm (@200 kHz)
Repetition rate	211.35 kHz or multiples of this value
Relative intensity noise	2.18%

References

[1] S. Yamashita, Y. Nakazaki, R. Konishi, O. Kusakari, "Wide and fast wavelength-swept fiber laser based on dispersion tuning for dynamic sensing", Journal of Sensors, Vol. 2009, 572835 (2009)

[2] Y. Takubo, S. Yamashita "High-speed dispersion-tuned wavelength-swept fiber laser using a reflective SOA and a chirped FBG", Optics Express, vol. 21, no. 4, pp. 5130-5139 (2013)

[3] A. Gh. Podoleanu, A. Bradu, "Master-Slave interferometry for parallel spectral domain interferometry sensing and versatile 3D optical coherence tomography", Optics Express, Vol. 21, No. 16, 19324-19338 (2013)

[4] Akira Takada, Makoto Fujino, and Shigenori Nagano, "Dispersion dependence of linewidth in actively mode-locked ring lasers", Optics Express 20, 4753-4762 (2012)

[5] W. Drexler, M. Liu, A. Kumar, T. Kamali, A. Unterhuber, R. A. Leitgeb, "Optical coherence tomography today: speed, contrast, and multimodality", Journal of Biomedical Optics 19(7), 071412 (2014)

[6] http://www.superlumdiodes.com/pdf/soa372.pd

[7] E. J. Jung, J.-S. Park, M. Y. Jeong, C.-S. Kim1, T. J. E., B.-A. Yu, S. Gee, J. Lee, M. K. Kim, "Spectrally-sampled OCT for sensitivity improvement from limited optical power", Optics Express 16(22), 17457- 17467 (2008)

[8] R. H. Huber, M. Wojtkowski, J.G. Fujimoto, "Fourier Domain Mode-locking (FDML): A new laser operating regime and applications for optical coherence tomography", Optics Express 14(8), 3225-3237 (2006)

[9] R. Huber, D. C. Adler, J. G. Fujimoto, "Buffered Fourier domain mode-locking: unidirectional swept laser sources for optical coherence tomography imaging at 370,000 lines/s", Optics Letters 31(20), 2975-2977 (2006)

[10] T.-H. Tsai; O. O. Ahsen; H.-C Lee; K. Liang; M. G. Giacomelli; B. Potsaid; Y. K. Tao; V. Jayaraman; M. F. Kraus; J. Hornegger; M. Figueiredo; Q. Huang; H. Mashimo; A. E. Cable; J. G. Fujimoto, "Ultrahigh speed endoscopic swept source optical coherence tomography using a VCSEL light source and micromotor catheter", Proc. SPIE 8927, Endoscopic Microscopy IX; and Optical Techniques in Pulmonary Medicine, 89270T (2014)

[11] N. Gisin et al., “Polarization mode dispersion of short and long single-mode fibers”, J. Lightwave Technol. 9 (7), 821 (1991)

[12] F. D. Nielsen, L. Thrane, K. Hsu, A. Bjarklev, P. E. Andersen, “Semiconductor optical amplifier based swept wavelength source at 1060 nm using a scanning Fabry–Perot filter and an YDFA-based booster amplifier”, Optics Communications 271, 197–202 (2007)

[13] H. F. Taylor, "Intensity noise and spontaneous emission coupling in superluminescent light-sources," IEEE J. Quantum Electron. 26, 94-97 (1990)

[14] M. Shtaif and G. Eisenstein, “Noise properties of nonlinear semiconductor optical amplifiers,” Optics Letters, vol. 21, pp. 1851–1853 (1996)

[15] B. R. Biedermann, Wolfgang Wieser, Christoph M. Eigenwillig, Thomas Klein and Robert Huber, “Dispersion, coherence and noise of Fourier domain mode locked lasers”, Optics Express, 17(12), 9947-9961 (2009)

8

Akinetic swept sources based on long dispersive cavities comprising dispersion compensating fibre

Introduction

In this chapter, a 1550 nm central wavelength AKSS which is entirely controlled electronically, with adjustable scanning rate and some control of the linewidth, with no mechanical means, is presented. The ring cavity comprises a special type of fibre, called dispersion compensating fibre (DCF). The ration between the SMF and DCF in the cavity is investigated. In single mode-locking operation, linewidths can be varied from 0.06 nm to over 1 nm in the static regime and the scanning rate can be varied up to several kHz. The DML mechanism, which was introduced in the previous chapter, is also integrated in the 1550 nm AKSS. Repetition rates of hundreds of kHz are achieved. Also, a comparison between 1550 nm AKSS that integrate FRM in a ring cavity and the ones that do not is also illustrated. Topographic OCT imaging at small repetition rates is demonstrated.

The chapter ends with an introduction in microresonators fabricated in glass and whispering gallery modes (WGM) and an investigation method of microresonators using the 1550 nm AKSS as alternative to the ultrabroadband optical source is presented.

8.1. Ring cavity

8.1.1. 1550 nm single mode-locked swept source

In this chapter, an AKSS which is entirely controlled electronically, with adjustable scanning rate and some control of the linewidth, with no mechanical means, is presented. The optical output is in the 1550 nm wavelength band. Linewidths can be varied from under 0.06 nm to over 1 nm in the static regime and the scanning rate can be varied up to several kHz.

The schematic diagram of the AKSS and the tuning mechanism are depicted in Fig. 8.1.1.1. The set-up uses a ring type cavity in which a semiconductor optical amplifier (SOA), model SOA-L-C-14-FCA (also known as CIP 1, from BT), operating at a central wavelength of 1550 nm, with a bandwidth larger than 50 nm, is used as gain medium. The SOA is secured in a typical Thorlabs mount equipped with a type 1 control board, customised with a bias tee circuit in order to accept RF input. The SOA is driven by a Thorlabs LDC 210C power supply, while temperature stability is ensured through thermo-electric cooling performed by a Thorlabs TEC 200C (sensor TH 20kΩ). The SOA is isolated by two polarization insensitive isolators, which ensure unidirectional lasing. Apart from the SOA, the ring laser cavity comprises two types of fibre: dispersion compensating fibre (DCF, Draka Elite DDU1171023, dispersion parameter of -140 ps/nm·km at 1550 nm) and single mode fibre (SMF Corning 28e(R), dispersion parameter of ≤18 ps/nm/km at 1550 nm). A 90:10 coupler determines a 10% output of the light in the laser cavity.

The tuning principle involved is that of mode-locking a dispersive cavity laser cavity and varying the frequency of the driving signal injecting the mode-locking. An Agilent 81160A radio frequency (RF) generator tunes the SOA, via an own custom made bias tee. Sweeping is externally triggered by a Hewlett Packard 8131A pulse generator. Measurements were performed by both static (manually changing the input signal frequency and amplitude) and dynamic tuning (by setting a central input mode-locking frequency f_m, the amplitude, a span value ΔF, and a sweeping frequency f_s), for various lengths of DCF and SMF. The laser output characteristics of the AKSS configuration are measured using an Agilent 86145B optical spectrum analyser, with a resolution of 60 pm. The AKSS operation in dynamic sweeping regime was evaluated by probing the channel spectrum of a Mach-Zehnder interferometer, the optical output characteristics being measured by a balanced photo-detector and displayed with a LeCroy Wave Runner 104 MXi-A 1GHz oscilloscope.

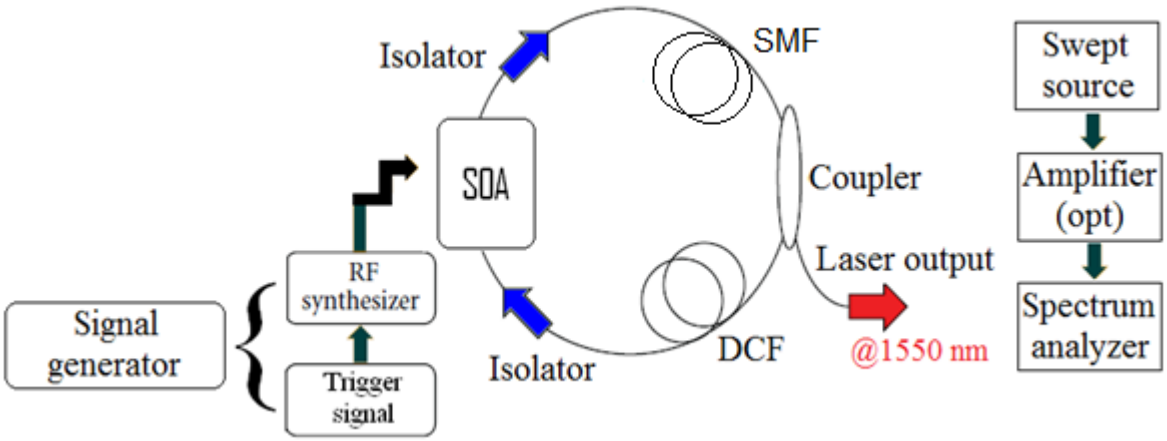

Fig. 8.1.1.1. Generic schematic diagram of a dispersion tuned 1550 nm AKSS

Several experiments were performed with different combinations of DCF and SMF lengths used in the laser cavity. In this paper, we will present results obtained with the following approximate ratios DCF/SMF: 15:1, 8:1, 4:1, 3:1 and 1:1.

When operating the SS in static regime, the values of mode-locking radio-frequencies can be determined to tune the laser within a bandwidth $\Delta\lambda$ measured by the OSA. The difference of frequencies denotes a static frequency band ΔF around each central mode-locking value, multiple of f_R.

Apart from the bandwidth, other defining parameters measured in the static regime are the contrast and the linewidth. The following measurements were made for a 5 $V_{peak\text{-}peak}$ amplitude sinusoidal RF signal injected into the SOA driven at 120 mA. At these parameters, the output optical power was approximately 1 mW.

The contrast C is defined as:

$$C = \frac{A_{max} - A_{min}}{A_{max} + A_{min}}, \qquad (8.1.1 - 1)$$

where A_{max} and A_{min} represent, respectively, the maximum and minimum amplitude of the SS optical output measured in static regime with the OSA. At mode-locking values within the 50-500 MHz frequency range, no C values smaller than 0.95 were achieved, regardless of the dispersive cavity configuration.

Fig. 8.1.1.2 illustrates that small linewidth values can be obtained using mode-locking frequencies in the range 450-500 MHz, while significantly larger linewidths occur for mode-locking frequency values under 200 MHz.

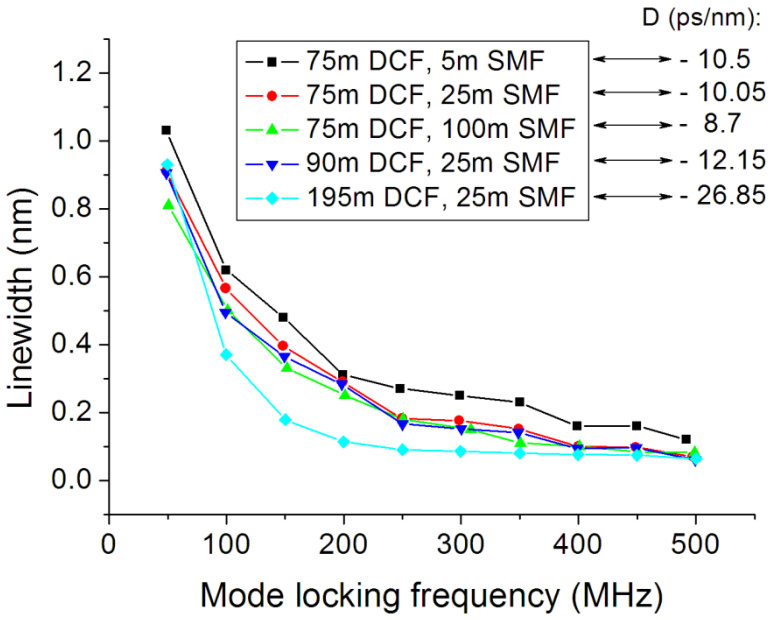

Fig. 8.1.1.2. Linewidth versus mode-locking frequency, for several combinations values of dispersion in the cavity

The best linewidth of 60 pm was achieved for a mode-locking frequency of 498.8 MHz, when the swept source laser cavity contained a 90 m length of DCF and a 25 m of SMF. This linewidth value matches the resolution of the optical spectrum analyser, meaning that the linewidth is better than the value measured. Similar values for the linewidth at large mode-locking frequencies were obtained for the other DCF/SMF ratios. In the case where long DCF is used in the cavity, the linewidth seems to decrease slowly with the increase in the mode-locking frequency, being less than 100 pm over the whole 200 - 500 MHz frequency band. On the other hand, when short SMF lengths were used in the cavity, the minimum linewidth was 150 pm.

Yamashita et al. [1] predicted a variation of linewidth proportional to $(f_{m0})^{1/2}$, contradicted by the trend in Fig. 8.1.1.2. However, the same reference suggests that smaller f_{m0} increases the instability of lasing wavelength and causes lasing broadening. This shows that the dependence of linewidth to the mode-locking frequency remains a subject for further studies. Takada et al [2] refers to effects on the wavelength tuning depending on the number

of roundtrips in the cavity, defining the maximum achievable single-wavelength tuning range as:

$$\Delta\lambda < \frac{c}{n_g}\frac{C_{FBG}}{f_m}, \qquad (8.1.1-2)$$

where n_g represents the group index of the fibre, and C_{FBG} represent the chirp parameter.

The variation of the tuning bandwidth $\Delta\lambda$ versus mode-locking frequency, f_m, is depicted in Fig. 8.1.1.3. The largest bandwidth, of approximately 38 nm, is achieved at 50 MHz mode-locking for a cavity employing 75 m DCF and 5 m SMF.

For a tuning bandwidth $\Delta\lambda$ and linewidth $\delta\lambda$ we define the number of scanning points as $P = \Delta\lambda/\delta\lambda$. For example, at a mode-locking frequency of 300 MHz, we obtain 221 points when using 195 m DCF, whilst only 94 with 75 m of DCF. In all cases, the lower the frequency (under 200 MHz), the larger the bandwidth. However, due to a faster increase in the linewidth than in the tuning bandwidth, less resolving points are obtained, such as 40. In all configurations, less tuning bandwidth is obtained when the SS is mode-locked above 200 MHz to 400 MHz. This may be explained by a lower amplitude signal delivered by the RF generator at larger frequencies, to the semiconductor chip.

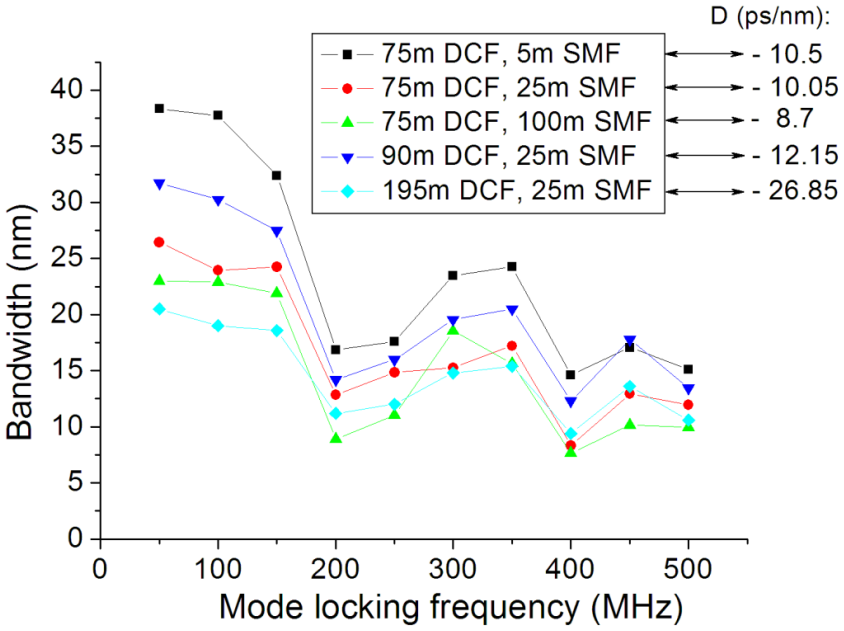

Fig. 8.1.1.3. Bandwidths measured in static regime for several values of dispersion in the cavity

We introduce a parameter, Alpha (α), as the percentage of DCF length out of the total cavity length in the ring, $\alpha\ (\%) = 100 \cdot (L_{DCF}/L)$. Further, we have plotted the values of linewidth measured at small (50 MHz) and, respectively, large mode-locking frequencies (500 MHz) versus α. The two graphs in Fig. 8.1.1.4 show that α has a slight effect on the linewidth, while more control on the linewidth is obtained through the frequency of the signal driving the SOA. Larger linewidths (>60 pm) are achieved for α values between 40-70%. Smaller linewidths (≈50 - 60 pm) are achieved at higher mode-locking frequencies, while the cavity length proportion of the dispersive element is about 80-90%. When approximately 95% of the cavity represents DCF, the linewidth is 2.5 times larger (≈150 pm).

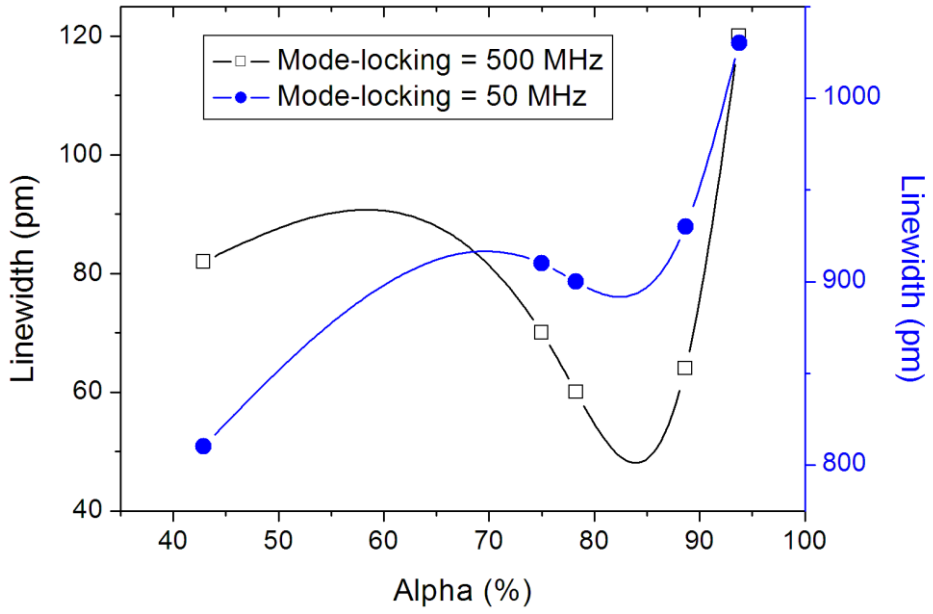

Fig. 8.1.1.4. Linewidth measured at small and large mode-locking frequencies versus the proportion of DCF in the SS cavity

Next, the AKSS was operated in dynamic regime. The maximum sweeping frequency of the signal delivered by the Agilent 81160A RF generator is 20 kHz. In Fig. 8.1.1.5, and respectively 8.1.1.6, we have plotted graphs of data collected with the OSA, for three sweeping frequencies: 1, 10 and 20 KHz. The SS was equipped with 195 m DCF, with either 5 m SMF or 100 m SMF. The other parameters were the same as above, i.e.: 5 V_{pp} RF signal amplitude on the SOA driven at 120 mA, mode-locking frequency f_m = 300.6 MHz and 300.1 MHz, respectively and ΔF = 150 KHz. If we apply these parameters in equation

(5), theoretically a slightly larger bandwidth is achieved when in the cavity we employ 100 m SMF, then the case when only 5 m length of SMF is used. This was confirmed in the experimental measurements, as for the SS equipped with 5 m SMF we obtained approximately 15 nm bandwidth, while for the SS fitted with more SMF we achieved around 16.5 nm.

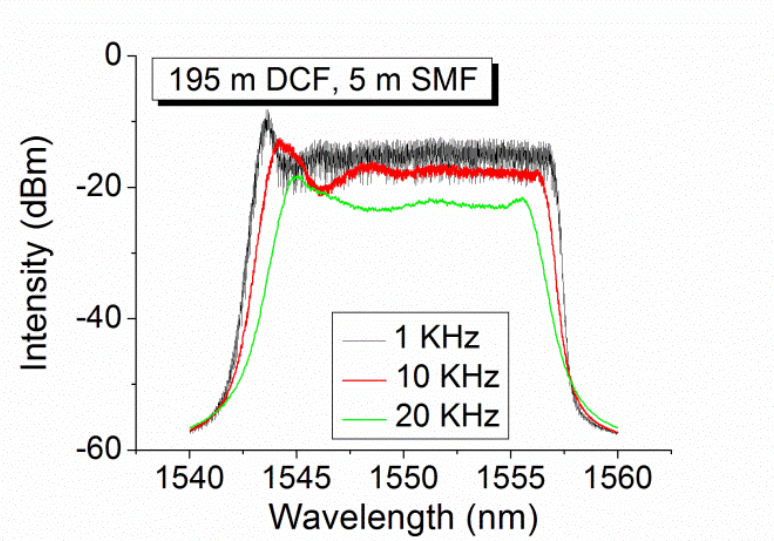

Fig. 8.1.1.5. Optical spectrum for three sweeping frequencies for the SS equipped with L_{DCF} *= 195 m and* L_{SMF} *= 5 m*

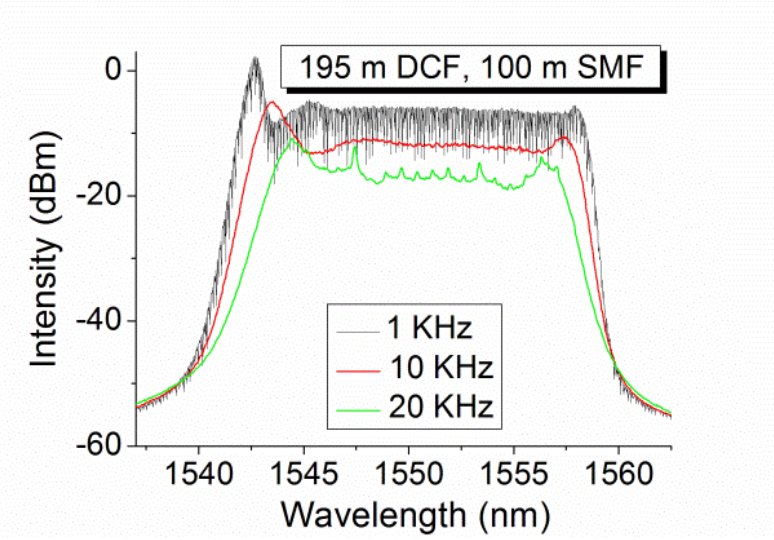

Fig. 8.1.1.6. Optical spectrum for three sweeping frequencies for the SS equipped with L_{DCF} *= 195 m and 100 m*

As the sweeping becomes faster, the SS configurations exhibit decays in both output power and bandwidth. On the other hand, by increasing the length of SMF, higher output power is achieved, of about 0.5 mW (corresponding to -3 dBm), measured at 1 kHz repetition rate. In both graphs, the bandwidth exhibits a slow decrease, being about 4 nm smaller at 20 kHz repetition rate.

Longer length means larger roundtrip in the cavity, although here the increase in power is attributed to reduction in dispersion. In order to increase the output power, a booster SOA similar to that used in the cavity was placed outside the cavity. With the booster driven at 300 mA, an output power of 12 mW was achieved. The SOA can be driven at a maximum of 600 mA, but amplified spontaneous emission (ASE) was noticeable.

The swept source based on the dispersion tuning principle was previously tested successfully in sensing applications [1]. The flexibility of this concept, given by the possibility of optimizing the output parameters by modifying the length and the composition of the ring cavity, makes it a very attractive option for OCT applications that require wide and fast SSs. Thus, we evaluated the AKSS comprising 195 m DCF and 5 m SMF in the cavity, mode-locked at 300.6 MHz and swept at 1 kHz rate by scanning through the channeled spectrum of a Mach-Zehnder interferometer. A Fast Fourier Transformation (FFT) of the photo-detected signal delivers an A-scan [3]. For optical path difference (*OPD*) values up to 5 mm, A-scan peaks were obtained with more than 10 dB above noise, as depicted in Fig. 8.1.1.7. A 6 dB decay is obtained at *OPD* = 0.8 mm.

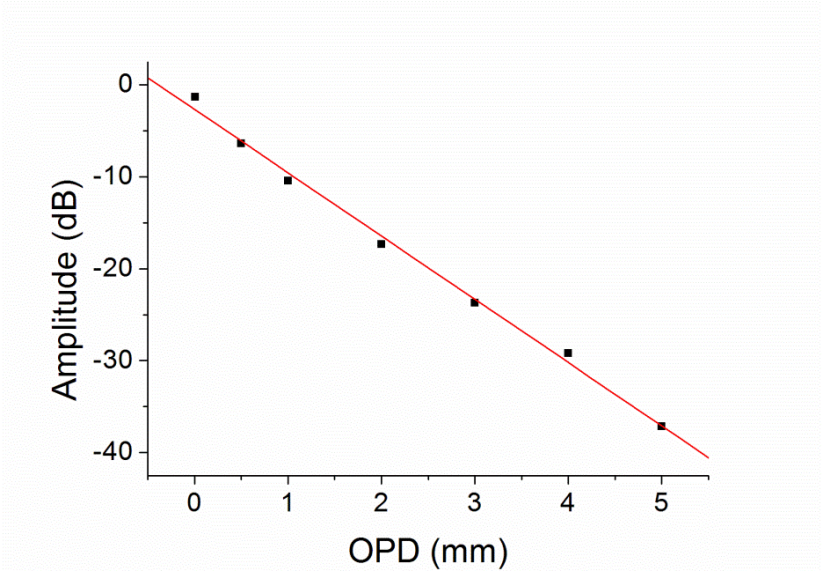

Fig. 8.1.1.7. Decay of modulation intensity with increasing OPD

The sensitivity of the interferometer, in case it is used for reflectivity measurement, is calculated as $20 \cdot \log(A_{OPD}/A_{noise})$, where A_{OPD} is amplitude of the FFT peak for an *OPD* close to 0, while A_{noise} represents the amplitude of the noise floor measured outside the peak [13]. A value of 93.3 dB was achieved. For a 20 nm tuning bandwidth, assuming a Gaussian shape of the spectrum, the axial resolution achievable is $0.44 \cdot \lambda^2/\Delta\lambda$ = 0.05 mm. As the sweeping speed increases, the A-scans showed a decrease in the axial range (OPD). This can be attributed to the fact that the coherence of the AKSS decreases with the increase of sweeping speed, due to a decrease of number of roundtrips in the cavity, as explained in [2].

In terms of tuning linearity, the width of the A-scan peaks obtained by FFT has shown insignificant change with the *OPD*, which represents an increase of only 0.2% at *OPD* = 5 mm, in comparison with the width of the A-scan peak at an *OPD* value close to zero. This suggests sufficient tuning linearity in optical frequency, i.e. no data resampling is needed when decoding the spectrum modulation.

To recap, a versatile AKSS is demonstrated, with controllable sweeping parameters. The main drive in developing such a source was achieving control of the coherence length. Such an AKSS is to be used in conjunction with novel OCT configurations that do not necessarily need narrow linewidths, such as coherence gated wavefront sensors and multiple path OCT configurations [1, 3], developed by our group. The linewidth is controlled by varying the mode-locking frequency. The sweeping speed could be up to 20 kHz (limited by the Agilent 81160A RF generator) and tuning bandwidth of 20 – 40 nm. Using a booster, the power was increased up to 12 mW. Further studies require optimization of the DFC:SMF ratio and use of a SOA with larger bandwidth for better control of the coherence length and enhanced axial resolution.

8.1.2. 1550 nm dual mode-locked swept source

The Fourier domain mode-locking (FDML) method was proposed by R. Huber et al., using a ring laser that included a long dispersion delay fiber, to eliminate the photon lifetime limitation and improve the laser sweep rate, achieving 285 kHz line rates [4] with later reports exceeding 1 MHz.

Yamashita et al. [1, 5] proposed an akinetic solution using mode-locking in a dispersive cavity, employed with DCF and achieved 250 kHz sweep rates. In order to achieve wide and fast tuning with a narrow spectral linewidth, they show that the dispersion characteristic of the DCF and modulation frequency should be as large as possible, while the cavity length should be as small as possible.

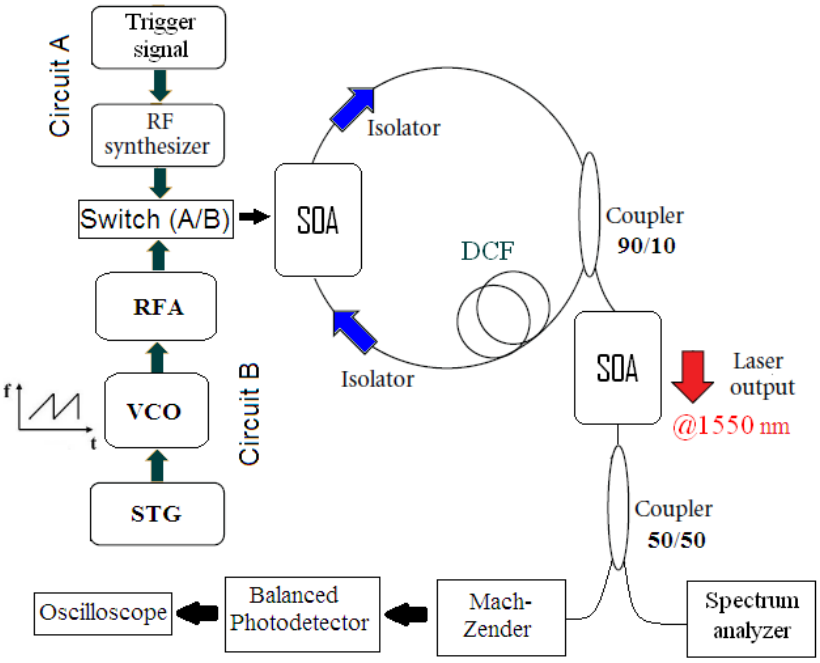

Fig.8.1.2.1. AKSS configuration with switching between two tuning circuits, where VCO - voltage controlled oscillator, STG - saw-tooth generator with bias control, RFA - radio frequency power amplifier

A switch with two positions, A and B, is used to perform two measuring regimes of operation. In position A of the switch, an Agilent 81160A radio frequency (RF) generator that can be swept in frequency up to 20 kHz is used to drives the SOA. Sweeping is externally triggered by a Hewlett Packard 8131A pulse generator. Measurements were performed by both static (manually changing the input signal frequency) and dynamic tuning (by setting a

central input frequency and span value), for various lengths of DCF and SMF. Here we present the linewidths and bandwidths versus the mode-locking frequency measured in the static regime, data collected through an Agilent 86145B optical spectrum analyzer (OSA).

In the position B of the switch we have employed the dual mode-locking mechanism. A low noise voltage controlled oscillator (VCO) and a Mini-Circuit amplifier are used to drive the SOA with a 5 V amplitude sinusoidal signal applied to the SOA in series with a 27 ohm resistor. Several models of VCOs were introduced in the dual mode-locking setup, ZX95-368+, ZX95-928 CA+, ZX95 – 1584+, ZX-1790+ and ZFL-1000VH and ZHL-42W amplifiers. The Agilent 81160A signal generator provides a saw-tooth signal with adjustable amplitude and bias used to control the tuning bandwidth and the central frequency of the VCO.

Output power is drawn out through the 90/10 coupler and represents 10% of the light in the cavity further amplified by a similar type of SOA.

The laser output characteristics of the swept source configuration are measured using an Agilent 86145B OSA, with a resolution of 60 pm. The coherence length of the source was evaluated by driving a Mach-Zehnder interferometer, terminated on a 50/50 coupler driving a New Focus balanced detector model 1817, DC-80 MHz, 900-1700 nm bandwidth, whose output is displayed with a LeCroy Wave Runner 104 MXi-A 1GHz oscilloscope.

Static characterization

First, we have evaluated the linewidths and bandwidths by switching to the position A and operating in static regime, by manually changing the input RF frequency. As it can be seen in Fig. 2, small linewidth values were obtained for mode-locking frequencies around 300-500 MHz, while larger linewidths occur for frequency values smaller than 200 MHz. The best linewidth of 0.060 nm (60 pm) was achieved for a mode-locking frequency of 499.7 MHz. This value matches the resolution of the OSA used, of 60 pm, meaning that the linewidth is very likely better than the value measured. On the other hand, linewidth broadening occurs at small mode-locking frequencies (under 200 MHz), as previously communicated [1, 6]. Therefore, we considered measuring the bandwidths for static mode-locking in the 200 MHz – 500 MHz interval, in steps of 10 MHz. A peak value of approximately 34 nm was measured for a 349.4 MHz frequency.

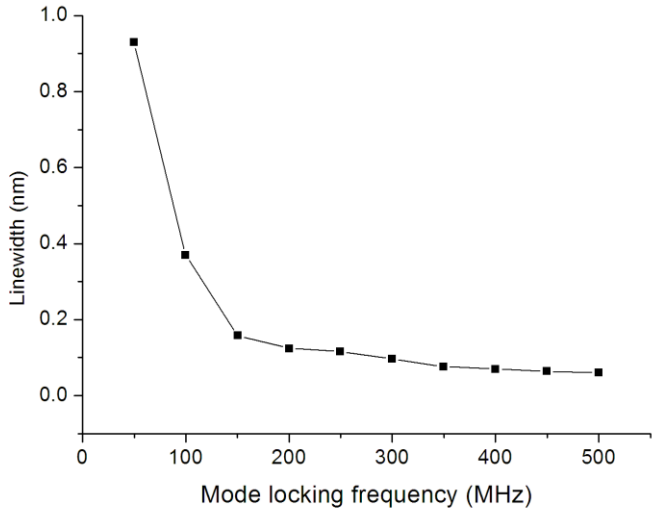

Fig. 8.1.2.2. Linewidth versus mode-locking frequency

Dynamic characterization

After that we have switched the system on the position B. By setting the signal amplitude on the pulse generator, with a certain offset, we tune the VCO at a certain central mode-locking frequency f_m. The decay of the optical output as the sweeping speed increases is illustrated in Fig. 8.1.2.4. At an amplitude value of 80 mV_{pp} for the ramps applied to the VCO, sweeping rates achieved are small, of no more than 10 KHz. We managed to basically cover the whole gain of the SOA and the bandwidth achieved at 1 KHz is approximately 35 nm. Same bandwidth is achieved at 2 kHz, but from 3 kHz onwards drop in gain is observed and the bandwidth is halved.

A second mode-locking mechanism is required in order to achieve fast sweeping, at a rate inverse proportional to the roundtrip. Thus, we have switched back to configuration A. An exact resonant frequency of the ring is found by driving the SOA with a sinusoidal signal delivered by the Agilent 81160A RF generator, and watching the signal on the oscilloscope while varying the frequency of the signal applied. We found resonances starting at $f_R \approx 800$kHz, which then repeat at every multiple of f_R, that represents the inverse round trip time in the cavity for the central wavelength of the SOA. To make sure that this measurement is accurate, we switched again to position B and the SOA was driven with ramps at multiple of f_R, for instance using one of the VCOs. We have studied the dependence of the photo-detected signal output of the interferometer for 0.1 mm, versus the frequency of the ramps applied to the VCO input, and obtained the graph in Fig. 8.1.2.5. In other words,

the peak amplitude value of resonance was measured at a peak value of the sweeping rate of 800 kHz. The ramps have 100% symmetry (as set on the RFG) and therefore are meant to drive the optical frequency from large to small values.

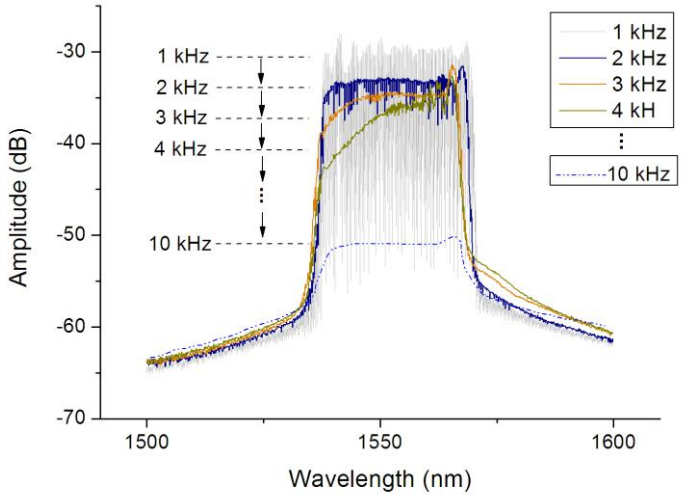

Fig. 8.1.2.4. Dynamic sweep optical output

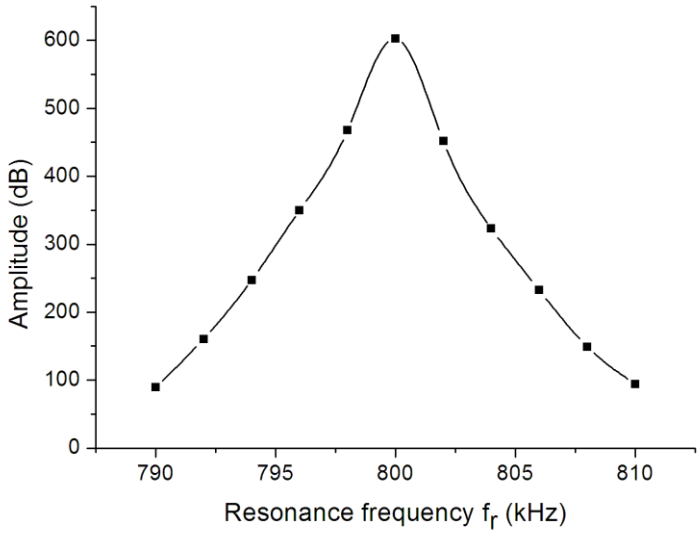

Fig. 8.1.2.5. Amplitude of the photo-detected signal versus the frequency of the ramps applied to the VCO

In order to be able to achieve the maximum sweeping rate, of 800 KHz, the amplitude of the ramp signal was raised to 10 V_{pp}.

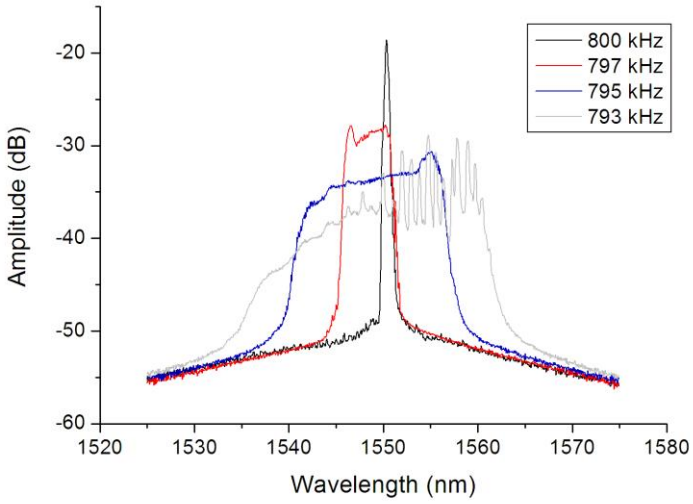

Fig. 8.1.2.6. Dynamic sweep characteristic at a mode-locking frequency f_m = 367.5 MHz, at several sweeping rates

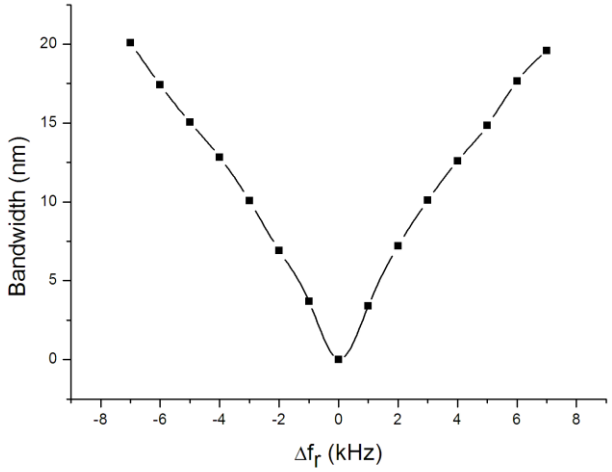

Fig. 8.1.2.7. Bandwidth versus the variation of sweeping rates around the resonance frequency of 800 kHz

For a mode-locking frequency of 367.5 MHz, at the sweeping rate of 795 KHz, we obtained an AKSS with a bandwidth $\Delta\lambda$ of 15.72 nm, as represented in Fig. 8.1.2.6. Without any optical amplification, the output power of the source is 1.1 mW. Using the SOA booster driven at 300 mA, we obtained an output power of 12 mW. The booster can deliver more power, but we stopped increasing the SOA current where the amplified spontaneous emission (ASE) had risen significantly.

While it was possible to tune the whole tuning bandwidth by plus minus 30 nm by modifying the bias applied to the VCO, it was not possible to achieve larger tuning bandwidths by driving the VCOs at 795 KHz. This is due to the limited tuning VCO bandwidth of 60 MHz for a swing of 10 V ramp applied at the maximum to its input. A simple calculation of 60 nm/15 nm = 4 shows that we would need a VCO with a 4 time larger frequency swing to achieve the available tuning bandwidth of 60 nm.

Another evaluation is that of frequency resolved points. This discussion makes distinction between the conventional drive of the dispersive cavity with a VCO tuned at a low frequency and between the dual locked regimes described here. In the first case, the RF frequency of the VCO is tuned within one locking band. In the dual locking regime, the VCO is tuned over many such locking bands.

The maximum deviation in frequency is f_m = 800 kHz, then at a sweeping frequency f_s =1 kHz, the number of resolved frequency points in the sweeping are $S = f_m/f_s = 800$. When driving the ring at f_R, the only way to maintain a large number of resolved frequency points is by jumping the optical frequency of the swept source from one band to the next, in steps of f_m. For the same number S, a deviation of frequency as high as $S \cdot f_m = 800 \cdot 800 \approx 640$ MHz. In other words, the optical frequency bounces over S mode-locking bands.

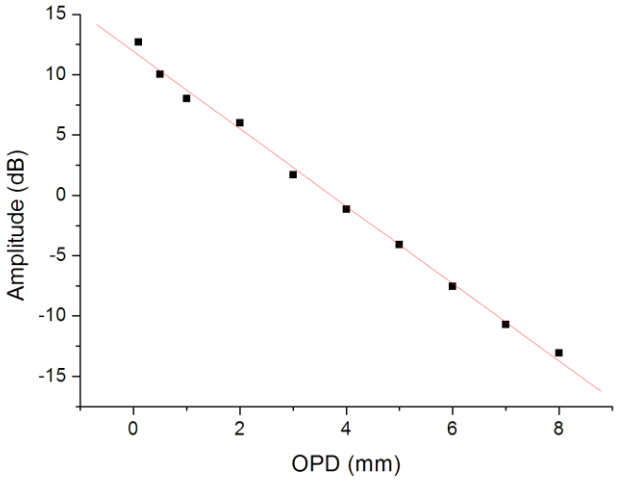

Fig. 8.1.2.8. Decay of modulation intensity with increasing OPD

Finally, we evaluated the AKSS mode-locked at 367.5 MHz, swept in frequency at 795 KHz, by scanning through the channeled spectrum of a Mach-Zehnder interferometer. By applying Fast Fourier Transformation (FFT) on the output signal for various values of

OPD, we have measured the FFT peaks and obtained the modulation intensity versus OPD, depicted in Fig. 8.1.2.8.

The sensitivity is calculated as $20 \cdot log(A_{OPD}/A_{noise})$, where A_{OPD} is considered the corresponding FFT peak amplitude value for the *OPD* close to "0", while A_{noise} represents the amplitude of the noised floor measured outside *OPD* [7]. For our AKSS a maximum sensitivity value of 93.32 dB was achieved without the booster and 95.5 dB with the booster at 12 mW.

An attenuation of 6 dB is obtained at OPD_{6dB} = 4.3 mm. Using as central wavelength λ_0 = 1550 nm, the graph in Fig. 8.1.2.8 leads to a 0.05 nm dynamic linewidth $\delta\lambda$.

A versatile electronically controlled dual mode-locked AKSS was demonstrated. As in other swept sources, using FP, MEMS, or polygon tuning filters, the recommendation for faster tuning rates is to reduce the cavity length. We presented here a configuration which uses a long DCF cavity length, in which case we implement the FDML principle, inspired by the step applied in the past when going from short cavity lengths using spectral tuning filters to resonant long cavity lengths. The SOA was driven at hundreds of MHz to produce mode-locking in the ring cavity, while the frequency of the electronic signal driving the SOA was swept at a rate inverse proportional to the cavity length.

Using such a DML configuration, operation at values around 800 kHz sweeping rate was demonstrated. Further optimization of the DCF length and the gain in the cavity was performed in order to achieve larger bandwidths and better sensitivity at large mode-locking frequencies. This will be presented in detail in the next chapters.

8.2. Ring cavity terminated on a Faraday Rotating Mirror

8.2.1. 1550 nm single mode-locked swept source

Configuration

The configuration of the AKSS experimented is shown in Fig. 8.2.1.1. This employs a SOA, model SOA-L-C-14-FCA (CIP 1, from BT), operating at 1550 nm, maximum current 500 mA and 3 dB bandwidth of 50 nm. The SOA is driven by a Thorlabs LDC 210C power supply. Temperature stability is ensured through thermo-electric cooling provided by a Thorlabs TEC 200C driver (sensor TH 20kΩ). The SOA is delimited by two polarization insensitive isolators I which ensure unidirectional lasing. The ring cavity also comprises a circulator CIR, which directs light through a 110 m length L_{DCF} of Draka Elite DDU1171023 DCF, with an anomalous dispersion parameter of -140 ps/nm·km at 1550 nm, terminated with a broadband Faraday rotating mirror (FRM), AFW, 60 nm bandwidth at 1550 nm. The total ring cavity length is approximately $L_{total} = L_{SMF} + 2 \cdot L_{DCF} = 255$ m.

Output power is drawn out through a 50/50 coupler and represents half of the light in the cavity further amplified by a similar type of SOA. The laser output characteristics of the swept source configuration are measured using an Agilent 86145B optical spectrum analyser (OSA), with a resolution of 60 pm. The coherence length of the source is evaluated by driving a Mach-Zehnder interferometer, terminated on a 50/50 coupler ending on a New Focus balanced detector model 1817, DC-80 MHz, 900-1700 nm bandwidth, whose output is displayed with a LeCroy Wave Runner 104 MXi-A 1GHz oscilloscope, with a sampling rate of 10 GS/s (10 Gyga Sample points per second).

As it can be observed, several changes were made from the initial setup. First of all, the 90/10 coupler was eliminated, as it was determined that a better trade-off between optical gain and output power is achieved using a 50/50 coupler instead. This is illustrated in Fig. 8.2.1.2. Also, the FRM was implemented, in order to cancel the polarisation effects in the cavity and also to halve the DCF length necessary in the cavity.

A switch with two positions, A and B, is used to drive the SOA in two regimes of operation. In position A, output from an HP8648C radio frequency signal generator (RFSG) swept synthesizer is used. In this regime, the excitation of signal frequency delivered by the

RF synthesizer is varied, to evaluate the static performance of the AKSS, in terms of its linewidth and tuning bandwidth.

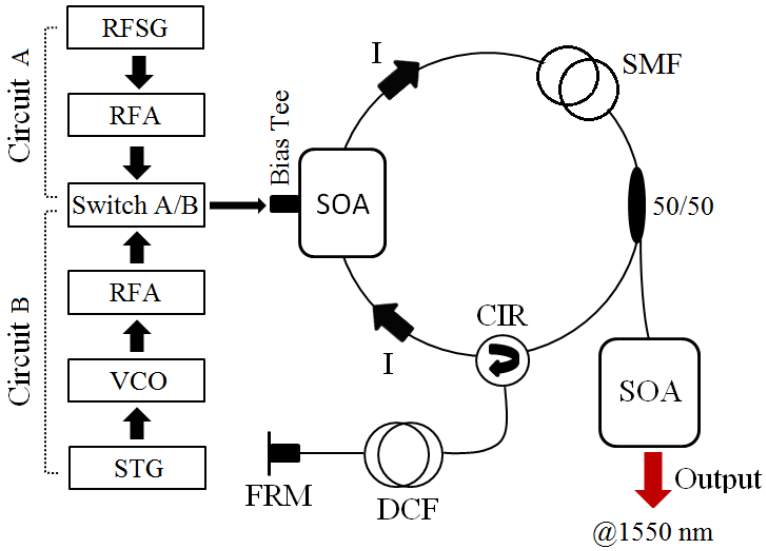

Fig. 8.2.1.1. AKSS configuration

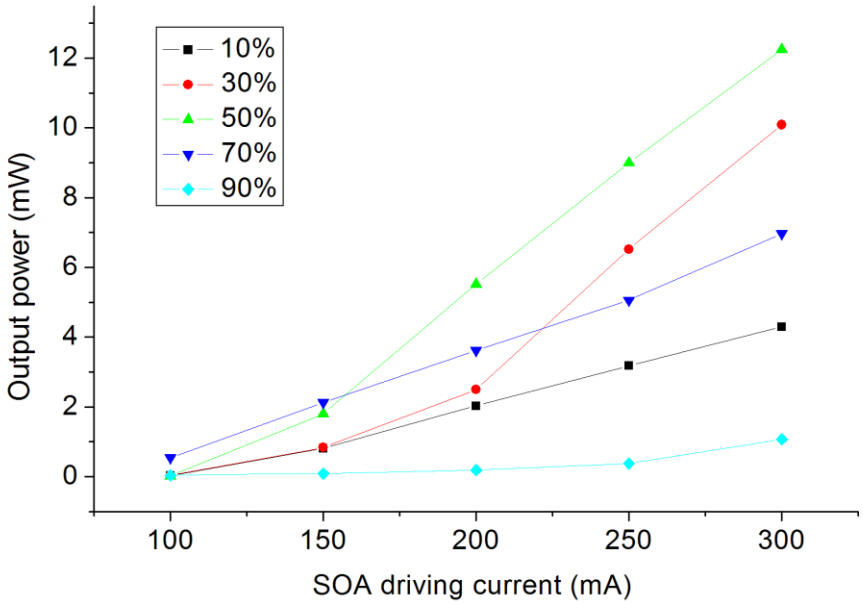

Fig. 8.2.1.2. Output optical power measured for measured for various couplers versus the driving current injected in the SOA

In position B of the switch, the AKSS is mode-locked according to the circuit B, which consists in a low noise voltage controlled oscillator (VCO, Mini Circuits ZX-928CA+) and a ZHL-42W Mini Circuits radio frequency amplifier, 26 dBm (RFA), that are used to drive the SOA with a 5 V amplitude sinusoidal signal applied to the SOA in series

with a 27 ohm resistor. The Agilent 81160A saw-tooth signal (STG) generator provides a saw-tooth signal with adjustable amplitude allowing a versatile control of the tuning bandwidth and of the central frequency of the VCO. In either positions of the switch, A or B, the RF signal is injected via a bias tee. Also by commuting to position B of the switch, the dual mode-locking RF mechanism is employed. The measurements and applications done using the DML mechanism will be detailed in the following chapters.

The principle involved is that of active mode-locking of a dispersive ring laser cavity. Dispersion is introduced by the DCF length. The rest of the ring is made of SMF, Corning 28e(R), dispersion parameter of ≤18 ps/nm/km at 1550 nm. Due to dispersion, the index of refraction depends on the optical frequency and therefore, f_R is different for different optical frequencies. By changing the frequency of the signal modulating the gain in the cavity, the optical frequency can be swept.

Parameter measurements

The total cavity length determines a total of -30 ps/nm anomalous dispersion in the system. First, the optical linewidth $\delta\lambda$ and tuning bandwidth $\Delta\lambda$ were evaluated by switching the switch to position A and operating in static regime, by manually changing the input RF frequency of the SOA driving signal. The best linewidth of 60 pm was achieved for mode-locking frequencies above 800 MHz, as shown by the graph depicted in Fig. 8.2.1.3. This value matches the resolution of the OSA used, of 60 pm, meaning that the linewidth is better than the one measured.

After that the system is switched to the position B. By changing the DC value of the signal delivered by the pulse generator, the central frequency f_m of the VCO is tuned statically. Sweeping rates achieved are no more than 100 kHz. The 3 dB bandwidth achieved at 1 kHz is approximately 60 nm. The decay of the optical output as the sweeping speed increases is illustrated in Fig. 8.2.1.4, and it can be noticed that by using the first mode-locking mechanism alone it is not possible to achieve high sweeping rates. Even with short lengths of the cavity, of a couple of meters, we could not achieve sweeping rates larger than 100 kHz, as predicted by [7], i.e. the decay of power with the sweeping rate is not due to the long length of fibre used. Nevertheless, if we compare the bandwidth and the sweeping rates achieved for the laser employing FRM presented here, they are considerably better than the ones presented in chapter 8.1.2. The bandwidth $\Delta\lambda$ is nearly doubled, while the maximum f_R is nearly 10 times larger than previously.

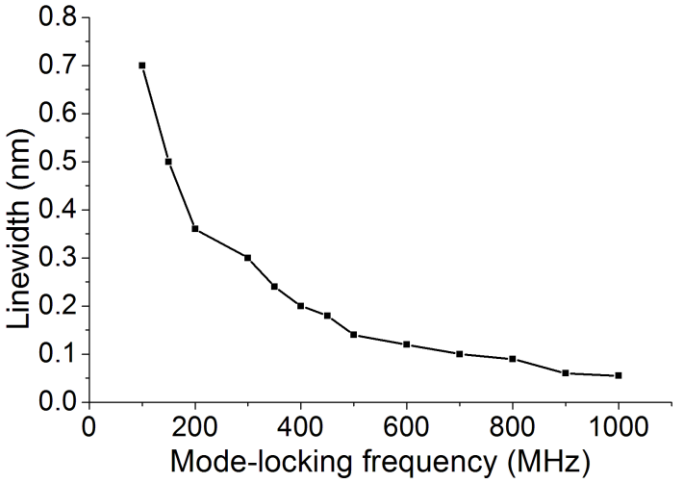

Fig. 8.2.1.3. Linewidth versus mode-locking frequency in the static regime (A)

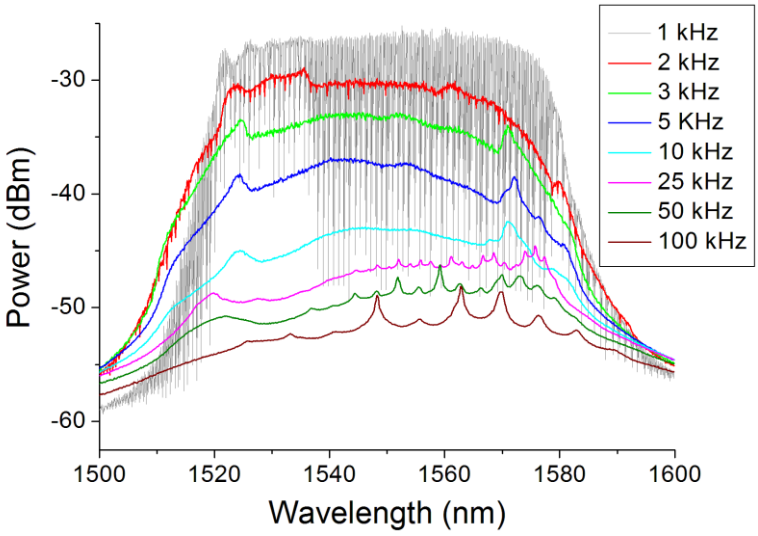

Fig. 8.2.1.4. Dynamic sweep optical output using the 1st mode-locking mechanism only

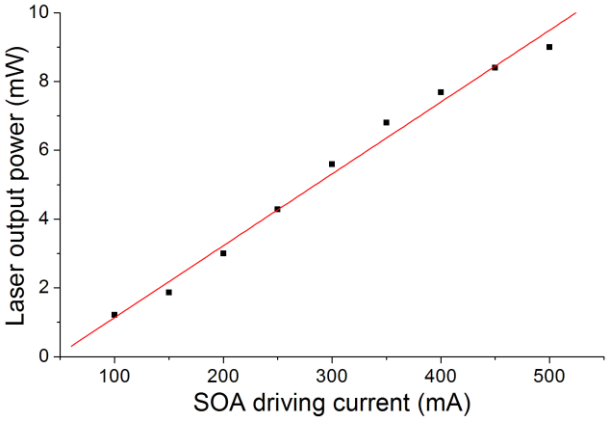

Fig. 8.2.1.5. The laser cavity 50% output power versus the SOA driving current

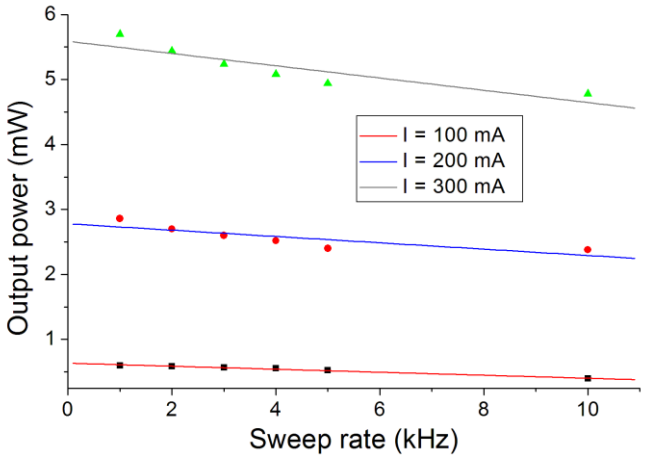

Fig. 8.2.1.6. The laser output power decay versus the sweep rate, for 3 different SOA driving currents

Without any modulation of the gain in the cavity, the maximum output power measurable for a current of 500 mA at the 50% output is 9.4 mW, as determined from the Fig. 8.2.1.5 (left). Driving the SOA at currents above 300 mA determines an increase in the ASE of the AKSS optical output. The laser output power decay for 100 mA, 200 mA, and respectively, 300 mA, versus the increasing sweep rate from 1 kHz to 10 kHz is represented in Fig, 8.2.1.6.

8.2.2. 1550 nm dual mode-locked swept source

In continuation, we have tested the dual mode-locking operation on the swept source described in Chapter 8.2.1 and illustrated in Fig. 8.2.1.1.

As mentioned in the previous chapter, the total cavity length determines a total of -30 ps/nm anomalous dispersion value in the system and the best linewidth of 60 pm was measured for mode-locking frequencies f_m greater than 800 MHz. The system was switched to the position B. Sweeping rates achieved were no more than 100 kHz, while the 3 dB bandwidth achieved at 1 kHz is approximately 60 nm.

Initially, the cavity length is adjusted to a value which determines f_R = 782 kHz and the VCO is driven with a signal of frequency f_m in the range 360-420 MHz. When the signal applied from the synthesizer to the VCO is swept at a sweeping rate of $f_S = f_R$, then the VCO spectrum consists in a comb of frequencies $f_m \pm f_R$, $f_m \pm 2f_R$, $f_m \pm 3f_R$ and so on, i.e. in 782 kHz steps. The resulting RF signal from the VCO is amplified and injected into the SOA gain medium of the AKSS. This generates a narrow band laser output, having a linewidth $\delta\lambda$ and f_R repetition rate. If $f_S = f_R$, no tuning is noticed. To perform tuning, sweeping needs to be performed at a detuned rate from f_R. Here is where the difference between the regime used and the one used in FDML [5] lasers comes from. Therefore, $f_S = f_R \pm \delta f_R$, in which case the VCO is tuned with a comb spectrum consisting in f_m, $f_m + f_R \pm \delta f_R$, $f_m + 2f_R \pm 2\delta f_R$, $f_m + 3f_R \pm 3\delta f_R$ and so on.

Therefore, for the ring cavity length considered, the tuning bandwidth is measured for several values of detuning, δf_R. The results are presented in Fig. 8.2.2.1. The larger the detuning, δf_R, less is the output power.

The cavity coefficient defined in equation (6.1 – 1) is evaluated from the slope $m = \delta\lambda \cdot N \cdot C_m$ calculated from the left graph illustrated in Fig. 8.2.2.1 (blue dashed line) as 18.72 nm/kHz.

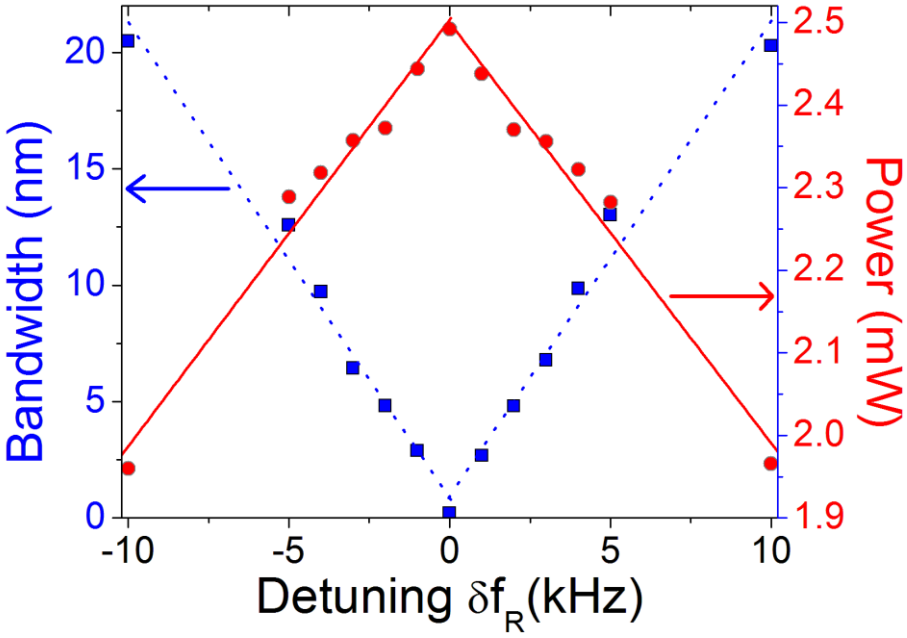

Fig. 8.2.2.1. DML AKSS tuning bandwidth (blue dotted line) and output power versus detuning (red solid line)

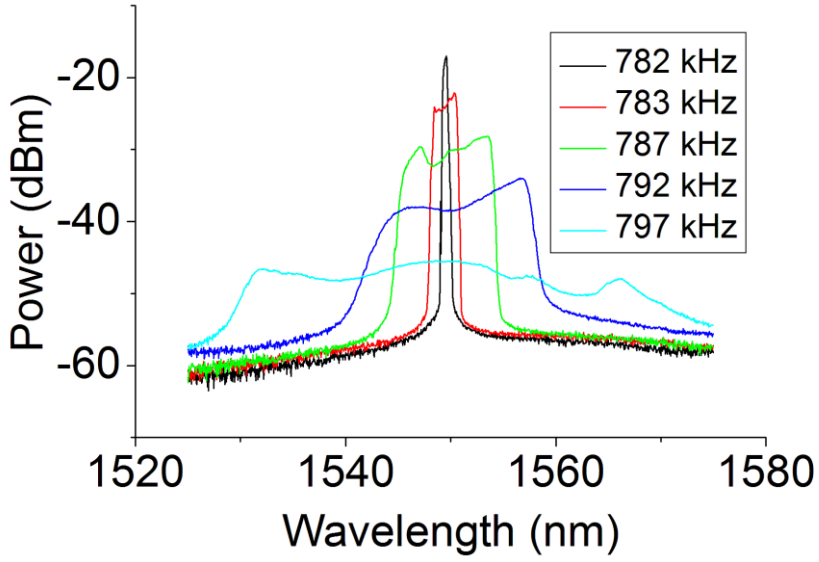

Fig. 8.2.2.2. DML optical spectrum in the dynamic regime for a cavity length determining an f_R = 782 kHz, for detuning δf_R = +1, +5, +10 and +15 kHz, respectively

Fig. 8.2.2.2 represents more explicitly the effects of the DML mechanism applied to the AKSS ring. When the frequency of the signal driving the VCO is swept at a rate $f_S = f_R$ = 782 kHz a narrow laser emission results. For a sweeping rate of $f_S = f_R+1$ = 783 kHz, the VCO is tuned from f_m to f_m+f_R+1 kHz, to f_m+2f_R+2 kHz, to f_m+3f_R+3kHz and so on, in the 880-940 MHz range, in 783 kHz steps. The emitted spectrum consists in a tooth comb having

a linewidth of 60 pm and a repetition rate of 783 kHz. For a sweeping rate of $f_S = f_R+5 = 787$ kHz, the VCO is tuned from f_m to f_m+f_R+5 kHz, to f_m+2f_R+10 kHz, to f_m+3f_R+15kHz and so on, in the 880-940 MHz range, in 787 kHz steps. The emitted spectrum consists in a tooth comb having a linewidth of 60 pm and a repetition rate of 787 kHz. Similar reasoning can be applied to each value of δf_R. Comparing with the results achieved before the FRM was employed in the cavity and presented in chapter 8.1.2, the bandwidths achieved are similar, but in the present case, there are no more ripples in the spectrum observed at larger detuning values.

The temporal output signal (mode-locking pulses) measured using a Newport 1611 1 GHz photodetector, for several values of detuning is represented in Fig. 8.2.2.3. There is a slow decrease in power until 10 kHz detuning.

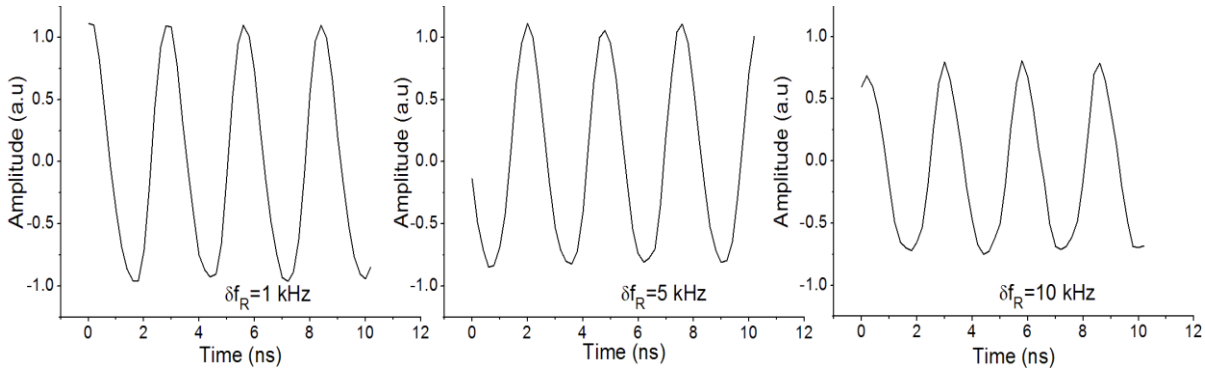

Fig. 8.2.2.3. Dynamic output measured for δf_R = 1 kHz, 5 kHz, and respectively, 10 KHz

For a mode-locking frequency of 920.4 MHz, at the sweeping rate of 792 KHz (10 kHz detuning from f_R), we obtained a tuning bandwidth of 15.82 nm, as shown in Fig. 8.2.2.2. Without any optical amplification, the output power of the source is 2.3 mW. Using the SOA booster driven at 300 mA, an output power of 12.8 mW is measured. The booster can deliver more power; however a trade-off is established between output power and percentage of amplified spontaneous emission (ASE).

The dependence of the optical output power and tuning bandwidth on the RF tuning range is depicted in Fig. 8.2.2.4, for two values of detuning, 5 kHz, and 10 KHz. The variation of tuning bandwidth with amplitude represents an expansion of the number of frequency resolved points in the tuned spectrum. For the same δf_R detuning value, there is a slight decrease in power as the VCO tuning range ΔF increases, while the bandwidth exhibits a significant increase.

The graphs depicted in Fig. 8.2.2.4 confirm equation (6.1 – 1). For constant f_R, C_m and $\delta\lambda$ values, the tuning bandwidth is proportional to the detuning δf_R. For example, for a 5 Vpp signal driving the VCO, corresponding to ΔF = 30 MHz, a $\Delta\lambda$ value of 7.86 nm is measured for δf_R = 5 kHz, and respectively 15.24 nm at 10 kHz. This discussion makes distinction between the conventional drive of a dispersive cavity with a VCO tuned at a low frequency and the DML regimes described here. In the first case, the RF frequency of the VCO is tuned within one locking band. In the DML regime, the VCO is tuned over many such locking bands, separated by f_R.

The DML tuning mechanism is also verified at multiple values of f_R. Equation (6.1 – 1) suggests that the tuning bandwidth, $\Delta\lambda$, is inverse proportional to f_R. For a 5.3 Vpp signal driving the VCO, a 15.75 nm $\Delta\lambda$ value is measured for a δf_R = 10 kHz detuning from f_R. For the same detuning, by modulating the VCO at sweeping rates of $2f_R$ (1.564 MHz), $3f_R$ (2.346 MHz), $4f_R$ (3.128 MHz) and $5f_R$ (3.910 MHz) we measured $\Delta\lambda$ as 7.9 nm, 5.5 nm, 4.2 nm and, respectively, 3.2 nm, fact that confirms the theoretical hypothesis. The proportional reduction in the tuning bandwidth is accompanied by insignificant power variation.

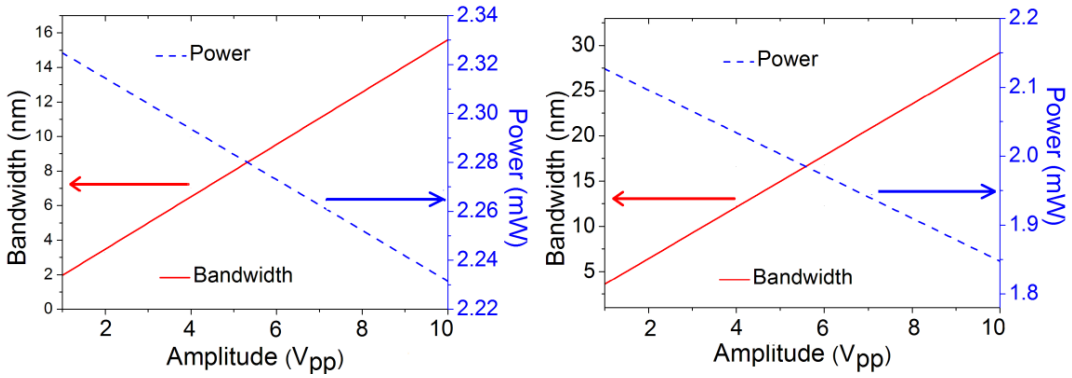

Fig. 8.2.2.4. AKSS optical output power (dashed blue line) and tuning bandwidth (solid red line) versus the amplitude of the ramp applied to the VCO input for a detuning of 5 kHz (left), respectively 10 kHz (right)

The spectrum of the RF signal of a carrier f_m when swept in frequency at a rate fs consists in a comb of frequencies separated by fs. The number of resolved frequency points within the spectrum, S, is given by the maximum frequency deviation, ΔF, divided by f_S. ΔF depends on the voltage applied to the tuning input of the synthesizer, when the switch in Fig. 1 is on A or to the input of the VCO when the switch is on B. If fs = 1 kHz, as ΔF is less than f_R = 782 kHz, maximum achievable for S would be 782. When driving the AKSS at a much

larger frequency f_R, the only way to maintain a large number of resolved frequency points is to jump the optical frequency of the swept source from one tuning band to the next, in steps of f_R. In the DML regime, a deviation of frequency as high as $S \cdot f_R = 782 \cdot 782 = 611.52$ MHz would therefore be needed.

The relative intensity noise (RIN) measurement requires a special study, in the same way a whole paper was dedicated to RIN in FDML [8]. There are some interesting peculiarities in translating the methods described in this paper into the DML AKSS that deserve a separate study. The laser is pulsed at the rate of RF mode-locking, and this presents a problem in measurement, as an average over several mode locked pulses is required, which equivalently translates in an average over a small window within the tuned spectrum.

The laser output was measured with a broadband Newport 1611 Indium Gallium Arsenium (InGaAs) Photoreceiver, 900-1700 nm, 30 kHz to 1 GHz (mentioned in the text already) and displayed in real time with a LeCroy 104Mxi-A oscilloscope (10 Gyga Samples/s). As described [8], there are two types of measurements, sliding-RIN and ortho-RIN. As commented [8], by increasing the numbers of samples in the sliding-RIN, this approaches the values of the ortho-RIN. Therefore, measuring the ortho-RIN should suffice. In the first instance we have registered 100 neighbouring photo-detected samples and determined the average of the mean power of a selected interval of 50 ns out of 1.28 μs of each sweep. Ortho-RIN was measured by calculating the standard deviation for 100 neighbouring samples (temporal profiles) at the same time interval (50 ns) within each sweep. For 1 mW output power we obtained for a detuning of 1 kHz 1.4%, for 5 kHz 1.65% and for 10 kHz 6.37%. Using a bandwidth of 1 GHz, these translate into RIN values of -127.1 dBc/Hz, -125.65 dBc/Hz and –113.91dBc/Hz respectively.

Next, we evaluated the dynamic linewidth $\delta\lambda$ of the DML AKSS, as the inverse of this parameter determines the axial range in OCT. A 255 m length AKSS cavity, mode locked at 920.7 MHz, swept in frequency at around 787 kHz and using the maximum $\Delta F =$ 60 MHz deviation achievable by driving the VCO at 10 V, is connected to a Mach-Zehnder interferometer. By applying a Fast Fourier Transformation (FFT) oscilloscope function on the output signal measured by the detector and displayed on the oscilloscope, for various values of optical path difference (*OPD*), we have measured the FFT peaks and obtained the modulation intensity versus *OPD*, as depicted in Fig. 8.2.2.5. The sensitivity *S* is given by $20 \cdot log(A_{OPD}/A_{noise})$, where A_{OPD} represents the corresponding FFT peak amplitude value for the chosen *OPD*, while A_{noise} is the amplitude of the noise floor measured outside the FFT peak [3]. A sensitivity value of 91.12 dB, (>90 dB is generally accepted as a good value in

OCT imaging applications), is obtained for an *OPD* value close to "0". Assuming a Gaussian shape for the tuning spectrum, and using the *OPD* value measured at 6dB decay (OPD_{6dB}) from Fig. 8.2.2.5 of 0.75 mm, this leads to a dynamic linewidth $\delta\lambda = \lambda^2/4 \cdot OPD_{6dB} = 0.8$ nm. In terms of tuning linearity, the width of the A-scan peaks obtained by FFT has shown insignificant change with the *OPD*, which represents an increase of only 0.4% at *OPD* = 5 mm, in comparison with the width of the A-scan peak at an *OPD* close to zero, as represented in Fig. 8.2.2.6. This suggests sufficient tuning linearity in optical frequency, i.e. no data resampling is needed when decoding the spectrum modulation.

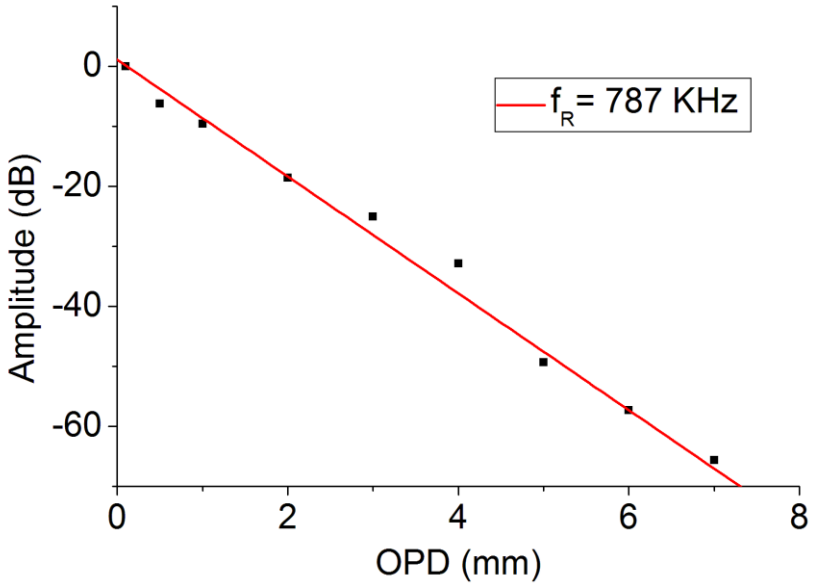

Fig. 8.2.2.5. Decay of modulation intensity with increasing OPD

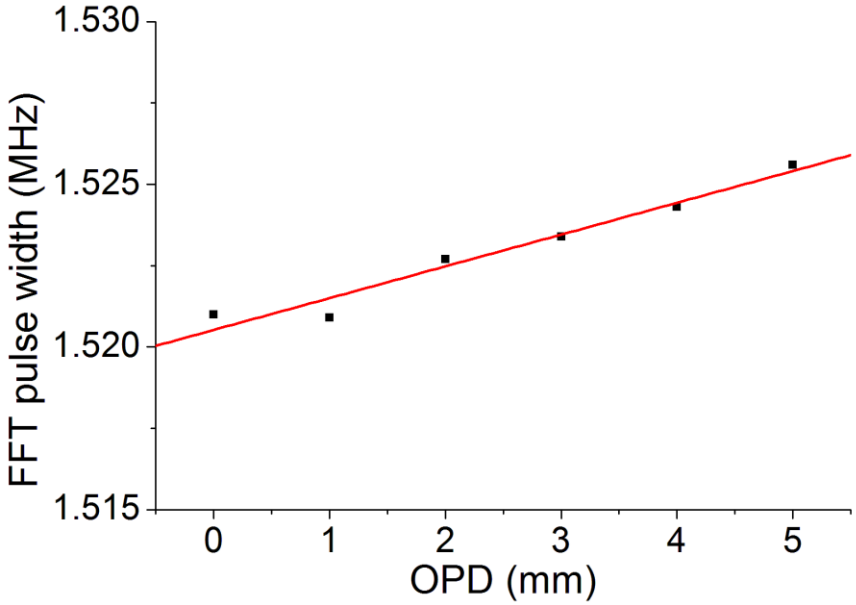

Fig. 8.2.2.6. A-scan pulse width versus OPD

Summing up, we can conclude that by using the DML principle, sweeping rates in the range of MHz are achievable, from a rate values of f_R = 782 kHz to up to 5 multiples of f_R, with a proportional decrease in the tuning bandwidth. Further optimization of the RF excitation can lead to larger tuning bandwidths and better sensitivity values. The DML mechanism allows MHz rates to be obtained directly, with no buffering [9], reducing the cost and complexity in producing a swept source.

8.3. 1550 nm AKSS-OCT application

While with the initial configuration of AKSS at 1550 nm, described in the chapter 8.1, we were not able to achieve good quality OCT images, a significant improvement was observed after integrating the FRM in the cavity; by connecting the upgraded AKSS to a classical OCT interferometer, as depicted in Fig. 8.3.1 we have managed to obtain a series of topographic images of pressure sensitive adhesive (as illustrated in Fig. 8.3.2) and other non-biological thin samples, like paper, transparent pressure sensitive tape (sellotape, as depicted in Fig. 8.3.3), superposed layers of the same type tape or thin glass slides. Further improvements in terms of instantaneous linewidth and power should determine a better penetration in depth.

The 1550 nm OCT system used in acquiring the A-scans and B-scans comprises the following elements: as optical source, the 1550 nm FRM based AKSS, connected to a Booster, SOA-L-C-14-FCA (CIP1 from BT), electronically controlled, or the Amonics Fibre Optical Amplifier (model AEDFA-PA-35-B-FA); the output from the booster is then connected to the broadband coupler which directs equal proportions of optical power towards both the reference and object arms. The light waves travelling in both the reference arm and object arm are collimated at the output of the 50/50 coupler. The reference arm comprises an assembly of two mirrors placed on a z-axis Newport motorized translation stage, capable of micrometric stepping. By using this assembly, the OPD can be adjusted in steps controlled by the translation stage displacement Z (where $OPD = 2 \cdot Z$). The object arm comprises a beam splitter (BS) which delivers 50% of the light to the sample assembly, comprising a galvo-scanner (GS) operated at a frequency of 10 Hz and low amplitude, a f = 20 mm (focal length) achromatic doublet lens and the sample. The distance between the GS and the lens and between the lens and the object is equal to the focal length f = 20 mm of the doublet. The light coming back from the object reaches the BS and 50% of it is redirected to a 50/50 coupler where it interferes with the light that passed through the reference arm. The interferometer ends with a balanced photo-detector.

The images were acquired using a computer fitted with a suitable LabView board which relays the data to a custom made LabVIEW software developed in the Applied Optics Group by Dr. Adrian Bradu. The AKSS was mode-locked at f_m = 920.7 MHz, having a 60 pm linewidth (measured in static regime), a measured bandwidth of approximately 60 nm, 1 kHz repetition rate, and 1 mW output power. For the imaging depicted in Fig. 8.3.2, the

SOA-L-C-14-FCA booster (CIP1 from BT) was used, obtaining a total optical power at the input of the OCT setup of approximately 8 mW. Respectively, for the imaging acquired and represented in Fig. 8.3.3, the Amonics Fibre Optical Amplifier was utilized, raising the total optical power at the input of the OCT system at approximately 10 mW. Due to losses in the system generated by injection in the fibres, the beam-splitter, the couplers and absorption in the object, only 17.9% of the initial power in the system is measured before entering the balanced detector, New Focus balanced detector model 1817, DC-80 MHz, 900-1700 nm bandwidth.

No software post processing or software averaging of images was performed. Also, no electronic gain was applied in the Lab View software application used to acquire the B-scans.

As illustrated in the figures 8.3.2 and 8.3.3 bellow, at 5 mm OPD the B-scans illustrating the topographical features of the pressure sensitive adhesive (better known as blutack), and respectively transparent pressure sensitive adhesive (more commonly known as sellotape) samples are faint. After this OPD value, we were not able to acquire further images, therefore the axial range of the AKSS needs improving in the future.

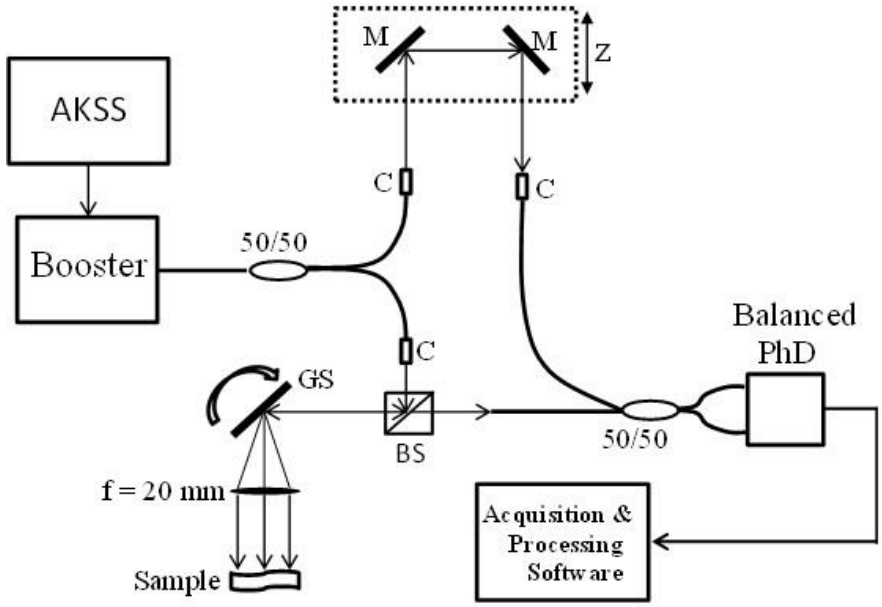

Fig. 8.3.1. 1550 nm OCT system, where C represents collimating assembly, M represents mirror and PhD represents photo-detector

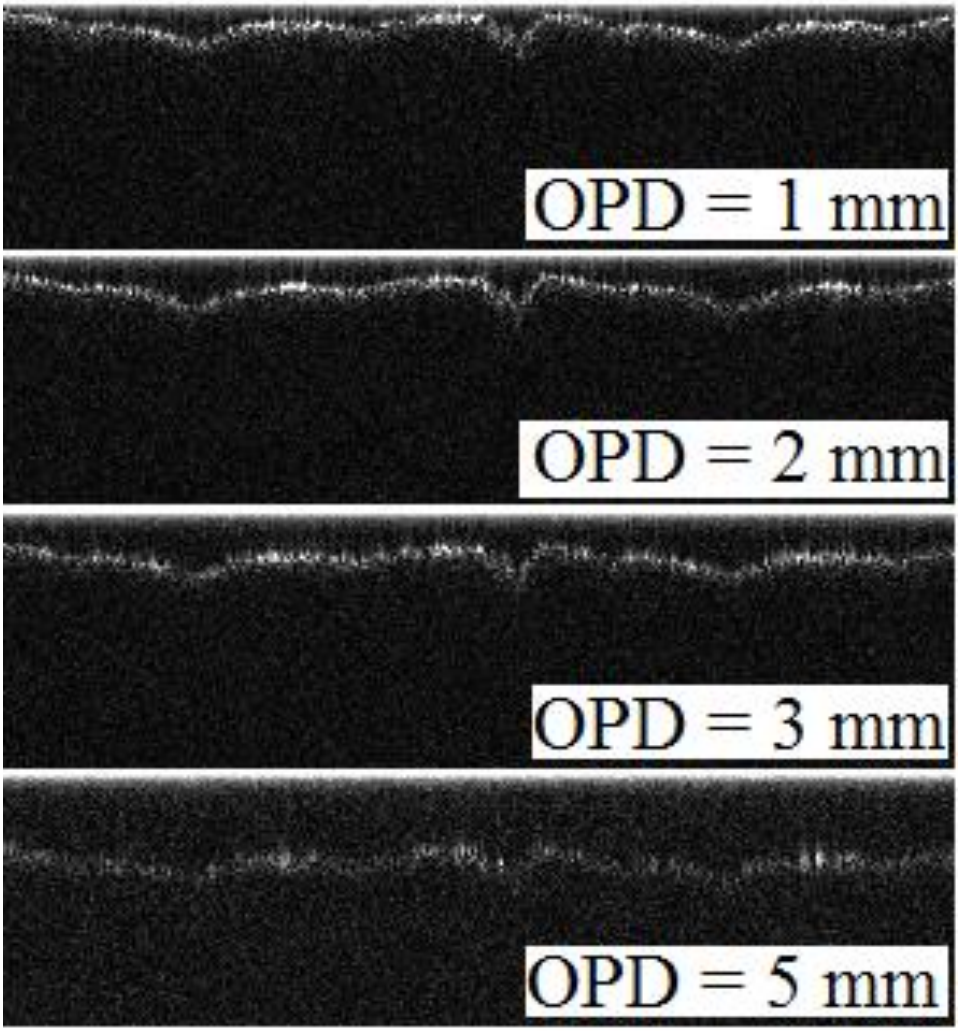

Fig.8.3.2. Topographic OCT image of pressure sensitive adhesive acquired at several OPD values

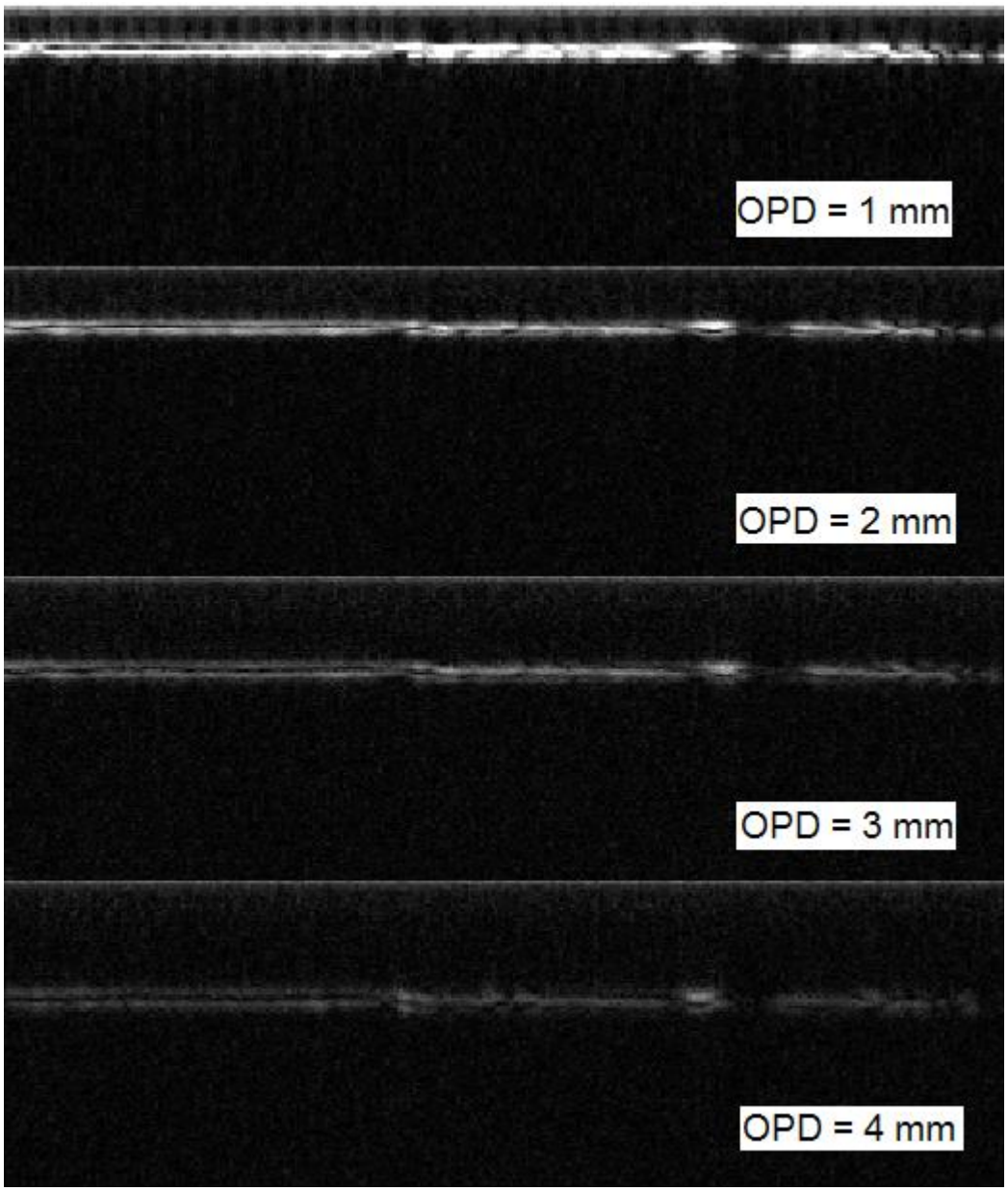

Fig.8.3.3. In depth OCT images of a thin film of adhesive tape acquired at several OPD values

8.4. Proposed application on measuring whispering gallery modes

The AKSS described in the Chapter 8.1, is also proposed as a viable tool in the characterisation of microresonators written in glass, by identifying the optical resonances (whispering gallery modes) and by evaluating other important optical properties, like the dispersion variation in glass. The relatively low power of the AKSS eliminates the potential temperature induced shifts in resonance patterns in a microresonator or any forms of thermal damage, especially in element doped resonators. The high repetition rates of at least 800 kHz (or multiples of this value) and the broadband output of the AKSS allow a fast and, respectively, a wide band characterisation around the 1550 nm central wavelength.

In continuation, we will introduce a brief theoretical description of microresonators and whispering gallery modes and also a classification of different types of microresonators.

8.4.1. Whispering gallery modes

The whispering gallery modes (WGM) are specific resonances of a wave field that are confined inside a given resonating cavity that are based on total internal reflection. The optical WGM present a lot of interest due to their practical properties. The microresonators designed and used to generate such optical resonances generally exhibit extremely high quality factors (Q-factors), low mode volumes, small size, and the possibility of operation in wavelengths of high interest (telecommunications for example). With the right technology (CO_2 laser shaping [10], filament based glass processing [11], chemical depositions [12] etc.) and perhaps environment (clean room facilities), fabrication of the on-chip integrated microresonators is versatile and quite straight forward.

In continuation, a brief theoretical description is presented, regarding WGM, resonance performance parameters, coupling WGM to resonators, and classification of the types of microresonators. This description insists on the particular case of microresonators embedded in SiO_2 glass [13].

The WGM were first discovered and theorised by John William Strutt (Lord Rayleigh), at the beginning of the XXth century, who revised a previous misconception that whispers could be heard across the St. Paul's Cathedral dome, London, but not at any intermediate position. He explained the phenomenon of the travelling whispers as a series of reflected sound rays making up chords of the circular gallery. From this point onwards, any

circular, hemispherical, elliptical or ellipsoidal enclosure often situated beneath a dome or a vault, in which whispers can be heard clearly in other parts of its walls, was defined as whispering gallery.

Nowadays, the notion of WGM was adopted in optics, in order to describe the wave propagation and light confinement by total internal reflection of light in various types of microresonators [14]. Such optical components are generally small in size, ranging from a few microns to nearly 1 mm, relatively easy to produce using either optical or chemical methods, and they represent an attractive solution applied in telecommunication devices [15], optical multiplexing [16], particle detection [17], biological investigation of viruses [18] and many more.

The WGM are explained by the general scalar wave theory. The WGM modes are commonly imagined as rays having a closed trajectory and being confined within the cavity by total reflections along the curved resonator surface.

Optimization of the coupling efficiency between the microresonator and a range of optical waveguides (fibre tapers, prisms) was investigated in several publications [19, 20]. Overall, the use of tapered fibre (<10 microns in diameter) is considered to be one of the most flexible coupling means. The material used in the design and execution of a microresonator determines if this device is either passive (if for example it is used as a narrow or broad band frequency filter) or active (if for example it is used as active medium in a microlaser). If the microresonator is further coated with specific types of composite layers or fabricated with a certain element within its structure, more tuning is achieved in terms of thermodynamic and optical properties. In this respect, several rare-earth-doped and Raman micro lasers with very low threshold have been demonstrated [21, 22].

In order to couple light in or out of the microresonator, it is necessary to use the overlapping of the evanescent field of the whispering gallery modes with the evanescent field of a phase-matched optical waveguide. The waves are totally internally reflected and focused by the surface. Due to minimal reflection losses these modes can reach high quality factors (*Q-factors*).

The resonator *Q-factor* of a resonator represents a measure of the strength of the damping its resonating oscillations, or for the relative linewidth. The term was originally developed for electronic circuits and for microwave cavities, but recently also became common in the context of optical resonators.

$$Q - factor = \omega_0 \frac{Stored\ energy}{Power\ loss} = \omega_0 \tau = \frac{\omega_0}{\Delta\omega_{FWHM}}, \quad (8.4-1)$$

where $\omega_0 = 2\pi\nu_0$ is the angular frequency, ν_0 is the resonance frequency, τ is the cavity lifetime. It is generally considered that *Q-factors* between 10^3 and 10^6 are high, while values above 10^7 are ultra-high. The equation (8.4 – 1) for the *Q-factor* can be interpreted in the following ways: the *Q-factor* measures the characteristic time for the exponential decay of the energy stored inside the resonator in terms of the number of full field oscillations, multiplied by 2π, thus, the larger in value the *Q-factor*, the longer the time in which the energy is stored within the resonator; on the other hand, the total energy of the circulating modes inside the resonator in a state of equilibrium is divided by the amount of energy that is injected in the resonator in the time of one full field oscillation. For a higher *Q-factor,* the total field intensity of the circulating modes is proportionally higher at the same pumping power.

Considering the case of a spherical resonator, the value of the *Q-factor* is influenced by several loss mechanisms, as suggested by the following expression:

$$Q_{int}^{-1} = Q_{mat}^{-1} + Q_{surf}^{-1} + Q_{sct}^{-1} + Q_{bd}^{-1}, \quad (8.4-2)$$

where Q_{mat} represents the intrinsic material absorption, Q_{surf} defines the surface absorption losses generated by the possible coating or particle contamination, Q_{sct} represents the scattering losses (mainly Rayleigh scattering) generated by the structural imperfections of the surface, and Q_{bd} describes the bending loss. The bending loss appears when the total internal reflection at a curved interface is incomplete and corresponds to a loss of energy in the case of a specific WGM. Q_{bd} is strongly dependent on *R*, the microresonator radius for a fixed wavelength.

The total *Q-factor* results from:

$$\frac{1}{Q_{tot}} = \frac{1}{Q_{int}} + \frac{1}{Q_{ext}}, \quad (8.4-3)$$

where Q_{ext} represents the contribution determined by the losses due to coupling of the resonator to an external mode.

Another important parameter that defines the microresonator performance is the finesse, noted from this point onwards as *Fin*, defined as the ratio between the spectral range *(SR)* and the resonance FWHM linewidth:

$$Fin = \frac{\Delta\omega_{SR}}{\Delta\omega_{FWHM}} = Q\frac{\Delta\omega_{SR}}{\omega_0} < Q \qquad (8.4-4)$$

While the $\Delta\omega_{SR}$ represents the distance between resonant peaks, the finesse is measured in order to determine the distance between the resonant peaks in terms of the number of FWHM linewidths that are exhibited between two consecutive resonant peaks. Generally, most resonators have relatively equidistant resonance values. The finesse thus gives important information regarding the effective resolution of the resonator. As illustrated in equation (8.4 – 4), *Fin* is proportional with the *Q-factor*.

The resonator mode volume V_{eff} is defined as the ratio of the total energy captured inside the resonator in a specific WGM and the maximum energy density of that mode:

$$V_{eff} = \frac{Enenrgy}{Max.energy\ density} = \frac{\int_V w(\vec{r})d^3\vec{r}}{max(w(\vec{r}))}, \qquad (8.4-5)$$

determined for the electromagnetic field *w* given by the following expression:

$$w(\vec{r}) = \frac{1}{2}\left(\varepsilon_0\varepsilon(\vec{r})\left|\vec{E}(\vec{r})\right|^2 + \frac{1}{\mu_0\mu(\vec{r})}\left|\vec{B}(\vec{r})\right|^2\right), \qquad (8.4-6)$$

where $\varepsilon_0\varepsilon(\vec{r})$ represents the total electric permittivity, $\mu_0\mu(\vec{r})$ the total magnetic permeability, $\vec{E}(\vec{r})$ the electrical field, and $\vec{B}(\vec{r})$ the magnetic field.

While for a resonator it is desirable to have *Q-factors* and *Fin* values as high as possible, small V_{eff} values as possible are expected.

8.4.2. Types of microresonators

WGM microresoantors typically have very high Q-factors and finesses at very low mode volumes. Their monolithic design is extremely efficient and can represent a viable alternative to the classical FP resonators, since they do not require any external mirrors or reflective optical fibre devices, like fibre Bragg gratings, to confine light. In continuation, a very brief description of the main types of microresonators, advantages and methods of fabrication will be illustrated.

Sphere resonator

One of the simplest microresonator geometries supporting WGM is a dielectric sphere with a refractive index higher than the surrounding environment (air or aqueous solution). The light wave trapped by the sphere resonator is continuously reflected back inside the sphere by total internal reflection at the cavity-air interface.

One of the first demonstrated optical microresonator is a liquid droplet with a near perfect spherical surface due to surface tension [23]. These droplets are impractical though, because they tend to evaporate and they are difficult to control. Therefore, the resonators based on solid materials (especially coated or types of ion doped glass) are more reliable and stable. Reproducible size and shape of the microsphere has been demonstrated with sphere *Q-factors* in the order of $10^9 – 10^{11}$.

Figure 8.4.2.1 depicts a spherical fused silica SiO_2 microresonator designed in the AOG and realised using the Vytran GPX34000 glass processing technology, through filament thermal shaping in iterative steps. The resonator was coupled in air between two parallel 10 μm fibre tapers. In this particular case, the resonator is meant to act as a filter. A broadband wave is transmitted through one taper channel, the light that is coupled into the microresonator is after that released in the other channel.

Other technologies of producing resonators rely on thermal shaping using CO_2 lasers [10]. The advantage of the spherical solid state resonators is that they are easily reproducible and they exhibit superior properties in terms of Q-factor and finesse.

At the moment, the spherical fused silica resonators designed to trap light in the visible range at a central wavelength of 633 nm (red) hold a record in terms of Q-factor,

$8 \cdot 10^9$, while in the invisible range, a crystalline cadmium fluoride (CaF_2) resonator has achieved a Q-factor of $3 \cdot 10^{11}$, in the telecom wavelength range, 1550 nm.

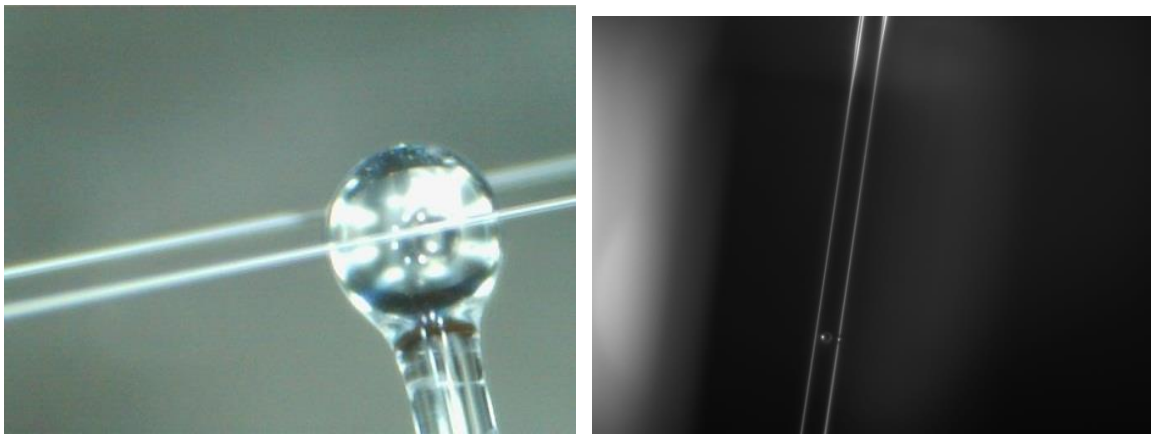

Fig. 8.4.2.1. Spherical silica micoresonator realised in the AOG using the Vytran glass processing technology, interfaced with two 10 µm tapered fibres viewed from lateral (left) and from above (right)

Disk resonator

The dielectric disks or cylinders are less efficient than the spherical microresonator. The polar curvature of a sphere confines and directs light, even if the light is not coupled around the equator. In the disk resonator, the beam can easily escape if it is sufficiently perturbed from propagating around the equator. Therefore, the disk resonators are known to exhibit reduced Q-factor, the best values being around 10^4 [24]. On the other hand, they are easier to fabricate and to integrate into chips or arrays and they have smaller mode volumes.

There are several methods used to fabricate such resonators: deep ultraviolet lithography, electron beam lithography and nano-imprinting lithography.

Toroid microresonator

A toroid microresonator [25] is made from a dielectric material (generally fused silica) in the shape of a solid toroid. The light waves can circulate by continuously bouncing off the toroid-air interface by total internal reflection. Such resonators are produced in two steps: first, the bulk material is removed by etching until the incipient shape of a toroid is achieved; after that, a CO_2 laser is used to smooth the edges and to produce the final shape of the

resonator. Such resonators are practical, because they can be easily integrated in optical chip circuits and also exhibit ultra-high Q-factor values, of the 10^8 order.

Bottle shape microresonator

An optical bottle resonator is produced from a silica optical fibre. Light coupled into this type of resonator is radially confined by continuous total internal reflection, but in addition axial confinement is achieved by the gradually changing thickness of the optical fibre.

The main advantage of such resonators is the ease of fabrication, by heating and stretching the optical fibre. Fig. 8.4.2.2 illustrates an example of such a resonator designed in the AOG, using the filament technology of the Vytran GPX – 3400 fibre glass processing equipment. The possibility to achieve ultra-high Q-factors (10^8) represents also an important characteristic.

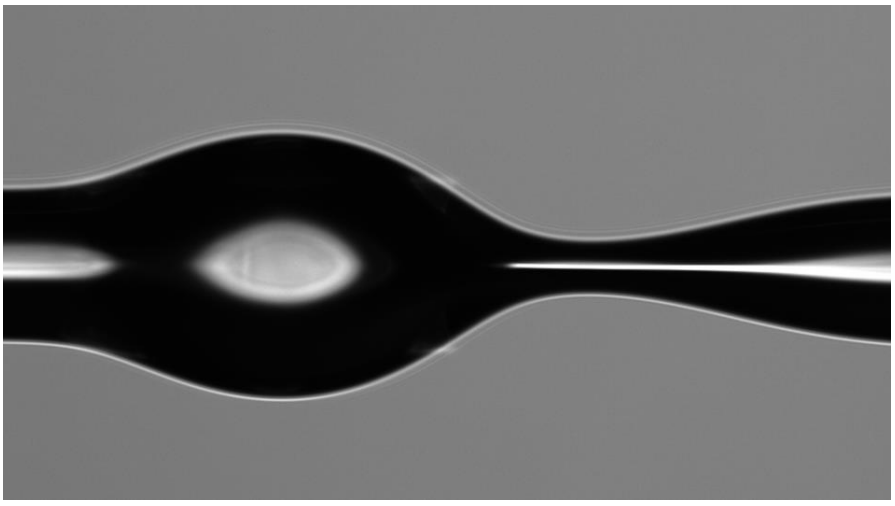

Fig. 8.4.2.2. 300 µm bottle microresonator created in 15 steps using filament technology

8.4.3. Microresonators written in glass

Geuzebroek et al [13, 26] described a type of microresonator fabricated from Si_3N_4 waveguide channels embedded in SiO_2 glass, vertically coupled to a Si_3N_4 ring, having a radius *R*, a technology that exhibited high finesse *F* and added a versatile thermal tuning capability. The structure is represented in Fig 8.4.3.1. A chromium thin film Ω-shape heater was employed to achieve thermal tuning.

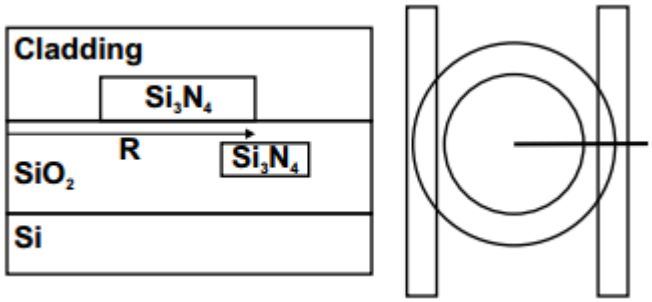

Fig. 8.4.3.1. Si_3N_4 microresonator structure embedded in glass

The effective index of the microresonator and the resonance wavelength change when the temperature is varied. The condition of resonance is described by the following expression for the index of refraction in the resonator n_{res}:

$$\frac{2\pi}{\lambda} R N_{eff} = n_{res}, \qquad (8.4-7)$$

where λ represent the wavelength, *R* the ring radius and N_{eff} the effective index of the mode propagating through the ring.

The shift in resonance wavelength $\delta\lambda_c$ represents a function of the effective refractive index change due to the tuning ΔN_{eff}:

$$\frac{\lambda \Delta N_{eff}}{N_{eff}} = \delta\lambda_c \qquad (8.4-8)$$

The developers of this microresonator structure demonstrated that a shift of the resonance wavelength as large as half of the free spectral range was possible with low power dissipations. The *Q-factor* of such devices is greater than 10^6.

The device was also demonstrated in optical switching experiments. The maximum switching speed is estimated by measuring at which point the amplitude of the received signal drops while increasing the frequency. A maximum switching frequency of around 2 kHz was obtained with a power dissipation of around 10 mW.

In continuation, a broadband characterization of a simplified version of this type of microresonator (only one waveguide channel coupled to the ring and no thermally induced tuning) is described. The method is based on using a dispersion tuned AKSS.

8.4.4. Broadband characterization of microresonators

A waveguide Si_3N_4 channel is coupled to a Si_3N_4 ring, the whole device being embedded in SiO_2 glass. Due to its design, the resonator can be used as a WDM filter, switch or modulator. It was previously shown that through temperature tuning its resonance wavelength can be varied [26].

Characterization with an ultrabroadband source

Using an ultrabroadband source, we acquired subspectra and determined the periodicity of resonances. The utilisation of a large broadband allows evaluation of periodicity of resonances with wavelength. This variation is attributed to the glass dispersion and in this way the index of refraction variation with wavelength can be obtained in a large spectrum.

The set-up illustrated in Fig. 8.4.8.1 comprises a Fianium Femptopower Supercontinuum source, emitting in a very broad spectrum range, 390-2600 nm. To avoid any thermally induced changes in the resonator, the source was set to operate at very low output power, of under 0.5 mW. The resonator assembly is fitted with two 125 µm fibres with FC/APC connectors, used as input and output ports. The output signal is acquired by an Agilent optical spectrum analyser. Fig. 8.4.4.2 depicts an example of the resonance dips measured with the spectrum analyser in a broadband region between 1550 nm and 1600 nm.

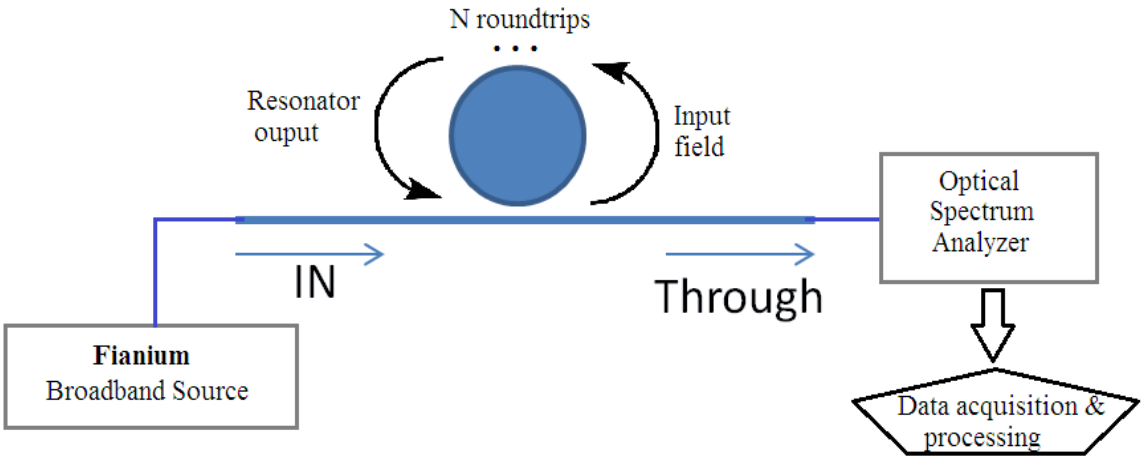

Fig. 8.4.4.1. Microring resonator investigating setup using a Fianium broadband source

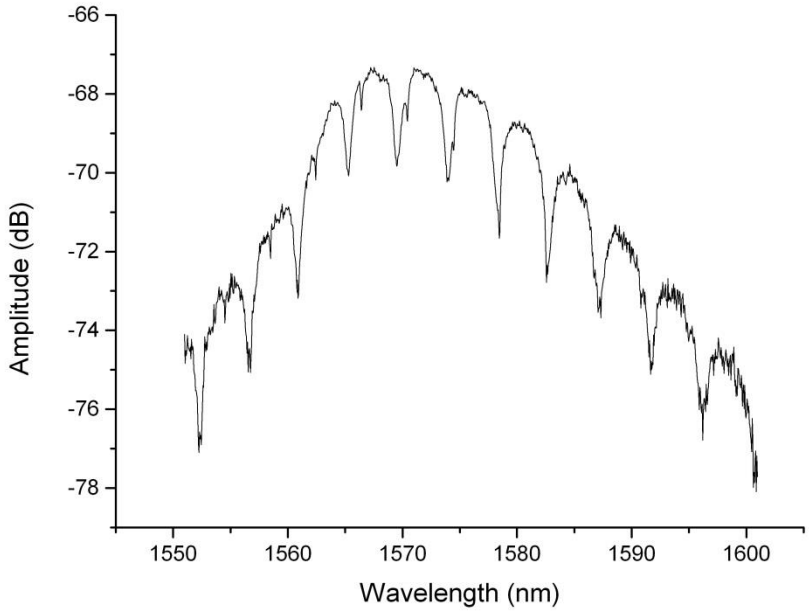

Fig. 8.4.4.2. Microresonator resonance dips measured in the 1550- 1600 nm wavelength region

We have studied several parameters, including the contrast, resonance linewidth and resonance repetition frequency.

Contrast

Using the optical spectrum analyser at a resolution of 0.06 nm, we have selected certain areas of the whole evanescent field coupled in the resonator in a wavelength span of 5-10 nm. We have studied the resonance peaks around the selected area, determining the maximum value of amplitude in the peak and the minimum value around the base. These are used to calculate the contrast using the following formula:

$$Contrast = \frac{A_{max} - A_{min}}{A_{max} + A_{min}}, \qquad (8.4.4 - 9)$$

where A_{max} and A_{min} represent the peak amplitude and, respectively, the base amplitude value. This is graphically represented in Fig. 8.4.4.3. The highest contrast value can be seen between 1450-1500 nm.

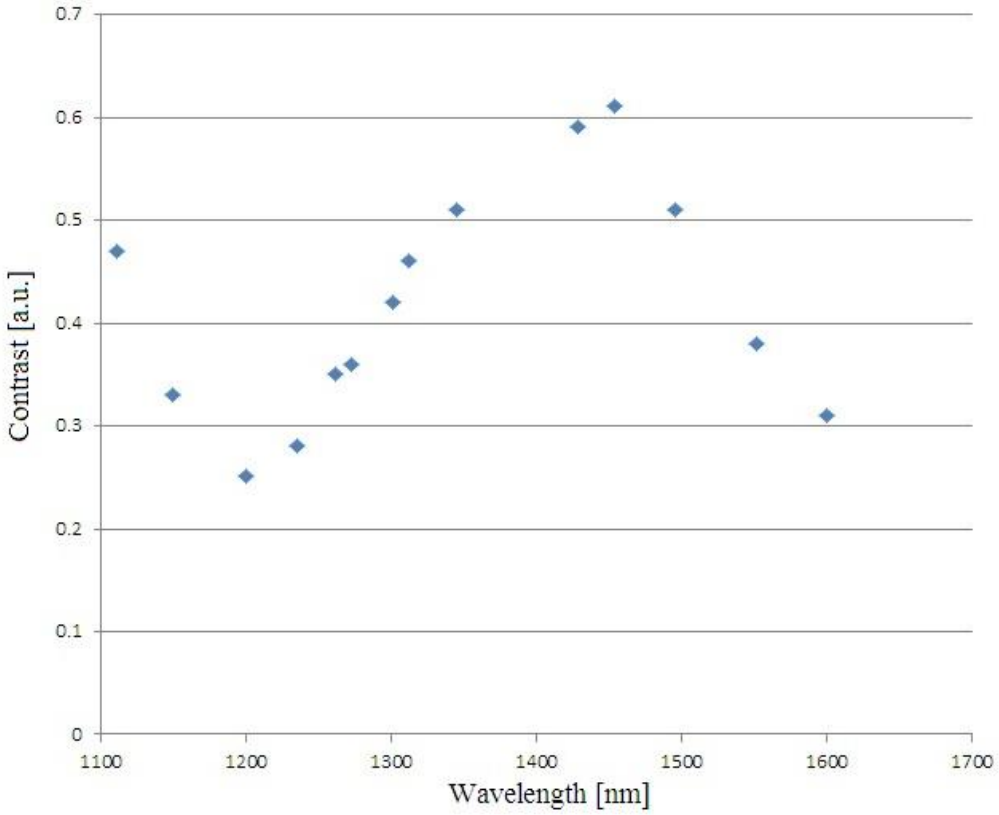

Fig. 8.4.4.3. Contrast of WGM resonances throughout the whole spectrum of light coupled into the microring resonator

Linewidth

As illustrated in Fig. 8.4.4.4, the smallest FWHM linewidth of about 0.25 nm can be observed around the 1300 nm central wavelength, in a range of 50-60 nm around this value. On the other hand, in this region, the amplitude of the signal is relatively low, as as shown by the contrast measurements.

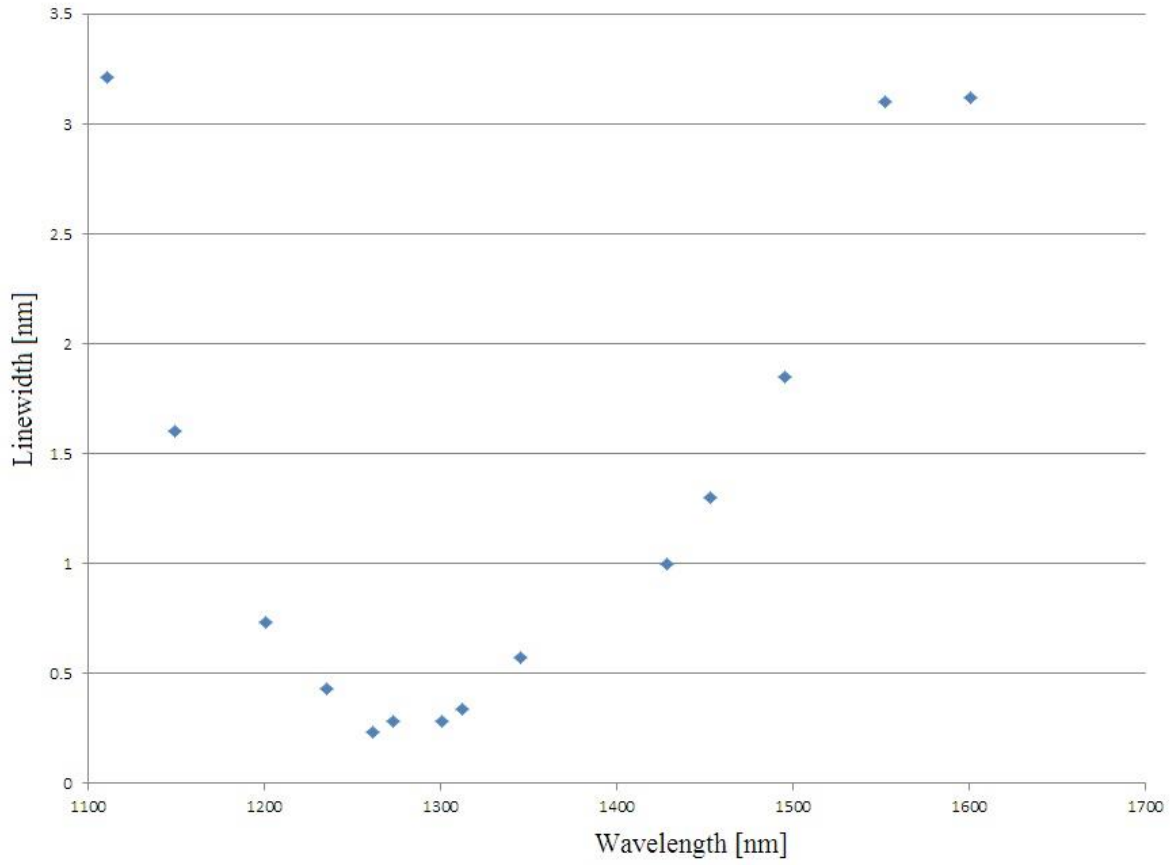

Fig. 8.4.4.4. Resonance linewidth measured along the 1100 – 1700 nm spectrum range

Repetition rate and finesse

By reorganising the data collected into values of frequency using the following formula:

$$\Delta f = \frac{c}{\Delta \lambda} \qquad (8.4.4 - 10)$$

the graphs measured with the spectrum analyser were redrawn. We then evaluated *Δf*, the periodicity in wavenumber (optical frequency), which defines the distance between two adjacent resonance peaks.

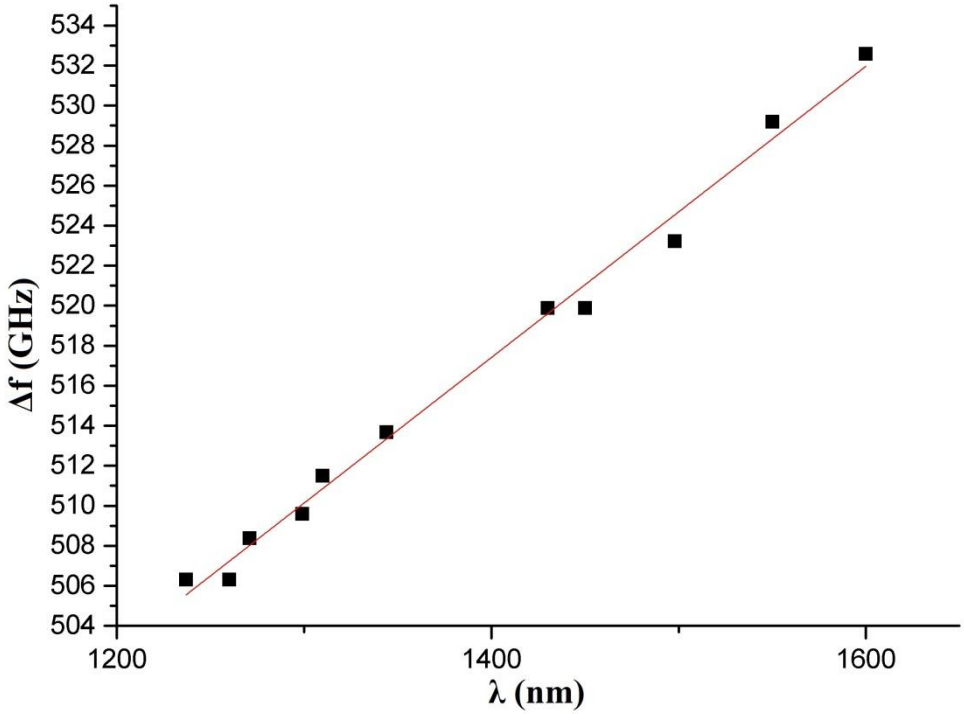

Fig. 8.4.4.5. Repetition frequency of resonance peaks Δf represented along the whole broadband spectrum, 1200-1600 nm

Although a straight constant graph was expected, the values plotted in the above graph (Fig. 8.4.4.5) show a linear increase of the resonances repetition rate throughout the broadband spectrum range. This is attributed to a decrease in the velocity of light in the resonator in respective with the increased wavenumber (or to an increase in the index of refraction). This is obtained by assuming that the periodicity is given by *c/L*, where *L* is the length of the resonator.

Having measured the linewidth and the repetition rate of the resonances in each wavelength region, the next step is to calculate the finesse Fin of the resonator. In the 1550 nm wavelength region for example, considering a *Q-factor* = 10^4, the distance between two resonances is 5 nm (as determined experimentally and illustrated in Fig. 8.4.4.2) and the linewidth of each resonance dip is 2 nm (as measured and plotted in Fig. 8.4.4.4), Fin is calculated 4000.

Measurements were taken at a constant room temperature (approx. 23^{o}C). Further tuning of the resonator (trough temperature change applied to the resonator) might show a change in the repetition frequency of resonances around certain central wavelengths.

Evaluation of dispersion in glass

The ultrabroadband characterisation of microresonators is a useful tool in evaluating the chromatic dispersion in glass, in this particular case the dispersion in the Si_3N_4 disc embedded in silica glass. The output signal acquired with the spectrum analyser showed that resonances occur not only in the band at which the resonator was designed for, 1550 nm, but well outside this band, in the 1200 – 1600 nm spectrum range, in certain selected areas of the whole evanescent field. Using the optical spectrum analyser at a resolution of 0.06 nm, we have explored the whole wavelength range 1200 to 1600 nm using small spans of 5- 10 nm. Larger spans required larger linewidth leading to less accuracy.

Within some bands, the resonances were not all defined to allow measurements, such as: 1100-1200 nm and 1600-1700 nm.

After the measurements, the wavelength scale was translated into frequency and a graph was compiled with the periodicity of resonances, Δf, measured in frequency versus the central wavelengths of the sub-bands used. As the graph shows, Δf exhibits a linear increase with the wavelength. The periodicity of resonances, or the free spectral range, is given by c_w/L, where c_w is the velocity of light in the waveguide and L represents the cavity length of the resonator. This can be further written as:

$$FSR_f = \Delta f = \frac{c}{2\pi R n_g}, \qquad (8.4.4 - 11)$$

where c represents the speed of light in vacuum, R the micro-ring radius, and n_g the group index of refraction [2]. The graph illustrated in Fig. 8.4.4.6 suggests that n_g decreases with wavelength. The chromatic dispersion is obtained by deriving equation (8.4.4 - 11) in respective to λ:

$$\left.\frac{dn}{d\lambda}\right|_{\lambda_0} = -\frac{c}{2\pi R}\frac{m}{\left(\Delta f|_{\lambda_0}\right)^2}, \qquad (8.4.4 - 12)$$

where $m = 0.07278 \cdot 10^{18}$ Hz/m represents the slope of the graph represented above.

We can therefore conclude that utilisation of modern available super continuum optical sources exhibiting ultra-broad bandwidth allows dispersion measurements of the material used to fabricate the microresonators.

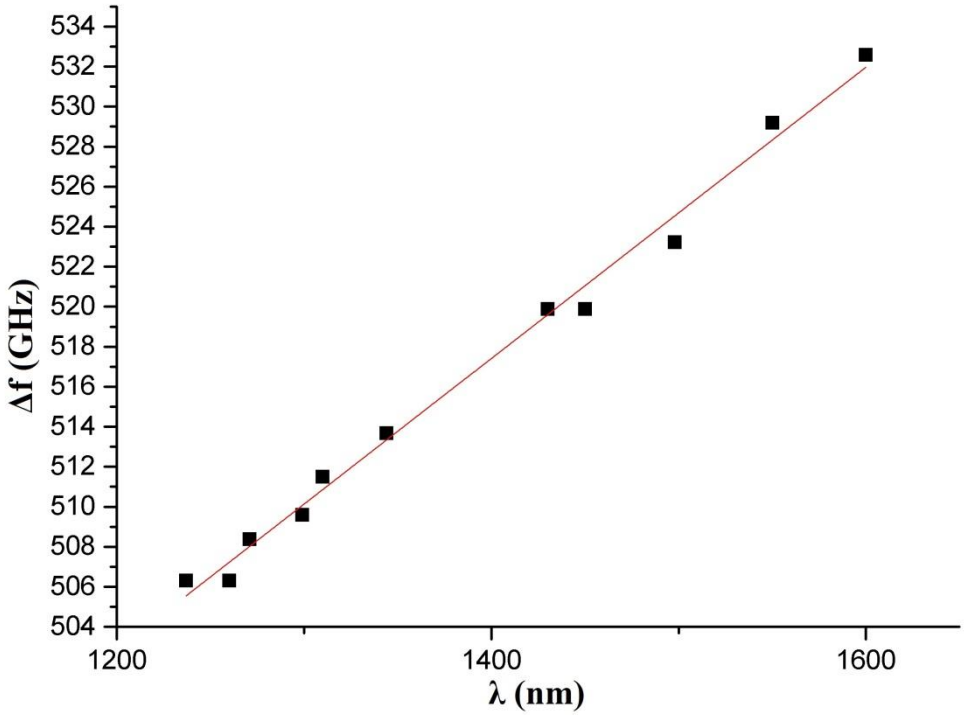

Fig. 8.4.4.6. Index of refraction variation with the wavelength

Proposed characterization with a 1550 nm akinetic swept source

The utilisation of modern available ultrabroadband super continuum optical sources allows microresonator parameter characterisation and dispersion measurements of the material used to fabricate the microresonators. In continuation, we will propose an investigation technique based on akinetic swept sources.

The microresonator investigation setup illustrated in Fig. 8.4.4.7 comprises a single mode-locked AKSS, identical with the one described previously and illustrated in Fig. 8.2.1.1, emitting in a $\Delta\lambda$ = 60 nm spectrum band around the central 1550 nm wavelength, having a linewidth of around 60 pm. The main limitation that might occur would be if the linewidth of the akinetic optical source is larger than the actual resonance linewidth. In order to be able to apply the proposed method, the laser linewidth must be at least equal or smaller than the resonance dip and the distance between two resonances, if a continuous measurement is desired. To avoid any thermally induced changes in the resonator, the source is set to operate at a low output power, of under 0.5 mW, while the room temperature was maintained at 300 K. The resonator assembly is a monolithic device fitted with two 125 µm fibres with FC/APC connectors, used as input and output ports. The output signal is acquired using an Agilent optical spectrum analyser and a Newport 1610 photodetector connected to a low-pass filter and displaying the signal acquired on a LeCroy Wave Runner 104 MXi-A 1GHz oscilloscope, having a maximum sampling rate of 10 Gyga Samples per second. The photodetector is further interfaced with a LabView acquisition board, calibrated and synchronised by the modulating signal driving the AKSS.

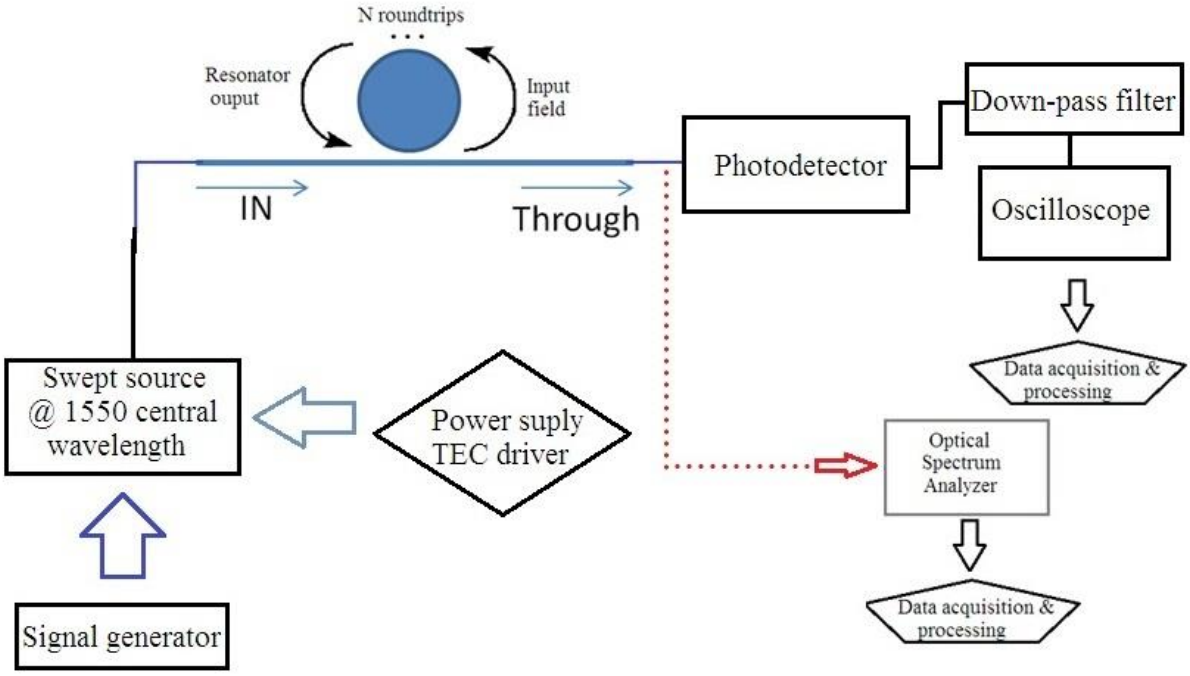

Fig. 8.4.4.7. Testing set-up for microring resonators

The principle of operation is described as follows: in one sweep, characterised by the frequency rate f_s, the whole $\Delta\lambda$ bandwidth is emitted by the AKSS. By multiplying the two parameters, we obtain the velocity V_{laser} of the laser line along the whole spectrum. For example, if f_s = 10 kHz and $\Delta\lambda$ = 60 nm, then $V_{laser} = f_s \cdot \Delta\lambda$ = 10Hz · 60nm = 0.1 · 60 nm/s = 0.006 nm/s = 6 pm/s. Let us suppose that the laser line has constant amplitude A_0 over the whole bandwidth $\Delta\lambda$. When the laser line enters a region of the spectrum where a resonance dip is located, this amplitude A_0 changes and this is measured by the photodetector. Using external real time acquisition software created in LabView, the time t_{res} where the variation in amplitude is registered is measured. Multiplying now $t_{res}/2$ with V_{laser} will give us the linewidth of the resonance dip at FWHM, λ_{dip}. Figures 8.4.4.8 and 8.4.4.9 depict and example of the entry of the scanning laser line in a resonator dip, and respectively passing over the resonance dip region.

Next step is to measure the distance between two consecutive resonances. At the exit from the dip, the amplitude returns to a value identical or slightly larger than the initial value. The time between two dips is measured, and by multiplying it with V_{laser} the distance between resonances is obtained. Having measured those values, the finesse of the resonator can be now calculated.

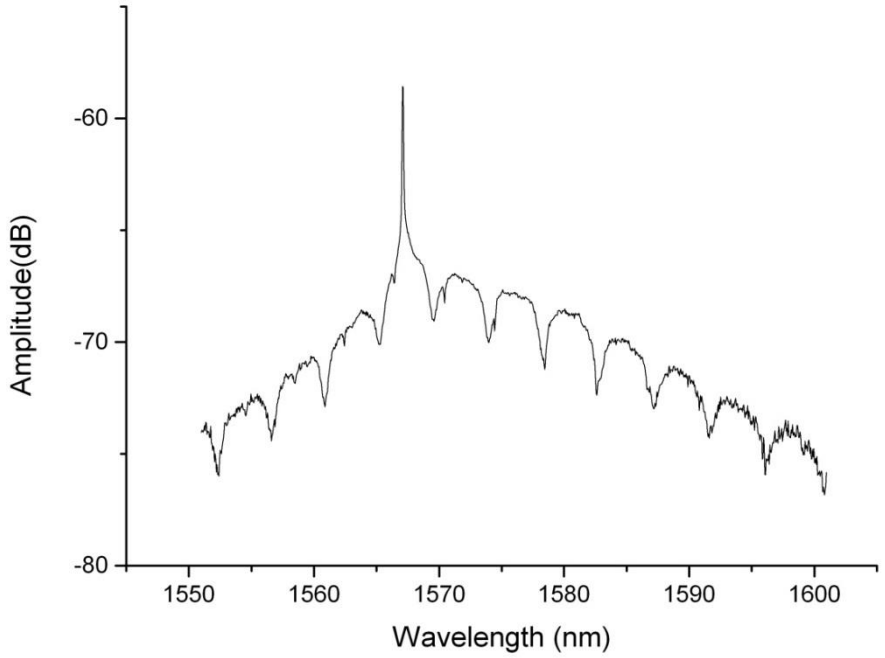

Fig. 8.4.4.8. Scanning laser line entering the 1570 nm resonance dip

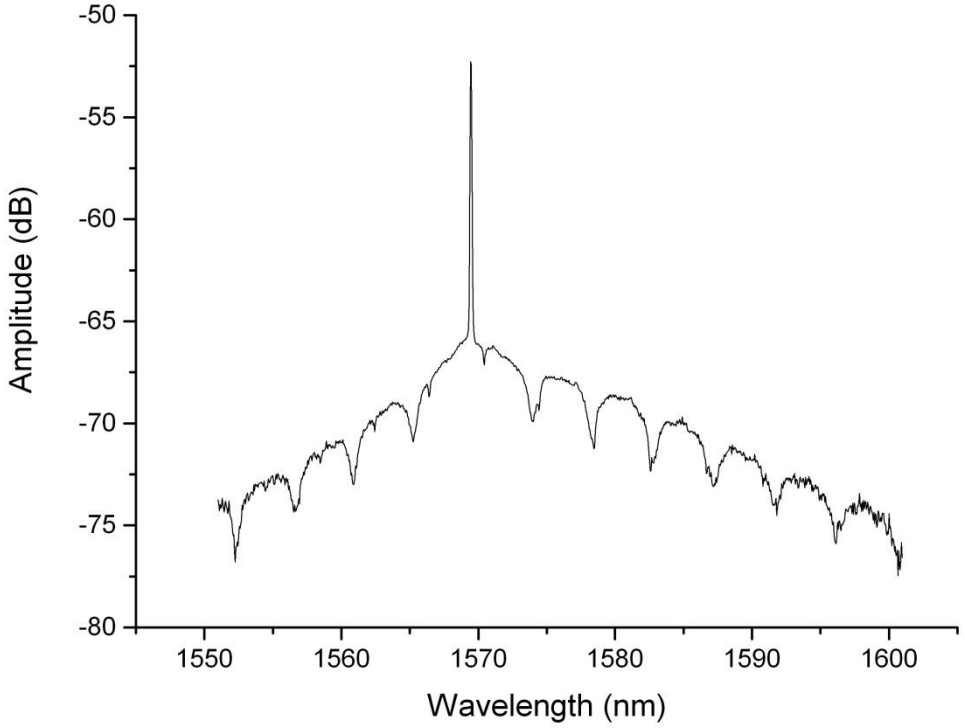

Fig. 8.4.4.9. Scanning laser line passing over the 1570 nm resonance dip

Repeating dynamically this measurement for all the spectral windows covered by the output bandwidth emitted by the swept source, the line shape function *g(k, t)* of the microresonator, where k represents the wavenumber defined as $2\pi/\lambda$, can be evaluated now. The resulting graph depicting the function *g* can be compared with the graph registered by optical analyser.

The photodetected signal *h(k, t)* represents the convolution between the function *g(k, t)* and the interrogating shape function *a(k, t)* of the AKSS (considered a Gaussian function in this case): $g \otimes a = h$. In order to determine the function *g(k, t)*, a more complicated mathematical deconvolution operation would be necessary, but the method proposed here eliminates this need and reconstructs the function from continuous dynamic measurement of data.

Having all the information regarding the resonance dip linewidth and repetition rate, the dispersion in glass for the studied resonator can be calculated as shown in the previous method, which employed the ultrabroadband source.

The main advantages of this proposed method in comparison with the method of characterisation using an ultrabroadband source are the faster acquisition rates, the versatility given by the possibility to dynamically change the AKSS output parameters, better software controlled measurement accuracy (the measurements done when using the ultrabroadband source were done manually, using measuring points provided by the spectrum analyser, adding more error when determining average values of linewidths and repetition rates). The main disadvantage of this method is the limited spectral window covered. In the present case, the resonators studied were designed for operation at 1550 nm, therefore a swept source emitting in the 1550 nm wavelength region is the obvious choice. But if there is a microresonator designed for a different wavelength, like 1060 nm, then a different swept source, emitting in the relevant spectral window, must be utilised.

Summary

To recap, a versatile AKSS was demonstrated, with controllable sweeping parameters. The sweeping speed achieved was up to 20 kHz (limited by the Agilent 81160A RF generator) and tuning bandwidth of 20 – 40 nm. Using a booster, the power was increased up to 12 mW.

After that, a versatile electronically controlled dual mode-locked AKSS was demonstrated. The SOA was driven at hundreds of MHz to produce mode-locking in the ring cavity, while the frequency of the electronic signal driving the SOA was swept at a rate inverse proportional to the cavity length. Using such a DML configuration, operation at large repetition rate values of 800 kHz was demonstrated.

When employing a broadband FRM in a swept source configuration using the DML principle, sweeping rates in the range of MHz are achievable, from a rate values of f_R = 782 kHz to up to 5 multiples of f_R, with a proportional decrease in the tuning bandwidth. Further optimization of the RF excitation can lead to larger tuning bandwidths and better sensitivity values.

The main parameters of the 1550 nm DML AKSS are illustrated in the following table:

Parameter	**Value**
Central wavelength	1550 nm
Mode-locking	100 – 1000 MHz
Maximum Output Power	12 mW
Linewidth	60 pm
Bandwidth	35 nm (@1 KHz), 27 nm (@800 kHz)
Repetition rate	782 kHz or multiples of this value

The main parameters of the 1550 nm DML AKSS employing FRM are illustrated in the following table:

Parameter	**Value**
Central wavelength	1550 nm
Mode-locking	100 – 1000 MHz

Maximum Output Power	12 mW
Linewidth	60 pm
Bandwidth	60 nm (@1 kHz), 38 nm (@800 kHz)
Repetition rate	782 kHz or multiples of this value
Relative intensity noise	1.4%

The main advantages of this proposed method of microresonator characterising using a DML AKSS at 1550 nm in comparison with the method using an ultrabroadband source are the faster acquisition rates, the versatility given by the possibility to dynamically change the AKSS output parameters and better software controlled measurement accuracy.

References

[1] S. Yamashita, Y. Nakazaki, R. Konishi, O. Kusakari, "Wide and fast wavelength-swept fiber laser based on dispersion tuning for dynamic sensing", Journal of Sensors, Vol. 2009, 572835 (2009)

[2] Akira Takada, Makoto Fujino, and Shigenori Nagano, "Dispersion dependence of linewidth in actively mode-locked ring lasers", Optics Express 20, 4753-4762 (2012)

[3] A. Gh. Podoleanu, A. Bradu, "Master-Slave interferometry for parallel spectral domain interferometry sensing and versatile 3D optical coherence tomography", Optics Express, Vol. 21, No. 16, 19324-19338 (2013)

[4] R. H. Huber, M. Wojtkowski, J.G. Fujimoto, "Fourier Domain Mode-locking (FDML): A new laser operating regime and applications for optical coherence tomography", Optics Express 14(8), 3225-3237 (2006)

[5] Y. Takubo, S. Yamashita, Photonics Technology Letters, "In-vivo OCT imaging using wavelength swept fiber laser based on dispersion tuning", vol. 24, no. 12, pp. 979-981, June 2012.

[6] R. F. Stancu, D. A. Jackson, A. G. Podoleanu, "Versatile Swept Source with Adjustable Coherence Length", IEEE Photonics Technology Letters 26 (16), 1629-1632 (2014)

[7] Y. Takubo, S. Yamashita, "High-speed dispersion-tuned wavelength-swept fiber laser using a reflective SOA and a chirped FBG", Optics Express, vol.21, no.4, pp.5130-5139 (2013)

[8] B. R. Biedermann, Wolfgang Wieser, Christoph M. Eigenwillig, Thomas Klein and Robert Huber, "Dispersion, coherence and noise of Fourier domain mode locked lasers", Optics Express, 17(12), 9947-9961 (2009)

[9] R. Huber, D.C. Adler, J. G. Fujimoto, "Buffered Fourier domain mode-locking: unidirectional swept laser sources for optical coherence tomography imaging at 370,000 lines/s", Optics Letters, 31(20), 2975-2977 (2006)

[10] M. Sumetsky, D. J. DiGiovanni, Y. Dulashko, X. Liu, E. M. Monberg, and T. F. Taunay, "Photo-induced SNAP: fabrication, trimming, and tuning of microresonator chains", Optics Express 20(10), 10684-10691 (2012)

[11] Akgul, M., Schneider, R., Zeying Ren, Chandler, G., Yeh, V., Nguyen, C.T.-C., "Hot filament CVD conductive microcrystalline diamond for high Q, high acoustic velocity micromechanical resonators", Frequency Control and the European

Frequency and Time Forum (FCS), 2011 Joint Conference of the IEEE International, pp. 1-6 (2011)

[12] Samadhan B. Patil, T. Adrega, V. Chu, J. P. Conde, "Thin film silicon MEMS microresonators fabricated by hot-wire chemical vapor deposition", Journal of Micromechanics and Microengineering, 16(12), 2730-2735 (2006)

[13] Geuzebroek, D. H., Klein, E. J., Kelderman, H., Driessen, A.," Wave-length tuning and switching of a thermo-optic micro ring resonator", in Proceedings of the 11th European Conference on Integrated Optics (ECIO), (Czech Technical University Prague, Prague, Czech Republic) (ISBN 80-01-02729-5), pp. 395-398 (2003)

[14] Matsko, A.B., Ilchenko, V.S. "Optical resonators with whispering-gallery modes-part I: basics.", Selected Topics in Quantum Electronics, IEEE Journal of 12, 3–14 (2006)

[15] A. Driessen et al., "Analysis of a microring resonator based ultra-compact transceiver for the access network.", Proc. Symposium IEEE/LEOS Benelux, pages 25-28, (2001)

[16] Dion J. W. Klunder, Chris G. H. Roeloffzen, Alfred Driessen, "A Novel Polarization-Independent Wavelength-Division-Multiplexing Filter Based on Cylindrical Microresonators", IEEE JOURNAL OF SELECTED TOPICS IN QUANTUM ELECTRONICS 8(6), 1294-1299 (2002)

[17] Jiangang Zhu, Sahin Kaya Ozdemir, Yun-Feng Xiao, Lin Li, Lina He, Da-Ren Chen, Lan Yang, "On-chip single nanoparticle detection and sizing by mode splitting in an ultrahigh-Q microresonator", Nature Photonics 4, 46 - 49 (2010)

[18] A. Gupta, D. Akin, R. Bashir, "Single virus particle mass detection using microresonators with nanoscale thickness", Applied Physics Letters 84(11), 1976-1978 (2004)

[19] Matsko, A.B., Ilchenko, V.S. "Optical resonators with whispering-gallery modes-part II: applications." , Selected Topics in Quantum Electronics, IEEE Journal of 12, 15- 32 (2006)

[20] Brent E. Little, J.-P. Laine, Hermann A. Haus, "Analytic theory of coupling from tapered fibers and half-blocks into microsphere resonators", Lightwave Technology, Journal of 17, 704-715 (1999)

[21] Hiremath, K., Hammer, M., “Circular Integrated Optical Microresonators: Analytical Methods and Computational Aspects”, Photonic Microresonator Research and Applications 156, 29-59 (2010)

[22] M. V. Chistiakova, A.M. Armani, “Cascaded Raman microlaser in air and buffer”, Optics Letters Vol. 37, Issue 19, pp. 4068-4070 (2012).

[23] J. D. B. Bradley, E. S. Hosseini, Purnawirman, Z. Su, T. N. Adam, G.Leake, D. Coolbaugh, M. R. Watts, “Monolithic erbium- and ytterbium-doped microring lasers on silicon chips”, Optics Express 22(10), 12226-12237 (2010)

[24] Tobing, L. & Dumon, P., “Fundamental Principles of Operation and Notes on Fabrication of Photonic Microresonators”, Photonic Microresonator Research and Applications 156, 1-27 (2010)

[25] Armani, A.M., Vahala, K.J., “Biological and chemical detection using ultra-high-Q toroidal microresonators”, Biophysical Society (2007)

[26] Geuzebroek, D.H., Driessen, A., “Ring Resonator based Wavelength Filters” in Venghaus, Herbert (Ed.), “Wavelength Filters for Fibre Optics”, pp. 341-379, Springer (2006)

9

Conclusions

Swept source optical coherence tomography represents a modern, non-invasive technique of tissue biomedical imaging, either *in vivo*, or *in vitro*, that uses fast swept narrow linewidth lasers within a sufficiently wide tuning bandwidth. In over a decade, several principles of swept sources have been reported so far, including in the Applied Optics Group at the University of Kent. A more recent interest was dedicated by the group into developing fast broadband akinetic swept lasers for OCT and other applications, like WGM, with the intention of eliminating mechanical devices susceptible to electrical shocks and introducing more fibre based elements that are meant to reduce costs as much as possible, to enhance laser output parameters and to achieve in the end a compact laser device.

The main achievement in this work was the development of a novel dual mode-locking mechanism. A first locking condition is imposed by driving the optical gain at a high frequency, to induce mode-locking, similar to the dispersion tuning method. A second locking mechanism, inspired from the practice of FDML applied to TFPF lasers, employs sweeping at a rate close to f_R, however in opposition to FDML, at essentially different values than f_R. To produce FDML, the roundtrip time needs to be increased to amenable values, which requires several hundreds of meters of fibre, i.e. this strategy is opposed to that suggested by FDML. Tuning of hundreds of kHz and even MHz level was achieved, and the DML operated sources were successfully applied in either scanning the channelled spectrum of basic interferometers or in topographic OCT imaging.

The integration of FRM in a ring laser cavity also represents an important contribution, because it facilitate the halving of the necessary fibre needed for dispersion tuning and also improved the optical output parameters of the DML swept lasers. Other significant contribution is represented by the creation of a 1060 nm small cavity ring laser

by integrating a totally reflective cFBG which acts as a highly dispersive element and facilitates tuning at hundreds of kHz.

Several AKSS configurations and mode-locking mechanisms were developed and studied and the results were illustrated in this thesis.

An electronically controlled AKSS at 1550 nm using mode-locking in a dispersive ring cavity was described. Active mode-locking was achieved by directly modulating the current of a SOA used as a gain medium. In the static regime, parameters such as linewidth, tuning bandwidth and contrast were measured, while the axial range was determined dynamically. Two types of fibre, DCF and SMF, are employed in the laser ring cavity. It is demonstrated that the relative lengths of the two types of fibre has little effect on the linewidth, while more control on the linewidth is obtained via the frequency of the signal driving the SOA. Linewidths less than 60 pm and over 1 nm were measured in the static regime while driving the SOA at 50 – 500 MHz. The narrowest linewidths were achieved where the proportion of dispersion compensation fibre in the cavity is 80-90% of the total length. The optical source is developed to respond to the demands of several OCT applications that do not necessarily need long coherence length swept sources.

An optical AKSS at 1060 nm, very short, comprising a 5 m SMF length fibre ring cavity, a SOA as gain medium and a 98% reflective CFBG used as dispersive element, was also presented. Active mode-locking was achieved by directly modulating the current of the SOA with sinusoidal signal of frequency equal to 10 and 20 times the cavity resonance frequency. In the static regime, linewidth narrower than 60 pm and a tuning bandwidth of 30 nm were achieved, while a 2 mW output power, without any optical booster, was measured dynamically at a sweep speed of 100 kHz. The axial range of the AKSS was evaluated by scanning through the channelled spectrum of a Mach-Zehnder interferometer.

In this thesis a configuration of an AKSS, similar in structure with that reported in dispersion tuning papers, which additionally implements a novel dual locking scheme (DML), inspired from the FDML procedure, was presented.

A fast DML AKSS, in the 1550 nm wavelength band, operated at high sweep rates up to 797 KHz, was developed. The SS comprises a voltage controlled oscillator (VCO) driven wideband semiconductor optical amplifier (SOA) along with dispersion compensation fibre (DCF), in a ring laser configuration. A Faraday rotating mirror (FRM) was employed in the cavity as reflective element in order to achieve better polarization control. By driving the optical gain medium at a high multi MHz frequency, multiple of the resonant frequency, f_R, equal to the inverse round trip time, a first mode-locking mechanism

is imposed. A second locking mechanism consists in sweeping the radio frequency of the locking signal at a rate slightly detuned from f_R. A dynamic linewidth of 0.05 nm is assessed by measuring the decay of interference signal strength versus *OPD* in a Mach-Zehnder interferometer. The DML mechanism allows MHz rates to be obtained directly, with no buffering, reducing the cost and complexity of the AKSS.

The fast and broad AKSS developed at 1060 nm central wavelength exhibited similar results in terms of power and coherence length, and plus, it was used in performing topographic OCT imaging at multiples of a repetition rate detuned from f_R.

Future work

The author proposes as future work the development of a GHz level electronic tuning mechanism, integrating combined VCOs, fully compensated for noise and any electronic resonances, that has the possibility to switch between several regimes of operations when tuning the gain of an AKSS cavity. Also, it would be necessary to improve the RF excitation conditions, to allow a more efficient use of higher frequencies, such as when operating at multiples of f_R. These improvements shall allow MHz sweep rates without the AKSS exhibiting significant decays in optical tuning. Furthermore, utilisation of several SOAs as gain media, emitting different IR broadband spectral windows can be considered in order to create a DML ultrabroadband source, in order to add versatility when such a device would be used in various applications, like OCT and biomedical research in general, material resistance, surface topography, microresonator and micro-optics research and so on.

More work is also required in order to achieve not only high sweeping rate (MHz level), but also sufficient tuning bandwidth (at least 100 nm) and output power values (wihout needing a booster for output amplification). The 1060 nm AKSS employing a FRM in the cavity halved the necessary fibre in the ring cavity and also showed improvement in output parameters compared with the AKSS without FRM. This proves the importance in handling polarisation in long fibre configurations. Further optimization of the RF tuning can lead to larger tuning bandwidths, improved linewidth and better sensitivity and axial range values. This refers to higher ac current through SOA, not possible to be achieved using the largest RF amplifier at hand, due to the RF circuit driving the SOA having too long leads. These behave like low pass filters. If SOA devices can be paired with waveguides, then

larger RF excitation becomes possible with immediate consequence in terms of dynamic linewidth that leads to larger axial range.

Further studies require optimization of the DCF:SMF ratio in the 1550 nm AKSS and use of a SOA with larger bandwidth for better control of the coherence length and enhanced axial resolution.

The author also proposed further developments in the short cavity lasers for other central wavelengths, like 850 nm, 1310 or 1550 nm. In comparison with optical fibres operational within other wavelengths bands (1060 nm, 1550 nm, 850 nm), the optical fibre at 1310 nm has 0 dispersion value. Therefore the dispersion tuning mechanism is no longer possible to apply and a model inspired from the distributed Bragg reflector (DBR) [14] lasers must be applied. A DBR is a laser that is made with a Bragg mirror (quarter-wave mirror) outside a gain medium.

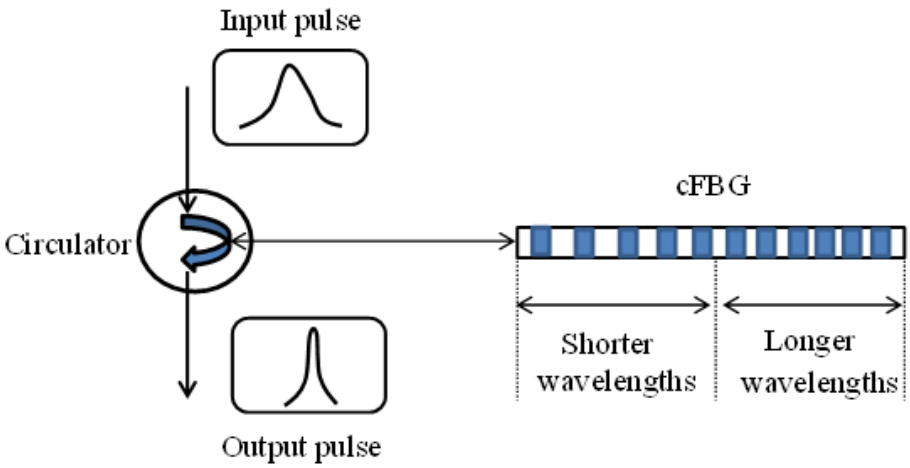

Fig. 9.1 CFBG principle of operation

In our case, the inline cavity proposed in Fig. 9.2 comprises a reflective SOA emitting at 1310 nm central wavelength as gain medium and a partially reflective cFBG.

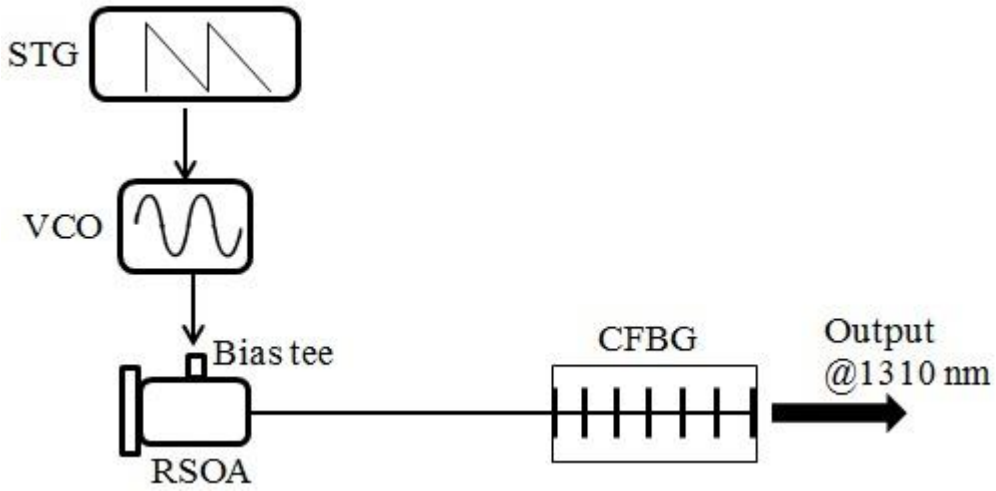

Fig. 9.2. Proposed 1310 nm short cavity wavelength swept laser

The wavelength of maximum reflectivity depends not only on the Bragg grating period but also on temperature and mechanical strain. In order to achieve tuning in a wider bandwidth as possible, a broadband cFBG is necessary.

The thesis also featured a proposed method of ultra-broadband characterization of micro resonators embedded in glass. This research is still in an incipient stage and the author intends to proceed in introducing the DML AKSS at 1550 nm into a microresonator investigation equipment.

Scientific dissemination

The work presented in this thesis led to 3 peer reviewed papers as first author, one US Patent application, one conference paper, 3 conference poster presentations and 5 conference oral presentations.

US Patent application

A. Podoleanu, R. F. Stancu, "Akinetic swept laser apparatus and method for fast sweeping of the same"

Peer reviewed papers

1. R. F. Stancu, D. A. Jackson, A. G. Podoleanu, "Versatile Swept Source with Adjustable Coherence Length", IEEE Photonics Technology Letters 26 (16), 1629-1632 (2014)
2. R. F. Stancu, A. G. Podoleanu, "Dual-mode-locking mechanism for an akinetic dispersive ring cavity swept source", Optics Letters 40(7), 1322-1325 (2015)
3. R. F. Stancu, A. G. Podoleanu, "Short ring cavity swept source based on a highly reflective chirped FBG", Photonic Sensors 5(3), 251-256 (2015)

Conference proceedings

Radu F. Stancu, David A. Jackson, Adrian G. Podoleanu, "Akinetic swept source with adjustable coherence length for SS-OCT", Proc. SPIE 9312, SPIE BiOS 931238-931238-5 (2015)

Conference oral presentations

1. Radu F. Stancu, Ramona Cernat, Adrian Bradu, David Jackson, Adrian Podoleanu "Ultrabroadband and Optical Swept Source Investigation of Microresonators Embedded in Glass", School of Physical Sciences Colloquium, University of Kent, September 2013

2. Radu F. Stancu, David A. Jackson, Adrian Gh. Podoleanu, “Versatile optical swept source for OCT applications”, Bran, Romania, Mai 2014
3. Radu F. Stancu, “Optical coherence tomography using akinetic optical sources”, International Conference for Physics Students 2014, Heidelberg, Germany, August 2014
4. Radu F. Stancu, "Building an imaging laser device - an interdisciplinary approach", Imaging the Optical Frontier - A Colloquium Exploring Opportunities for Intergroup Collaboration, 4th of November 2014, University of Kent, UK
5. Radu F. Stancu, Adrian G. Podoleanu, “1060 nm Dual Mode-Locked Akinetic Lasers”, ROMOPTO, September 2015, Bucharest, Romania

Conference poster presentations

1. R.-F. Stancu, A. Bradu, David A. Jackson, A. Podoleanu, “Whispering Gallery Modes in tapered structures created using filament processing technology”, International Conference for Physics Students 2013, Edinburgh, UK, Aug. 2013
2. Radu F. Stancu, David A. Jackson, Adrian Gh. Podolean, “Versatile optical swept source for OCT applications”, University of Kent - Electronics and Digital Arts School Research Conference, UK, Jan. 2014
3. R. F. Stancu, D. A. Jackson, A. G. Podoleanu, “Akinetic swept source with adjustable coherence length for SS-OCT”, SPIE Photonics West 2015, BIOS, San Francisco, USA, Feb. 2015